Novel Deposition Methods for Metal Dithiolenes

Simon Dalgleish

A thesis submitted in fulfilment of the requirements
for the degree of Doctor of Philosophy
to the
University of Edinburgh
2010

Abstract

Square planar metal *bis*-dithiolenes are interesting targets for incorporation into electronic and optoelectronic devices as they characteristically display multiple stable redox states, coupled with strong absorption at particularly low energies. This work focuses on novel methods for the formation of thin films of metal *bis*-dithiolenes for incorporation into devices.

The synthesis, structure and spectroscopic properties of a novel class of polymerisable heteroleptic nickel dithiolene complex, containing pendent thiophene units, [Ni(R_2pipdt)(b-3ted)] are described [R = Bz (**3a**), ^{i}Pr (**3b**); pipdt = piperazine-3,2-dithione; b-3ted = *bis*-(3-thienyl)-1,2-ethylenedithiolene]. Electrooxidation of (**3a**) showed it to incorporate into a polymeric film over an electrode surface, which consisted of intact dithiolene units, by covalent linking of the pendent thienyl groups. This polymer film showed some redox activity, with the intense, low energy, absorption red-shifted by 4360 cm^{-1}. Co-polymerisation of (**3a**) with thiophene yielded a highly conductive film, with the intense, low energy, absorption red-shifted to a lesser extent (3500 cm^{-1}). The films displayed interesting optical properties, however, their use was restricted by their poor redox activity, thought to be due to poor ion transport through the films.

The synthesis of two novel dithiolene ligand systems, containing pendent polymerisable indolyl groups (mi-5edt and mi-5hdt), are described, and their incorporation into complexes investigated for nickel [Ni(mi-5edt)$_2$ (**6**) and Ni(mi-5hdt)$_2$ (**8**)], and copper {[Cu(mi-5edt)$_2$][TMA] ([**7**][TMA]) and [Cu(mi-5hdt)$_2$][TMA] ([**9**][TMA])} investigated [(mi-5edt) = 1-(*N*-methylindol-5-yl)-ethane-1,2-dithiolate and (mi-5hdt) = 1-(*N*-methylindol-5-yl)-hex-1-ene-1,2-dithiolate, TMA = tetramethylammonium]. Each complex was characterised in terms of its structure, redox and optical properties, and the effect of the ligand design, and the metal centre, compared. The complexes of nickel were shown to yield polymer films under electrooxidative conditions, through covalent linking of the indolyl groups, with superior redox activity to **3a**, and with

an equally intense low energy absorption. The monoanionic complexes of copper were shown to deposit, under electrooxidative conditions, as neutral molecular films that were otherwise unobtainable by conventional solution techniques.

The incorporation of the more soluble novel indolyl functionalised nickel dithiolene **8** into electronic devices was investigated. Electrochromic devices were formed using poly-**8** as the active layer. The devices were able to switch their optical absorption profile at 860 nm through three absorbing states by application of a suitable potential difference across the film. Field-effect transistors were fabricated using a molecular film of **8** as the active layer. The devices showed ambipolar charge transport properties, though with a bias for *n*-channel operation, with mobilities $\mu \approx 1$ x 10^{-4} $cm^2V^{-1}s^{-1}$. Photovoltaic devices were formed from a blended film of **8** with P-3HT and with MDMO-PPV [P-3HT = regioregular poly-3-hexylthiophene, MDMO-PPV = poly(2-methoxy-5-(3',7'-dimethyloctyloxy)-1,4-phenylene-vynylene)]. **8** was shown to contribute to the photocurrent at wavelengths beyond the polymer component, thus harvesting more visible light, however efficiencies below 0.1 % suggested inefficient charge transport by **8** in the film.

Structurally continuous films of Ni(b-3ted)$_2$ (**10**) could be formed by a process of electrodeposition. The formed films displayed conductivities 40 times greater than for conventional solution cast films. By a detailed study of the level of residual ion doping, the molecular packing, and the morphology of the films, this improved performance was attributed to the formation of a more dense polycrystalline array, with larger crystallites, which formed good electronic contact with the electrodes, and with each other. This electrodeposition technique was used to fabricate field-effect transistors from **10**. The devices showed poor mobilities ($\mu \approx 1$ x 10^{-8} $cm^2V^{-1}s^{-1}$), owing to the poor intermolecular overlap of the dithiolene units in the solid-state, but suggested this technique to be suitable for a wide range of semiconductors, with more favourable electronic properties, as an alternative to conventional vapour or solution deposition.

Declaration

I do hereby declare that this thesis was composed by myself and that the work described within is my own, except where explicitly stated otherwise.

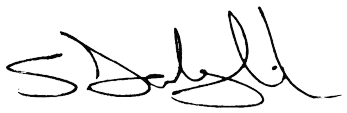

Simon Dalgleish
September 2010

Acknowledgements

First and foremost, I would like to express my thanks to Neil Robertson for giving me the opportunity to work for him. Over the past three years, he has supported me in many capacities; as a supervisor he helped me to target my research, redirecting projects when they wondered off course; as a tutor he has helped me make the change from as an organic synthetic chemist to a materials scientist; as a careers counsellor he has supported me in finding a postdoc position, and stood me in the best stead for my future career.

Changing fields for a PhD can be a daunting experience, however it is to the credit of the University of Edinburgh that they have developed such an 'open-door' atmosphere to the research school, that knowledge can be sought so freely in the department from the many experts that the University has acquired.

With this in mind, I would like to express my deepest gratitude to the many people at Edinburgh University that have helped me during my PhD. In particular, I would like to thank Carole Morrison and Patricia Richardson for their tireless help with computational chemistry. For useful discussions about electropolymerisation, I would like to thank Andy Mount and John Henry. I would like to thank the Edinburgh Crystallography Service, especially Fraser White, for resolving crystal structures. For helping to keep my organic chemistry up to scratch I would like to thank Hamish McNab. I would also like to thank Peter Tasker for always taking an interest in my work and for always having a story to tell. I would like to thank Alan Taylor and Marika DeCremoux for managing so well the Mass Spec, and NMR services, respectively.

I have been lucky enough to collaborate with some fantastic groups during my PhD. I would like to thank Paola Deplano for allowing me the opportunity to work with her at the University of Cagliari. I would also like to thank Luca Pilia for his help, and for making me feel so welcome during my stay in Cagliari. I would like to thank Kunio Awaga, and all his group members, for a very successful collaboration with Nagoya

University. I would like to thank Neil Greenham, and his group for their help during a collaboration with the University of Cambridge. I would also like to thank Thomas Anthopoulos at Imperial College for his collaboration.

I would also like to thank the Robertson group, both past and present, for their friendship, and for useful discussions.

Almost finally, I would like to thank my friends and family for their support during my PhD. I would especially like to thank Louisa Reissig (Dalgleish) for supporting me, in every sense of the word, over the past year. In particular, I would like to thank her for her help whilst writing this thesis - I would not have submitted on time, and in time for our trip to Japan, without her help. For the thankless task of proof reading this thesis, for sorting out my reference library, for helping with formatting, and for her tireless help with the quantum mechanics of computational chemistry, I would like to say a huge thank you.

Finally, I would like to thank the EPSRC for funding my PhD, and the COST network and the Japanese Science and Technology Agency (JST) for additional funding for conferences and collaboration.

Structures

Structures synthesised in this work

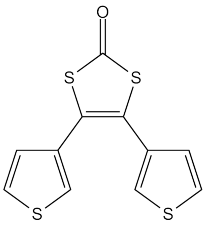

'b-3ted' precursor
bis-(3-thienyl)-ethylene1,2-dithiol-2-one
(**1**)

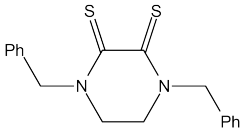

Bz_2pipdt
1,4-dibenzyl-piperazine-
3,2-dithione
(**2a**)

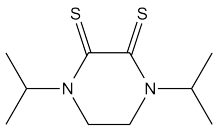

Bz_2pipdt
1,4-isopropyl-piperazine-
3,2-dithione
(**2b**)

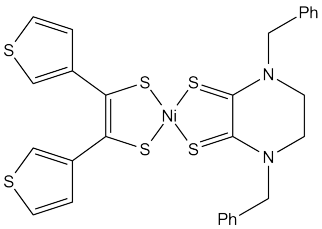

[Ni(Bz_2pipdt)(b-3ted)]
(**3a**)

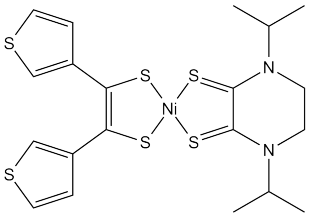

[Ni($^{i}Pr_2$pipdt)(b-3ted)]
(**3b**)

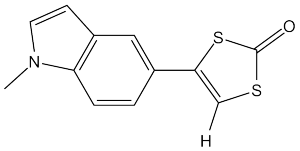

'mi-5edt' precursor
1-(*N*-methylindole-5-yl)-ethene-1,2-dithiol-2-one
(**4**)

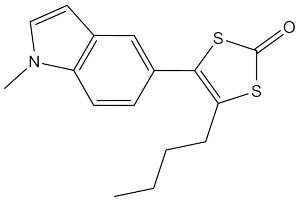

'mi-5hdt' precursor
1-(*N*-methylindole-5-yl)-hex-1-ene-1,2-dithiol-2-one
(**5**)

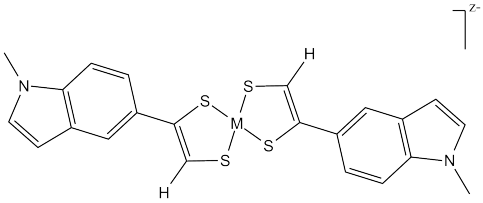

$[M(mi\text{-}5edt)_2]^{z-}$
M = Ni (**6**)
M = Cu (**7**)

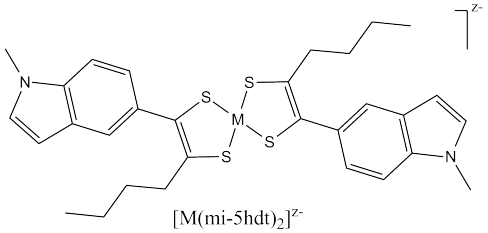

$[M(mi\text{-}5hdt)_2]^{z-}$
M = Ni (**8**)
M = Cu (**9**)

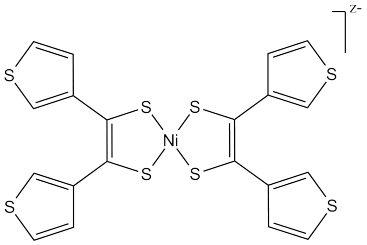

$[Ni(b\text{-}3ted)_2]^{z-}$
(**10**)

Structures referred to in this work

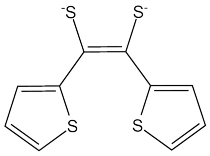

bis-(2-thenyl)-ethylene-1,2-dithiolate
b-2ted

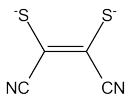

maleonitrile dithiolate
mnt

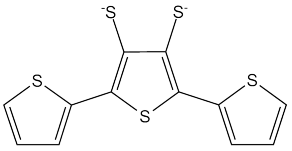

4,6-*bis*-(2-thienyl)-thieno-[3,4-d]-dithiolate
b-2tted

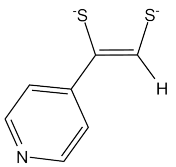

1-(pyridin-4-yl)-ethylene-1,2-dithiolate
4-pedt

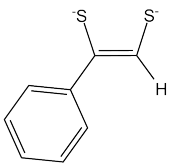

1-phenyl-ethylene-1,2-dithiolate
ped

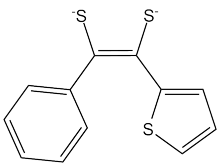

1-phenyl-(2-thienyl)-ethylene-1,2-dithiolate
ped

Abbreviations

AcOH	-	Acetic acid
AIBN	-	2,2-azobis(2-methylpropionitrile)
BHJ	-	Bulk heterojunction
b-2ted	-	*bis*-(2-thienyl)-ethylene-1,2-dithiolene
b-3ted	-	*bis*-(3-thienyl)-ethylene-1,2-dithiolene
b-2tted	-	4,6-*bis*-(2-thienyl)-thieno-[3,4-d]-dithiolate
^{t}BuOK	-	Potassium *tert*-butoxide
CIGS	-	Copper indium gallium selenenide/sulfide
CV	-	Cyclic voltammetry
CVD	-	Chemical vapour deposition
DCM	-	Dichloromethane
(TD-)DFT	-	(Time-dependent) density functional theory
DMF	-	Dimethyl formamide
DMSO	-	Dimethyl sulfoxide
DSSC	-	Dye-sensitised solar cell
ECD	-	Electrochromic device
EIS	-	Electrochemical impedance spectroscopy
Et_2O	-	Diethyl ether
EtOAc	-	Ethyl acetate
EtOH	-	Ethanol
EQE	-	External quantum efficiency
FET	-	Field effect transistor
(C)GTO	-	(Contracted) Gaussian type orbital
(TD-)HF	-	(Time-dependent) Hartree-Fock
HMDS	-	Hexamthyldisilane
HOMO	-	Highest occupied molecular orbital
HTM	-	Hole transport material
IC	-	Internal conversion
ILCT	-	Inter-ligand charge transfer
(N)IR	-	(Near) infrared
ISC	-	Intersystem crossing
ITO	-	Indium tin oxide
LC	-	Liquid crystal
LDA	-	Lithium diisopropylamine
LUMO	-	Lowest unoccupied molecular orbital
MeCN	-	Acetonitrile
MeOH	-	Methanol

mi-5edt	-	1-(*N*-methylindol-5-yl)-ethane-1,2-dithiolate
mi-5hdt	-	1-(*N*-methylindol-5-yl)-hex-1-ene-1,2-dithiolate
MO	-	Molecular orbital
MML′LCT	-	Mixed metal-ligand to ligand charge transfer
mnt	-	Maleonitrile dithiolate
MS	-	Mass spectroscopy
NaOMe	-	Sodium methoxide
NBS	-	*N*-bromosuccinimide
NHE	-	Normal hydrogen electrode
NEt_3	-	Triethylamine
NLO	-	Non-linear optic
NMR	-	Nuclear magnetic resonance
OFET	-	Organic field effect transistor
OTTLE	-	Optically transparent thin layer electrochemistry
PAH	-	Polycyclic aromatic hydrocarbon
PCBM	-	(6,6)-phenyl-C_{61}-butyric acid methyl ester
PCM	-	Polarised continuum model
ped	-	1-phenyl-ethylene-1,2-dithiolate
4-pedt	-	1-(pyridin-4-yl)-ethylene-1,2-dithiolate)
PES	-	Potential energy surface
P-3HT	-	Regioregular poly-3-hexylthiophene
pipdt	-	piperazine-3,2-dithione
PL	-	Photoluminescence
PPh_3	-	Triphenyl phosphine
(MDMO-)PPV	-	Poly(2-methoxy-5-(3′,7′-dimethyloctyloxy)-1,4-phenylene-vinylene
p-2ted	-	1-phenyl-(2-thienyl)-ethylene-1,2-dithiolate
PV	-	Photovoltaic
PVD	-	Physical vapour deposition
RMS	-	Root mean square
SCRF	-	Self consistent reaction field
SEM	-	Scanning electron microscopy
TBA	-	Tetrabutylammonium cation
TCNQ	-	7,7,8,8-Tetracyanoquinodimethane
TEA	-	Tetraethylammonium cation
THF	-	Tetrahydrofuran
TLC	-	Thin layer chromatography
TMA	-	Tetramethylammonium cation
TOF	-	Time-of-flight
TTF	-	Tetrathiafulvalene
UV	-	Ultraviolet
VOA	-	Variable optical attenuator
XRD	-	X-ray diffraction

Symbols

A	-	Area
	-	Absorbance
c	-	Velocity of light
	-	Concentration
C_i	-	Capacitance
d	-	Thickness
Δ	-	Thermal energy
E	-	Energy
	-	Electrochemical potential with respect to a given reference
$E_{1/2}$	-	Midpoint between E_p values of a redox process
E_g	-	Band gap
E_p	-	Electrochemical potential at maximum current
$\mathcal{E}_0$	-	Wave amplitude
ϵ	-	Molar extinction coefficient
ϵ_0	-	Electric field
η_{global}	-	Global efficiency
F_i	-	Fock operator
ff	-	Fill factor
h	-	Planck's constant
$\hbar$	-	Dirac's constant
$\mathcal{H}$	-	Hamiltonian operator
I	-	Current
	-	Intensity
I_{DS}	-	Source-drain current
I_p	-	Peak current
I_{SC}	-	Short circuit current
J	-	Current density
J_{ij}	-	Coulomb operator
K_{ij}	-	Exchange operator
k_B	-	Boltzmann's constant
l	-	Azimuthal quantum number
	-	Path length
L	-	Channel length
λ	-	Wavelength
μ	-	Mobility
	-	Electric dipole moment
μ_{ij}	-	Transition dipole moment between state i and j

μ_{lin}	-	Mobility as measured in the linear regime
μ_{sat}	-	Mobility as measured in the saturation regime
N_A	-	Avagadro's number
ν	-	Frequency
ω	-	Radial frequency
	-	Angular velocity
p	-	Probability
P_{in}	-	Input power
P_{max}	-	Maximum power
P_{out}	-	Output power
Ψ	-	Wavefunction
Q	-	Charge
R	-	Resistance
ρ	-	Density
	-	Electron density
	-	Resistivity
S	-	Total spin quantum number
σ	-	Conductivity
t	-	Time
T	-	Temperature
T_c	-	Critical temperature
T_i	-	Kinetic energy of i
τ	-	Lifetime
v	-	Scan rate
V	-	Potential
V_{DS}	-	Source-drain voltage
V_{GS}	-	Gate voltage
V_i	-	Potential energy of i
V_{OC}	-	Open circuit voltage
V_T	-	Threshold voltage
W	-	Channel width

Contents

Chapter 1

Introduction

Metal dithiolenes have been the subject of sustained and fervent interest since the seminal work of Schrauzer and Mayweg in the early 1960s (see Fig. 1.1) [Schrauzer 62]. As well as their role in many biological systems [Stiefel 04], they have found most widespread application within the field of materials chemistry. Their magnetic properties have been investigated, and have provided the field with great insight into the study of magnetic ordering processes [Coronado 04]. A thorough account of their magnetic properties can be found in [Robertson 02], but is not considered further in this work. Their optical properties have been harnessed to develop stable dyes that are active in the near infrared (NIR) region of the electromagnetic spectrum [Mueller-Westerhoff 91]. Their conductive properties have been tuned to develop semiconductors [Cho 07], molecular metals [Nunes 07] and superconductors [Cassoux 99], due to their multiple stable reduction and oxidation (redox) processes, and highly planar molecular geometry, allowing for efficient intermolecular electronic interaction in the solid-state. This thesis concerns the application of square planar metal *bis*-dithiolene complexes to electronic materials (see Fig. 1.2).

Square planar metal *bis*-dithiolenes are attractive targets for electronic applications because they display a high degree of communication between the ligands, through the metal center. This allows for a large degree of delocalisation of electron density in the frontier orbitals [both the highest occupied, and lowest unoccupied molecular orbitals (HOMO and LUMO, respectively)], promoting extensive intermolecular interaction in the solid-state. The name dithiolene corresponds to a class of sulfur-containing ligand, where the ligand binds to a metal through two (di-) sulfur (-thiol-) atoms, linked by carbon atoms in a conjugated (-ene) arrangement [McCleverty 68]. The number of carbon atoms linking the sulfurs can be either one (1,1-dithiolenes) or two (1,2-ditholenes). For the purposes of this work, only 1,2-dithiolenes are considered, and are herein referred to as dithiolenes, and thus the properties discussed in relation to dithiolenes correspond only to those of 1,2-dithiolenes. For practical reasons, only a brief overview of dithiolenes is presented here, with a more detailed discussion of various

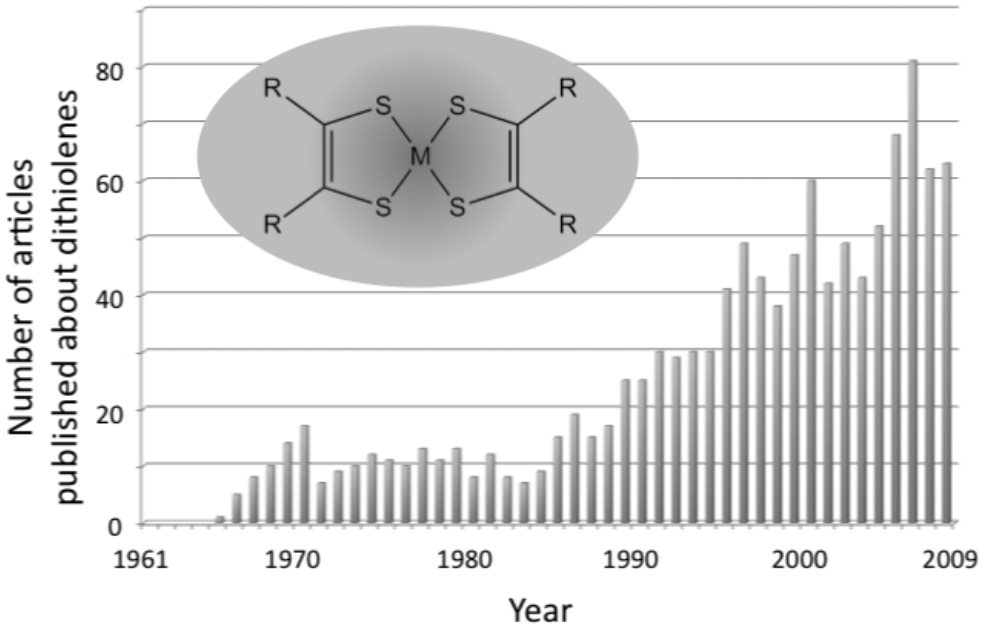

Figure 1.1: Yearly publications on the subject of metal ditholenes, as obtained by a year-by-year search for 'dithiolene' using the keyword search function of SciFinder2007 (CAS); (inset) chemical structure of of a neutral metal (M) dithiolene.

aspects of dithiolene chemistry presented in each chapter, once aspects of the theory relevant to the study of these systems has been introduced in chapter 3.

Metal dithiolenes characteristically show an intense absorption in the NIR part of the electromagnetic spectrum (see section 3.3), and show high thermal and photochemical stability [Mueller-Westerhoff 91]. This has led to their investigation in many optical applications. Their most developed optical application is their use for Q-switching (NIR) lasers [Mueller-Westerhoff 91, Fabian 92], where the NIR absorption can be reversibly quenched at high light intensities (as all dye molecules are in the excited state), resulting in temporary bleaching of the dye, and the release of a short laser pulse from the device. They have also been studied as non-linear optical (NLO) chromophores [Curreli 04, Deplano 10], where a non-linear response of the dithiolene to applied intense electromagnetic radiation results in a change of the frequency (ν) of the radiation (*e.g.* frequency doubling) upon passing through the material. The mechanism by which a material achieves optical non-linearity is derived by a consideration of how the symmetry of the material behaves under high light intensities. The theory of optical non-linearity is beyond the scope of this work, however, a detailed description of the mechanism can be found in [Kanis 94].

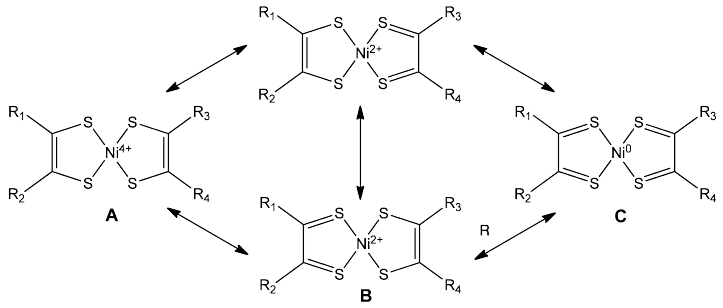

Figure 1.2: Possible resonance forms, and naming guide for neutral nickel dithiolenes.

Dithiolenes show highly tuneable absorption profiles, as well as sufficiently long excited state lifetimes ($\tau \approx 1$ ns) upon light absorption (see section 3.3) to be investigated for their incorporation into photovoltaic devices (see section 6.4) [Kuebler 96]. In recent years, a great deal of interest has been focussed on the development of multi-functional metal dithiolene complexes, where the individual properties can interact to perform a novel function [Faulmann 04]. Beyond being of academic interest, an interplay between their optical, magnetic and conductive properties might lead to the development of optoelectronic or magnetooptic materials for novel device construction.

Many metal dithiolenes provide examples of 'non-innocent' complexes [Jørgensen 66], where the exact oxidation state of the metal center is unclear. Conventionally, transition metal complexes are thought of as undergoing redox chemistry at the metal center, however in 'non-innocent' complexes, the ligands play a role in the redox behaviour of the complex, making the assignment of a formal oxidation state for the metal rather ambiguous (see Fig. 1.2). For the series $[Ni(S_2C_2Me_2)_2]^z$, which has been isolated in three oxidation states (z = -2, -1, 0), [Szilagyi 03] showed, by a combined spectroscopic and theoretical approach, that the dominant contribution to the HOMO, in each oxidation state came from the ligand sulfur orbitals. This assignment was supported by [Bachler 02], who went on to show that this bonding motif was not exclusive to dithiolenes, and that for the ortho-semiquinolato type ligands, the amount of diradical character increased in the order S < N < O. This bonding description helped to explain the reactivity of dithiolenes towards olefins, as observed by [Wang 01], as being due to an electrophilic addition[1] of the olefin to the *bis*-dithiolene, rather than to the metal center. This unusual reactivity has since been suggested as a novel method of olefin

[1] Where the double bond is broken to form two new single bonds.

extraction and purification.

Metal *bis*-dithiolenes, of the general structure [NiL′L] (where L and L′ are ligands on either side of the complex), fall into two distinct structural classes: homoleptic dithiolenes (L=L′), and heteroleptic dithiolenes (L≠L′) (see Fig. 1.2). For the purposes of this thesis, where the ligand is unsymmetrically substituted (herein referred to as unsymmetrically substituted dithiolenes), these complexes have been grouped with the homoleptic dithiolenes, due to their broadly similar properties. Where the ligands are different on either side of the complex, such systems are termed heteroleptic dithiolenes.

Homoleptic dithiolenes Homoleptic nickel *bis*-dithiolenes, where the ligand system is the same on both sides of the complex, are best thought of as a resonance hybrid of the limiting forms **A** and **C** (see Fig. 1.2) [Mueller-Westerhoff 91]. Formal oxidation state determination of the metal thus becomes ambiguous, and such complexes are best characterised in terms of their electronic structure. The nature of the R groups play a key role in the electronic structure of the resulting complexes. Electron donating substituents (such as -NMe_2) raise the energy of the HOMO orbital more than that of the LUMO, whilst electron withdrawing substituents (such as -CN and -CF_3) lower the level of both the HOMO and LUMO orbital, favoring the formation of anionic species [Bigoli 02, Curreli 04]. This simple structural change has a large effect on the properties on the resulting complex: a smaller HOMO/LUMO energy separation means that the low energy electronic transition, characteristically in the visible/NIR (Vis/NIR) region of the electromagnetic spectrum, can be tuned to particularly low energy - the origin of their application as Q-switch NIR laser dyes (see Tab. 1.1) [Mueller-Westerhoff 87]. A typically low lying LUMO orbital for such complexes also suggests their application as electron transporting (n-type) semiconductors, and also combined electron and hole transporting (ambipolar) semiconductors for electronic applications. This is due to the energy barrier for charge injection into the LUMO orbital being small for commonly used metallic electrodes, as well as greater stability of the of the n-channel to atmospheric degradation (see sections 2.6.1 and 6.3) [Anthopoulos 07].

The ability to tune the energy of the frontier orbitals in this manner makes metal *bis*-dithiolenes interesting targets for optical [Hill 95], electronic [Anthopoulos 07], and perhaps optoelectronic application (see section 6.2) and, as a result, a great many complexes have been reported using a diverse range of ligand systems to tune the physical and electronic properties of the materials in question [Mueller-Westerhoff 91].

Substituent -R	Solvent	Wavelength / nm
-CF_3	pentane	713
-H	hexane	720
-CH_3	chloroform	774
-Phenyl	chloroform	866
-2-Thienyl	chloroform	952
-SC_4H_9	chloroform	1104

Table 1.1: Ligand substituent effects on the lowest energy electronic transitions in nickel dithiolenes [Mueller-Westerhoff 91].

Heteroleptic dithiolenes Conversely, relatively few examples of heteroleptic metal *bis*-dithiolenes (see Fig. 1.2) have been reported [Deplano 10], reflecting their increased synthetic complexity. As well as possessing many of the properties of their symmetric analogues, they display some unique, and useful properties, derived from their asymmetric structure. Heteroleptic nickel *bis*-dithiolenes, where the ligand system is different on both sides of the complex, are electronically polarised towards one of the limiting forms **A** and **C** (see Fig. 1.2) [Chen 98]. π donor substituents (where the SCCS group is connected to electron donating groups, such as -NR_2) raise the energy of the HOMO and LUMO orbitals, and have been termed 'push' ligands, whilst π acceptor ligands (where the SCCS group in connected to electron withdrawing groups, such as -CF_3) lower the energy of both molecular orbitals, and have been termed 'pull' ligands. This gives the resultant heteroleptic complex *push-pull* character. The effect of this is to give the low energy absorption inter-ligand charge transfer character (ILCT), a requirement for second order non-linear optic materials [Kanis 94].

Both homo- and heteroleptic metal dithiolenes have been applied in a myriad of applications, from a laboratory scale to industrially produced devices, and it is testament to the size and importance of the field that the yearly publications are still increasing, with new applications still being discovered.

The content and organisation of this thesis

In this work, the application of square planar metal *bis*-dithiolene complexes to electronic materials is discussed. The introduction to such complexes presented above is needfully brief, and focusses on the key properties of metal dithiolenes in general terms. For a thorough discussion of their functionality, it is necessary, first, to consider the theory behind the observed properties, such as their conductivity, redox behaviour and light absorption. Only after this, specific aspects of their functionality can be considered, and discussed in relation to the underlying theory behind their functionality.

Chapter 2 discusses the theory of electrical conductivity in organic materials (those which contain C-H bonds) in general, and compares and contrasts them to inorganic systems (those that do not contain C-H bonds) (see sections 2.2 and 2.3). The discussion focusses on the different structural classes of organic conductive materials, and highlights particular examples where superior performance has been observed, and relates their performance to aspects of their structure. Following this, several common devices that can be formed from organic conductive materials, and that are relevant to this study, are considered, as well as suitable methods for depositing the materials for device manufacture (see sections 2.6 and 2.7).

Chapter 3 describes the experimental methods used extensively in this work for the study of dithiolenes in electronic applications; namely electrochemistry, electronic absorption spectroscopy and computational modeling (see sections 3.2, 3.3 and 3.4, respectively). The discussion focusses on the underlying theory of the techniques, as well as describing how the techniques have been used for the studies carried out in the following chapters.

The development of a novel class of polymerisable heteroleptic nickel *bis*-dithiolene is described in chapter 4. The work is described in relation to previous studies on polymerisable dithiolene complexes, and shows that heteroleptic dithiolene complexes can also be incorporated into polymer films, however their polymerisation results in significant changes in the observed redox and optical properties of the polymer film, when compared to the molecular system.

Chapter 5 describes the synthesis and characterisation of two novel polymerisable dithiolene ligand systems, and investigates their ability to form complexes of nickel and copper. The chapter outlines particular aspects of ligand design that should be considered when developing polymerisable ligand systems, as well as for the synthesis of complexes. The study compares the distinct physical and electronic properties imposed by the ligand design, as well as the choice of the complexed metal.

In chapter 6, several devices are constructed using a nickel dithiolene generated in chapter 5, namely electrochromic switches (see section 6.2), field-effect transistors (see section 6.3) and photovoltaic devices (see section 6.4). The performance of the formed devices is discussed in relation to previous studies on dithiolene based devices, where possible, or to the state-of-the-art existing for the developed devices.

The formation of structurally continuous thin films of metal dithiolenes, by a process of electrodeposition, is investigated in chapter 7. The relative advantages and disadvantages of this technique are discussed in relation to conventional solution based deposition techniques, and the applicability of electrodeposition to other organic conductive materials is considered.

At the end of this thesis, the most important results are summarised. These results are considered in terms of their suitability to electronic application for device manufacture. Future directions are suggested, where appropriate, for the continued development of dithiolenes for electronic application.

Chapter 2

Theory and discussion of organic semiconductors

2.1 Introduction

Organic electronics has been an area of increasing interest in both academic and industrial circles since the beginning of the 20^{th} century, when McCoy and Moore announced that 'it is possible to prepare composite metallic substances from non-metallic constituent elements' [McCoy 11]. Since then, focus has broadened from organic amalgams [McCoy 11], to encompass purely organic systems [Allard 08], and organic-inorganic hybrids, ranging in size from the molecular to the polymeric scale, and possessing a range of electrical functions, including organic metals (high electrical conductivity), semiconductors (electrical conductivity under an external stimulus) and superconductors (electrical conductivity with zero resistance). Organic semiconductors (see section 2.3) have found applications in many fields conventionally dominated by inorganics, such as field effect transistors (FETs) (see sections 2.6.1 and 6.3), and photovoltaics (PVs) (see sections 2.6.2 and 6.4). Many materials have been developed, and tuned to suit these applications, but what is common to all is the ability to conduct electrical current (I) when an electrical potential difference (V) is applied across the material.

Conductivity (σ) is the product of the number of charge carriers (n) multiplied by the charge constant (e) multiplied by the charge mobility (μ), thus it is μ that is the intrinsic property of conductive materials.

$$\sigma = n \cdot e \cdot \mu \tag{2.1}$$

When investigating the electrical conductivity (σ) of a material, it is essential to consider the mechanism by which the charge carriers propagate through the material. Much of the behaviour of inorganic systems (those that do not contain C-H bonds) can

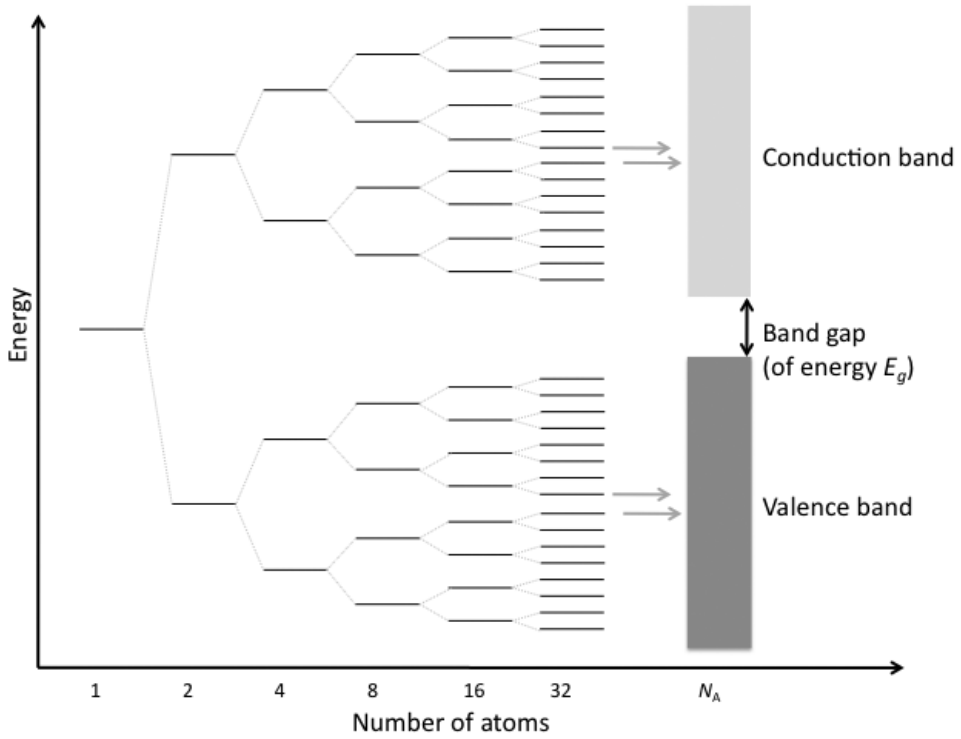

Figure 2.1: The origin of band theory, showing coalescence of orbitals into continuous bands as the number of atoms increases towards Avagadro's number (N_A = 6.022 x 10^{23} mol^{-1}).

be explained by a model known as band theory (see section 2.2). Whilst there exist fundamental differences in the way many organic materials conduct electric current, and in some instances, the mechanism is still not wholly understood, some of the concepts of band theory can be applied (with caution) to understand molecular interactions in the solid-state of organic materials.

2.2 Inorganic semiconductors and band theory

On bringing two atoms together, certain atomic orbitals overlap with each other, and split to form molecular orbitals (molecular orbital theory), with the in-phase addition of these orbitals giving rise to a bonding orbital, and the out-of-phase addition giving rise to an *anti*-bonding orbital. As the number of atoms in the system increases, so too does the number of bonding and *anti*-bonding interactions. For a bulk material, the number of atoms is comparable with Avagadro's number (N_A = 6.022 x 10^{23} mol^{-1}), and the energy difference between the individual bonding and *anti*-bonding orbitals is small enough to be considered continuous, leading to a bonding 'band' (valence band)

and an *anti*-bonding 'band' (conduction band) (see Fig. 2.1). The gap between these bands (band gap, of energy E_g) represents a region where there are no energy levels. Where there exist empty energy levels within a band, electrons can move freely within the band, and the material can act as a metallic conductor.

For systems where the valence band is full of electrons, and the conduction band empty, the material will act as an insulator as there are no mobile charge carriers to propagate electrical current. However, where the size of the band gap (E_g) is such that electrons can be promoted by an external stimulus (such as light of energy $E = h\nu > E_g$, where h is Planck's constant and ν is the frequency of the photons), the material can then conduct electrical current by means of the promoted electrons and residual holes, and the material is thus described as a semiconductor. A semiconductor is therefore a special type of insulator, where the band gap is sufficiently small (usually a few electron volts) to allow the promotion of electrons into the valence band, generating mobile charge carriers. It is only these mobile charge carriers (the promoted electrons and the residual holes) that can carry current (I) under a potential bias (V), and it is these charge carriers that are responsible for the measured conductivity (σ) of a material (see Eq. 2.1).

2.3 Organic semiconductors and the hopping model

The mechanism of charge transport in organic semiconductors is, in many instances, still not completely understood. Conductivity mechanisms are, rather, assigned on a case by case basis, after the collection of reliable experimental data [Karl 03]. Some aspects of band theory apply to organic semiconductors, especially for single crystals, which have a large degree of long range order. However, organic molecules are usually held together by weak van der Waals interactions,[1] and thus typically have very narrow bands, comparable with thermal energy k_BT (where k_B is the Boltzmann constant, and T the temperature). For more disordered semiconductors, band theory breaks down due to the loss of this long range order, and conductivity in such systems is better described by a thermally-assisted hopping of charge carriers between discreet molecules. In this instance, thermal fluctuations temporarily reduce the potential energy barrier to charge transport between molecules, and an electron can effectively 'hop' from one molecule to the next, thus charge propagation is facilitated by the transfer of charge between local neutral species. Because of the often lower than cubic symmetry of organic single crystals, charge transport in highly crystalline organic semiconductors is generally anisotropic, meaning there exists an axial dependence to the transport of

[1] A type of non-bonding interaction between molecules.

holes and electrons [Karl 03].

Once mobile, the charge carriers can undergo several fates. In an ideal situation, when connected to an external circuit, each injected charge carrier would be injected at one electrode, migrate through the material unperturbed, and leave at the other electrode. However, in reality, especially for a disordered semiconductor, the situation is far from ideal, and, as a result, the migration of the injected charge carriers is hindered by their becoming localised, or 'trapped'. These charge 'traps' are lower lying energy levels in which the charge carriers can become localised, and are usually associated with impurities or crystal imperfections [Gutmann 67]. Once localised, the charge carrier remains for a finite amount of time (t_{trap}), proportional to the depth of the trap, and the energy of the charge carrier. For shallow traps, the residence time may be short, with carrier liberation effected by thermal energy gained from vibrations within the structure (lattice vibrations). If the trap is deep, the residence time may be much longer.

For unipolar systems, where only one type of charge carrier is present, charge trapping reduces the mobility of the charge carriers in the material, and hence the conductivity (see Eq. 2.1), by decreasing the speed with which the carriers migrate between the electrodes.

For a system where both holes and electrons are present, such as in a PV device (see section 2.6.2), where a charge carrier becomes trapped, the chance of recombination with an opposing charge carrier is increased. However, where interaction between two opposite charge carriers does not lead directly to recombination, there remains a region of local excitation (exciton) in the semiconductor, which may also propagate through the material. Since the exciton is an electron-hole pair, it carries no net charge, so does not respond to an applied electric field, but rather diffuses through the semiconductor until the exciton decays (returning to the ground state), or the charges separate. If the exciton decays, the charge carriers are lost, and can play no further role in propagating charge. However, if the exciton separates, the charge carriers become mobile, and can once again propagate charge.

Compared to inorganic semiconductors, the excitons formed in organic semiconductors are generally strongly bound as the dielectric constant of organic materials is usually low, compared to inorganic semiconductors, and thus the Coulombic attraction, which is a binding interaction between the two opposite charges, extends over a greater volume, than for inorganic semiconductors. Because of this, they are proposed to play an

important role in charge transport in devices such as photovoltaics, especially where the extent of intermolecular interaction in the semiconductor is small [Liang 70].

The number of charge carriers (n), and hence the conductivity (σ) (see Eq. 2.1), is dependent on a balance between charge carrier generation and recombination:

$$n = n_{th} + \Delta n \cdot exp^{-t/\tau} \tag{2.2}$$

where n_{th} is the number of electron-hole pairs generated by thermal excitation, Δn is the number of additional pairs generated upon application of an electric field, t is the time and τ is the lifetime of charge carriers with respect to recombination. For semiconductors in general, whilst an increase in temperature (T) increase the extent of vibrational scattering processes (phonon scattering[2]), the dominant effect of an increase in T is to increase σ by promoting more electrons to the conduction band, and by reducing the residence time for charge carriers in traps.

2.4 Measurement of mobility

It has been shown above that it is the mobility (μ) of the charge carriers that is the intrinsic property of a semiconductor, and thus it is necessary to quantify this property in order to properly characterise a given semiconductive material. There are many ways of measuring charge-carrier mobility (μ) [Karl 03]; one common technique is to measure the time-of-flight (TOF) mobility (μ) of the charge carriers [Kepler 60]. The TOF apparatus allow the mobility of electrons (μ_{elec}) and holes (μ_{holes}) in a semiconductor to be separately determined (see Fig. 2.2). The semiconductor must be photoconductive, as charge carriers are generated by a short excitation pulse of photons (of energy $E = h\nu$). The semiconductor (of thickness d) is sandwiched between two transparent electrodes, to allow photons to excite the semiconductor, and held under an applied potential (V). The excitation pulse generates charge carriers at the surface of the semiconductor of the same sign as that of the illuminated electrode and, once generated, these carriers then drift, under the applied field, to the second electrode. By measuring the current density (J) as a function of time (t), the time taken for the charge carriers to drift through the semiconductor (t_{drift}) may be observed by the abrupt change in current (see Fig. 2.2). From these measurements, the charge carrier mobility (μ) may be calculated using the equation [Kepler 60]:

$$\mu = d^2/V \cdot t_{drift} \tag{2.3}$$

[2]The same effect decreases the conductivity in metals

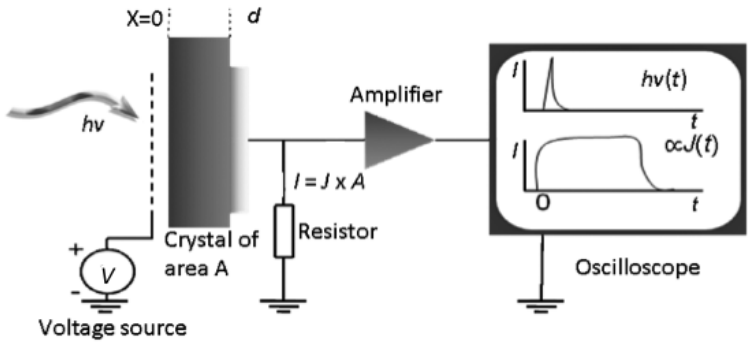

Figure 2.2: Illustration of time-of-flight (TOF) mobility apparatus; $h\nu$ is equal to the energy of the incident photon focused onto a single crystal of a photoconductor of thickness d and active area A; J is the current density measured as a function of time (t), with t_{drift} being the time taken for charge carriers to drift through the semiconductor a distance $X = d$.

The TOF technique yields very accurate information about each charge carrier in a material, as μ_{elec} and μ_{holes} may be separately determined. The terms n-type and p-type are often used to describe the type of charge carrier being measured in a semiconductor (n and p denoting electron transport and hole transport, respectively). Semiconductors often show a preference for one type of charge carrier, related to, among other things, the nature of the imperfections found in the material. Such materials can be described as being either n-type, or p-type on the basis of their dominant charge carrier. It should be noted that TOF is an idealised system which often does not predict how the material will perform upon incorporation into an electrical device (*vide infra*).

An alternative method for measuring the mobility is by forming a field effect transistor (FET). A FET is an electrical device, which is incorporated into almost every electrical appliance, with the function of switching electrical current on or off under an applied external electric field. A more detailed description of its structure and operation is given in section 2.6.1, however, at this stage it is sufficient to consider the basic operating principal, in relation to measuring the mobility (μ). FETs are a useful way of measuring the mobility (μ) of charge carriers across a semiconducting thin film, or crystal, between two electrodes [Horowitz 98b]. Such devices have the advantage of being able to vary the number of charge carriers in the semiconductor, by varying an external electric field. By doing so, the semiconductor can be turned ON (where mobile charge carriers are developed in the semiconductor), or OFF (where no charge carriers are developed in the semiconductor[3]). The ON/OFF ratio can be calculated as the ratio of the current recorded in the ON state, compared to the OFF, and is often reported as a property

[3]In reality, some charge carriers remain in the semiconductor, but at a much lower concentration.

of a semiconductor, relative to the FET design used. By measuring the current passed between the two electrodes (I), as a function of the potential of the applied external electric field (V), the mobility (μ) may be determined (see Eqs. 2.4 and 2.5 in section 2.6.1).

FET measurements often yield very different mobility values (often termed μ_{FET}) compared to TOF. This is, in part, due to the sensitivity of FETs to imperfections in the semiconducting layer, with any trapping of charge carriers necessarily being interpreted as a lower charge carrier mobility (μ). However, the orientation of the molecules, with respect to the electrodes, also has a large effect on the recorded mobility. For thin film measurements from FET devices, the mobility is measured parallel to the film, between the electrodes, whereas for TOF, the mobility is measured perpendicular to the film. Since charge transport in organic semiconductors is generally anisotropic (see section 2.3), this can lead to very different values for the measured mobility.

Other, more specialist, techniques have been extensively reviewed elsewhere [Mort 82, Bray 55, Gelinck 96, Pope 99, Farchioni 01], however, in the first instance, these simple methods can serve as a useful preliminary filter for determining the potential of novel semiconductive materials.

2.5 Structural types of organic semiconductors

Organic semiconductors can be divided into two discrete types; low molecular weight molecules (see section 2.5.1), such as perylene and pentacene, and conjugated polymers (see section 2.5.2) such as polythiophene and polypyrrole. What is common to both is the presence of a large amount of electronic orbital delocalisation, through extensive π-bonding.[4] It is perhaps easier to imagine the flow of electrons along the conjugated backbones of organic polymers, but for a current to flow in an organic semiconductor, some degree of intermolecular interaction is necessary to allow local transfer of charge carriers, either by an incoherent hopping between molecules (see section 2.3), or a more coherent spreading out, or delocalisation, of electron density between several molecules. For this reason, how the molecules arrange in the solid-state (the packing structure) becomes of paramount importance when developing such materials.

Since the beginnings of organic electronics, such a great number of systems has been developed, for investigating both molecular and polymeric semiconductive materials,

[4] A diffuse bonding description between two (or more) atomic orbitals, characterised by being unsymmetrical with respect to the bond axis.

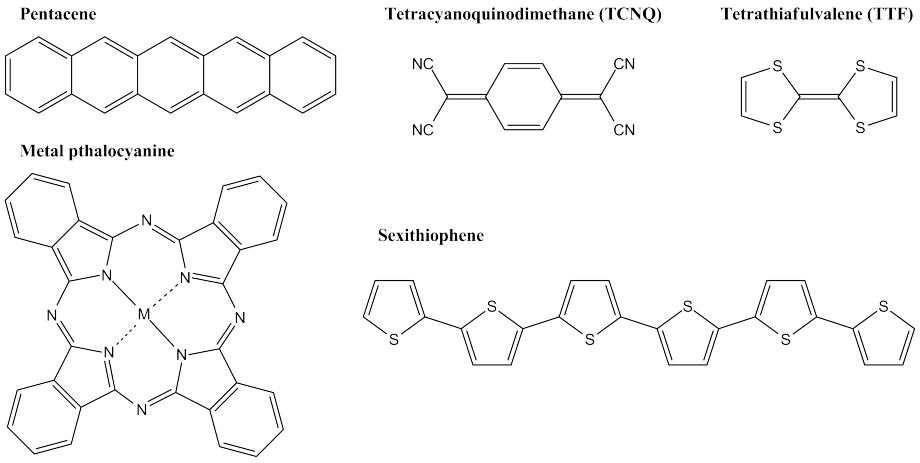

Figure 2.3: Structural diversity of small molecules investigated as molecular semiconductors.

that it would be impossible to cover all of them in this introduction. Therefore, further discussion is limited to the structural trends, and the breakthroughs reported in the field. The molecular and polymeric systems are discussed separately (see sections 2.5.1 and 2.5.2, respectively) and, where necessary, more in depth reviews are suggested.

2.5.1 Molecular semiconductors

Fig. 2.3 shows a small collection of the structural types of molecules investigated as molecular semiconductors, however, the landscape of molecular semiconductors is dominated by two particular fields; polycyclic aromatic hydrocarbons (PAHs) and tetrathiafulvalene (TTF) derivatives, described by [Bendikov 04] as 'the bricks and mortar of organic electronics'.

Polycyclic aromatic hydrocarbons (PAHs) PAHs have emerged as serious rivals to the (historically) silicon-dominated semiconductor market, and from this field emerged the first commercially available organic FET using pentacene. The high mobility of holes ($\mu > 3$ cm^{2}V^{-1}s^{-1}) in pentacene thin films [Yamashita 09], and μ being an order of magnitude greater in single crystals [Jurchescu 06b], has helped to boost research in this area, and the field has since broadened to incorporate pendant groups, heterocycles and metal centres (see Fig. 2.3).

The charge-transport properties of such materials are determined by the degree of molecular ordering, the energy and intermolecular overlap of the orbitals, and by the degree of chemical or structural defects [Brédas 02]. Rubrene, a substituted acene, has shown μ of 15 cm^{2}V^{-1}s^{-1} as a single crystal [Sundar 04], and this high mobility

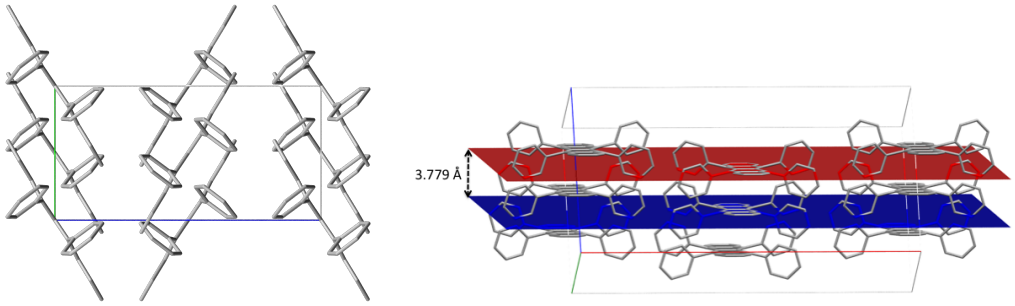

(a) (b)

Figure 2.4: Room temperature crystal structure of rubrene obtained by single crystal X-ray diffraction, showing: (a) herringbone packing of the molecules; (b) short interplanar distance of 3.779 Å [Jurchescu 06a].

can be attributed to excellent π-overlap[5] achieved through its herringbone-type crystal structure, and a short interplanar distance of 3.779 Å at room temperature (see Fig. 2.4).

Investigation into larger (hetero)cyclic systems has led to, among other things, the possibility of liquid crystalline (LC) semiconductors, where the materials can flow like a liquid, whilst retaining the structural ordering of a solid. Such a system brings 'order' and 'dynamics' into a field that benefits from both [Tant 05]. A greater order in a semiconductor increases μ by reducing the density of traps, and hence, improvements in conductivity (σ) can be observed. Traps are usually associated with dislocations (crystal imperfections) or grain boundaries (interface between crystallites) (see Fig. 2.5(a)). Even a perfect crystal will degrade over time, thus increasing the amount of traps and, as a result, reducing σ of a material. Dynamics is introduced through the ability of a LC to self-heal. By warming LCs above their isotropic critical temperature (T_c), the system becomes fluid, and can rearrange in an energetically favourable conformation. By variation of the conjugated core, the intramolecular electronic properties can be tuned, whilst variation of the flexible peripheral chains allows control over the self-assembly [Sergeyev 07]. Discotic LCs, which have a large aromatic core, and thus readily adopt a π-stacked arrangement (see Fig. 2.5(b)), have been shown to have band widths as large as 1.1 eV, approaching that of graphite (1.0 - 1.4 eV) [Crispin 04], and charge carrier mobilities of the order of μ = 0.2 - 1.3 $cm^2V^{-1}s^{-1}$ [Jones 04], with equally impressive exciton diffusion length (the role of excitons in organic semiconductive materials was discussed in section 2.3), often exceeding 70 nm [Markovitsi 01]. However, charge transport is often rigorously

[5] A process by which the π systems on different molecules interact in the solid-state.

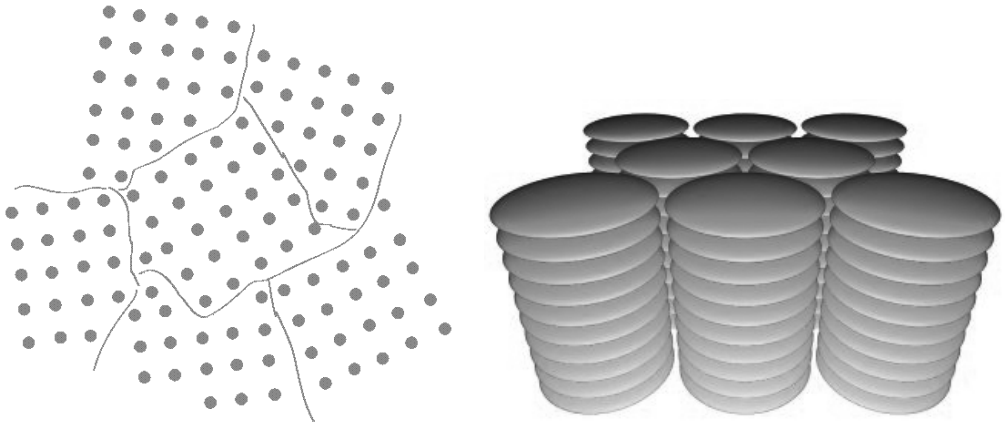

(a) (b)

Figure 2.5: Illustrative representation of (a) grain boundries; (b) columnar stacking of discotic liquid crystals.

uniaxial and, this can lead to complications for the deposition of correctly oriented molecules for efficiently operating devices.

Tetrathiafulvalene (TTF) derivatives Introducing heteroatoms into organic molecular semiconductors can have many beneficial effects upon the properties of the material, in terms of their solubility (and hence processability), or ease of functionalisation (for tuning the physical or electronic properties). Sulfur makes a particularly attractive heteroatom for incorporation, since it has a larger van der Waals radius[6] than carbon and, as such, electronic communication between the organic molecules can be increased by establishing longer range intermolecular interactions. One example where this has been achieved is in TTFs.

Since its discovery in the 1970s, tetrathiafulvalene (TTF), and its many derivatives, have been of intense interest in the field of conductive materials. Combined with the diffuse sulfur orbitals, the particularly rigid core structure of TTF forms strong intermolecular interactions in the solid-state. The TTF moiety can undergo several reversible oxidation processes (see section 3.2.1.1), corresponding to sequential loss of an electron, without significant reorganisation of its geometry (see Fig. 2.6).

Whilst the neutral form of TTFs has been exploited for semiconductor application, fractional oxidation states of TTFs have been utilised to develop metallic and, more recently, superconductive behaviour [Yamada 04]. The high electrical conductivity

[6] A hard sphere model for the size of an atom.

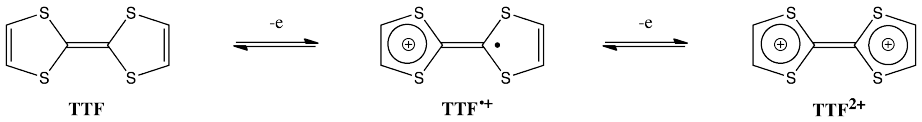

Figure 2.6: Reversible redox behaviour of tetrathiafulvalene (TTF), showing its three stable, isolatable oxidation states.

of TTF salts can be attributed to efficient π-stacking of its oxidised derivatives, as a result of its planarity and its high symmetry, which promotes charge delocalization, thus minimising the repulsions between like charges (Coulombic repulsions). Numerous examples of TTF based semiconductors, and metallic conductors [Kobayashi 04] have been reported since Wudl's [TTF]Cl in 1972 [Wudl 72] and Ferraris' TTF-TCNQ (TCNQ = tetracyanoquinodimethane, see Fig. 2.3) in 1973 [Ferraris 73], though, to date, no TTF-based materials have been used industrially for electronic application [Bendikov 04].

The majority of applications rely on TTFs donor functionality, resulting from a high HOMO level, though work has been done to lower the LUMO level to create, for example, low band-gap polymers [Elandaloussi 96].

Other systems of note After the oligoacenes (such as pentacene and rubrene), oligothiophenes are the most intensively studied class of molecules for organic FET (OFET) application [Allard 08]. Their relative ease of synthesis, and large capacity for substitution, has seen improvements in the mobilities (μ), ON/OFF ratios, as well as solubility and processability - important criteria for large scale device manufacture [Halik 03]. Mobility measurements in such systems show a predominant hole transport (p-type behaviour). This has been attributed to extrinsic effects, such as oxygen or water contamination acting as electron traps [Horowitz 98a, Chua 05, Dodabalapur 05].

Incorporating metals into OMCs allows for fine tuning of the energies and distribution of the frontier orbitals (HOMO and LUMO) by modification of the ligands, or by changing the metal centre. This is important for improving the strength of interaction between neighbouring molecules, or for the fine tuning of the conductive properties, such as the development of ambipolar conductivity (the ability to transfer holes and electrons effectively in the same material) (see section 6.3). One major obstacle for such systems is that the coordinating ligands often bind weakly to the metal centre, and present a strong electronic barrier between the metal and the ligand, thus leading to low electroactivity. However, metal dithiolenes (see chapter 1) make particularly attractive targets for electronic applications because they display a high degree of communication

between the ligands, through the metal centre. Enhancing the coordination bonding strength in these, and other complexes, is becoming an area of fervent activity in the field of organic conductive materials, to develop more efficient metal-ligand coupling, whilst maintaining the processability of the complex [Su 00, Zhao 01].

Many examples of molecular semiconductors have been developed with a HOMO/LUMO gap in the range ∼0.2-2.0 eV, and some have found uses in devices, such as in PVs (see section 2.6.2) [Martín 98], and FETs (see section 2.6.1) [Dimitrakopoulos 02], but for their full potential to be realised in these, and other more specialist applications, their long-term stability (both mechanical and environmental) must become the focus of future work.

2.5.2 Polymeric semiconductors

One method for reducing the energy gap between the HOMO and LUMO orbitals, to a level useful for electronic application, is to increase the extent of electronic delocalisation through conjugation. From section 2.2, it can be seen that increasing the number of interacting orbitals decreases the separation between the bonding and *anti*-bonding orbitals, as discreet orbitals become bands. Increasing the extent of conjugation can be achieved, relatively easily, by the linking of π-delocalised molecular systems by polymerisation.

The field of semiconducting polymers has grown along side that of the molecular semiconductors, and has benefitted from the insight gained from these inherently more characterisable molecular systems. The same design criteria apply when developing new semiconducting polymers: extensive π-overlap between neighbouring molecules, sufficient solubility to be processed as solution cast films, the ability to form extensive crystalline domains, tunable energy levels to allow efficient doping of holes (or electrons), and good environmental stability. However, they possess one distinct advantage over their molecular counterparts, and that is their flexibility [Allard 08]. Although low molecular weight materials can display high charge carrier mobilities (μ), due to the formation of extensive polycrystalline domains, they are often very susceptible to mechanical strain, with performance deteriorating over time and use. Semiconducting polymers, however, are far more resistant to such strains, and have therefore brought about the dawn of truly 'plastic electronics'.

Polythiophenes are perhaps the most extensively studied systems, and have yielded some of the highest values of μ from FETs made by solution methods [Sirringhaus 99].

The first polythiophene described by [Tsumura 86] comprised an unsubstituted chain of thiophene rings, and showed a charge carrier mobility μ = 1 x 10^{-5} $cm^2V^{-1}s^{-1}$, and an ON/OFF ratio of 10^3. The first semiconducting polymer to exhibit charge carrier mobilities (μ) in the 0.1 $cm^2V^{-1}s^{-1}$ range was regioregular poly-3-hexylthiophene (P-3HT) [Sirringhaus 99], which now serves as something of a benchmark for semiconducting polymers, due to its relative ease of synthesis and processing [McCulloch 09]. New and improved systems are being reported each month, as aspects of structure and function are related and understood [Arias 10].

Polythiophenes can be synthesised by chemical [McCullough 98], or electrochemical methods (see section 3.2.1.2) [Roncali 92]. The former is usually achieved by a metal assisted cross-coupling of a (substituted) 2,5-bromothiophene, with chain length determined by the amount of catalyst present in the reaction (catalyst loading). The latter is usually achieved by oxidation of a (substituted) thiophene solution at an electrode (working electrode) in an electrochemical cell (see section 3.2) to produce a radical which, in concentrated solutions, quickly couples to a second thiophene or thiophene radical, and chain growth continues until the potential is switched off (or the film becomes insulating). Chemical polymerisation is a more useful method of forming high quality material on a large scale for future processing, whilst electrochemical polymerisation is a quick and convenient method of assessing a material's polymerisation potential, and the electrochemical properties of the resultant film *in situ*.

By limiting the extent of polymerisation, materials can be developed that possess many of the advantages of the polymer, such as increased conjugation, whilst maintaining many of the advantages of molecular systems, such as their characterisability and processability. Such systems are not strictly polymers, but bridge the gap between the molecular and the polymeric, and are generally referred to as oligomers [or where the number of linked units is defined, x-mers (where x = di-, tri-, tetra-... for 2, 3, 4... linked units, respectively)].[7]

One group of molecules that have been shown to link with a defined number of units is indoles. Indoles have been of sustained interest since the early 1980s, as both oligomeric and polymeric semiconductive materials, due to their formation of a large aromatic core upon polymerisation, coupled with their ease of functionalisation (see Fig. 2.7). In 1992, [Bartlett 92] electrodeposited films of poly-(indole-5-carboxylic acid) from the

[7] Sexithiophene is also an oligomer, but is considered in section 2.5.1 as a molecular semiconductor.

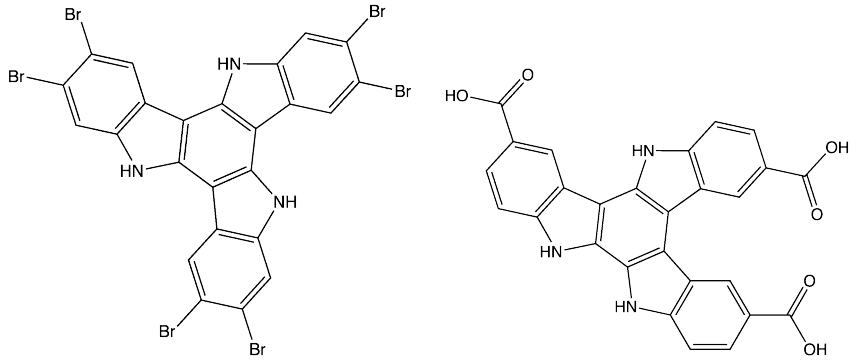

(a) (b)

Figure 2.7: Connectivity of reported indole trimers: (a) symmetric indole trimer formed by reaction of Br_2 with indole [Robertson 00]; (b) asymmetric indole trimer, formed from indole-5-carboxylic acid either chemically with $FeCl_3$, or electrochemically [Mackintosh 94a].

monomer (see section 3.2.1.2), and soon after [Billaud 95] reported the first chemical polymerisation of an indole using $FeCl_3$, thus providing a scalable route to these potentially interesting systems. Since then, advancements have been made in the area at Edinburgh University, with [Mackintosh 94b] fully characterising the asymmetric indole trimer formed by electropolymerisation by ^{1}H NMR, and [Robertson 00] forming a highly functionalised symmetric indole trimer by the simple addition of bromine to indole (see Fig. 2.7). Though these discrete trimers are not technically polymers, the large increase in aromaticity, developed by oxidative coupling of indole units, results in extensive delocalisation across a large aromatic core, thus possessing many similarities to polymeric aromatic systems, whilst maintaining the desireable properties of molecular systems.

2.6 Organic semiconductor devices

Organic semiconductors are interesting systems for study, to characterise the fundamental mechanisms of charge transport, however, their improved processability, and superior stability to mechanical strain, make them desirable targets for incorporation into devices. In this section, some common devices that have been developed from organic materials, that are relevant to this work, are discussed, namely field-effect transistors (FETs) (see section 2.6.1) and photovoltaics (PVs) (see section 2.6.2). A brief discussion of different film forming techniques, suitable for the development of devices from organic semiconductive materials, is also given (see section 2.7).

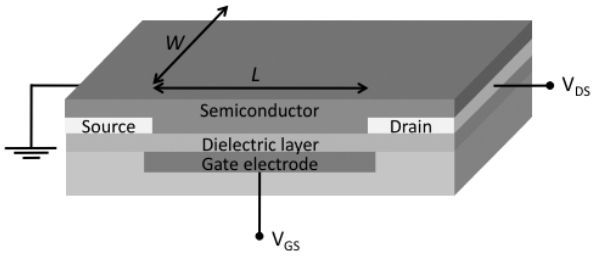

Figure 2.8: Illustration of the structure of a basic bottom contact field-effect transistor (FET), with semiconductor of active area defined by a channel length = L and channel width = W. The device is subjected to a potential bias V_{DS} between the source and drain electrodes, under an applied electric field induced by gate bias V_{GS}.

2.6.1 Field-effect transistors (FETs)

Field-effect transistors, as mentioned in section 2.4, are a useful way of measuring important properties of semiconductive materials, but are also devices in their own right. Worldwide, the global consumption of transistors is set to reach 10 billion per person per annum, as they find uses in everything from pocket calculators to space rockets [Grossmann 06]. The first organic FETs (OFETs) had charge-carrier mobilities (μ_{FET}) of less than 10^{-2} $\mathrm{cm^2V^{-1}s^{-1}}$ [Allard 08], far below that of an inorganic equivalent, based on amorphous silicon (α-Si) ($\mu \approx 1$ $\mathrm{cm^2V^{-1}s^{-1}}$) [Allard 08]. However, sustained research and investment in the field has seen μ_{FET} for thin films exceed 3 $\mathrm{cm^2V^{-1}s^{-1}}$ with ON/OFF ratios greater than 10^8 [Yamashita 09]. Such performance rivals that of α-Si, which is currently used for many low-end electronic devices. This investment has been encouraged by the possibility of cheaper, flexible devices formed by solution processing, that would be impossible to achieve with conventional inorganic semiconductors.

The basic FET consists of three electrodes: the source and drain electrode, between which charge-carriers migrate through the active layer, and the gate electrode which induces the charge-carriers, and is separated from the other two electrodes by a dielectric layer (see Fig. 2.8). The active layer of the semiconductor should contain few intrinsic charge carriers in the 'OFF' state so that a bias over the transistor yields little current between the source and drain electrode (I_{DS}). Application of a gate-to-source voltage (V_{GS}) should generate charge carriers of the opposite sign at the semiconductor active layer/dielectric layer interface, causing an increase in I_{DS}. For a device to be practically useful, this difference (ON/OFF ratio) should be large, of the order $\sim 10^5$, and the threshold voltage (V_T) (the voltage applied to the gate that is required to effect

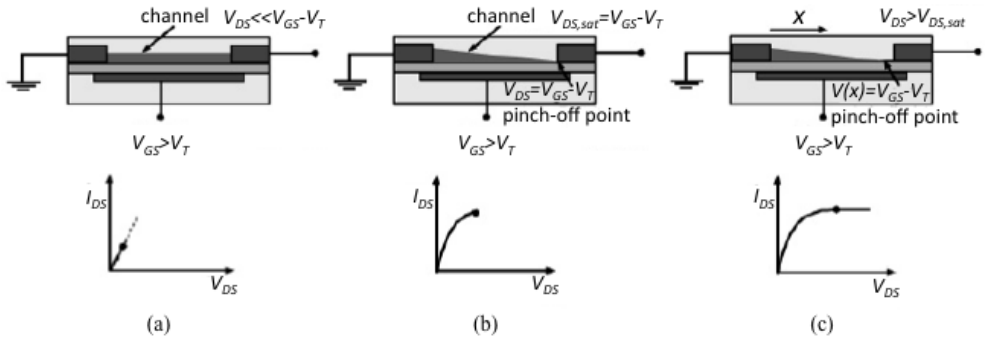

Figure 2.9: Illustrations of operating regimes of field-effect transistors, where V_{DS}, V_{GS} and V_T are the drain, gate and threshold voltages, respectively, and I_{DS} is the drain current: (a) linear regime; (b) start of saturation regime at pinchoff; (c) saturation regime (above) and corresponding current-voltage characteristics (below). Figure modified from [Zaumseil 07].

this change [Horowitz 98b]) small, for the device to operate efficiently. On application of V_{GS}, the Fermi level of the semiconductor move in response to the applied field, and is either raised in energy, to generate holes in the valence band (hole accumulation mode), or lowered in energy, to generate electrons into the conduction band (electron accumulation mode) [Horowitz 98b].

By applying a potential difference between the source and drain electrodes (V_{DS}), the charge carriers drift in response to the applied field. At low V_{DS}, I_{DS} is directly proportional to V_{DS} (see Fig. 2.9 (a)):

$$I_{DS} = \frac{W}{L} \cdot \mu_{lin} \cdot C_i \cdot (V_{GS} - V_T) \cdot V_{DS} \tag{2.4}$$

where W is the channel width (usually the length of the source or drain electrode), and L is the channel length (the distance between the source and drain electrodes), and C_i is the capacitance of the dielectric layer (which is a measurable property that describes a material's ability to hold electric charge). μ_{lin} is the mobility calculated by this method (in the linear regime of a plot of I_{DS} against V_{DS}).

As V_{DS} becomes of the order of the effective gate voltage (V_{GS} - V_T) (see Fig. 2.9 (b)), a further increase in V_{DS} does not significantly increase the I_{DS} as the field between the drain and the gate drops to zero. This is known as the pinch-off voltage, after which a space-charge limited saturation regime is achieved (see Fig. 2.9 (c)), where the current is no longer proportional to (V_{DS}):

$$I_{sat} = \frac{W}{2L} \cdot \mu_{sat} \cdot C_i \cdot (V_{GS} - V_T)^2 \tag{2.5}$$

where μ_{sat} is the mobility calculated in this region (in the non-linear regime of a plot of I_{DS} against V_{DS}).

2.6.2 Photovoltaics (PVs)

Another system where organic materials have seen progress is in the field of photovoltaics. The PV market is currently dominated by bulk inorganics, namely silicon (either crystalline or amorphous), CdTe devices, III/V devices such as gallium arsenide (GaAs) and, more recently, CIGS (copper indium gallium selenide/sulfide) but, due to their high cost, or high toxicity, alternative technologies are being sought [Grätzel 01]. A PV device performs two basic functions - photogeneration of charge carriers, and separation of these charge carriers to conductive contacts. Silicon cells consist of a *p*-*n* junction, which is formed when an *n*-type and a *p*-type semiconductor are brought into contact. In practice this is done by doping the silicon with a small amount of an element that can either accept electrons (*p*-doping, with *e.g.* aluminium) or donate electrons (*n*-doping with *e.g.* with phosphorous). This creates holes or electrons in the *p*- or *n*-type silicon, respectively. On either side of the junction, the Fermi level[8] is forced into coincidence by the diffusion of electrons from the *n*-type to the *p*-type, leaving positive ions behind, thus causing the valence and conduction bands to bend. This creates an electric field (ϵ_0), or diode, in the region between the semiconductors (depletion region) (see Fig. 2.10). When the device is illuminated with an energy greater than the band bap of the semiconductor ($E = h\nu > E_g$), an electron may be promoted to the conduction band, creating an electron-hole pair. If these electron-hole pairs are generated in the depletion region (or can diffuse into this region before recombining), they can be separated by the electric field, and one quantum of charge can flow through the circuit, thus the junction acts as energy converter for light to electricity (see Fig. 2.10).

The thermodynamic limit for energy conversion in single junction cells is 31 %, as holes or electrons generated by photons of an energy above that of the band gap of the material lose this excess energy as heat. This limit can be improved by having multiple junctions arranged in series to absorb efficiently across the solar spectrum, but this greatly increases manufacturing costs. First generation solar cells, based on a single junction doped silicon wafer, have shown efficiencies of ∼24 % in the laboratory, but this falls to between 5 and 15 % for commercial modules, with a lifetime of about 30 years, corresponding to an energy payback time of 2-4 years [Armaroli 07].

[8] Which is a theoretical energy level, below which the energy levels are full, and above which the energy levels are empty.

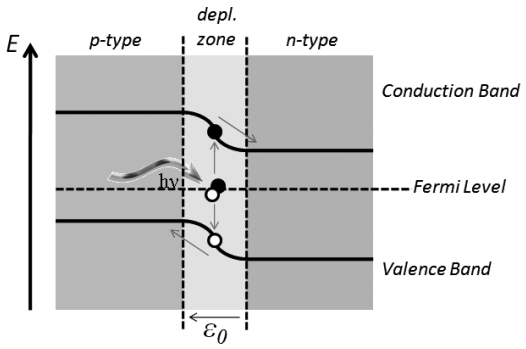

Figure 2.10: Illustration of the structure of an inorganic p-n junction photovoltaic, where photons (of energy $h\nu$) seperate charge carriers, which are separated by a built in electric field (ϵ_0), for charge collection at the electrodes, to power an external load.

Over the last ten years, interest has grown in solid-state organic systems containing both p-type and n-type semiconductor blends. The mechanism of light to electricity conversion is different to the inorganic junction cells; when light falls on a blend of donor and acceptor organic species, a tightly bound exciton is generated, which diffuses to the donor-acceptor interface, where it is separated into a hole and electron [Sergeyev 07]. Because charge separation occurs exclusively at the interface between the species, efforts have been made to increase the surface area of the interface by optimising the component ratios in the blend, or structuring on the nano-scale [Mayer 07]. The energy conversion is still low ($\sim$6 %) for such devices, but cheap materials, low manufacturing costs, and the possibility of lightweight, flexible, large-scale devices, makes them a promising candidate in the renewable energy market. Such a system is considered in more detail in section 6.4.

Another PV system that has gained a great deal of attention over the last 15 years is the dye-sensitised solar cell (DSSC), or Grätzel Cell, so named after its inventor Michael Grätzel [O'Regan 91]. In these cells, charge separation is initiated at a dye that is designed to absorb light over a broad region of the solar spectrum. This dye is bound to an inorganic semiconductor so that, upon photoexcitation, it may inject an electron into the conduction band of the inorganic semiconductor. The dye is then regenerated by accepting an electron from a hole transport material (HTM), which can be thought of as carrying the resulting hole to the counter electrode, thus achieving charge separation (see Fig. 2.11). Optimisation of the dyes is an area of fervent activity [Spiccia 04, Argazzi 04, Polo 04], and has resulted in a range of dyes, all competing to improve light harvesting, electron injection rates (from the dye into the inorganic semiconductor) and dye regeneration (reduction of the dye after it has

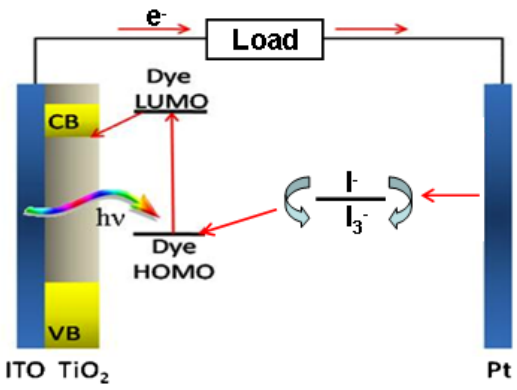

Figure 2.11: Illustration of the structure of a dye-sensitised solar cell (DSSC), excited with photons (of energy $h\nu$), where CB and VB are the conduction and valence bands in the TiO_2, connected to an indium tin oxide (ITO) coated transparent glass electrode, and the cell completed with a platinum electrode (Pt).

injected an electron). Efficiencies of 11 % have been reported on a laboratory scale, but are much lower for larger devices [Armaroli 07].

The most efficient DSSCs use a solution redox electrolyte based on I^-/I_3^- as a HTM, however this reduces the lifetime of the cell, and adds to manufacturing complexity, due to the volatile and corrosive nature of the electrolyte [Robertson 06]. Organic semiconductors have been suggested as a potential HTM replacement in such cells, as they could offer a longer cell lifetime, and cheaper manufacturing costs, making DSSCs a powerful technology for light-to-energy conversion.

The performance of a solar cell is characterised by its overall efficiency. This is defined as the ratio of output to input power (see Eq. 2.6), which can be calculated from observing the current (I), as a function of applied voltage (V), whilst the device is illuminated (see Fig. 2.12). By scanning the potential (V) across the device, the point at which no current flows through the cell can be determined; this is called the open circuit voltage (V_{OC}). On scanning the potential (V) to the point where minimum resistance is observed, the short circuit current (I_{SC}) can be determined. The maximum power (P_{max}) of the cell is calculated where the product of I and V is greatest. For a given device, P_{max} is affected by many factors, including the series resistance of the device, and the efficiency of charge collection, and therefore, a fill factor (ff) is included (based on the difference between the theoretical and observed P_{max} of the device) to correct for how far from ideality the device behaves. The efficiency is therefore given as a ratio

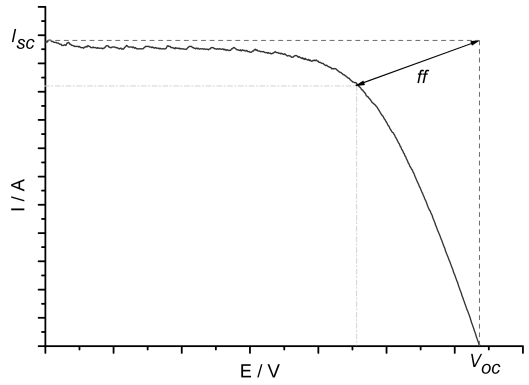

Figure 2.12: Typical IV curve for a photovoltaic device, showing the short circuit current (I_{SC}) and open circuit voltage (V_{OC}). The fill factor (ff) is calculated as the difference between the theoretical and observed maximum power output of the device (P_{max}), where the theoretical P_{max} is determined as the product of I_{SC} and V_{OC}, and the observed P_{max} is determined as the maximum product of I and V.

of the power out (P_{out}) over the power in (P_{in}):[9]

$$\eta_{global} = \frac{P_{out}}{P_{in}} = \frac{I_{SC} \cdot V_{OC} \cdot ff}{P_{in}} \tag{2.6}$$

2.7 Thin film formation

One advantage of organic semiconductors is their improved solubility in common organic solvents. As a result, expensive techniques that are required for the deposition of inorganic semiconductors, such as physical vapour deposition (PVD) and chemical vapour deposition (CVD), can often be replaced by softer, cheaper techniques such as drop or spin coating, or Langmuir-Blodgett film formation (*vide infra*).

PVD involves the vaporisation of a material in a vacuum, and deposition onto a substrate. Since the substrate is much cooler than the vaporisation source, the vapour recombines on the surface of a substrate, thus depositing the material, generally as a polycrystalline film of controllable thickness. This mechanism is distinct from CVD, which involves the chemical reaction between vapours to produce the required species, which then condense on the substrate to form the compound. Both PVD, and CVD can, and have been used to deposit organic semiconductors, however they are energy intensive techniques, and are unsuitable for large scale application due to the difficulty

[9]Devices are routinely tested using a solar simulator modeling a particular spectral distribution, which delivers 1000 Wcm^{-2}.

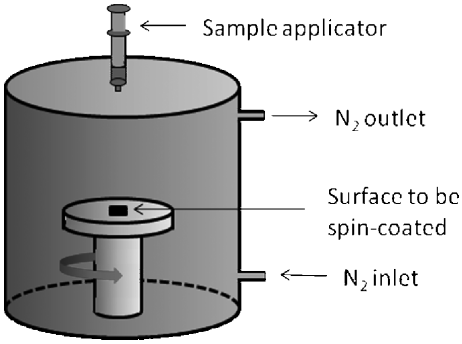

Figure 2.13: Design of a basic spin coater.

of achieving a large evacuated volume.

Solution deposition techniques, on the other hand, are much cheaper as they do not require high temperatures, or low pressures, and therefore are far better suited to large scale production.

Drop coating is a common technique for depositing potential semiconductors onto substrates, such as FETs, to initially screen their performance. By dissolving the material in a suitable solvent, the material may be dropped onto the substrate and, upon evaporation, yield a film of the semiconductor. The technique is quick and easy to perform, needing no specialised equipment, however the process yields poor film uniformity, and often results in films of varying thickness (d), and grain size, as droplets move over the substrate upon evaporation. However, some groups have used this technique successfully, even for materials of poor solubility where, in such cases, a partially dissolved suspension can be dropped onto the substrate which then evaporates to yield a polycrystalline film [Matsushita 05].

Conversely, spin coating can apply a uniform film of a semiconductor of reproducible thickness to a substrate. By this technique, the semiconductor is dissolved in a volatile solvent, and applied dropwise to a rotating substrate, which coats evenly as the solution spreads out by centrifugal force (see Fig. 2.13). The film thickness (d) and morphology can be tuned by variation of the speed of rotation, and thus can form more reproducible, higher quality films, than by drop coating. This is a simple technique for testing the ability of a material to form a continuous film across a substrate, and can also be used to make devices of reproducible quality, such as FETs, and can therefore be used to accurately determine properties, such as charge mobility (μ).

Films of very accurate thickness can be deposited by the Langmuir-Blodgett technique. This method is based on dip coating, where a single monolayer is added to a substrate on every immersion (or emmersion) into (or from) the solution [Peterson 90]. Various claims of molecular ordering in such films have raised the profile of this technique, as the role played by order in conductive materials is well known [Germer 38,Peterson 84].

Chapter 3

Experimental methods

3.1 Introduction

Many experimental techniques have been used throughout the course of this PhD. Some data were obtained as part of a service system [namely, elemental analysis, Accurate mass determination by Mass Spectrometry (Acc-MS), and structure determination by single crystal X-Ray Diffraction (XRD)], and some were obtained through conventional operation of equipment present in the department [namely, ^{13}C and ^{1}H Nuclear Magnetic Resonance (NMR), and Nominal mass determination by Mass Spectrometry (Nom-MS)]. For such techniques, only a brief outline of the experimental setup and equipment is given for reference in the relevant section, as the utilisation of these techniques is considered routine. Where necessary, for a more extensive discussion of these techniques, the reader is pointed toward the relevant literature that the author feels gives a clear description, and overview of the technique in question.

For techniques used as part of a collaboration with other groups, such as those outlined in chapter 6 [namely, thin film XRD and Scanning Electron Microscopy (SEM)], the measurements were taken under the supervision of trained operators and, as such, only a brief outline of the experimental setup is given in the relevant sections.

For techniques used extensively, or in an unconventional manner throughout this work, namely electrochemistry, electronic absorption spectroscopy and computational calculations, a more in-depth discussion in given in this chapter (see sections 3.2, 3.3 and 3.4, respectively). For these techniques, particular attention is drawn to the choice of experimental parameters, as well as the limitations of the data obtained.

3.2 Electrochemistry

Electrochemistry is an invaluable tool for characterising the oxidation and reduction (redox) properties of materials. Either in solution, or in the solid-state, electrochemical

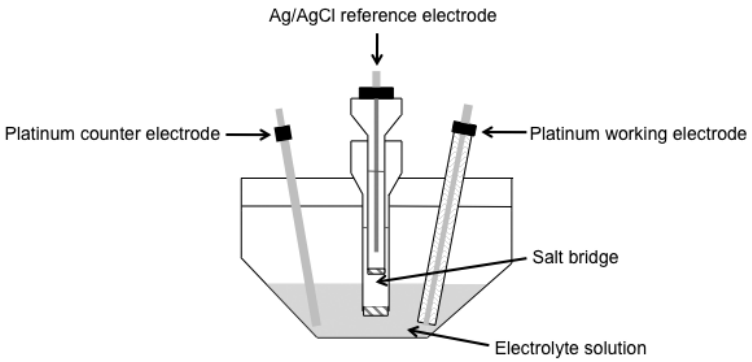

Figure 3.1: A three electrode electrochemical cell setup used for routine electrochemical analysis.

analysis can yield useful information on the spatial location, and energy of the frontier orbitals. This information is vital to organic electronics, as it helps to assess the likely success or failure of a given material in its desired application.

3.2.1 Theory

By measuring current (I) as a function of applied voltage (in this section denoted E), the redox processes of electroactive species can be investigated. For routine operation, a three electrode system, comprising a working, a counter and a reference electrode, is generally used (see Fig. 3.1). In such a setup, a potential (E) is applied across an electrolyte solution (*vide infra*), containing the material under invesigation, between the working and counter electrode, and held relative to the reference electrode. This reference electrode consists of a half cell with a known redox potential, separated from the bulk by a salt bridge to stop diffusion of the active species into the reference, or *visa versa*. The counter, and working electrodes are usually made from an inert metal that is stable under the given reaction conditions, so no contamination of the bulk occurs, and thus the redox processes observed at the working electrode are a result of the active species and electrolyte used (*vide infra*). The counter electrode should be of sufficient surface area that it does not limit the current entering the cell, and is generally much larger than the working electrode.

The potential difference between the counter and working electrode is modulated, relative to the reference electrode, by a potentiostat. For the purposes of this work, the redox properties of the studied materials were investigated by cyclic voltammetry (CV), either in solution, or as films deposited on the working electrode (see section 3.2.1.1).

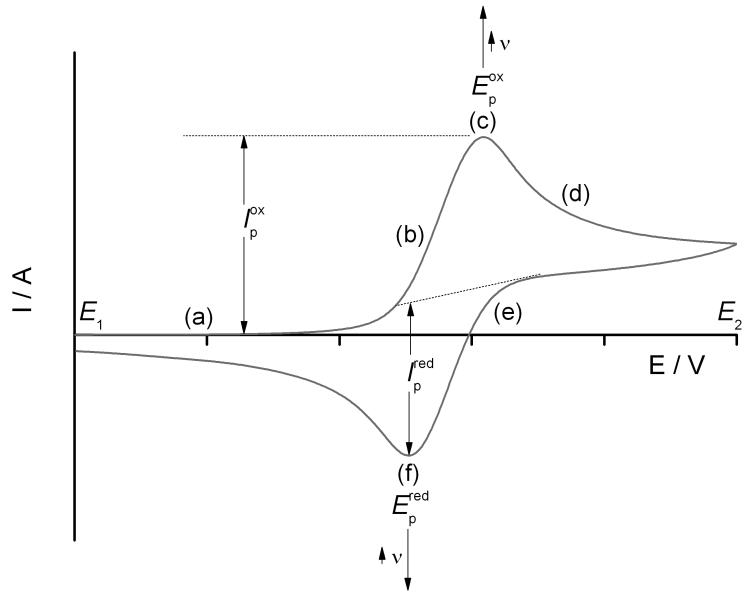

Figure 3.2: An idealised plot of current I vs. potential E for an electrochemically reversible one electron process, corresponding to the $[M]^0/[M]^{+1}$ redox couple, as investigated by scanning the potential E between potentials E_1 and E_2, and back again. For an electrochemically reversible process, the peak current $|I_p|$ of the oxidation and reduction processes (I_p^{ox} and I_p^{red}, respectively), should increase linearly with the square root of the scan rate v, but the potentials of peaks E_p, for the oxidation and reduction process (E_p^{ox} and E_p^{red}, respectively) should not change with scan rate (v). The points (a) to (f) denote regions of interest described in the text.

In a standard setup, the electrolyte solution consists of the active species (usually at low concentrations) dissolved in a solvent with a high concentration of an ionised salt. The electrolyte performs several important functions necessary for the proper operation of the cell. The electrolyte increases the conductivity of the solution to avoid solution resistance effects, which can lead to Joule heating, and non-uniform current/potential distributions. At high concentrations, it eliminates migration as a mechanism for mass transport of the electroactive species, and thus allows only the diffusion-controlled processes to be studied.

3.2.1.1 Cyclic voltammetry

A cyclic voltammogram is generated by scanning the potential linearly from a potential E_1 to a potential E_2, and then reversing the direction of the scan (from E_2 to E_1), and measuring the current response, which can then be plotted as a function of the potential (see Fig. 3.2).

On scanning the potential (E) to more positive potentials (from E_1 to E_2), initially

no current (I) should be passed at the working electrode, as E is insufficient to induce oxidation of the active species in the cell [region (a) Fig. 3.2]. As E is scanned, I increases as E becomes sufficient to induce oxidation [region (b)]. The increase in I is initially exponential in form as E is scanned, as a steep concentration gradient is developed in the vicinity of the working electrode (the Nernst diffusion layer). As the active species in this layer becomes depleted, further oxidation is restricted by the diffusion of active species from the bulk to the electrode surface. This mass transport is slow on a CV timescale, and therefore the rate of oxidation decreases as the concentration of active species is depleted. This is shown by the shallowing of the slope as region (b) is traversed. At point (c), a balance between the increasing rate constant (due to a steeper concentration gradient), and the decreasing concentration of active species (due to slow mass transport) is reached, and this is known as the peak current [in general I_p (I_p^{ox} for oxidation, I_p^{red} for reduction)]. From point (c), I decreases as the oxidation process becomes diffusion controlled [region (d)]. As the direction of scan is reversed (from E_2 to E_1), active species continues to be oxidised at the working electrode, until E becomes sufficient to re-reduce the oxidised species [region (e)]. At this point, the current response of the reduction process (I_p^{red}) resembles that of the the oxidation process (I_p^{ox}), though with opposite sign [point (f) Fig. 3.2].

At faster scan rates (v), the diffusion layer is thinner, and thus a steeper concentration gradient is set up, resulting in an increase in $|I_p|$. The two parameters are linked by the Randles-Sevčik equation [Greef 85], and from this, one finds I_p to be proportional to the gradient at the electrode surface, which is determined by v, if the concentration of electroactive species is assumed to be constant throughout the course of the experiment:

$$I_p \propto v^{1/2} \tag{3.1}$$

If the oxidised species is stable under the experimental conditions, and capable of relinquishing the electron back to the working electrode, and if the rate of electron transfer between the active species is fast (on an electrochemical timescale), the process can be thought of as being electrochemically reversible. By scanning the same electrolyte solution at different scan rates (v) (typically five rates between 10 and 100 mVs^1), sufficient data can be obtained to assess the relationship between I_p and v. A simple test for electrochemical reversibility would be to plot I_p as a function of $v^{1/2}$. If the plot is linear, and passes through the origin, the process can be proposed to be electrochemically reversible. In order for the process to be stated as fully electrochemically reversible, however, further diagnostic tests should be performed. Where possible, each of the tests below should be satisfied in order to state

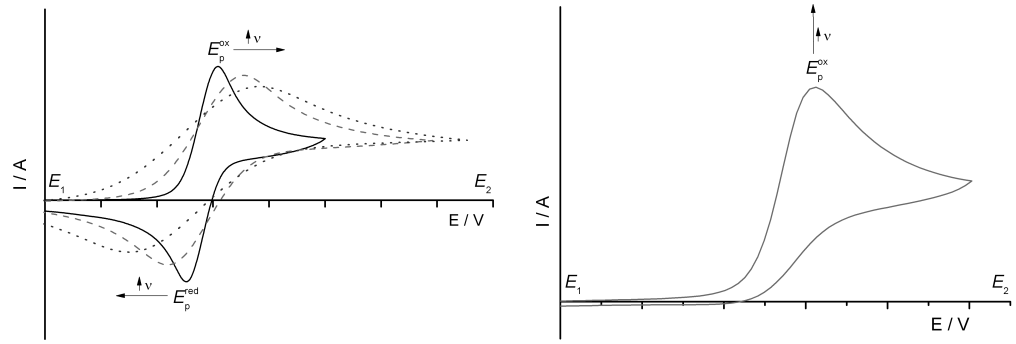

(a) (b)

Figure 3.3: An idealised plot of current I vs. potential E for a cyclic scan between E_1 and E_2: (a) an electrochemically irreversible process, corresponding to the $[M]^0/[M]^{+1}$ redox couple at increasing scan rates (v), showing E_p for the oxidation and reduction processes (E_p^{ox} and E_p^{red}, respectively) changing with v; (b) a chemically irreversible process corresponding to the oxidation of $[M]^0$, with E_p^{ox} increasing with v.

an electrochemical process as reversible (at 25°C) [Greef 85]:

- $I_p \propto v^{1/2}$
- E_p is independent of v
- $\Delta E_p = E_p^{red} - E_p^{ox} = 59/n$ mV, where n is the number of electrons involved in the process
- $|I_p^{red}/I_p^{ox}| = 1$
- at potentials beyond $E_p, I^{-2} \propto t$

Where the rate of electron transfer is slowed to the timescale of mass transport, incomplete oxidation (reduction) occurs at the working electrode, and the shape of the CV changes with v as I_p^{ox} (I_p^{red}) shifts to more positive (more negative) potentials (see Fig. 3.3(a)). At slow scan rates (v), the CV may resemble that of a reversible reaction, as the rate of electron transfer is faster than v, however, at higher v, electron transfer becomes comparatively slow, and the shape of the CV will change by way of an increased peak separation. Since Eq. 3.1 no longer holds, such a process may also be characterised by a non-linear relationship between I_p and $v^{1/2}$, as the kinetics of electron transport are slowed.

If the process shows no reverse peak, it is found to be chemically irreversible. In this instance, the active species may undergo a chemical change upon oxidation (reduction), such that a reverse sweep cannot return the species to its original state.

The principals of cyclic voltammetry have been considered from the viewpoint of a single oxidation process of a species. Where there are multiple redox processes, the principles described still apply, but with I_p calculated as the difference between the residual current from the previous process, and the peak current of the new process. The potential of a redox couple is generally reported as $E_{1/2} = (E_p^{ox} + E_p^{red})/2$, with the difference in energies of different redox couples ($E_{1/2}^2$ and $E_{1/2}^1$) given as $\Delta E_{1/2} = E_{1/2}^2 - E_{1/2}^1$. Of course, the same principles hold for a reduction process, though with the sign and initial scan direction reversed.

Application of electrochemistry to potential semiconductors For most electronic applications, the materials are used in the solid-state, where chemical reactions are limited to intramolecular, or nearest neighbour processes, and the speed of electron transfer is often orders of magnitude faster than the scan rate (v) of cyclic voltammetry. Therefore, for a material to be of interest as a potential semiconductor, the redox processes need not be electrochemically reversible, nor even chemically reversible by solution analysis. What is important is the ($E_{1/2}$) of the redox processes, as they can be used to approximate the levels of the orbitals (or bands), for efficient energy level matching in devices. [D'Andrade 05] showed that the oxidation potential, as measured by CV, could be related to the ionisation potential in the solid-state. Since the ionisation potential is the energy required to remove one electron from a molecule, this effectively describes the energy of the HOMO orbital of the molecule, and can be calculated as:

$$E_{HOMO} = (-1.4 \pm 0.1) \cdot (q \cdot E_{1/2}^{cv}) - (4.6 \pm 0.08) \text{ eV} \tag{3.2}$$

Where $E_{1/2}^{cv} = E_{1/2}^{act} - E_{1/2}^{ref}$ ($E_{1/2}^{act}$ is the $E_{1/2}$ of the active species and $E_{1/2}^{ref}$ is the $E_{1/2}$ of the ferrocene/ferrocinium reference couple), and q is the charge. From this, the energy levels of the frontier molecular orbitals (or bands) can be calculated, and related to the work function of metals commonly used as electrodes for devices, such as field-effect transistors.

It is possible to compare directly electrochemical experiments, and hence values of E_{HOMO}, run in different media (*i.e.* different solvents, or electrolytes). Though the choice of solvent, as well as supporting electrolyte, are known to effect the relative separations of redox couples ($\Delta E_{1/2}$) [Barrière 02], the effect is often relatively small (compared with the inherent errors in approximating solid-state properties from solution data), and thus systems that impose particular constraints on the electrolyte

medium (*e.g.* through their solubility or stability) can be directly compared with the results obtained in other media. The choice of reference electrode can also be negated by interconversion between reference half cells, and is usually given relative to the normal hydrogen electrode (NHE), an agreed standard for thermodynamic calculations [Pavlishchuk 00]. In this way, a huge amount of data can be collated, and directly compared, almost independent of the experimental conditions, to relate aspects of structure to function for electronic materials, and to assess their potential for incorporation into electronic devices.

It is also possible to investigate the redox properties of solid-state systems directly by CV. This is a common technique for assessing the band energies (or E_{HOMO}) for conducting organic polymers. The polymers can be deposited by solution methods (such as spin or drop coating, as described in section 2.7), or formed by electropolymerisation (see section 3.2.1.2), onto the working electrode, and the redox properties investigated. A distinction should be made at this point between conducting films, and redox active films, as the behaviour of each system is distinct. For the purposes of this work, we restrict our discussion to redox active films, but for a more in depth discussion of both film types, see [Vyas 10], and references therein.

The voltammograms of solid-state, redox-active, systems display some distinct differences, compared to solution-based systems, mostly due to negation of diffusion effects of the active species. However, far from simplifying the situation, the electrochemical behaviour of redox active films is more complicated. For an oxidation process, when the applied potential (E) reaches the oxidation potential of the redox-active species in the film, the electron transfer from the electrode surface to the film is accompanied by a simultaneous ionic transfer from the electrolyte to the film to maintain the electro-neutrality. Thus, a simultaneous electron-transfer and mass-transfer process is required. Efforts to characterise this process have been made by [Vyas 10], and others, using electrochemical impedance spectroscopy[1] (EIS), however, for estimating the energies of the polymer bands, sufficient information can be obtained by CV alone. The voltammograms of redox active polymers are generally run at slower scan rates (v) than for solution based systems ($\sim$10 mVs^{-1}) to observe the behaviour of the total thin film sample. In an ideal experiment, for an electrochemically reversible process, the oxidation and reduction peaks would be symmetrical, with peak potential separation $\Delta E_p = E_p^{ox} - E_p^{red} = 0$ mV (see Fig. 3.4). For such a system, I_p is no longer related to $v^{1/2}$ (Eq. 3.1), but to the scan rate (v) itself (see Eq. 3.3), thus reversibility can be

[1] A technique that investigates how the polarisation (seperation of positive and negative charge) of a material changes in response to an oscillating electric field of changing frequency.

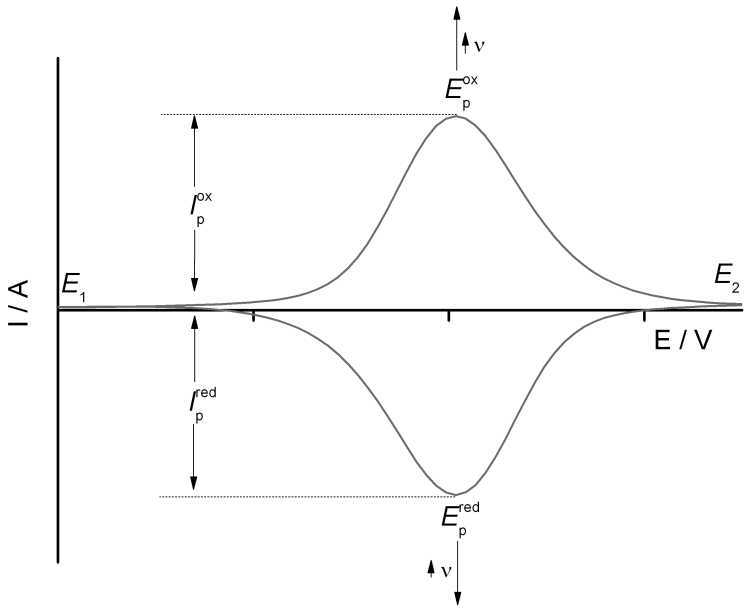

Figure 3.4: An idealised plot of current I vs. potential E, cycling between E_1 and E_2, for an electrochemically reversible process of a surface bound species, corresponding to the $[M]^0/[M]^{+1}$ redox couple. For an electrochemically reversible process, the peak current $|I_p|$ of the oxidation and reduction processes (I_p^{ox} and I_p^{red}, respectively) should increase linearly with the scan rate v, but the potentials of peaks E_p, for the oxidation and reduction process (E_p^{ox} and E_p^{red}, respectively) should not change with scan rate (v).

assigned by a linear relationship between I_p and v:

$$I_p \propto v \tag{3.3}$$

3.2.1.2 Electrodeposition

Electrodeposition can be used as a method of preparing thin films of conductive materials over the working electrode. The broad field of electrodeposition covers the processes of electrocrystallisation, galvanostatic (constant I) and potentiostatic (constant V) film growth, and electropolymerisation, and has been used to fabricate novel materials, as well as known materials, with properties distinct from those formed by solution methods (as described in section 2.7). The process relies on the formation of species with a reduced solubility in the electrolyte medium, such that their continued formation results in their deposition on the working electrode.

Electrocrystallisation is generally conducted under galvanostatic control at very low

current (I) levels, since constant I ensures a constant growth rate, and low I ensures a slow growth, favoring the formation of well formed single crystals on the electrode. For metal dithiolenes, electrocrystallisation has led to the formation of novel salt species, and has led to the discovery of superconductivity in these systems. These, and other electrocrystallised systems are discussed elsewhere [Batail 98].

Under galvanostatic control, but at higher values of I, thin films may be formed on the electrode, as the rate of deposition is too great to facilitate single crystal formation. Galvanostatic control again results in the constant rate of growth of a film. However, if the species generated is sensitive to potential (E), for example by having several redox processes with a small $\Delta E_{1/2}$, or where decomposition is observed soon after oxidation, films may also be grown under potentiostatic control [Valade 05].

Electropolymerisation has been used to prepare conducting, and redox active polymer films (see section 2.5.2). In general, oxidation of the active species results in the generation of a radical, which can couple to another radical, forming a covalent bond, and thus propagating chain growth. The nascent chain has a reduced solubility in the electrolyte medium and, as a result, deposits over the electrode surface, with film growth continuing until E is reduced (or switched off), and can no longer generate a radical. Polymer films can be grown by potentiostatic or galvanostatic methods, or by repeated cycling of E past E_p^{ox} of the system. A thorough account of the process can be found in [Waltman 86], with significant contributions to the field by groups of Roncali (poly-thiophenes *e.g.* [Roncali 92]), Waltman (poly-pyrrole *e.g.* [Waltman 84a]) and Mount (poly-indole *e.g.* [Mount 99]).

As films formed by electrodeposition are grown on the working electrode, their electrochemical behaviour may be studied directly by transferring the working electrode to a monomer-free electrolyte solution. Where necessary, the generated material may be characterised by other analytical techniques by modifying the working electrode. A transparent conducting electrode, such as indium tin oxide (ITO) coated glass, may be used to allow the electronic absorption properties of the film to be investigated (see section 3.3). Interdigitated electrode arrays may be used to investigate the conductive properties of the film (see section 2.4) or, for thicker films, the amount of material generated may be sufficient to characterise by conventional analytical means, such as by ^{1}H NMR or elemental analysis.

3.2.2 Experimental parameters

Electrochemical experiments were performed in a glass cell in dry solvent [dimethylformamide (DMF) (Sigma-Aldrich), dichloromethane (DCM) (stored over KOH, distilled over P_2O_5) or acetonitrile (MeCN) (Sigma-Aldrich)], and solutions were degassed with N_2 before use. The electrolyte used for analysis was tetrabutylammonium tetrafluoroborate ($TBABF_4$), and was prepared from tetrafluoroboric acid and tetrabutyl ammonium hydroxide, and recrystallised 5 times from water and dried under vacuum at 60°C for 2 weeks. In Chapters 6 and 7, alternative electrolytes were used to serve a desired purpose, electrochemical grade $TEABF_4$ (TEA = tetraethylammonium) (Sigma-Aldrich) and $TEAPF_4$ (Sigma-Aldrich), and these were dried overnight under vacuum at 60°C before use.

All electrochemical data were obtained using a type III μAutolab potentiostat, connected to a PC, and controlled using General Purpose Electrochemical System (GPES) software.

Cyclic voltammetry was performed at room temperature on a ∼1 mM monomer solution, with 0.3 M electrolyte (except for DMF where 0.1 M was sufficient) in a three electrode cell. The working electrode was a ∼3 mm^2 Pt disc. The reference electrode was Ag/AgCl (sat. KCl), calibrated against a ferrocene/ferrocenium standard (+0.55 V) in the background electrolyte, and the counter electrode was a Pt rod.

Electrochemical polymerisation was performed at room temperature on a ∼10 mM monomer solution, and was achieved by potential cycling to oxidising potentials, under the same experimental conditions as for CV. Electrodeposition experiments were performed at room temperature on a ∼10 mM monomer solution, and was conducted by potentiostatic control, under the same experimental conditions as for CV.

3.3 Electronic absorption spectroscopy

The energy levels of different processes within a material can be studied by looking at the response of a material to applied electromagnetic radiation. Depending on the applied frequency (ν) of the electromagnetic radiation, different processes within that system can be probed. For example, the microwave region is useful for looking at the rotation of molecules, the IR region can probe the vibration of particular functional groups, and the visible and UV regions are suited to studying the electronic transitions within molecules. It is these transition that yield the most information on the nature

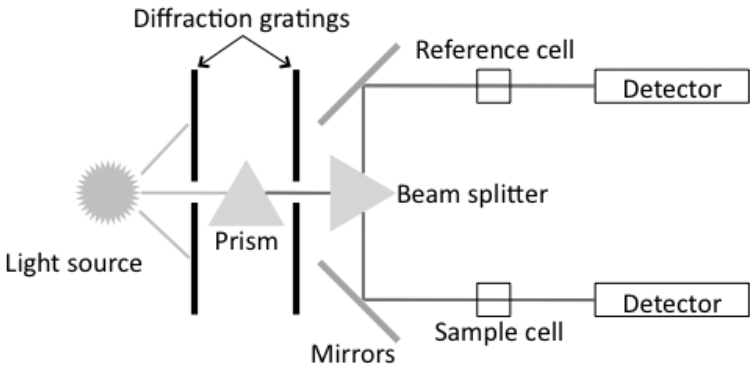

Figure 3.5: A two path length setup used for routine electronic absorption spectroscopy, where the sample absorption can be corrected relative to a reference sample (that is identical to the sample cell, except for the material under study).

of the electronic orbitals, and it is these transitions that are considered in this section.

3.3.1 Theory

By focusing light of different frequencies (ν) on a sample, and observing how much light is absorbed, as a function of ν, a great deal of information can be obtained about the energy levels, as well as the nature of the orbitals themselves. In order to probe such processes, an experimental setup should include a light source, a mechanism for tuning the frequency (ν) of the incident beam, and a detector, placed after the sample chamber for collecting the emergent beam (see Fig. 3.5). In order to accurately determine the absorption [$A = \log_{10}(I_0/I)$, where I_0 and I are the incident and emergent intensities of the beam] of the sample, the setup should include a reference cell that is identical to the sample cell, except for the material under study. This is done to provide a background spectrum that can be used to negate the absorptions of the medium in which the sample is contained. This is routinely done by splitting the beam into two paths; one for the sample, and one for the reference, which allows the absorption to be calculated as the ratio between the two cells [$A = \log_{10}(I_{ref}/I_{sam})$,where I_{ref} and I_{sam} are the emergent intensities of the beam from the reference and sample, respectively].

Transitions between energy levels are due to the absorption of incident radiation by a molecule. The electronic transitions in the UV/Vis region of the electromagnetic spectrum arises from the simultaneous stimulation of vibrational and rotational energy levels. From Fig. 3.6, one can see the vibrational and rotational energy levels in two different electronic states. For energy levels separated by energy ΔE, which is the sum of the change in electronic (ΔE_{elec}), vibrational (ΔE_{vib}), and rotational energy

(ΔE_{rot}), excitation is achieved by light of energy $h\nu$ (where h = Planck's constant):

$$\Delta E = h\nu = \Delta E_{elec} + \Delta E_{vib} + \Delta E_{rot} \tag{3.4}$$

One can generally assume that a transition occurs within a stationary nuclear framework, because the nuclear masses are much larger than the electronic masses, therefore the nuclear locations remain unchanged during a transition, and readjust once the electrons have adopted their final distribution. This is the basis of the Frank-Condon principle. The electronic transition changes the distribution of electrons within the molecule, and the nuclei have to respond to the new force field, leading to vibrational transition, themselves leading to rotational transitions. Therefore, the most probable transitions are to vibrationally excited states that most resemble the ground state geometry. This results in a series of discreet transitions in the absorption spectrum, with their individual intensity reflecting the closeness of geometry between the ground and different vibrationally excited states [Förster 04].

For polyatomic (molecular) systems, the spectra would become very complicated, very quickly, as the number of atoms in the molecule increases, and hence the number of possible transitions increases accordingly. However, the spectra of molecular systems are simplified by two key processes. From Molecular Orbital (MO) theory, one can see that atomic orbitals in a molecule interact on the basis of their symmetry to form molecular orbitals, which can be bonding, *anti*-bonding or non-bonding in nature. In such systems, discrete atomic excitations are generally replaced by transitions between molecular orbitals, thus reducing the number of possible transitions in a molecular system. Secondly, such systems are routinely investigated in solution, where interaction with the solvent effectively broaden out the vibrational/rotational structure, resulting in a smooth curve. Therefore, the resulting shape of the absorption spectra of molecular systems in solution is given by electronic transitions between molecular orbitals comprising all the atoms that make up the orbitals. Though a large amount of information is lost because of these processes, the resulting spectra are still very useful as the frequency (ν), and intensity of the absorption (A) are highly characteristic of the molecule under study.

Vibrational fine structure can be observed, in some instances, where the interaction with the solvent is slight (as in the case of non-polar solvents, such as hexane), or for systems where there is no solvent present, such as for vapour phase analysis, or where the material is deposited as a thin film. In the latter case, not only can the vibrational structure be observed, but also effects arising from the interaction between molecules;

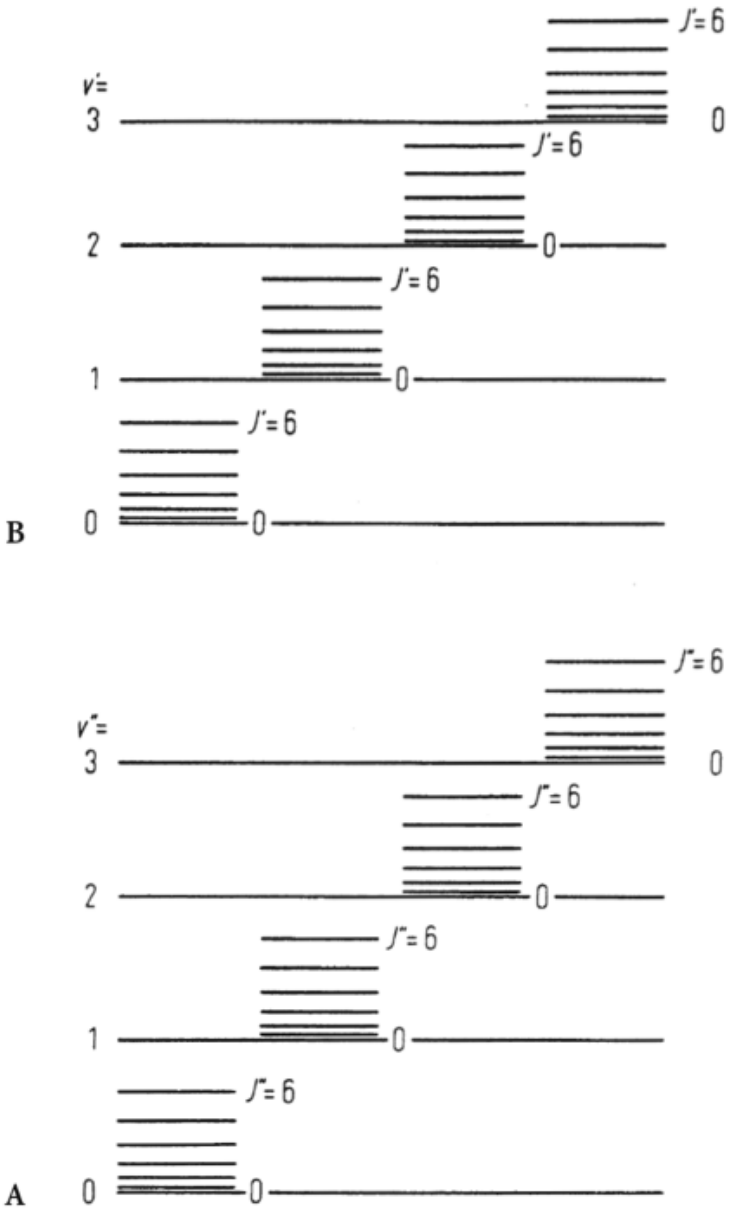

Figure 3.6: A pictorial representation of vibrational (v) and rotational (J) sublevels of two electronic states of a molecule (**A** and **B**). Figure reproduced from [Förster 04].

for a highly delocalised system, such as in the case of polycyclic aromatics, efficient packing of the π systems can lead to a broadening of the energy levels (see section 2.2), resulting in a shift of the peaks to lower energy (bathochromic shift).

Once excited from the ground state, the molecule has a limited lifetime (τ) in the excited state, and can undergo several processes in order to return to the ground state (see Fig. 3.7).

$$\tau = \frac{1}{\text{rate of emission} + \text{rate of non-radiative decay}} \tag{3.5}$$

The excited state could decay radiatively (emission), releasing a photon as the molecule returns to the ground state. Where no change in the spin state of the electron occurs, this process is known as fluorescence. The energy could also be released non-radiatively by a process known as internal conversion (IC), where the energy is converted to vibrational modes of the molecule (non-radiative decay). Alternatively, a change of the spin state can occur from a singlet to a triplet, by a process known as intersystem crossing (ISC). Although a forbidden process (*vide infra*), such a transition can occur for molecules that exhibit a large amount of spin-orbit coupling.[2] From this state, the electron can either decay non-radiatively by a series of ISC processes, or radiatively by a process known as phosphorescence, which, again is a spin forbidden process, and thus happens on a characteristically longer timescale than for fluorescence. Therefore, fluorescent and phosphorescent (known collectively as luminescent) processes can be differentiated by the lifetime (τ) of their excited states.

3.3.2 Interpretation of spectra

From Eq. 3.4, one can see the frequency (ν) of incident radiation required to achieve a transition is proportional to the energy (ΔE) required to invoke the transition, and can therefore be used to characterise a particular electronic transition. ν is more commonly reported as a wavelength ($\lambda = c/\nu$, where c is the speed of light) in units of nm, or as a wavenumber ($\overline{\nu} = 1/\lambda$) in units of cm^{-1}.

As mentioned above, from MO theory, one can think of atomic orbitals in molecules interacting to form bonding (σ and π orbitals), *anti*-bonding (σ^* and π^* orbitals) and non-bonding orbitals[3] (n orbitals). The bonding orbitals can be either σ or π in nature, with the former characterised by being symmetrical, and the latter, unsymmetrical

[2] A form of electromagnetic interaction between the electron's spin and its orbital angular momentum.

[3] Which resemble the atomic orbital(s) of the non-bonding atom.

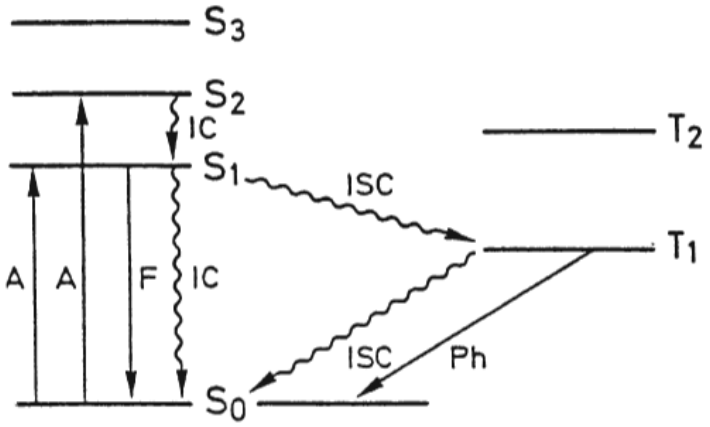

Figure 3.7: Term diagram for electronic transitions, showing absorption (A), fluorescence (F), phosphorescence (Ph), internal conversion (IC), and intersystem crossing (ISC). Figure reproduced from [Förster 04].

with respect to the bond axis. The electrons are bound much tighter in a σ bond as a result of the increased overlap of the atomic orbitals, and as such, electronic transitions from a $\sigma \rightarrow \sigma^*$ orbital occur at much higher energy [often in the vacuum UV range (100 - 200 nm)] than from a π orbital, and are rarely observed under routine absorption spectroscopy, and are often associated with bond dissociation. The π and n electrons require less energy to be excited, and thus electronic transitions between the $\pi \rightarrow \pi^*$ and $n \rightarrow \pi^*$ can be observed in the UV/Visible region of the electromagnetic spectrum. In general, the n electrons, are bound less tightly to their atoms than the π electrons, and usually require less energy to excite (though not invariably). These generalisations are illustrated in Fig. 3.8, and show that, for more conjugated systems, the electronic absorptions occur at lower energy. On the basis of a particle-in-a-box approach, it can be seen that the energy of the observed transition decreases with conjugation, resulting in an absorption at longer wavelengths (λ).

So far, the electronic absorption spectra has been considered to be derived indiscriminately from any electronic transition that is of the energy of the incident photons. However, if this were the case, the resulting spectra would be broad and featureless, since molecular systems contain many electronic states. This is not the case, as certain restrictions are imposed on the spectroscopic transitions. These lead to a series of selection rules that govern whether a transition is allowed (and thus observed) or forbidden (and thus not observed). These rules are derived from the symmetry and multiplicity of the ground and excited state wavefunctions. In reality, 'forbidden' transitions are often observed due to the disruption of symmetry

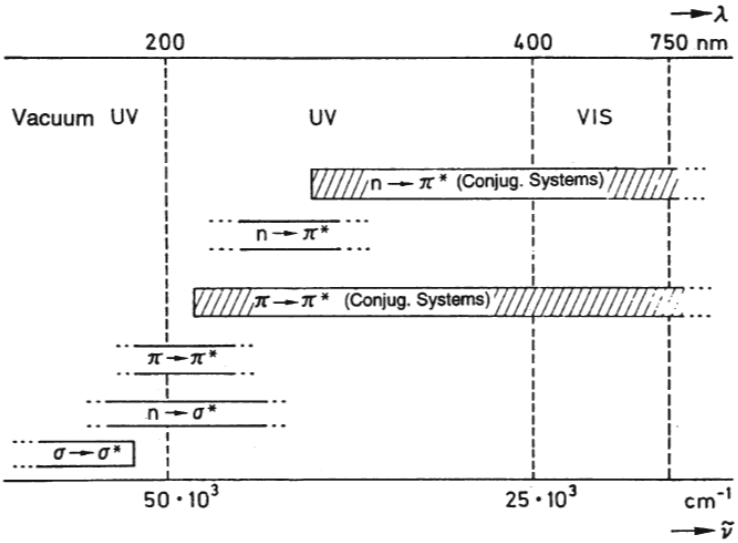

Figure 3.8: Ranges of absorption for different electronic transitions between occupied bonding (σ and π) and non-bonding (n) orbitals, and *anti*-bonding orbitals (σ^* and π^*). The typical energies of the transitions are given in wavenumbers ($\overline{\nu}$), and as wavelengths (λ). Figure reproduced from [Förster 04].

by molecular vibrations (such as for d→d transitions in transition metal complexes) or substitution, however their intensity is characteristically much weaker than for 'allowed' transitions. Therefore the intensity of an observed transition yields important information on the nature of the electronic orbitals involved in the transition.

The rules governing possible transitions between molecular orbitals are derived from the symmetries of the orbitals involved. A complete mathematical derivation of the selection rules can be found in [Atkins 05], however for the purposes of this work it is sufficient to consider their implications.

The first rule concerns the multiplicity of states, and suggests that the total spin quantum number (S), which effectively describes the state of the electrons in an orbital, should not change during a transition ($\Delta S = 0$). This forbids the transition between singlet and triplet states. As discussed earlier, this does not alway hold, especially for complexes of the lower d block elements, where their electronic spin angular momentum is heavily coupled to the orbital angular momentum. In this instance, spin forbidden transitions are often observed, though are of low intensity.

The second rule concerns the orbitals of the ground and excited states, and suggests that the azimuthal quantum number (l), which defines the orbital angular momentum,

must change during a transition ($\Delta l = \pm 1$). This rule is derived from a consideration of the symmetry of the atomic orbitals, and shows that, for a transition to be allowed, the parity (which describes how the orbital responds to inversion) should change during a transition. The labels 'g' (*gerade*) and 'u' (*ungerade*) are used to describe whether an orbital remains the same, or changes under inversion. It can be shown that transitions between $g \rightarrow g$ and $u \rightarrow u$ are forbidden as they result in net zero value for the electric transition dipole moment, which is effectively a gauge for the probability of a transition [Förster 04]. This forbids transitions between s→s or p→p or d→d orbitals. For molecular systems, this has implications particularly on non-bonding orbitals, as they are better described by their individual atomic orbitals. In the case of d→d transitions in transition metal complexes, however, these transitions are often observed, though are characteristically weak. For rigorously centrosymmetric complexes of the d-block elements, weak transitions ($\epsilon \leq 100$ dm^{3}mol^{-1}s^{-1}) are often observed due to vibrational modes that disrupt the centrosymmetry in the molecule. These are known as Laporte-forbidden transitions. For complexes without a centre of symmetry, such as tetrahedral complexes, these transitions are more intense ($\epsilon \approx 250$ dm^{3}mol^{-1}s^{-1}). Such transitions are known as Laporte-allowed transitions.

A further consideration for interpreting the intensity of a transition is the degree of spatial overlap of the ground and excited state wavefunctions. For systems that have a high degree of overlap, the resulting transition will be more intense than for a low degree of overlap. This is especially apparent for the $\pi \rightarrow \pi^*$ transition within organic molecules, as they often display a large degree of spatial overlap.

It has previously been shown that the wavelength of the maximum absorption (λ_{max}) yields important information regarding the energy of a particular transition and, now by consideration of the intensity of the absorption (A), the type of transition can also be characterised. The intensity of the absorption (A) is commonly reported as the molar extinction coefficient (ϵ), which has units of 1000 cm^{2}mol^{-1}, though, by convention, these are never expressed. The molar extinction coefficient is related to A by a combination of the Lambert law, which states that the fraction of incident light absorbed is independent of the intensity of the source, and the Beer law, which states that the absorption is proportional to the number of absorbing molecules, yielding the formula:

$$A = log_{10}\frac{I_0}{I} = \epsilon \cdot l \cdot c \tag{3.6}$$

where I_0 and I are the intensities of the incident and transmitted light, respectively, l is the path length through the absorbing solution (in units of cm), and c is the

concentration (in units of mol/dm^3). The cell used should be transparent in the region of the spectra under study, and have a uniform path length (l) for accurate measurement of the molar extinction coefficient (ϵ). By measurement of the absorption spectra, relative to a blank cell (identical to the measured cell, save the studied species), the energy (λ_{max}) and the intensity (ϵ) of the transitions can be determined. For accurate assignment of ϵ, at least three measurements should be recorded over a concentration range of at least an order of magnitude, with ϵ given as the gradient of a plot of absorption (A) as a function of concentration (c). It should be noted that at higher concentrations (c), the plot can deviate away from linearity due to aggregation effects, in which case, lower concentrations (c) should be used.

3.3.3 Application to metal dithiolenes

Many metal dithiolenes characteristically show an intense (ϵ = 15,000 to 40,000), long-wavelength (above 700 nm) transition, unsurpassed by other transition metal complexes and, as such, have been used as NIR laser dyes [Mueller-Westerhoff 91]. Resolution of this transition yields detailed information on the relative energies of the frontier orbitals, and thus can be used as a tool for assessing the potential for these systems in electronic, or optical application. The body of literature devoted to the absorption properties of metal dithiolenes is vast (see *e.g.* [Mueller-Westerhoff 87]), and thus, this discussion is limited to studies relevant to this work, namely square planar *bis*-dithiolenes of nickel and copper.

The absorption properties of nickel *bis*-dithiolenes are perhaps the most widely studied of all the metal dithiolenes, due to their low cost, their ease of synthesis, and their highly tunable absorption properties [Mueller-Westerhoff 91]. Extensive theoretical treatment, combined with thorough experimental data, have shown the low energy transition of neutral nickel dithiolenes to be due to a $\pi \rightarrow \pi^*$ transition between the HOMO and the LUMO orbitals, which are spread over the whole dithiolene core (see Fig. 3.9) [Waters 06, Szilagyi 03]. This is due to a large amount of metal-ligand covalency (effectively the amount to which the nickel and sulfur orbitals mix).

From our previous discussion, one can see that the intensity of this low energy HOMO→LUMO transition is due to the fact that it is a spin allowed transition between orbitals with a high degree of spatial overlap and, in the case of centrosymmetric dithiolenes, it is also Laporte-allowed. Such a transition is far more intense than for most other types of transition metal complexes, which usually show weaker d→d transitions in this region of the spectra (*vide infra*). For the dithiolene redox series

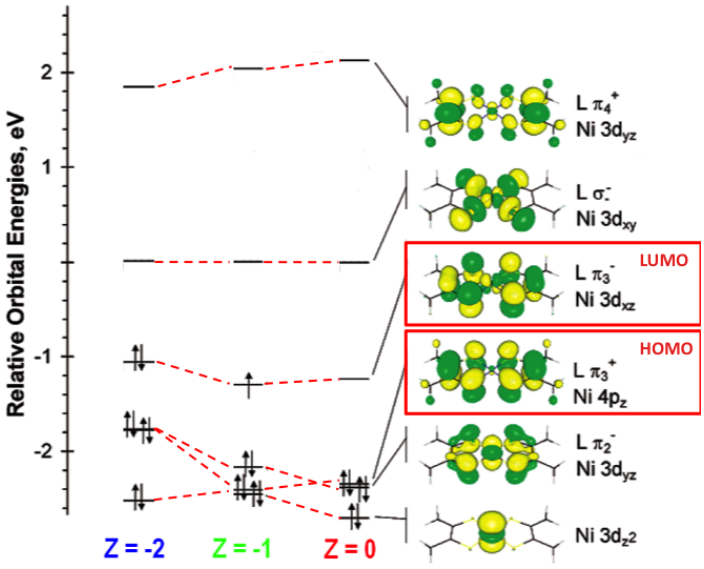

Figure 3.9: Orbital picture of the nickel *bis*-dithiolene redox series, with symmetrised geometry from the X-ray structure of $[Ni(S_2C_2Me_2)_2]^Z$ (where Z = 0, -1, -2), calculated at the B88P86/BS5 level of theory (see section 3.4.1). The metal and ligand orbitals that constitute the molecular orbital are described in terms of their individual identity (*e.g.* for the HOMO orbital, Ni $4p_z$ and L π_3^-, describe the metal and ligand orbitals comprising the molecular orbital, respectively). Figure modified from the original [Szilagyi 03].

$[NiL_2]^{z-}$ (where z = 0, 1, 2), the redox active orbital is predominantly ligand based (S $3p_z$), though with some metal character (Ni $3d_{xz}$) (see Fig. 3.9). Sequential reduction of the neutral complex corresponds to the sequential filling of this orbital, thus tuning, and eventually switching off the low energy $\pi \rightarrow \pi^*$ transition for the mono- and direduced states, respectively.

The absorption properties of copper *bis*-dithiolenes have been, comparably, less intensively studied [Sarangi 07]. One reason for this is the instability of neutral copper dithiolenes, prohibiting the study of a complete redox series, as for the nickel dithiolenes described above [Szilagyi 03]. To date, only two neutral copper dithiolene complexes have been reported in the literature [Ueda 98], and for these complexes, no optical data are reported. Both these complexes are formed from TTF substituted dithiolene ligands, which are thought to stabilise the radical of these neutral copper dithiolenes over their large delocalised core (see section 2.5.1). By comparison with the nickel dithiolene redox series, one could expect the readily isolatable, more stable monoanionic copper dithioleness $[CuL_2]^{1-}$, to show only weak NIR absorption, if any, as they are isoelectronic with the the dianionic nickel dithiolenes $[NiL_2]^{2-}$. Since the redox active orbital (formally the LUMO in the neutral nickel dithiolene) is filled for the

monoanionic copper dithiolene, the intense $\pi \rightarrow \pi^*$ transition, observed for the neutral and monoanionic nickel dithiolene, is switched off. Any absorption observed in the NIR region for the mono- or direduced copper dithiolene would therefore be due to d→d transitions, and would accordingly be weak. If, however, a stable neutral copper dithiolene were to be studied by absorption spectroscopy, one would expect it to display an intense NIR transition, comparable to the isoelectronic $[NiL_2]^{1-}$ species.

These studies demonstrate the practical importance of absorption spectroscopy. For metal dithiolenes, by recording their absorption spectra, and assessing the energy and intensity of the observed transitions, one can validate bonding models proposed by other experimental or theoretical techniques, and observe how the nature of the ligand affects the relative energies of the frontier orbitals.

3.3.4 Spectroelectrochemistry

From the preceding discussion, it is evident that a powerful extension to absorption spectroscopy would be achieved by coupling the technique with electrochemistry, in order to investigate the absorption properties of oxidised and reduced species *in situ*. This technique is particularly useful for observing the change in absorption properties on forming species that otherwise may not be easily isolated (due to *e.g.* air instability).

Metal dithiolenes have been shown to have multiple stable redox states, with distinct absorption properties and, as such, are particularly suited to this technique. The fundamentals of electrochemistrty have been discussed above (see section 3.2). For *in situ* analysis, several modifications must first be made to the electrochemical setup in order that the absorption properties can be studied. The most common technique for spectroelectrochemical analysis is Optically Transparent Thin Layer Electrochemistry (OTTLE), and it is this that shall be considered here. Modification can be made to the experimental setup, where additional requirements are placed on the design (see section 6.2), but in the first instance, OTTLE provides a relatively simple method for *in situ* analysis.

The electrochemical cell is designed to be transparent to enable the absorption spectra to be recorded (see Fig. 3.10). The cell is generally a thin quartz cuvette to allow the transmission of light through the sample, but also to ensure the complete oxidation or reduction, in the pathlength of the spectrometer, on a short timescale. The working electrode should be large to facilitate swift generation of redox species, but should also be transparent, and is generally a Pt/Rh gauze. The working electrode is isolated

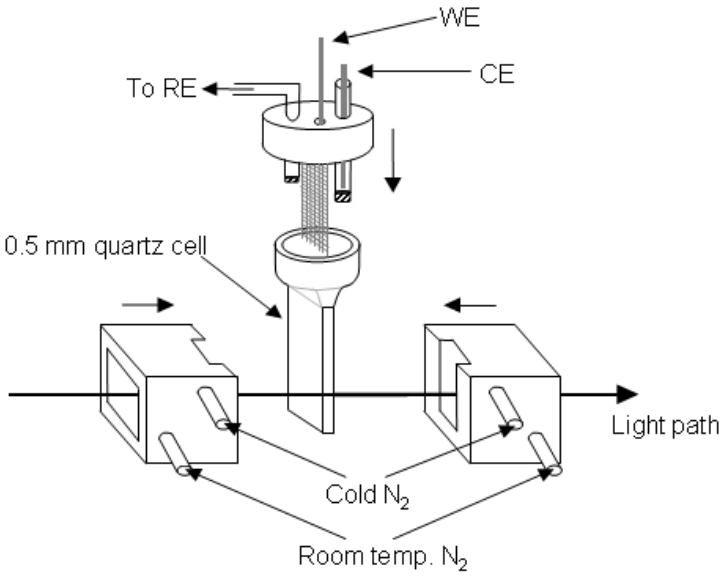

Figure 3.10: A three electrode electrochemical cell setup used for *in situ* measurement of the electronic absorption spectra upon an applied potential (E). The working electrode (WE), counter electrode (CE) and reference electrode (RE) are housed in a quartz cell, and held in place by a teflon cap.

from the bulk cell by an inert teflon sleeve, to avoid bulk electrolysis of the cell, and restrict redox processes of the active species to the pathlength of the spectrometer. The reference and counter electrodes are located in the reservoir above the pathlength, and held in place by a teflon cap. In this instance, the counter electrode is also placed in a salt bridge to stop the redox processes of the active species from occurring at the counter electrode. Where necessary, the cell can be cooled by a stream of pre-cooled nitrogen. This is routinely done to improve the reversibility of redox processes, by slowing the rate of decomposition. To avoid frosting of the cell, dry nitrogen is used to purge the cell of atmospheric moisture. The UV/Vis spectra can then be recorded continually, whilst applying a potential sufficient to induce a redox change. Long term reversability of an electrochemical process can be assessed in this way if the spectra can be returned to its original state upon application of a sufficient potential to re-reduce or re-oxidise the species.

3.3.5 Experimental parameters

UV/Vis/NIR measurements were recorded in laboratory grade solvents in a quartz cell of path length $l = 10$ mm on a Perkin-Elmer Lambda 9 spectrophotometer, controlled by a datalink PC, running UV/Winlab software v1.6 (Perkin-Elmer). Solution deposited thin films were investigated by spin coating onto quartz substrates, and electrogenerated

polymer films investigated by electropolymerisation onto fluorine doped tin oxide (FTO) coated glass electrodes, and fixed perpendicular to the beam in the UV cavity.

OTTLE measurements were recorded in a cell of path length $l = 0.5$ mm using dry DMF and 0.1 M $TBABF_4$ as supporting electrolyte in a three electrode cell. The working electrode was a Pt/Rh gauze, the reference electrode was Ag/AgCl (sat. KCl), and the counter electrode was a platinum wire.

3.4 Computational modeling

Computational calculations can be performed to support experimentally observed data, or to predict the properties of novel materials. Caution must be exercised, however, when performing calculations, as the results obtained are based on mathematical solutions to the information given. Therefore, if the information going in is wrong, the information coming out will be wrong. In addition, computational models, as the name suggests, use varying levels of approximation when deriving a solution, thus, even if the information going in is right, the information coming out may still be wrong. One further scenario can be envisioned where, if the data going in is wrong, but the answer coming out is right, and in agreement with some experimental data, false conclusions may be drawn. With this in mind, where possible, one should always support computational data with thorough experimental data.

Computer modeling uses complex mathematical derivations to approximate the properties of molecules. With the emergence of an increasing number of user-freindly interfaces for running calculations, a rigorous understanding of the mathematics is not strictly necessary to derive sensible computational solutions, but rather a thorough understanding of how the maths is implemented, and the resulting limitations understood. With this in mind, this discussion focusses on the application of the theory, rather than the maths itself. A more rigorous mathematical treatment of computer modeling can be found in [Atkins 05].

Where successful, computational modeling can help to understanding many properties of molecules, including some particularly relevant to this work, such as their geometry (see section 3.4.2), their absorption spectra (see section 3.4.3), or their conductivity (see section 3.4.4), and the methods used to calculate these properties are discussed below.

3.4.1 Energy calculations of single molecules

Various properties of molecules can be calculated from first principles by solving the Schrödinger equation. Such calculations are described as *ab initio*. Since the calculations do not require any empirical input, and are based purely in quantum mechanics, the calculated properties can be compared with experimental data and the accuracy of the modeling, thereby, assessed. For properties that do not change with time, such as the molecular geometry (see section 3.4.2), they can be calculated by solving the time independent Schrödinger equation [Atkins 05].

$$\mathcal{H}\Psi = E\Psi, \tag{3.7}$$

where Ψ is the wavefunction, and E the energy. $\mathcal{H}$ is an operator, known as the Hamiltonian, and comprises all the energy terms for a given system. Therefore, for a system of nuclei (n) and electrons (e):

$$\mathcal{H} = T_e + T_n + V_{en} + V_{ee} + V_{nn}, \tag{3.8}$$

where T_i and V_{ij} are the corresponding kinetic and potential energies, respectively.

Due to the mathematical complexity of Eq. 3.7, the energy cannot be calculated analytically for any system, and thus certain approximations have to be made in order to simplify the calculation.

Since electrons are light, compared to nuclei, they can be assumed to adapt instantaneously to any change in the position of the nuclei, and thus depend only on the position of the nuclei, and not on their momentum (Born-Oppenheimer approximation). By making this assumption, the Hamiltonian can reduced to an electronic Hamiltonian:

$$\mathcal{H}_{elec} = T_e + V_{en} + V_{ee}, \tag{3.9}$$

as, for a given nuclear arrangement $T_n = 0$ and $V_{nn} =$ constant. The Schrödinger equation can then be solved for each nuclear arrangement:

$$\mathcal{H}_{elec}\Psi_{elec} = E_{elec}\Psi_{elec}, \tag{3.10}$$

where Ψ_{elec} is the electronic wavefunction and E_{elec} the electronic energy. It should be noted that, to calculate the total potential energy for a particular nuclear arrangement, the nuclear repulsion must still be taken into account ($E_{tot}^{pot} = E_{elec} + V_{nn}$). This approximation holds well for molecules in their electronic ground state, but can break

down when modeling excited states, large amplitude vibrations, or the motions of light nuclei [Atkins 05, Richardson 01].

Even by making this approximation, however, the Schrödinger equation cannot be solved analytically for systems larger than H_2^+. This is because of the term V_{ee} in Eq. 3.9, which accounts for the interaction between electrons. This interaction is governed by two principles. The first is the fact that two electrons of the same spin cannot occupy the same region in space (Pauli principle). The second is the Coulombic repulsion between electrons which, for electrons of the same spin, is also affected by the Pauli principle. In order to account for the Pauli principle, a specific form of the overall wavefunction is used (a Slater determinant), and spin orbitals are introduced, where Ψ can be described as the product of its spatial and spin wavefunctions (Ψ_r and Ψ_s, respectively). Using this special form of the wavefunction, the Pauli principle is satisfied, however, its effect on the electrostatic interaction between the electrons is still not known [Atkins 05].

Two different computational methods have been developed which differ in the theoretical approach used to deal with the interaction between electrons (V_{ee}); the first is Hartree-Fock (HF) theory, and the second is density Functional Theory (DFT), and these will be looked at separately.

Hartree-Fock (HF) theory HF theory accounts for the interaction between electrons by considering each electron to interact with an average field of the other $n-1$ electrons [Atkins 05]. The Hamiltonian is replaced by a Fock operator, which comprises the one electron hamiltonian h_i, and a correction term to account for the electron-electron interaction. This term is made up of the Coulomb operator (J_{ij}), which takes into account the classical Coulombic repulsion, and a modification to the Coulombic repulsion (K_{ij}) to account for the Pauli principle.

$$\begin{aligned} F_i &= h_i + \sum_{j \neq i} [2J_{ij} - K_{ij}] \\ J_{ij} &= \int \Psi_i(1)\Psi_j(2)\frac{1}{r_{12}}\Psi_i(1)\Psi_j(2)\, d\tau_{12} \\ K_{ij} &= \int \Psi_i(1)\Psi_j(2)\frac{1}{r_{12}}\Psi_i(2)\Psi_j(1)\, d\tau_{12} \end{aligned} \tag{3.11}$$

This approximation only considers the electron-electron interaction to a very small extent. In order to approximate the electron coupling more rigorously, Post HF methods have been developed, however such calculations are difficult to perform, and

are computationally demanding and, as such, are only suitable for small molecules, and are therefore beyond the scope of this work (for a more detailed description of HF and Post HF theory see [Atkins 05]).

Density functional theory (DFT) DFT applies a different theoretical approach when calculating the energy of a system, whereby the ground-state energy, and all other ground-state electronic properties, can be determined solely by a consideration of the electron density $\rho(r)$ [Atkins 05]:

$$\rho(r) = \sum_{i=1}^{n} |\Psi_i(r)|^2, \tag{3.12}$$

where Ψ_i are the one-electron spatial orbitals. This simplifies the calculation to a large extent, allowing for the study of larger systems, such as those investigated in this work. The energy of the system is here given by the functional $E[\rho]$[4]:

$$E[\rho] = T_e + V_{en} + V_{clas,ee} + E_{xc}, \tag{3.13}$$

where T_e is the kinetic energy of the electrons, V_{en} the electron-nucleus attraction and $V_{clas,ee}$ is the classical Coulomb interaction, and E_{xc} is the exchange and correlation energy, which takes into account all non-classical electron-electron interactions. However, the exact form of E_{xc} is not known.

Many different functionals (forms of Eq. 3.13) have been developed, each differing in the extent to which the correlation is considered. In this work, the Becke three parameters hybrid exchange was used with the Perdew-Wang 1991 correlation functionals (B3PW91) [Perdew 92, Perdew 96]. This exchange functional was found to give superior agreement between the calculated and observed geometry (as given by single crystal XRD), compared to the correlation functional of Lee, Yang, and Parr (B3LYP) [Lee 88], which is commonly used for the study of purely organic compounds [Paier 07].

Self consistent field For both HF and DFT, the 'answer' has to be known already before performing the calculation [Atkins 05]. For HF, this is the wavefunction (see Eq. 3.11), and for DFT, this is the charge density distribution, itself calculated form a wavefunction (see Eq. 3.12). This problem is solved for HF (DFT) by proposing a set of trial wavefunctions (charge density) and, from this, a new energy and set of wavefunctions (charge density) can be calculated. These new wavefunctions (charge

[4] E is a functional, which is a function of a function.

density) are then used as the input for the next calculation, and the process is repeated until convergence is achieved (*i.e.* where the change in energy, and the wavefunctions (charge density), do not change by more than a predefined threshold).

This trail and improvement method is computationally demanding as, at each stage, a wavefunction (charge density) must be calculated. This puts certain restrictions on the size of the systems that can be studied. This process can be simplified by approximating the spatial wavefunction by a linear combination of known basis functions (Φ):

$$\Psi_r = \sum_i c_i \Phi_i \tag{3.14}$$

In this case, the calculation ceases to be one of solving one of solving complicated wavefunctions, but rather a more simple calculation of linear equations to find the best coefficients (c_i) to describe the orbitals. The accuracy of such a calculation is necessarily dependent on the size and quality of the basis set used.

Many functions have been developed, which can be used as basis functions, each differing in the accuracy with which they describe the shape of the orbitals. One of the most common basis functions, and the ones used in this work, are gaussian type orbitals (GTOs), used due to their simple behaviour in calculations [Atkins 05].

Gaussian type orbitals (GTOs) A simple GTO only approximates an orbital very crudely, therefore a linear combination of GTOs [known as a contracted GTO (CGTO)] is usually used to model an orbital:

$$CGTO = \sum_i d_i GTO_i \tag{3.15}$$

The coefficients d_i can be obtained by modeling the individual atomic orbitals. These then remain fixed throughout the calculation. This approximation holds well for the core electrons, however, for the valence electrons, whose orbitals are modified due to the effect of bonding, the description is much poorer. To model this effect, two (or more) basis functions can be used (which can be simple or contracted GTOs) in Eq. 3.14 to model the valence orbitals. This allows for changes in the shape of the orbitals during the calculation, and not just their relative size. Basis sets which allow two (or more) basis functions for the valence orbitals, but only one for the core orbitals, are known as split valence basis sets.

A further modification to the basis set can be made to model polarisation effects,

caused by the distortion of the shape of the electron cloud of one atom by the electron cloud of its neighbour atom. Such an effect can be better modeled by including orbitals of a higher quantum number (l) than are normally filled for the atom, for example, p-orbitals for a hydrogen atom. Such functions are known as polarisation functions.

When modeling anions or excited states, since the electrons may be located further from the nucleus than in the ground state, diffusive basis functions may be added, which model a larger spatial region for the orbital.

In this work, the basis set used was 6-31G* [Ditchfield 71, Rassolov 01], which is a split valence basis set, where G stands for gaussian type orbitals. The core orbitals are modelled with one basis function which is a contraction of six GTOs, while the valence orbitals are modelled with two basis functions (one consisting of three GTOs and the other of one GTO). The basis set includes a polarisation function (denoted *), which adds six d-type polarisation functions on each of the atoms Li through Ca, and ten f-type polarisation functions on each of the atoms Sc through Zn [Gaussian 03].

Previous studies of metal dithiolenes have used various different basis sets to model their ground state properties. The works of [Szilagyi 03] and [Sarangi 07], discussed in section 3.3.3, used a split valence polarisation basis set (6-311G* [Krishnan 80]) to describe the metal atom. In this work, no significant improvement could be observed by using this basis set, in terms of agreement of structure (see section 3.4.2), or absorption properties (see section 3.4.3) with experimentally observed values. Further to this, the increased size of the systems studied in this work meant that the calculations became computationally very expensive [up to 30 times longer for 6-311G*, than for 6-31G* for a geometry optimisation with coupled frequency calculation (see section 3.4.2)].

Having decided upon a level of theory, the electronic energy (single point energy) is calculated, and from this, a number of molecular properties can be determined. Further discussion of these properties is limited to those investigated in this work.

3.4.2 Geometry optimisation

As discussed in section 3.4.1, the calculated potential energy is dependent on the arrangement of atoms within the molecule. This dependence is illustrated in Fig 3.11 for a 2D example. By plotting the energy with respect to nuclear coordinates, several points can be identified on the potential energy surface (PES), based on an analysis of the first derivative (slope) and the second derivative (curvature), also known as the

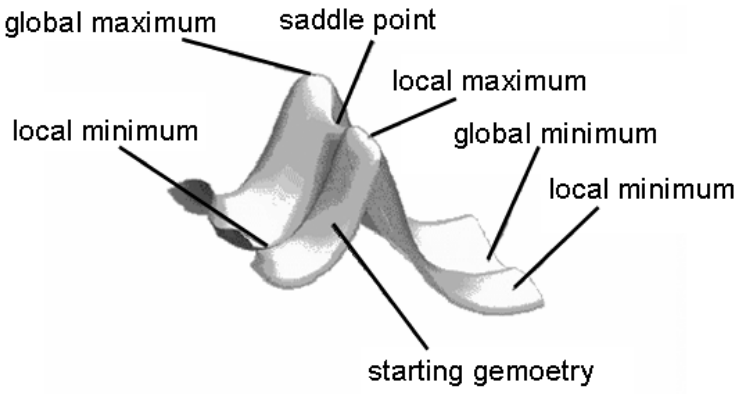

Figure 3.11: General form of a 2D potential energy surface.

Hessian matrix:

- **Maximum** The slope is zero, the curvature is negative in all directions.
- **Minimum** The slope is zero, the curvature is positive in all directions.
- **Saddle Point** The slope is zero, the curvature is negative in at least one direction, and positive in at least one other.

At each of these points, the first derivative of the potential energy is zero, meaning that all the forces exerted on the nuclei by the electrons and the other nuclei are balanced. These points are known as stationary points. Where the second derivative is positive in all directions, the structure is at an energy minimum (equilibrium structure), which can either be the global, or a local minimum.

When performing a geometry optimisation, the whole potential PES cannot be calculated, as this would require immense computational cost, and thus a search algorithm is used, starting from an initial geometry, and leading to an equilibrium structure that is generally close to that of the initial geometry. This highlights the point made at the start of section 3.4 - if the information going in is wrong, then the information coming out can be wrong - and thus a sensible starting geometry is essential for a sensible calculated geometry. In this work, where possible, the starting geometry was that obtained by single crystal XRD.

Most algorithms, including the Berny optimisation algorithm, as used in this work, lead to a geometry in which the magnitude of the forces are sufficiently close to zero, with the degree of closeness stipulated by a pre-defined tolerance limit and, at this point, the calculation is deemed to have converged [Gaussian 03].

The Berny algorithm propagates by calculating the energy of the initial structure. From this the first derivative is calculated and the second derivative (Hessian matrix) estimated.[5] A quadratic function is fitted, based on these values, and a minimum is identified on that function. If the minimum lies within a pre-set radius (trust radius) that determines the maximum step size from the first point, then the step is always accepted. If it lies outside the trust radius, the step size is reduced to the perimeter of the trust radius, and the minimum on that perimeter accepted.

The potential energy of this new point is calculated and, from this, the first derivative is calculated and the Hessian estimated. From these values, a polynomial function is fitted between this point and the best previous point. The better the estimate of the Hessian (*i.e.* the more previous points for comparison) the greater the accuracy of the polynomial that is fitted.

If the latest point is the best so far, the minimum on the polynomial is always accepted. However, if only a quadratic function could be fitted, then the process is the same as for the first step. If the latest point is not the best so far, the minimum on this polynomial is only accepted if it lies between the latest and best previous points. If the polynomial fails to propose a minimum, then a new position is taken as the midpoint between the latest and best previous points.

This process is repeated until a stationary point is found. This point is determined against default criteria preset in Gaussian: the maximum force component, the root mean squared (RMS) force, the maximum step component, and the RMS step. These default criteria can be adjusted when a calculation struggles to converge, however, this can lead to greater errors in the calculation.

As already mentioned, this algorithm leads to the stationary point closest to the starting geometry. Therefore, a range of equilibrium conformations can be found, by providing different starting geometries. The global minimum, being the most stable equilibrium conformation, can only be found, if all minima are found, and their energy values compared.

Local minima can be differentiated from saddle points by comparison of their second derivatives. For an energy minimum, the Hessian of the PES must be positive in all

[5]The calculation of the second derivative is computationally demanding, and is thus approximated numerically based on the position of other known points on the PES.

directions, whist for a saddle point, the Hessian is negative in at least one direction, and positive in at least one other. The Hessian is estimated during a geometry optimaisation, however a simple method for extracting the data, often to a higher degree of accuracy can be achieved by performing a frequency calculation after optimisation is complete. Since the calculated frequencies of vibration are directly related to the values of the Hessian matrix [Atkins 05], the absence of negative frequencies proves the absence of negative values in the Hessian, thus confirming the stationary point to be a minimum.

3.4.3 Time-dependent calculation

So far, only time-independent calculations have been considered. These calculations are, essentially, ground-state models which, as such, exclude the interaction of matter with time-dependent fields. In this section, only the influence of matter with 'small' external potentials, as in the case of photoabsorption, are considered. Such a calculation can be described by linear response theory [Marques 04]. This is not the case for 'large' external potentials, which are harder to model, and are not discussed as they are not relevant to this work.

In order to model properties that arise from interaction with time-dependent fields, the time-dependent Schrödinger equation must be solved [Atkins 05]:

$$\mathcal{H}(t)\Psi(t) = i\hbar\frac{\delta\Psi(t)}{\delta t} \tag{3.16}$$

From the time-independent calculation, the energies $E_n^{(0)}$ and wavefunctions $\Psi_n^{(0)}$ of the unperturbed ground-state are known. By combining Eq. 3.16 with Eq. 3.7, one can obtain the time-dependence of the unperturbed ground-state wavefunctions $\Psi_n^{(0)}(t)$:

$$\Psi_n^{(0)}(t) = \Psi_n^{(0)} e^{-iE_n^{(0)}t/\hbar} \tag{3.17}$$

It can be seen that, in the stationary state, the time-dependence is only expressed in the phase of the wavefunction, and the energies are set by the time-independent calculation.

As for the time-independent energy calculation, where the ground-state wavefunctions were approximated by a linear combination of basis functions (in the form of atomic orbitals), for time-dependent calculations, the time-dependent perturbed wavefunctions can be approximated by a linear combination of the unperturbed time-dependent wavefunctions:

$$\Psi(t) = \Sigma a_n(t)\Psi_n^{(0)}(t) \tag{3.18}$$

If such a system interacts with an external field, the Hamiltonian $\mathcal{H}(t)$ of the system can be rewritten as a combination of the time-independent Hamiltonian $\mathcal{H}^{(0)}$ and the time-dependent perturbation $\mathcal{H}^{(1)}(t)$:

$$\mathcal{H}(t) = \mathcal{H}^{(0)} + \mathcal{H}^{(1)}(t) \tag{3.19}$$

Putting this Hamiltonian into Eq. 3.16, and rewriting the wavefunctions as described in Eq. 3.18, one obtains [Atkins 05]:

$$i\hbar \sum_n \frac{\delta a_n(t)}{\delta t} \Psi_n^{(0)}(t) = \sum_n a_n(t) \mathcal{H}^{(1)}(t) \Psi_n^{(0)}(t) \tag{3.20}$$

From this equation, one can therefore observe how the occupation $a_n(t)$ of the unperturbed wavefunctions $\Psi_n^{(0)}(t)$ changes with time, under the influence of an external field $\mathcal{H}^{(1)}(t)$. For example, if one imagines a system where at $t = 0$, $a_0^{(0)} = 1$ and $a_n^{(0)} = 0$ for $n \geq 1$, which means that the wavefunction is the same as that of the unperturbed wavefunction of level $E_0^{(0)}$. One can then calculate the probability $p_1(t)$ of finding the system at level $E_1^{(0)}$, and thus $a_1(t) \neq 0$, after time t_1 by:

$$p_1(t_1) = |a_1(t_1)|^2 \tag{3.21}$$

By looking how the occupation of the wavefunction varies with time, one can observe between which atoms the transition occurs. For example, if in the ground-state, the molecular orbital is mainly centred around atom m, and after a transition, around atom n, then a transition between $m \rightarrow n$ has occurred.

If one wants to calculate how $a_1(t)$ evolves with time (ignoring all other states), one needs to solve:

$$i\hbar \frac{\partial a_1(t)}{\partial t} \Psi_1^{(0)}(t) = 1 \cdot \mathcal{H}^{(1)}(t) \Psi_0^{(0)}(t) \tag{3.22}$$

Rewriting the time-dependent wavefunctions in terms of their time-independent wavefunctions, as in Eq. 3.17, and multiplying by Ψ^*, and integrating over all space and over time t, to look at t_1, one obtains:

$$a_1(t_1) = \frac{1}{i\hbar} \int_o^{t_1} dt \Psi_1^{(0)*} \mathcal{H}^{(1)}(t) \Psi_0^{(0)} e^{-i\Delta E_{10} t/\hbar} \tag{3.23}$$

Where $\Delta E_{10} = 2\pi\hbar\nu_{10}$. Therefore, ν_{10} is the frequency of radiation that induces a transition between E_0 and E_1.

In the case of absorption spectroscopy, $\mathcal{H}^{(1)}(t)$ is an oscillating electromagnetic field

$E(t) = \mathcal{E}_0 cos(\omega t)$ (where $\mathcal{E}_0$ is the wave amplitude), of radial frequency $\omega = 2\pi\nu$, which is described for direction z as:

$$\mathcal{H}^{(1)} = -\mu_z \mathcal{E}_0(t)\cos(\omega t) \tag{3.24}$$

where μ_z is the dipole moment of the molecule in direction z, one can calculate [Atkins 05]:

$$\Psi_1^{(0)*}\mathcal{H}^{(1)}(t)\Psi_0^{(0)} = -\mathcal{E}_0\cos(\omega t)[\Psi_1^{(0)*}\mu_z(t)\Psi_0^{(0)}] \tag{3.25}$$

as only the dipole moment depends on the orientation. This leads to a definition of the transition dipole moment $\mu_{10} = \Psi_1^{(0)*}\mu_z(t)\Psi_0^{(0)}$, and is determined by the overlap of the orbitals in the ground and excited state. From Eq. 3.21, one can see how the probability of a transition is determined by the time-dependent coefficients $a_1(t)$. Therefore, by inserting Eq. 3.25 into Eq. 3.23, one can show that, for early times, *i.e.* $t \ll 1/\omega$, apart from on time t, the probability of a transition depends only on the transition dipole moment:

$$p_1(t) \sim \mu_{10}^2 \cdot t^2 \tag{3.26}$$

In summary, one can see that, by observing how the occupancies of the ground-state electronic wavefunctions $\Psi_n^{(0)}$ evolve with time t, under the influence of an applied electromagnetic field, one can model the electronic transitions observed in the absorption spectra of real molecules.

In order to accurately calculate the energy of a transition for real systems in solution, the effect of the solvent has to be taken into account, especially for polar or hydrogen bonding solvents [Charlot 07, Vlček Jr. 07]. The ground-state of the molecule favours a particular arrangement of solvent molecules. However, electronic transition occur too rapidly for a complete reorinetation of the solvent molecules to adjust to the new electronic distribution. Therefore, for polar solvents, the upper electronic state is stabilised to a lesser extent, and the energy separation of the states is thus larger than for non-polar solvents.

One method for accounting for this effect is to use a Self Consistent Reaction Field (SCRF). Here, a distribution of solvent molecules is proposed around the molecule. This arrangement will change the geometry of the molecule. This new geometry of the molecule leads to a new arrangement of solvent molecules which, in turn, will lead to a new geometry for the molecule. This process is repeated until a stable arrangement is found (within pre-defined convergence criteria). One should note that, for different input geometries, different solvated structures will be achieved [Gaussian 03].

Solvation can be modeled in various ways [Tomasi 05]. In this work, a Polarised Continuum Model (PCM) was used, in which the solvent is characterised as a sphere of a given radius, a given density, a given dielectric moment ϵ and a given dielectric constant (at infinite frequency ϵ_{inf}) [Gaussian 03]. These input parameters are defined for many solvent molecules, however, for certain solvents (such as DMF) these have to be input manually. The program builds up the cavity[6] for the molecule by using the United Atom Model, which models a sphere around each solute heavy atom, or atom group: hydrogen atoms are enclosed in the sphere of the atom to which they are bound. The model is then smoothed by rolling a sphere of a defined radius (generally the solvent modeled radius) to approximate the reentrant parts of the cavity surface. By doing this, the so-called solvent excluding surface, where solvent molecules cannot penetrate, can be modeled [Cossi 02, Cancès 97, Tomasi 05]. This method provides an accurate definition of the solute-solvent boundary.

As already mentioned in section 3.4.1, DFT is often used to model large systems computationally, rather than HF theory. For time-dependent calculations, this only became possible once the description of such phenomina was incorporated into DFT by Runge and Gross in 1984 [Runge 84]. This work generalised the underlying theorem of DFT, that all time-independent properties can be calculated from the electron density, rather than the wavefunctions, to time-dependent systems. TD-DFT theory can be viewed as the exact reformulation of the time-dependent quantum mechanical description (described above), where the fundamental variable is no longer the many-body wavefunction, but the electron density. By considering the time-dependence of the potentials and the density in Eq. 3.13, this leads to:

$$E[\rho(t)](t) = T_e(t) + V_{en}(t) + V_{clas,ee}(t) + V_{xc}(t) + V_{ext}(t) \tag{3.27}$$

where, in the case of absorption spectroscopy, $V_{ext}(t)$ is the oscillating electromagnetic field. Despite the complicated mathematical basis of this theory (see *e.g.* [Marques 04, Gross 06]), the improved speed of calculation, compared to TD-HF has led to it becoming the most widely used electronic structure method for calculating vertical electronic excitation energies. Apart from certain exceptions, TD-DFT excitation energies are generally remarkably accurate, typically to within a fraction of an electron volt [Doltsini 06].

No further consideration of the mathematics of TD-DFT is given, as it is not

[6] The 'hole' in the solvent continuum in which the solute lies.

necessary to the understanding of the results obtained in this work and, since the calculations were run using pre-defined Gaussian parameters, the work described can be followed by consultation of the Gaussian manual [Gaussian 03]. If a more rigorous description of the mathematics is desired, the reader is directed to the above references [Marques 04, Gross 06].

3.4.4 Band structure calculation

Modeling of solid state properties can be achieved using DFT. The principle is similar to that of single molecule calculations, however, the studied systems are now a periodic array of molecules, whose individual wavefunctions and energies are no longer discreet and, as such, the basis sets must account for the translational symmetry of the system.

A complete description of the theory behind the modeling of solid state properties by DFT is beyond the scope of this work, as the calculations were performed, and the data analysed, by Dr. Carole Morrison at the University of Edinburgh. For a thorough introduction to solid-state properties, the reader is directed to [Ashcroft 76], whilst for calculation of these properties, the reader is directed to [Crystal 06].

3.4.5 Experimental parameters

Geometry optimisation for isolated molecules was carried out using the Gaussian 03 package [Frisch 04], running on a SUSe 9.x Linux HPC cluster, comprised of 68 AMD Opteron processing cores, provided by the EaStChem Research Computing Facility (Hare cluster). Where available, the X-ray crystallographic coordinates for the starting structures were utilised, and where necessary, the structures were modified using ArgusLab 4.0. The wavefunction was expanded using the Pople 6-31G* basis set for all atoms [Ditchfield 71, Rassolov 01], and coupled to the Becke three parameters hybrid exchange and the Perdew-Wang 1991 correlation functionals (B3PW91) [Perdew 92, Perdew 96]. Optimised structures were subsequently verified as minima on the potential energy surfaces by the absence of negative values in the frequency calculations. The molecular orbital isosurfaces were generated using the cubegen utility in Gaussian 03 and visualised using ArgusLab 4.0.

TD-DFT calculations were carried out in the presence of the Tomassi polarisable continuum model (PCM) in a DCM, or MeCN solvation field [Cancès 97], with the first 50 singlet transitions calculated. Simulated spectra were generated using Gausssum 2.1 freeware program, using a full-width half-maximum value of 3000 cm^{-1}.

Single-point energy calculations of periodic molecular arrays were undertaken using the CRYSTAL06 package [Dovesi 06], running on an SUSe 9.x Linux HPC cluster consisting of 148 AMD Opteron processing cores, provided by EaStChem Research Computing Facility (Burke cluster). X-ray crystal structures provided the input models. Standard 6-31G** basis sets [Francl 82, Hariharan 73, Rassolov 98] were used throughout, while the exchange and correlation were included by use of the B3LYP hybrid functional [Lee 88]. This method has been previously shown to give band dispersions and gap widths in good agreement with experiment for a wide range of materials [Muscat 01, Perger 03]. Calculations were terminated once the energy convergence fell below 10^{-6} au. Electronic band structures were sampled using a $4\times4\times4$ Monkhurst-Pack mesh [Monkhorst 76], and subsequently visualised along with atom-projected densities of states plots.

Chapter 4

Towards polymerisable heteroleptic nickel *bis*-dithiolenes

4.1 Introduction

The incorporation of metal dithiolenes into polymer films offers the possibility of stabilising, within a stable organic framework, the rich redox and optical properties of the dithiolene [Kato 04]. Metal dithiolenes with pendent thienyl groups have therefore made attractive target monomers as they can combine the desirable properties of polythiophene, such as conductivity, flexibility, and good stability [Roncali 92], with those of the dithiolene [Pozo-Gonzalo 02]. The originative work of Pickup *et al.* on polymerisable metal dithiolenes showed a 2-thienyl substituted nickel dithiolene [Ni(b-2ted)$_2$] (b-2ted = *bis*-(2-thienyl)-ethylene1,2-dithiolene) to covalently link by maintaining a potential (E) sufficient to oxidise the pendent thienyl groups [Kean 01]. Polymerisation was achieved under potentiostatic control, with film growth monitored by the maintaining of current (I) with time (t). The film was shown to be conducting by its continued growth, and showed redox functionality similar to that of the monomer. This work was later extended to include other nickel dithiolenes, including heteroleptic and unsymmetrically substituted ditholene systems, and showed that polymer films could also be deposited by potential cycling [Kean 02]. [Pozo-Gonzalo 02] further extended the field to look at dithiolenes with a fused thiophene backbone, for systems of nickel, platinum and gold, and showed each system to polymerise under potential cycling. [Anjos 08] showed polymerisation of a 3-thienyl substituted nickel dithiolene [Ni(b-3ted)$_2$] (**10**) (b-3ted = *bis*-(3-thienyl)-ethylene1,2-dithiolene) to yield an insulating film under similar conditions to those used by Pickup *et al.* The observed poor conductivity in **10** was thought to be due to low structural regularity, caused by excessive cross-linking of the thiophene groups. However, the group showed that conducting films of **10** could be produced by copolymerisation with thiophene, either by maintaining an oxidising potential, or by potential cycling [Anjos 08].

Heteroleptic dithiolene complexes (where L≠L′) are desirable targets within materials chemistry, as the frontier orbitals may become localised on different ligands, and thus a HOMO→LUMO transition would have inter-ligand charge-transfer (ILCT) character - a requirement for second-order NLO chromophores (see section 1) [Vogler 82, Curreli 04]. Such molecules generally have improved solubility in common organic solvents due to their permanent ground state dipole and, as such, higher solution concentrations are achievable, improving the processability of these materials. The bonding motif in heteroleptic nickel *bis*-dithiolene systems can be thought of as being [Ni(II)(dithione)(dithiolate)] in character, where the electron donating dithione pushes electron density towards the electron withdrawing dithiolate, leading to their being termed *push-pull* complexes [Curreli 04]. Asymmetric nickel *bis*-dithiolenes containing the R_2pipdt ligand (pipdt = piperazine-3,2-dithione) have previously been reported [Geary 07, Chen 98]. Their low energy absorption, as well as their packing structure and solid-state properties, can be easily tuned by simple variation of the R group. Such asymmetric complexes allow fine tuning of the structural and electronic properties through one ligand, whilst maintaining the functionality imposed by the other [Chen 98, Bigoli 01]. Such heteroleptic dithiolenes are also desireable candidates for polymerisation due to the potential for fine tuning of the properties of the resultant film.

The synthesis of heteroleptic nickel dithiolenes is complicated by the observed lability of the dithiolene ligand. In some instances, this can be advantageous, providing a synthetic route through ligand scrambling of the homoleptic analogues [Chen 98, Geary 07], but often, this method leads to mixed products, especially for more electronically similar mixed ligand dithiolenes. By mixing equimolar amounts of symmetrical dianionic and dicationic *bis*-dithiolene salts, [Bigoli 01] showed almost quantitative conversion to the mixed ligand nickel dithiolene in a number of cases. This route is highly ligand dependent, and works best when the mixed ligand target is distinctly M[dithione][dithiolate] in character. Such lability is more typical for nickel dithiolenes. Under identical conditions, both palladium and platinum dithiolenes more commonly precipitate as a charge transfer salt of the symmetrical metal dithiolenes, although mixed ligand complexes have recently been prepared [Pilia 09]. This presumably reflects the improved orbital overlap of a larger metal with the diffuse p orbitals of sulfur. For more electronically similar mixed ligand nickel dithiolene complexes, statistical product mixtures are common, with the desired product isolatable, in many cases in poor yield, by successive recrystallisation, or column chromatography [Kato 97]. An alternative route is achieved by stoichiometric reaction of free ligand with a mono-dithiolene, and has been shown by various groups to yield sufficient quantities of the mixed ligand

product. [Chen 98] demonstrated this method by the reaction of a stable α-dithione with $Ni(mnt)_2(NH_3)_2$ (mnt = maleonitriledithiolate) in solution.

Coupling by oxidative electropolymerisation is, by far, the most studied route to polymeric materials based on metal dithiolenes. Though such a technique is suitable for many niche applications, especially where the redox behaviour of the material needs to be controlled [McDonagh 00, Vickers 05], for larger scale applications, such materials need to be synthesised and processed in bulk by chemical means. The inherent complications of chemical polymerisation, such as harsh conditions, and difficult purifications, represent a substantial future challenge in the field, and one that will need to be addressed before such systems find widespread application in materials science. However, whilst chemical polymerisation techniques are being developed, the insight offered by electropolymerisation is perhaps sufficient to assess the potential of such materials, and screen them for future development and, by substituting the conventional working electrode for a flexible or transparent electrode, the potential of these polymeric materials may already be realised in devices, such as optical switches and photovoltaics [Würthener 01].

In this chapter, the synthesis and characterisation of two electrochemically-polymerisable heteroleptic nickel *bis*-dithiolene complexes is reported. These have been designed with a controlled number of polymerisable thiophene units per molecule to enable formation of high-quality redox active films, and to allow straightforward tuning of the optical properties of these molecules and films.

4.2 Results and discussion

4.2.1 Synthesis

Full experimental details for the syntheses of the b-3ted ligand precursor **1** [Roberts-Bleming 03] and R_2pipdt (R = Bz **2a** R = ^{i}Pr **2b**) [Curreli 04, Geary 07, Isaksson 81, Bigoli 02] have previously been reported, and ligand formation was effected in similar yields to the published procedures. Both [Ni(Bz_2pipdt)(b-3ted)] **3a** and [Ni($^i Pr_2$pipdt)(b-3ted)] **3b** were synthesised by analogous routes (see section 4.4): **1** was treated with sodium methoxide in dry methanol under a nitrogen atmosphere, and to this was added a mixture of $NiCl_2 \cdot 6H_2O$ and **2a/b** in methanol (see scheme 4.1). The crude product precipitated immediately as an air stable green solid, which was filtered after being stirred for 1 hour, and washed with cold methanol. The crude product was dissolved in DCM and passed through a silica plug, and the solvent removed to

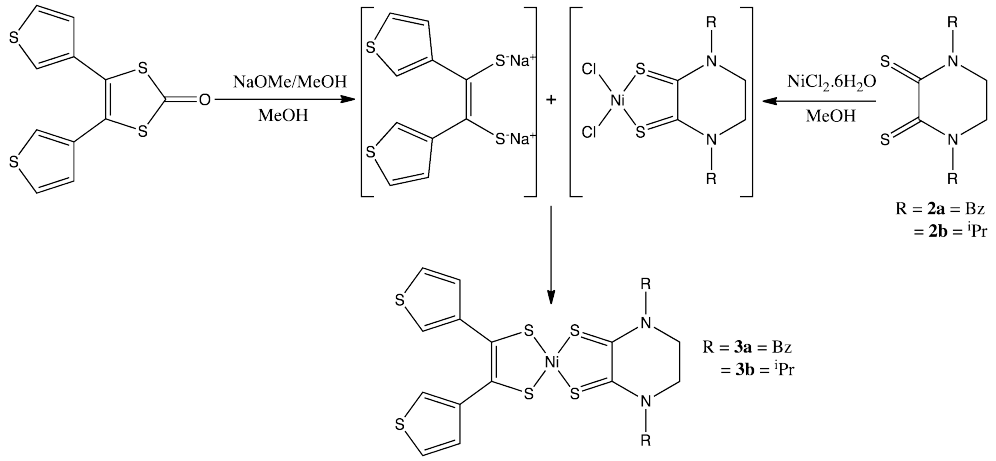

Scheme 4.1: Synthetic route toward [Ni(R_2pipdt)(b-3ted)].

afford pure product as a green precipitate for both complexes. The overall yield of both complexes was low (< 20 %) due to the formation of a large quantity of, what was thought to be, mixed symmetric salts. Crystallisation by slow diffusion of ether into DMF yielded analysable, solvent-free, crystals of each target materials as dark green needles (see section 4.4.1).

Attempts to improve the yield of **3a** by adding a methanolic solution of the sodium salt of **1** to dry, preformed [Ni(Bz_2pipdt)Cl_2] in MeOH were unsuccessful, yielding a similar ∼20 % of isolated product after the same work up as before. This suggested that it was more likely the lability of the ligands (*vida infra*) than the presence of water that reduced the yield of mixed ligand product.

4.2.2 Structure

Both **3a** and **3b** crystallised with the central Ni atom coordinated by four S atoms in an approximately square planar environment, with Ni-S coordination bonds broadly similar on both sides of the complex. Within the central NiS_4C_4 core, the C-C bond on the b-3ted ligand is significantly shorter than that of the R_2pipdt (0.123(5) Å for **3a** and 0.129(4) Å for **3b**), while the C-S bonds are shorter on the R_2pipdt than the b-3ted (0.068(3) Å for **3a** and 0.059(3) Å for **3b**). These results are consistent with previous studies of *push-pull* complexes [Curreli 04, Chen 98], and confirm the C-S π^* and C-C π nature of the frontier MOs on the b-3ted ligands [Curreli 04]. A comparison of the C-S bond lengths with those reported for free ligand analogues of R_2pipdt [Chen 98], and b-3ted [Hursthouse 03], shows good agreement, which confirms the [Ni(dithione)(dithiolate)] nature of both complexes (see Fig. 4.1; see Tab. 4.1).

Bond	Bond Length / Å		
	Observed α phase	Observed β phase	Calculated B3PW91/6-31G*
Ni(1)-S(2)	2.1341(9)	2.1384(7)	2.134811
Ni(1)-S(5)	2.1209(10)	2.1328(6)	2.134602
Ni(1)-S(16)	2.1593(9)	2.1677(7)	2.149570
Ni(1)-S(30)	2.1662(10)	2.1494(7)	2.156362
S(2)-C(3)	1.755(3)	1.750(2)	1.753897
S(5)-C(4)	1.755(3)	1.762(2)	1.754215
S(16)-C(17)	1.687(3)	1.691(2)	1.701575
S(30)-C(29)	1.688(3)	1.686(2)	1.705678
C(3)-C(4)	1.357(5)	1.355(4)	1.367752
C(17)-C(29)	1.480(5)	1.479(4)	1.461147
Angle	Angle Size / °		
	Observed α phase	Observed β phase	Calculated B3PW91/6-31G*
S(2)-C-C-S(5)	4.10	5.91	2.47
S(16)-C-C-S(30)	14.83	8.80	3.27

Bond	Bond Length / Å		
	Observed	Calculated B3PW91/6-31G*	Free Ligand
Ni(1)-S(2)	2.1404(7)	2.135826	
Ni(1)-S(9)	2.1338(7)	2.135628	
Ni(1)-S(16)	2.1700(8)	2.149133	
Ni(1)-S(23)	2.1604(8)	2.150504	
S(2)-C(3)	1.754(3)	1.754347	1.755(2)
S(9)-C(10)	1.751(3)	1.754382	1.727(2)
S(16)-C(17)	1.694(3)	1.705061	1.660(5)
S(24)-C(23)	1.691(3)	1.705139	1.668(5)
C(3)-C(10)	1.350(4)	1.367818	1.350(2)
C(17)-C(24)	1.479(4)	1.463379	1.532(6)
Angle	Angle Size / °		
	Observed	Calculated B3PW91/6-31G*	
S(2)-C-C-S(9)	0.62	2.15	
S(16)-C-C-S(23)	20.17	0.70	

Table 4.1: (above) Selected bond lengths of **3a** (for the solvent free α phase, and solvent incorporated β phase (left)) and solvent free **3b** (right), showing a good general agreement of calculated bond lengths of isolated molecules, and a good correlation of the bond lengths with those of structurally characterised free ligand analogues [Servaas 89, Hursthouse 03], confirming the [Ni(dithiolate)(dithione)] nature of the complex. (below) Selected torsion angles of **3a** (both α and β phase) (left) and **3b** (right) showing an overall square planar coordination geometry. The large difference of the solvent free structures, compared to calculated structures represents a strain away from planarity induced by the bulk of the ligand environment.

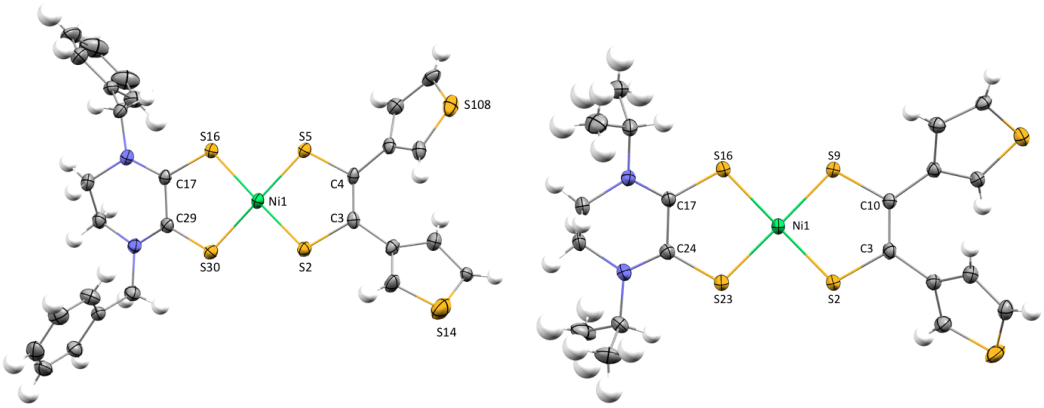

(a) **3a** (b) **3b**

Figure 4.1: Single crystal X-ray structures, with relevant atom numbering scheme, and thermal ellipsoids at 50 % probability for (a) **3a** and (b) **3b**. Both complexes show an, overall, square planar dithionlene core, with thiophene groups twisted out of the molecular plane. Positional disorder was observed for S108 (not shown), and was modeled at 95 %;

Examination of the packing structure of both complexes shows the R group to have a large effect on how the molecules arrange in the lattice. **3a** forms a herringbone arrangement (Fig. 4.2(a)) with an interplanar distance of 4.659 Å (see Fig. 4.2(c)), whereas **3b** forms head-to-tail puckered sheets (see Fig. 4.2(b)) with an interplanar distance of 3.949 Å (see Fig. 4.2(d)). Both complexes display a relatively large interplanar distance due to the out-of-plane twist of the thiophene groups; in addition, the bulk of the Bz group prohibits close packing of the NiS_4C_4 cores in **3a**. Some disorder was observed for **3a** due to a rotation of the C(4)-thiophene bond. This gave a 95 % probability of a thiophene orientation as shown in Fig. 4.1(a). This disorder is likely due to the increased bulk of the benzyl groups, resulting in a larger inter-planar distance (see Figs. 4.2(c) and 4.2(d)), and poorer orbital overlap of the thiophene groups between molecules. It should be noted that for a second batch of crystals, using a larger reservoir of Et_2O, faster crystallisation of **3a** resulted in the formation of crystals with a different space group (β phase), that showed incorporation of one equivalent of DMF (see Tab. 4.1 (left)). In this case, no disorder was observed and, though all core bond lengths were broadly similar, a more planar structure was observed.

4.2.3 Spectroscopic studies

Electronic absorption spectroscopy was performed on **3a** and **3b**, as nickel dithiolenes characteristically show a strong absorption in the NIR region of the spectrum that

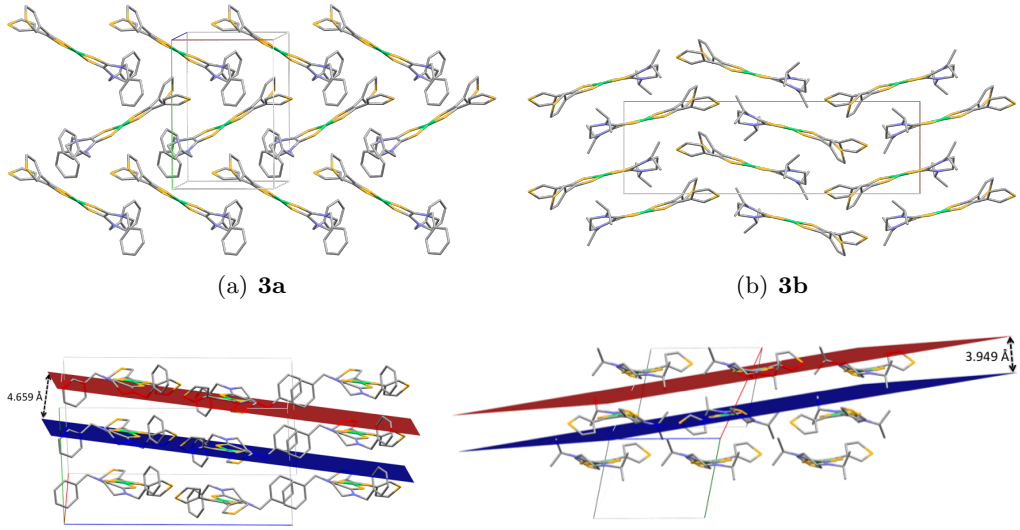

(a) **3a** (b) **3b**

(c) **3a** (d) **3b**

Figure 4.2: Single crystal X-ray data showing: (a) packing structure of **3a** in a herringbone packing arrangement; (b) packing structure of **3b** in a head-to-tail puckered sheet arrangement; (c) a minimum interplanar distance in **3a** of 4.659 Å, due the increased steric bulk of the benzyl groups; (d) a minimum interplanar distance in **3b** of 3.949 Å, due to the reduced steric bulk of the isopropyl groups.

corresponds to HOMO→LUMO transition, and thus resolution of this absorption can yield detailed information on the relative energies of the frontier orbitals.

UV/Vis/NIR spectroscopy of **3a** and **3b** in DMF showed an intense peak in the UV region [322 nm (31,056 cm^{-1}) for both **3a** and **3b**], and a single peak in the NIR region [940 nm (10,638 cm^{-1}) and 928 nm (10,776 cm^{-1}) for **3a** and **3b**, respectively] (see Figs. 4.3(a) and 4.3(b)). It is this low energy absorption that provides the most information about the electronic structure of these complexes as it is attributed to a HOMO→LUMO transition that, for a heteroleptic nickel dithiolene, is predominantly inter-ligand charge transfer (ILCT) in character (see chapter 1) [Vogler 82]. This is caused by the dissimilar contribution of the two ligands to the frontier orbitals. The value of λ_{max} is greater for **3a** than **3b**, indicating a smaller HOMO/LUMO gap, which is in agreement with conclusions drawn from electrochemical studies (see section 4.2.5). Spectra were obtained in a range of solvents, and both complexes were shown to have negative solvatochromic behaviour, where the increase of solvent polarity shifts the absorption to higher energy (hypsochromic shift) (see Fig. 4.3(c)). This suggests that more polar solvents stabilise the ground state of both **3a** and **3b** to a greater extent than the excited state, and thus both complexes have a more pronounced dipole moment in the ground state [Curreli 04]. This, combined with the non-centrosymmetric crystal

structures for **3a** and **3b** make them potentially interesting systems for the investigation as second order NLO chromophores (see chapter 1) [Pilia 09].

To further characterise the nature of the frontier orbitals, the change in the absorption spectrum of **3a**, upon reduction and oxidation, was studied in 0.1 M $TBABF_4$/DMF at -40°C by OTTLE. The measurements were performed at low temperature to slow the rate of decomposition, and improve the reversibility of the redox processes, as OTTLE measurements are taken over a longer timescale than cyclic voltammetry (see section 4.2.5). Complete reduction to the monoanion was achieved by holding the potential (E) at -0.8 V, until no further change in the absorption profile was observed (see Fig. 4.3(d)). The NIR band of the neutral complex collapsed as a new band at lower energy grew in at 1028 nm (9,728 cm^{-1}). A reduction in the intensity of the UV band at 322 nm (31,056 cm^{-1}) was also observed, and a shoulder to the existing peak grew in at 365 nm (27,397 cm^{-1}). Neutral **3a** could be rapidly and reversibly regenerated by holding the potential at +0.1 V. Oxidation of **3a** at +0.8 V again resulted in the collapse of the NIR band, and the formation of a lower energy transition at 1294 nm (7,728 cm^{-1}). This species proved unstable over the course of the experiment, as the peak gradually collapsed to the baseline, followed by a steady decrease in the intensity of all other bands.

The spectro-electrochemical (OTTLE) experiment suggested that the monoanionic complex was stable in solution over long time scales, but that the cationic species was affected by processes of an unknown nature (such as precipitation or decomposition), which reduced its stability over long periods in solution. The OTTLE experiments showed that the switching of redox states of these complexes generates distinct electronic absorptions in the NIR region. This behaviour suggests these materials to be of interest as polyelectrochromic NIR dyes for electrochromic devices [Charlot 07].

4.2.4 Computational studies

Computational modeling can be used to support experimental data of many molecular properties, such as geometry, and electronic absorption behaviour, or bulk-properties, such as conductivity, and is a useful tool for the visualisation of the electronic origins of these properties (see section 3.4).

Ab initio single molecule calculations were carried out in the gas phase, using the same level of theory as detailed in section 3.4. Studies on **3a** and **3b** suggested that, although the frontier orbitals are spread over the whole molecule, the HOMO is largely

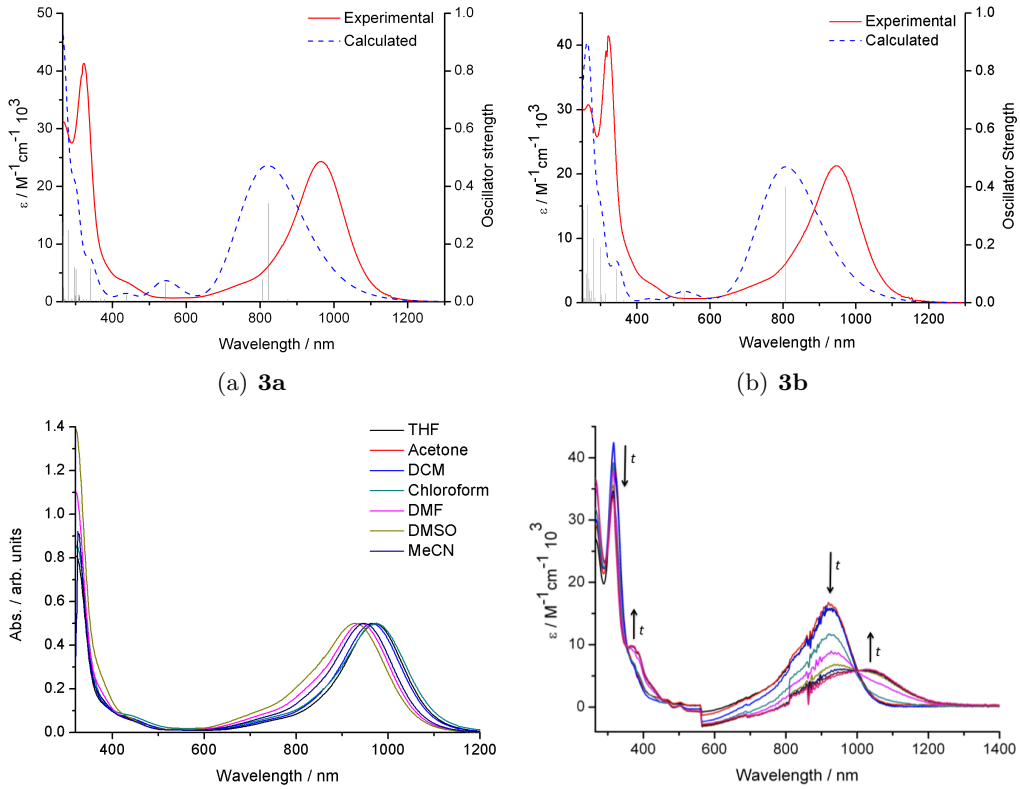

(a) **3a** (b) **3b**

(c) **3a** (d) **3a**

Figure 4.3: UV/Vis/NIR absorption spectra, where the absorption intensity is given as the molar extinction coefficient (ϵ): (a) experimental and calculated spectra of **3a** in DCM; (b) experimental and calculated spectra of **3b** in DCM. Both spectra show an overestimation of the energy of all the calculated transitions, but good qualitative agreement for the transitions; (c) solvatochromic studies of **3a**, showing negative solvatochromism for the NIR absorption, suggesting a large ground state dipole moment (the intensity of the spectra are normalised with respect to the NIR absorption); (d) optically transparent thin-layer electrochemistry (OTTLE) of **3a** under reductive conditions (-0.8 V), showing the formation of a stable monoanion, with a NIR absorption at lower energy than **3a**. (Jump at 560 and 805 nm, as well as spike at 880 nm are artefacts of the spectrometer).

b-3ted in character, whilst the LUMO is almost entirely located on the R_2pipdt (see Fig. 4.4; see Tab. 4.2 (below)). Geometry optimisation of both complexes showed excellent agreement of the bond lengths with the observed X-ray data, however, the degree of planarity in the central NiS_4C_4 core was overestimated (see Tab. 4.1 (below)). These large deviations away from X-ray data may be due to constraints imposed by the crystal lattice, as the calculations were run on isolated molecules.

Following optimisation, information regarding the nature of the electronic transitions for **3a** and **3b** were sought using time-dependent density functional theory (TD-DFT) (see section 3.4.3). This was done to model the electronic absorption spectra (see section 4.2.3), and probe the origins of the individual absorptions. Calculations were carried out using a polarisable continuum model of DCM ($\epsilon = 8.93$), as previous computational studies of other charge-transfer systems in the gas phase have been shown to drastically underestimate the energy of the electronic transitions [Charlot 07].

The calculated contributions to the low energy band in **3a** were shown to be 54 % HOMO→LUMO, and thus predominantly ILCT in character, with a further 16 % contribution from the HOMO-3→LUMO transition. The HOMO-3 orbital was calculated to be a pure Ni $3d_z{}^2$ orbital, thus giving the transition some metal character. Therefore, the transition can be better described as a mixed metal-ligand to ligand transition (MML′LCT). For **3b**, the low energy absorption was calculated to be 65 % HOMO→LUMO in character, with only a very minor (2 %) contribution from the HOMO-2→LUMO transition. The HOMO-2 orbital was calculated to be predominantly thienyl based, thus reducing the metal contribution to the transition, compared to **3a**. This may account for the reduced intensity of the NIR absorption observed for **3b**, compared to **3a** (ϵ = 11,400 and 15,800, respectively) (see Figs. 4.3(a) and 4.3(b); see Tab. 4.2 (above)).

The calculations overestimated[1] the energy of all the observed transitions for both **3a** and **3b** by ∼1550 cm^{-1}, for each transition, but showed good qualitative agreement between the calculated and observed spectra for both complexes (see Figs. 4.3(a) and 4.3(b)). A transition from the HOMO-2→LUMO was calculated but not observed for both complexes [543 nm (18,416 cm^{-1}) for **3a** and 528 nm (18,927 cm^{-1}) for **3b**]. If the energy of this transition was also underestimated by the calculation, it may account for the weak shoulder peak of the low energy transition in the observed spectra of both complexes (see Figs. 4.3(a) and 4.3(b)). This overestimation of the calculated energies

[1]The relative change in the energies of the transitions are quoted in wavenumbers ($\overline{\nu}$) as it is a linear scale with respect to energy (E).

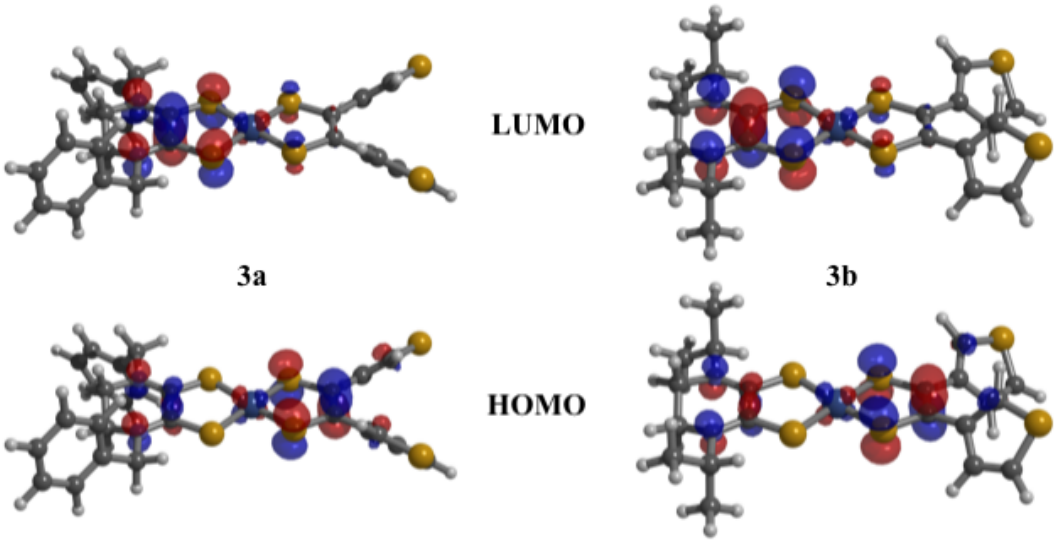

Figure 4.4: Frontier molecular orbitals of **3a** (left) and **3b** (right), suggesting the HOMO to be localised predominantly on the b-3ted ligand, and the LUMO on the R_2pipdt liand, giving the complexes 'push-pull' character.

of the transition processes is not uncommon for charge transfer species [Vlček Jr. 07]. In general, DFT modeling of charge transfer species treats the excited electron as originating in the spatial region of the acceptor site, instead of the distant donor. This results in a poor approximation of the energies of the orbitals involved. Added to this, the polarisable continuum model used in this study is limited insofar as it only mimics non-specific solvation, and does not account for other, more complex, effects that occur in real systems, such as specific solvent coordination, or the observed solvatochromism of these complexes. Despite this, the reasonable qualitative agreement of the spectra suggests that the origins of the transitions had been correctly modeled.

So far, only the properties of single molecules of **3a** and **3b** have been modeled. In order to explore the bulk properties of these complexes in the solid-state, calculations were performed on the bulk materials, using the single crystal unit cell data obtained by XRD. Calculations were performed by Dr. Carole Morrison using the CRYSTAL06 code [Dovesi 06] to investigate the degree of molecular overlap, and develop a band structure for both materials. Visualisation of densities-of-states plots showed that the calculated distribution of the frontier orbitals in the crystal structures was in agreement with the calculations performed on isolated molecules (see Fig. 4.5(a)). The band dispersion plots, shown along pathways cutting through symmetry significant k-points in reciprocal space (see Appendix A.1), are given in Fig. 4.5(b). The maxima and minima of the valence and conduction bands, respectively, lie upon the same k-vector,

Complex	Wavelength / nm	Osc. Strength	Major contributions
3a	822.1	0.3406	HOMO→LUMO (54 %)
3b	807.5	0.4017	HOMO→LUMO (65 %)

Complex	Orbital	Orbital location %		
		Ni	b-3ted (SCCS)	R_2pipdt (SCCS)
3a	HOMO	9.93	62.25 (48.03)	27.82 (9.96)
	LUMO	8.54	13.11 (11.87)	78.35 (49.19)
3b	HOMO	11.73	63.13 (49.03)	25.14 (8.40)
	LUMO	7.76	17.20 (10.29)	75.04 (49.12)

Table 4.2: TD-DFT data: (above) calculated energies and intensities of the NIR transition observed in **3a** and **3b** (see Figs. 4.3(a) and 4.3(b)); (below) calculated contributions to the frontier molecular orbitals of **3a** and **3b**. The data confirm the low energy absorption to be due to transitions between orbitals localised on different ligands, suggesting the HOMO→LUMO transition to be predominantly ILCT in nature.

in each case, for both **3a** and **3b**, and thus both complexes are suggested to have a direct band gap. For **3a**, the HOMO and LUMO bands appear at around -4.5 eV and -2.6 eV, respectively, with a minimum band gap of ∼1.54 eV (805 nm). For **3b**, the HOMO and LUMO bands are around -4.2 eV and -2.5 eV, respectively, and with a calculated band gap slightly larger at ∼1.59 eV (779 nm). A greater degree of band dispersion (shown by a broadening of the bands) is calculated for **3b**, which in turn can be attributed to the closer packing of the NiS_4C_4 cores in the crystal lattice, and thus greater intermolecular interaction of the molecular orbitals in the solid-state (see Appendix A.1).

In summary, computer calculations were used to model some of the molecular, and bulk properties of both **3a** and **3b**. The calculations showed good agreement of the molecular structure, as observed by XRD, however, significant differences in the degree of planarity of the dithiolene core were observed, possibly due to the negation of lattice constraints in the single molecule calculations. The modeling of the electronic absorption spectra showed poor agreement in the energies of the transition, though the shape, and intensity, of the transitions were well described, allowing the origin of the NIR absorption to be proposed as being a HOMO→LUMO transition that was predominantly ILCT in nature. Modeling of the complexes in the solid-state allowed the band structures of the complexes to be derived. Greater band dispersion was suggested for **3b**, suggesting greater intermolecular interaction of the frontier orbitals, which is in agreement with the closer packing of the dithiolene cores in **3b**, as observed by XRD.

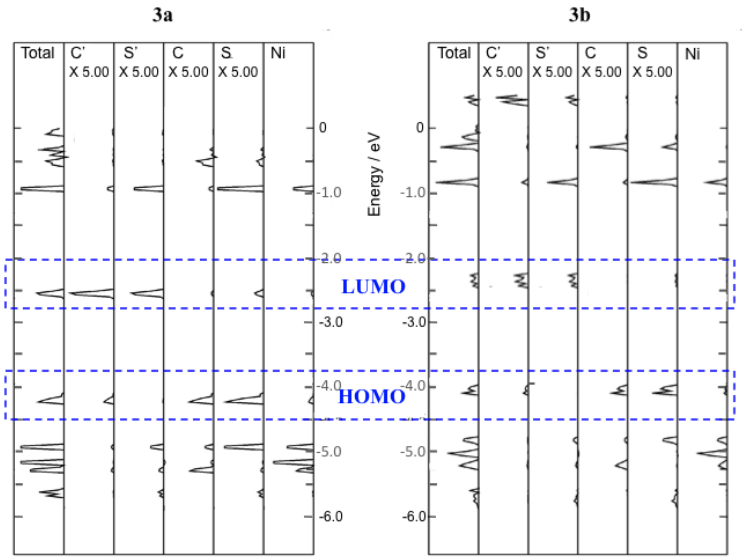

(a)

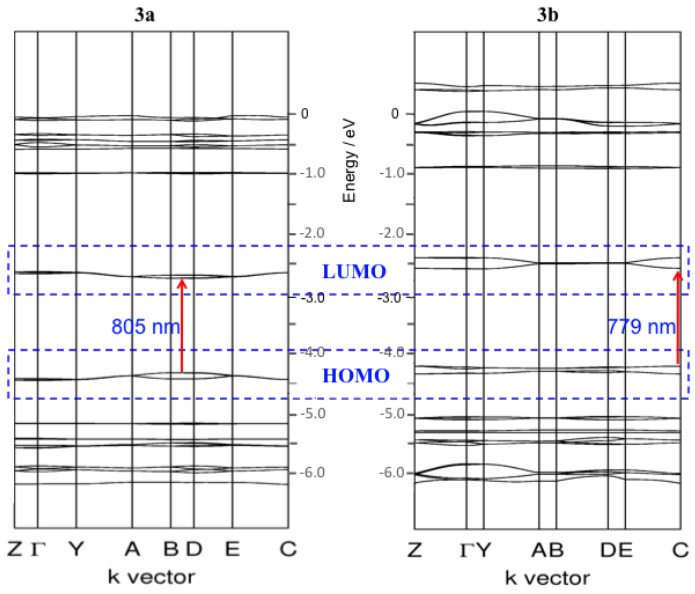

(b)

Figure 4.5: Visualisation of solid-state calculations using CRYSTAL06: (a) densities-of-states plots of **3a** and **3b**, showing the energies and contributions (as intensities) for the NiS_4C_4 to orbitals, with the frontier orbitals highlighted, where C and S relate to the b-3ted and C′ and S′ relate to the R_2pipdt; (b) band structure of **3a** and **3b**, with the bands derived from the frontier orbitals highlighted. The band structure is derived by repeated sampling of the energy levels as a path is mapped between symmetry significant k-points in the Brilloin zone (see appendix A.1). Greater band dispersion is observed in **3b**, consistent with the closer packing of the dithiolene cores in the crystal lattice.

Name	$E^1_{1/2}$ / V	$E^2_{1/2}$ / V	$E^3_{1/2}$ / V	$E^4_{1/2}$ / V	$E^5_{1/2}$/ V
2a		-1.24	+1.13*		
2b		-1.40[§]	+1.01*		
3a	-1.09	-0.59	+0.46	+1.11*	+1.38*
3b	-1.26	-0.68	+0.42	+1.05*	+1.38*
Poly-**3a**	-0.68*	+0.02	+0.40	+0.98*	+1.18*

Table 4.3: Redox potentials of the free ligands **2a** and **2b** [Geary 07], complexes **3a** and **3b**, and a poly-**3a** coated platinum electrode. All processes are reversible, unless otherwise stated; *irreversible, [§]quasi reversible.

4.2.5 Electrochemical studies

The electrochemistry of **3a** and **3b** was investigated as metal dithiolenes characteristically show multiple stable redox processes, corresponding to reduction (and in some cases oxidation) of the dithiolene core. Resolution of these processes can yield information, not only on the energy of the frontier orbitals, but on their distribution over the molecule.

3a and **3b** were each studied by cyclic voltammetry in a solution of 0.1 M $TBABF_4$ in DMF (see Fig. 4.6(a)). Both complexes show three electrochemically reversible one-electron redox processes [confirmed by the peak shapes and the linear plots of current (I) *vs.* the square root of scan rate (v) (see section 3.2.1.1, Eq. 3.1)] (see Fig. 4.6(a)). The two processes at negative potentials were assigned to the sequential reduction of the complexes, $[MLL']^{0/1-}$, $[MLL']^{1-/2-}$, as zero current (I) was observed at applied potential $E = 0$, suggesting this to be the neutral form for both complexes. The reversible process at positive potentials for both complexes was assigned to their oxidation, $[MLL']^{0/1+}$, indicating the formation of a stable cation under cyclic voltammetric analysis (scan rates (v) sampled at five intervals between 10 and 100 mVs^{-1}), though was shown not to be stable throughout the course of an OTTLE experiment (*vida supra*). Two irreversible peaks were seen above +1 V (not shown in Fig. 4.6(a)), and were assigned to sequential oxidation of the thiophene groups, by comparison with previous studies [Kean 01, Kean 02, Anjos 08] (*vide infra*) (see Tab. 4.3).

Each redox process occurred at a more positive potential for **3a** than **3b**, thus the nature of the R group is shown to affect the redox behaviour of the dithiolene core. Greater variation in the redox processes at negative potentials (for **3a** and **3b**, a difference of 0.17 V for $E^1_{1/2}$ and 0.09 V for $E^2_{1/2}$) than at a positive potential (for **3a** and **3b**, a difference of 0.04 V for $E^3_{1/2}$) lends experimental weight to the computational data

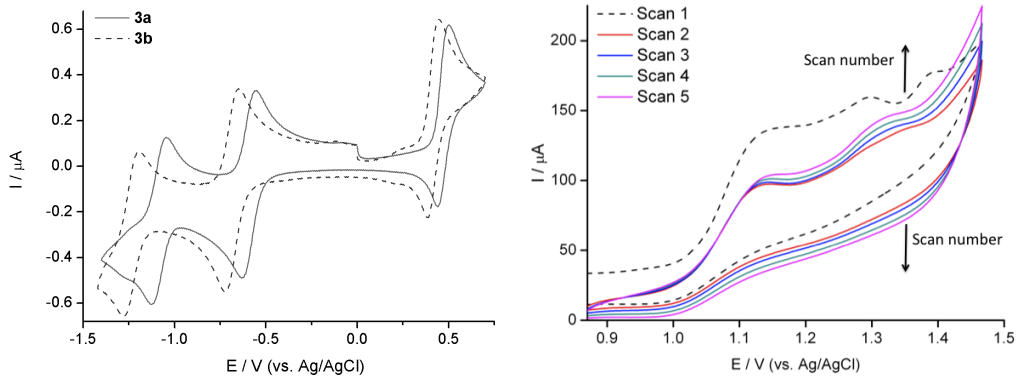

(a) **3a** and **3b** (b) **3a**

Figure 4.6: Cyclic voltammetry in 0.3 M $TBABF_4$/DCM, measuring current (I), in response to an applied potential (E): (a) a single scan (v = 100 mVs^{-1}) of **3a** and **3b**, showing three reversible redox processes, with redox levels tuneable through the nature of the R-group. Starting E was 0.0 V and the initial direction of the sweep was to positive E; (b) potential (E) cycling (v = 100 mVs^{-1}) of a concentrated monomer solution of **3a** between +0.87 V and +1.47 V. Currents at all potentials increase with potential cycling (scan number) after the first scan, indicating the deposition of a conducting film.

which suggested the LUMO to be predominantly located on the R_2pipdt ligand (*vida supra*); since the reduction processes correspond to filling of the LUMO orbital, greater variation in the reduction potentials with the changing R group suggests the LUMO to reside predominantly on the R_2pipdt ligand. This assignment agrees with previous work on electronically analogous systems containing the R_2pipdt ligand [Curreli 04,Geary 07], which concluded that the more electron rich $^i Pr_2$pipdt raises the energy of the LUMO more than that of the HOMO [Curreli 04]. If this is the case, one could expect that the NIR absorption to be at a higher energy for the more electron rich $^i Pr_2$pipdt substituted complex (**3b**). This is indeed the case, as observed by the higher energy NIR absorption in **3b**, compared to **3a** (see section 4.2.3).

In order to demonstrate the potential for this new class of complex to be incorporated into conducting films, polymerisation of **3a** was investigated by scanning to potentials sufficient to oxidise the thienyl groups [Kean 01]. This complex was chosen due to its superior solubility in common organic solvents, and its greater optical absorbance in the NIR range, thus making it easier to process and characterise. Higher concentrations were used to improve the efficiency of coupling at the working electrode by reducing the time between radical formation, and subsequent coupling. Initial polymerisation experiments, performed in DMF, were shown not to form films on the working electrode upon cycling. This was attributed to the observed solubility of the nascent films in

DMF. On switching to DCM, at a monomer concentration of ∼10 mM, potential cycling between +0.87 and +1.47 V resulted in the deposition of a conducting film (see Fig. 4.6(b)). Cycling to +1.47 V was sufficient to induce the oxidation of both thiophenes, and on cycling, a steady increase in peak current ($|I_p|$) was observed (after an initial drop in current after the first scan) which continued for many cycles. Such a current response is indicative of the deposition of a conducting film, as current can only be passed at the working electrode if the surface remains conducting, and the increase in peak current ($|I_p|$) indicates the increasing quantities of redox active material deposited on the electrode. By comparison with previous studies by [Anjos 08], who monitored the effect of the polymerisation process on the C-H stretches of the thiophene ring for Ni(b-3ted)$_2$ (**10**) by interfacial IR spectroscopy, it is assumed that the electrochemical process observed in this range corresponds to the covalent linking of the thiophene groups at the α-position, resulting in polymeric growth on the electrode surface.

To investigate the redox properties of the generated polymer films, and to compare them to the monomer, the working electrode, with the grown film, could be transfered to a monomer free electrolyte solution. Cycling of this film between +1.00 and -1.00 V, in this solution, initially showed none of the redox processes observed for the monomer. However, on cycling to greater potentials (E) (+1.50 and -1.30 V), three redox processes emerged at -0.68 V ($E^1_{1/2}$), +0.02 V ($E^2_{1/2}$) and +0.40 V ($E^3_{1/2}$), and remained over many cycles (see Tab. 4.3; see Fig. 4.7(a)). On comparison with the cyclic voltammetry of the monomer, the redox process at positive potential ($E^3_{1/2}$) appears largely unchanged, whilst the redox processes at negative potentials are shifted to more positive potentials (∼400 mV for $E^1_{1/2}$ and ∼600 mV for $E^2_{1/2}$). The more facile reduction, observed, may be due to stabilisation of the LUMO upon polymerisation. Alternatively, these differing shifts may reflect the need to incorporate a different counterion upon reduction, compared with oxidation.

In order to develop the redox processes in the film, the film needed to be cycled to higher potentials (E). This 'conditioning' process seemed to be required to activate the film. One reason for this may be that higher potentials (E) force ion transfer through the film, restructuring it, to allow improved ion transport at less forcing potentials (E) [Mount 99]. The initial potential cycling, and film formation experiment, should lead to the deposition of neutral or cationic film products, with associated BF_4^- counterions. However, film cycling to generate reduced species requires bulky TBA^+ ion transport through the film to preserve electron-neutrality. Cycling the film to more negative potentials (E) may enable film restructuring to allow such ion transport.

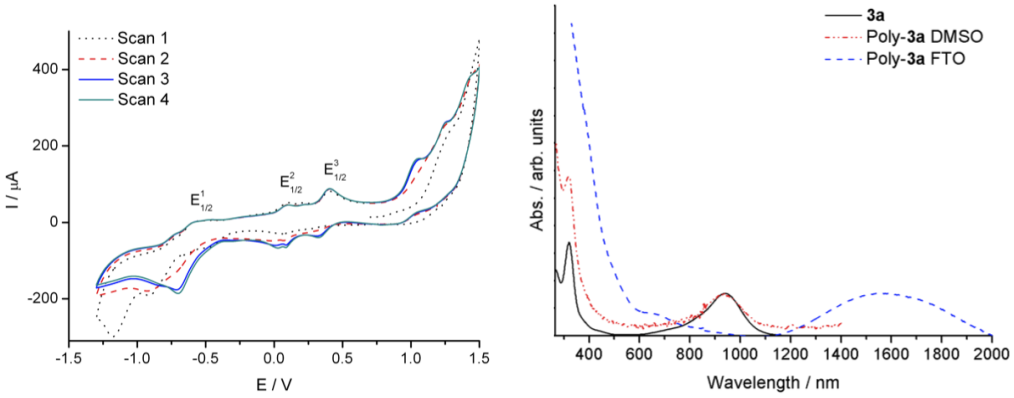

(a) (b)

Figure 4.7: Redox and optical properties of poly-**3**: (a) cyclic voltammetry, showing the current (I) response to applied voltage (E) ($v = 100$ mVs^{-1}) of a poly-**3a** coated platinum electrode in 0.3 M $TBABF_4$/DCM, showing dithiolene-like redox behaviour preserved upon polymerisation; (b) UV/Vis/NIR spectra, normalised with respect to the NIR absorption intensity, of **3a** in DMSO, poly-**3a** on FTO, and dissolved poly-**3a** in DMSO, confirming dithiolene incorporation into a polymer film, and significant red-shifting of the low-energy absorption.

Investigation of the UV/Vis/NIR absorption properties of the grown films allows the energies of the electronic transitions to be determined and, by comparing with the absorption properties of the monomer, the effect of polymerisation on the frontier orbitals to be determined (see Fig. 4.7(b)). To investigate these processes, films were grown on fluorine-doped tin oxide (FTO) coated glass electrodes. Initial analysis of the grown films (gold in colour) was complicated by a broad absorption over the entire spectral range (not shown in Fig. 4.7(b)); however, by washing the electrodes in DMSO, and thereby removing the more soluble portions of the film, the nature of the film could be ascertained. For the soluble portion (that dissolved in DMSO), the absorption around 250 - 500 nm is indicative of thiophene linkage, as an increase in the breadth and intensity of the UV absorption is consistent with increased conjugation in the polymer chain [Kean 01], however, the relatively small red-shift of the UV absorption [(poly)-thiophene based] suggested that the chain lengths of the dissolved portion were short. Unequivocal evidence for incorporation of the intact dithiolene complex moieties was demonstrated by the characteristic near-IR absorption around 950 nm. In comparison, the insoluble portion of the film, that remained after washing with DMSO, showed stronger absorption across the 400-800 nm region, consistent with its lower solubility being due to longer polymer chains. Having been washed, a very distinct near-IR absorption was observed, centred around 1550 nm, considerably red-shifted (by 4360 cm^{-1}) from the absorption of **3a**. This red-shift may be due to strong interaction

between dithiolene complexes and the polythiophene backbone, or due to absorption by ionic dithiolene units (*vide supra*) stabilised in the solid-state system. In either case, such a pronounced red-shift is indicative of an interplay between the conductive polythiophene backbone and the optically active dithiolene unit.

In an effort to further explore the structural and electronic properties of the polymer films of **3a**, hybrid films of poly-**3a** and thiophene were produced. Initially, by adding 10 mM of thiophene to the monomer solution, the potential (E) was cycled between +0.87 and +1.47 V, as for pure **3a**. The formed films showed no change in the redox and optical properties of the polymer film, compared to that of the homopolymer of **3a**. Thiophene is known to require high potentials (E) to achieve its oxidation [Roncali 92], thus the scanning region used for **3a** was perhaps insufficient to effect thiophene incorporation into the film. By increasing the scanning region to more positive potentials (E) (between -0.23 and +2.37 V), extensive deposition of a conducting film could be achieved, that was visibly distinct from the homopolymer of **3a** (by its brown colour). The film was shown to highly conducting by the large increases in $|I_p|$ for sequential scans (see Fig. 4.8(a)).

On moving the working electrode with the grown film, to monomer-free electrolyte solution, the redox properties of the film could be investigated. The film showed a broad redox process across the region of interest for the dithiolene monomer **3a** (not shown), which resembled the redox behaviour of polythiophene [Roncali 92]. No distinct redox processes, reminiscent of **3a**, could be observed in this region, as any processes were possibly obscured by the dominant polythiophene processes.

In a similar manner to the homopolymer of poly-**3a**, films could be grown on FTO coated glass electrodes to investigate the electronic absorption properties of the film. The deposited copolymer films showed a broad absorption over the entire NIR range (see Fig 4.8(b)). The grown films were insoluble in all common solvents, and thus no improvements in the resolution could be achieved by washing the film, as was seen for poly-**3a**. In order to confirm that the broad NIR absorption was due, at least in part, to the dithiolene component, and thus confirm that **3a** had been incorporated into the film, the spectra was compared to a film of pure polythiophene, grown under identical conditions to the copolymer. In comparison with the spectrum of a polythiophene film, distinct differences in the spectra could be observed in the NIR range. The hybrid film showed intense NIR absorptions centred around 950 nm (shoulder) and 1400 nm (peak) (see Fig. 4.8(b)), that were absent from the polythiophene film. These can reasonably be attributed to incorporated dithiolene units, with both these low-energy absorptions

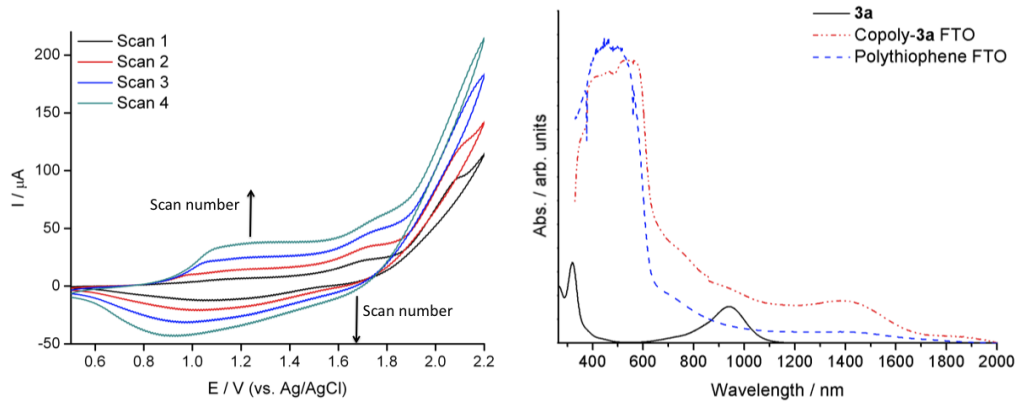

(a) (b)

Figure 4.8: Redox and optical properties of a poly-**3**/thiophene copolymer: (a) the current (I) response to potential (E) cycling (v = 100 mVs^{-1}), between -0.23 V and +2.37 V, of a concentrated monomer solution of **3a** and 10 mM of thiophene. Peak currents ($|I_p|$) increase with potential cycling, indicating the deposition of a conducting film; (b) normalised UV/Vis/NIR spectra, with respect to the NIR absorption, of **3a** in DMSO, a **3a**/thiophene copolymer on FTO, and polythiophene on FTO. Spectra suggest incorporation of dithiolene units into the film.

comparable to those observed in the soluble and insoluble portions, respectively, of the homopolymer of **3a** (see Fig. 4.7(b)). The intermediate red-shift of the lowest energy NIR absorption, to 1400 nm, rather than 1550 nm as for the homopolymer, suggested that incorporation of thiophene into the film reduces the extent of red-shifting of the NIR band in the polymer. Because of this, it might be possible, by careful stoichiometric control of the copolymer components, to accurately tune the NIR absorption profile, of a hybrid polymeric film of (co)poly-**3a** over a wide range of wavelengths.

In an effort to tune the NIR absorption of (co)poly-**3a** by varying the ratio of **3a** to thiophene in the electrochemical cell, copolymerisation was performed on 10 mM **3a** with 0, 5, 10 and 20 mM thiophene added to the electrochemical cell. As outlined above, in order to oxidise the thiophene to couple in the polymer film, the potential (E) was scanned between -0.23 and +2.37 V. For 0 mM thiophene, cycling between these potentials did not result in the deposition of a film, as shown by the passing of zero current after the first cycle (not shown), and the absence of a NIR absorption by UV/Vis/NIR spectroscopy of an FTO coated glass electrode used as a working electrode. It therefore seemed that the higher potentials required to oxidise the thiophene resulted in the formation of an insulating film on the working electrode, and the decompostion of the dithiolene unit within that film. On adding thiophene to the electrochemical cell, the films formed for different thiophene concentrations

were shown to be similar to that of Fig. 4.7(b) under all thiophene concentrations. Though the reasons for this are not completely understood, this may represent another example of what has been termed the 'polythiophene paradox' [Roncali 92] - where the oxidation potential required to achieve polymerisaion of thiophene is close to that required to destroy the nascent film. Thus, perhaps what is observed, on scanning to higher potentials (E), is the incorporation of stabilised dithiolene monomer species in a polythiophene film. By using appropriately substituted thiophene monomers, perhaps the oxidation potential could be reduced sufficiently to incorporate into films at a similar potential to the polymerisation of **3a**.

4.3 Conclusions

Two novel heteroleptic *bis*-1,2-dithiolene complexes were prepared, containing a readily-tuneable auxiliary ligand (R_2pipdt) and a ligand with polymerisable thienyl groups, attached at the 3-position (b-3ted). Both complexes were structurally and electronically characterised and showed that, by simple variation of the R group, the solid-state and electronic properties of such complexes could be controlled. Experimental data were supported by computational calculations on isolated and solid-state models, and the results suggested that the properties of analogous complexes may be qualitatively predicted by such techniques.

Cyclic voltammetry of both complexes displayed three electrochemically reversible redox processes, including the formation of a *quasi*-stable cation, suggesting such complexes may have potential as ambipolar semiconductors for field-effect transistors. A negative solvatochromic response was shown in both complexes, and therefore further investigation might look their potential as second-order NLO chromophores.

Electrochemical polymerisation of **3a** was shown to form a redox-active film, with distinctive dithiolene redox and optical properties, though heavily modified upon polymerisation, yielding a very low energy absorption in the NIR. This absorption could be modified by copolymerisation with thiophene, and thus such polymer systems may be of interest as low-energy photoreceptors.

4.4 Experimental

[Ni(Bz_2pipdt)(b-3ted)] (3a) To a stirred solution of sodium (13.4 mg, 0.583 mmol) in dry MeOH (10 ml) under a nitrogen atmosphere was added **1** (82.3 mg, 0.292 mmol) and the reaction mixture stirred for 1 hour. **2a** (85.8 mg, 0.292 mmol) and $NiCl_2{\cdot}6H_2O$

(69.4 mg, 0.292 mmol) were dissolved in MeOH (5 ml) and added to the reaction mixture. After 1 hour the crude product was filtered in air and washed with cold MeOH. The crude product was dissolved in DCM and passed through a silica plug. The solvent was removed yielding a green precipitate, which was recrystallised from DMF/Et_2O yielding the title compound as dark green needles (30.7 mg, 16 %). δ_H (250 MHz; $CDCl_3$) 3.76 (s, 4H, H_e), 5.1 (s, 4H, H_d), 6.68 (dd, 2H, J = 5.0, 1.3 Hz, H_c), 7.16 (dd, 2H, J = 3.0, 1.3 Hz, H_b), 7.31 (dd, 2H, J = 5.0, 3.0 Hz, H_a), 7.34-7.52 (m, 10H, -Ph); MS (ESI) (m/z): 639 $[M+1]^+$. Anal calcd for $C_{28}H_{24}N_2S_6Ni$: C, 52.6; H, 3.8; N, 4.4. Found C, 52.2; H, 3.9; N, 4.1. λ_{max} = 940 nm ($\epsilon = 15.8\times10^3$ $M^{-1}cm^{-1}$).

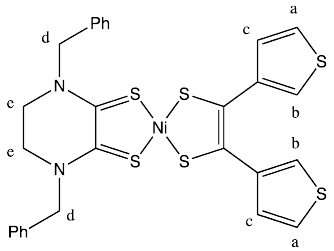

[Ni(^{i}Pr$_2$pipdt)(b-3ted)] (3b) To a stirred solution of sodium (14.0 mg, 0.609 mmol) in dry MeOH (10 ml) under a nitrogen atmosphere was added **1** (85.8 mg, 0.304 mmol) and the reaction mixture stirred for 1 hour. **2b** (70.0 mg, 0.304 mmol) and $NiCl_2{\cdot}6H_2O$ (72.3 mg, 0.304 mmol) were dissolved in MeOH (5 ml) and added to the reaction mixture. After 1 hour the crude product was filtered in air and washed with cold MeOH. The crude product was dissolved in DCM and passed through a silica plug. The solvent was removed yielding a green precipitate, which was recrystallised from DMF/Et_2O yielding the title compound as dark green needles (28.3 mg, 17 %). δ_H (250 MHz; $CDCl_3$) 1.32 (d, 12H, J = 6.6 Hz, H_d), 3.60 (s, 4H, H_f), 5.0 (sep, 2H, J = 6.6 Hz, H_e), 6.69 (dd, 2H, J = 5.0, 1.3 Hz, H_c), 7.13 (dd, 2H, J = 3.0, 1.3 Hz, H_b), 7.31 (dd, 2H, J = 5.0, 3.0 Hz, H_a); MS (ESI) (m/z): 543 $[M+1]^+$. Anal calcd for $C_{20}H_{24}N_2S_6Ni$: C, 44.2; H, 4.4; N, 5.2. Found C, 44.5; H, 4.2; N, 5.2. λ_{max} = 928 nm ($\epsilon = 11.4\times10^3$ $M^{-1}cm^{-1}$).

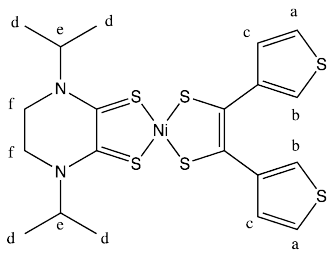

4.4.1 X-ray crystallography

[Ni(Bz$_2$pipdt)(b-3ted)] (3a) α phase Dark green blocks (dimensions 0.57 × 0.23 × 0.12 mm^3) $C_{28}H_{24}N_2Ni_1S_6$, T = 150 K, space group P2$_1$/n, M$_r$ = 639.62, monoclinic, a = 9.2735(3) Å, b = 13.5383(4) Å, c = 22.4070(7) Å, β = 91.326(2)°, V = 2812.39(15) Å^3, D_c = 1.511 Mg m^{-3}, μ = 1.157 mm^{-1}, no. of reflections for cell = 6682, Θ_{max} = 29.546°, Z = 4, 22463 reflections collected, unique [R_{int}] = 7306 [0.054], T_{min}/T_{max} = 0.70/0.87, parameters 352, R_1 [F> 4$\sigma(F)$] = 0.0521, wR = 0.1355, $\Delta\rho_{max}/e$ Å^{-3} = 1.23, $\Delta\rho_{min}/e$ Å^{-3} = -0.91.

[Ni(Bz$_2$pipdt)(b-3ted)]·DMF (3a) β phase Dark blue blocks (dimensions 0.24 × 0.21 × 0.18 mm^3) $C_{28}H_{24}N_2Ni_1S_6$, C_3H_7NO, T = 100 K, space group P-1, M$_r$ = 712.71,a = 10.52540(10) Å, b = 11.7787(2) Å, c = 14.0567(2) Å, α = 68.7530(10)°, β = 79.7120(10)°, γ = 81.4280(10)°, V = 1591.35(4) Å^3, D_c = 1.487 Mg m^{-3}, μ = 1.034 mm^{-1}, no. of reflections for cell = 9915, Θ_{max} = 26.413°, Z = 2, 36045 reflections collected, unique [R_{int}] = 6493 [0.027], T_{min}/T_{max} = 0.75/0.83, parameters 379, R_1 [F> 4$\sigma(F)$] = 0.0317, wR = 0.0796, $\Delta\rho_{max}/e$ Å^{-3} = 0.50, $\Delta\rho_{min}/e$ Å^{-3} = -0.39.

[Ni(^{i}Pr$_2$pipdt)(b-3ted)] (3b) Dark green blocks (dimensions 0.29 × 0.28 × 0.10 mm^3) $C_{20}H_{24}N_2Ni_1S_6$, T = 150 K, space group P2$_1$/n, M_r = 543.53, monoclinic, a = 9.4169(2) Å, b = 27.4559(7) Å, c = 10.0584(2) Å, β = 114.9350(10)°, V = 2358.18(9) Å^3, D_c = 1.531 Mg m^{-3}, μ = 1.365 mm^{-1}, no. of reflections for cell = 7654, Θ_{max} = 29.613°, Z = 4, 16512 reflections collected, unique [R_{int}] = 6040 [0.036], T_{min}/T_{max} = 0.68/0.87, parameters 262, R_1 [F > 4$\sigma(F)$] = 0.0440, wR = 0.1109, $\Delta\rho_{max}/e$ Å^{-3} = 0.77, $\Delta\rho_{min}/e$ Å^{-3} = -0.59.

Chapter 5

The rational design of a new family of metal *bis*-dithiolene

5.1 Introduction

In the previous chapter, it was shown that heteroleptic dithiolenes, containing pendent 3-thienyl groups, could be incorporated into polymer films by electrochemical polymerisation. From this study, and previous investigations into 3-thienyl substituted dithiolenes [Anjos 08], the formed polymers display only weak redox activity, compared to the monomers, when incorporated into a polymer film. One reason for this is thought to be the presence of multiple polymerisation sites in the monomer unit, resulting in extensive cross-linking in the polymer film, reducing the redox activity by hindering ion transport through the film. In order to investigate this, it was necesary to design new ligand systems that, through their structure, reduce the extent of cross-linking, by reducing the amount of polymerisation terminals in the monomer unit.

In this chapter, the synthesis of two novel ligand systems with pendent polymerisable indolyl groups is described, and the formation of complexes of copper and nickel are investigated. These ligands have been designed with a single polymerisation terminal, per ligand moiety, to enable formation of high-quality redox active films, whilst allowing the tuning of the physical properties through substitution of the dithiolene ring (see Figs. 5.1(a) and 5.1(b)).

The design of new ligand systems is an important consideration for all coordination chemists, to ensure that the desired functionality of the material under investigation is achieved. However, for metal dithiolenes, the ligand design takes on an additional role due to the non-innocent nature of many dithiolene complexes, since the whole ligand system plays a part in determining the redox behaviour of the complex - and thus can be vital in determining the success or failure of the resulting complexes in their desired application. For this reason, a great many ligand systems have been designed that,

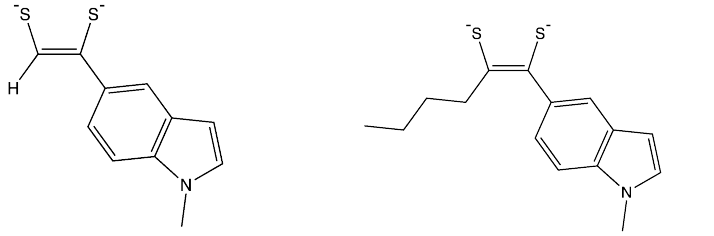

1-(*N*-methylindol-5-yl)-ethene-1,2-dithiolate
= mi-5edt

(a)

1-(*N*-methylindol-5-yl)-hex-1-ene-1,2-dithiolate
= mi-5hdt

(b)

Figure 5.1: Target ligands for novel dithiolene complexes, with polymerisation potential through a pendent indolyl group: (a) 1-(N-methylindole-5-yl)-ethene-1,2-dithiolate (mi-5edt) '**4**'; (b) 1-(N-methylindole-5-yl)-hex-1-ene-1,2-dithiolate (mi-5hdt) '**5**'. Both ligands are depicted in their deprotected form (from the dithiol-2-one), indicated by quotation marks 'x'.

as well as tuning the ligand functionality in aspects such as solubility or reactivity, also tune the electron density on the dithiolene SCCS core. When designing a new dithiolene ligand system, the functionality is the first consideration in the process - in this study, that is the incorporation of a pendent polymerisable group - and then the redox levels of the resultant complexes can later be tuned in by the inclusion of electron withdrawing/donating substitents.

Neutral nickel dithiolenes characteristically show a strong absorption in the NIR region of the electromagnetic spectra (see section 3.3.3), coupled with multiple stable redox states, and therefore, the formation of stable polymer films of these materials is of interest for fast optical switching applications. Such switchable systems might find application in the telecommunications field as a variable optical attenuator (VOA) [Monk 07]. Switching of signal transmission intensity in the NIR region (800-2000 nm) is useful in signal modulation for silica fibre-optics as they are most transparent in the NIR region [McDonagh 00].

The synthesis of novel dithiolene ligands is not just of interest for nickel dithiolenes, as many metals have been shown to complex with this ligand motif (see *e.g.* [Mueller-Westerhoff 87]). Similar to dithiolenes of nickel, copper dithiolenes also form *bis*-dithiolene complexes that show multiple stable redox processes, and can form in a square-planar conformation, and thus are also of interest for the development of conductive materials, due to their close packing of the planar dithiolene cores [Rabaça 09]. In addition, in the neutral state, copper dithiolenes are paramagnetic, due to an unpaired electron on a, formally, copper(II) metal centre. The formation

of stable films of such materials would be of interest for magnetic applications, such as the shielding or induction of small magnetic fields (magnetoshielding or magnetoinductive application, respectively) [Morin 94], as well as their incorporation into magnetoelectronic devices due to fast switching of their redox state.

Ligand synthesis

Isolation of stable ligands is desirable as it allows the ligand systems to be made in bulk, for subsequent screening with a range of metals under a range of conditions. However, only in very specialised, highly resonance stabilised examples can dithiolene ligands be prepared and isolated as free ligands [Isaksson 81], and thus a great deal of work has been devoted to developing stable metal dithiolene ligand precursors, and this is reflected in the plethora of literature devoted to dithiolene ligand design, addressing the various synthetic constraints imposed by the desired functionality of the ligand (see *e.g.* [Stiefel 04] and [Mueller-Westerhoff 91]). The synthesis of polymerisable dithiolene ligands possesses its own constraints as the synthesis of such systems is complicated by the reactivity of the polymerisation terminals, and thus often requires the use of less-aggressive techniques to facilitate the desired transformation.

Two main synthetic routes have been developed in the literature that are suitable for the general preparation of polymerisable dithiolene ligand precursors; either via an α-halo carbonyl, and subsequent reaction with a xanthate ester salt (see scheme 5.1 route A), or via an alkyne, and subsequent free radical reaction with xanthogen disulfide (see scheme 5.1 route B). Both routes yield a 1,3-dithiole-2-one which can readily and stoichiometrically be deprotected to form a 1,2-dithiolate salt *in situ* for reaction with an appropriate metal salt. If necessary, the resultant complexes can then be oxidised under mild conditions to afford the neutral species.

Synthesis via the α-halo carbonyl

For the synthesis via the α-halo carbonyl, Charlton *et al.* showed, very successfully, the synthesis of two 4,5-dithiophen-x-yl[1,3]dithiol-2-ones, where x = 2-thienyl [Charlton 97, Charlton 98] or x = 3-thienyl [Anjos 08], via a benzoin condensation reaction of the appropriate starting thiophenecarboxaldehydes. The α-hydroxy ketones could then be converted in high yield under mild conditions to the α-chloride by reaction with CCl_4 and PPh_3. Reaction with potassium ethyl xanthate, followed by acid mediated ring closure yielded the target dithiol-2-ones in 30-50 % overall yield. Though this method is useful for symmetrically substituted pendent dithiolenes, the reaction is complicated, and in some cases fails completely for cross condensation, or for systems

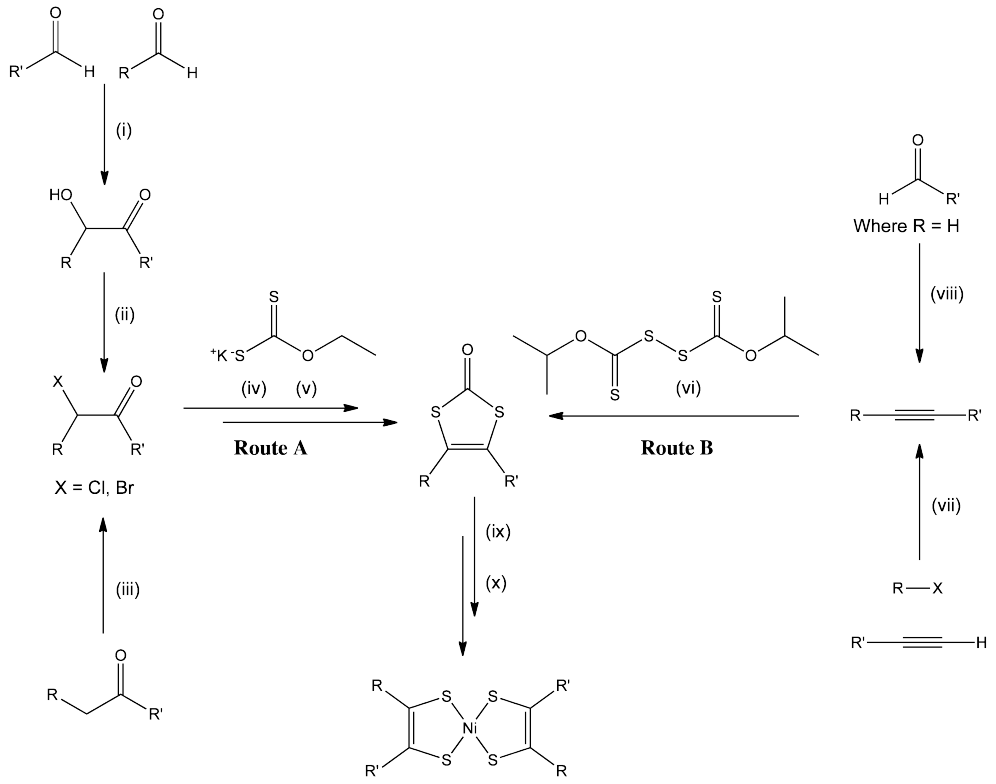

Scheme 5.1: Suitable synthetic routes to symmetric polymerisable nickel dithiolenes, from commercially available starting materials: (i) 3-benzyl-5-(2-hydroxyethyl)-4-methyl-1,3-thiazolium chloride (cat.), NEt_3, EtOH, Δ; (ii) PPh_3, CCl_4/DCM; (iii) $CuBr_2$, EtOAc, Δ; (iv) KS(CS)OEt, acetone; (v) HBr/AcOH; (vi) diisopropyl xanthogen disulfide, AIBN [2,2-azobis(2-methylpropionitrile)], benzene, Δ; (vii) $Pd(PPh_3)_2Cl_2$, CuI, NEt_3; (viii) $(Ph_3P^+CH_2Br)Br^-$, ^{t}BuOK, THF, -78°C; (ix) [TMA][OH], $NiCl_2{\cdot}6H_2O$, MeOH, THF, or NaOMe/MeOH $NiCl_2{\cdot}6H_2O$, TBABr; (x) I_2, MeCN, or [O].

that are particularly electron deficient. This is due to the fact that the benzoin reaction relies on a delicate balance of proton donor and acceptor ability of the aldehydes. Where the reaction fails, direct α-halogenation of a ketone can afford the desired α-haloketone in similarly high yields [Roberts-Bleming 03]. Care should be taken for such a transformation as halogenation using bromine or *N*-bromosuccinimide (NBS) would result in premature polymerisation of the ligand [Robertson 00]. Bromination can be achieved in such sensitive systems by using $CuBr_2$ [Roberts-Bleming 03] and the resultant α-bromide can then be converted in similar yields to the desired dithiol-2-one as suggested in scheme 5.1.

Synthesis via the alkyne

A perhaps more versatile route to dithiol-2-ones was devised by [Gareau 98]. They showed that alkynes could be readily converted to the target dithiol-2-one by reaction with diisopropyl xanthogen disulfide using 2,2-azobis(2-methylpropionitrile) (AIBN) as a radical initiator. The usefulness of this route originates from the wide availability of alkynes due to the versatility of the Sonogashira (and other) coupling reactions. High yielding alkyne-forming reactions can, and have, been designed for a huge number of commercially available aryl halides. [Kean 02] showed such a route to be suitable for both symmetrically and unsymmetrically thienyl substituted *bis*-aryl alkynes. Although reductions in yield are observed, the originative work by [Gareau 98] showed the reaction to proceed even for very bulky substituents, thus this quick method remains a powerful general route into 1,3-dithiole-2-ones.

Other synthetic routes

The two routes described above represent perhaps the most versatile and efficient general routes toward a stable dithiolene ligand precursor. Other routes have also been developed that are suitable for the synthesis of polymerisable dithiolene ligand precursors, though they generally impose some specific constraint on the ligand formed.

[Pozo-Gonzalo 02] achieved a dithiol-2-one with pendent thiophene groups by coupling thiophene carboxaldehydes directly to a vinylene trithiocarbonate. This elegant route afforded the dithiolene fused to a thiophene backbone ($Ni(b\text{-}2tted)_2$) (b-2tted = 4,6-*bis*-(2-thienyl)-thieno-[3,4-*d*]-dithiolate) (see scheme 5.2). The effect of this structural constraint is discussed in [Pozo-Gonzalo 02]; however, the fused thiophene backbone is an intrinsic outcome of this route, and thus is not a general route to dithiolene precursors.

One of the simplest routes to dithiolene ligands goes via the conversion of an α-dione directly into a stable dithione using P_4S_{10} or Lawesson's reagent. This is a quick and mild route to dithiolene ligands [Isaksson 81], however it is only possible in heavily resonance stabilised and structurally constrained systems, such as for the R_2pipdt ligand series described in chapter 4, and thus is only suitable in a limited number of cases. Related to this, direct reaction of an α-hydroxy ketone with P_4S_{10} remains a useful, quick and relatively mild route to metal dithiolenes [Waters 64, Schrauzer 65, Sung 02] (see scheme 5.3), however the yields obtained are often poor, due to the lack of stoichiometric control over the subsequent metal coupling, prohibiting its use for heteroleptic systems.

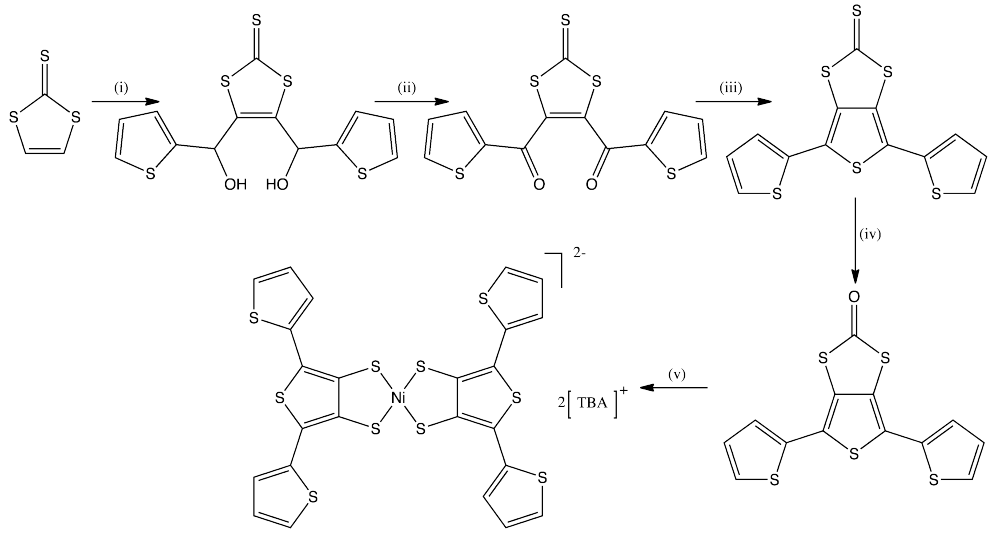

Scheme 5.2: Synthetic route towards a polymerisable nickel dithiolenes, containing a fused terthiophene backbone, described by [Pozo-Gonzalo 02], and references therein: (i) LDA, -78°C, THF, thiophenecarboxaldehyde, then repeat; (ii) MnO_2, CH_2Cl_2; (iii) $Hg(OAc)_2$, CH_2Cl_2, AcOH; (iv) P_4S_{10}, $NaHCO_3$, 1,4-dioxane, Δ; (v) NaOEt, THF, Δ, TBABr, $NiCl_2{\cdot}6H_2O$.

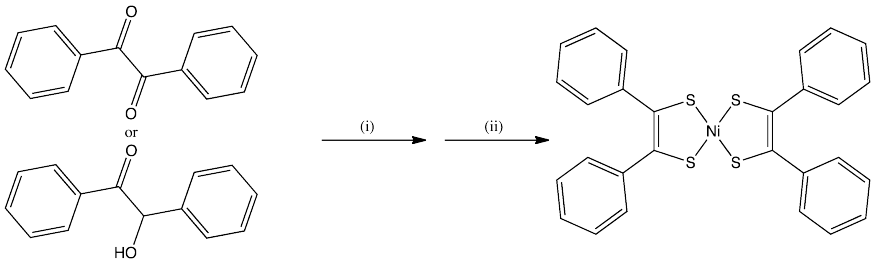

Scheme 5.3: Non-stochiometric route towards nickel dithiolenes, described by [Sung 02], and references therein: (i) P_4S_{10}, 1,4-dioxane, Δ, filtration; (ii) $NiCl_2{\cdot}6H_2O$.

Formation of complexes

The synthesis of metal dithiolenes from dithiol-2-ones has been well documented in the literature; however, for polymerisable ligand systems, certain restraints are put on the synthesis and isolation of the target complexes, imposed by the sensitivity of the ligand to oxidation. The problems encountered in the synthesis of heteroleptic metal dithiolenes was covered in the previous chapter (see section 4.1), and are somewhat distinct from those of homoleptic dithiolenes. From a substituted dithiol-2-one ligand precursor, the desired homoleptic metal dithiolene can be readily afforded by a stoichiometric reaction with a base, such as tetramethylammonium hydroxide ([TMA][OH]) or NaOMe, followed by the addition of the appropriate metal salt (and counterion salt, where an anion is to be isolated) (see scheme 5.1). The dianion may

be observed in some cases, but is readily oxidised in air to the monoanion or, in some cases, the neutral species [Anjos 08]. For polymerisation, the neutral species is preferable to avoid the complication of deposition of the neutral monomer on the electrode [Kean 02, Anjos 08]. For more conventional non-polymerisable dithiolene systems, oxidation of the dithiolene anion is most commonly achieved with elemental iodine [Anjos 08,Kean 02], however, for more sensitive systems, less aggressive methods have been employed. [Anjos 08] achieved improved yields over the iodine oxidation by leaving an acetone solution of the TMA salt of **10** open to atmospheric oxidation. By either method, the reduced solubility of the neutral species in polar solvents, compared to the anion, is a useful tool for affording pure, crystalline samples of a neutral symmetric metal dithiolene.

5.2 Results and discussion

The target ligand precursors **4** and **5** [where **4** and **5** are the dithiol-2-one protected forms of 1-(*N*-methylindol-5yl)-ethene-1,2-dithiolate (mi-5edt) and 1-(*N*-methylindol-5yl)-hex-1-ene-1,2-dithiolate (mi-5hdt), respectively (see Figs. 5.1(a) and 5.1(b))], were designed to incorporate a single polymerisable indolyl group per ligand moiety in order to improve polymer film quality and, by reducing the amount of cross-linking in the polymer, to improve counter-ion transport through the film. This allowed for a modifiable ligand terminus that could be used to tune the physical and/or electronic properties of the resulting complexes (see Fig. 5.1). Complexes of nickel and copper were targeted to compare the behaviour of these structurally analogous *bis*-dithiolene systems, with respect to their redox, optical and physical properties.

5.2.1 Synthesis

Towards M(mi-5edt)$_2$ (where M = Ni = 6, where M = Cu = 7)

The route to the ligand precursor was developed in order to be quick, and easily tuneable to allow future investigation into the effect of different alkyl substituents on the electronic and physical properties of the complexes, and resultant films. Due to the simplicity of the [Gareau 98] route, synthesis of the dithol-2-one ligand precursor, via the alkyne, was decided upon. In the first instance, a Sonogashira route to 5-ethynyl-1-methylindole was investigated [Sonogashira 02]. Using 5-iodoindole as an indolyl feedstock, this reaction furnished 5-ethynyl-1-methylindole in variable to good yield (75 %) [Hénon 06]. This could then be methylated using NaH and MeI in THF in near quantitative yield. Since 5-iodoindole is a particularly expensive indole feedstock, attempts were made to use the cheaper 5-bromoindole as a starting material, but no

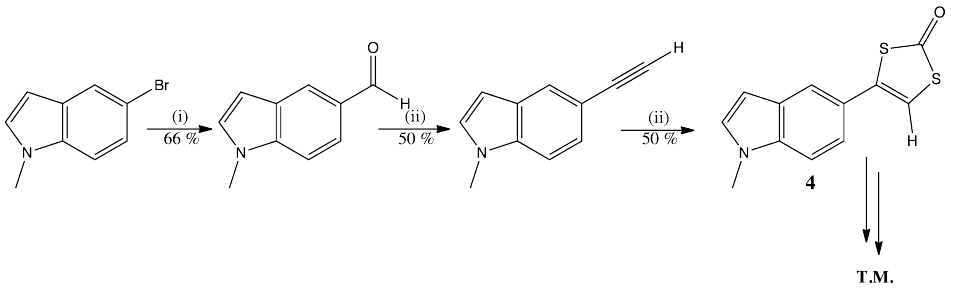

Scheme 5.4: Synthetic route towards **4**: (i) Mg, tetrahydrofuran (THF), microwave, DMF; (ii) $(Ph_3P^+CH_2Br)Br^-$, ^{t}BuOK, THF, -78°C; (iii) diisopropyl xanthogen disulfide, AIBN, benzene, Δ.

product could be observed under a range of Sonogashira conditions. This, coupled with the high cost of a 3 mol % palladium catalyst loading, required for the transformation, meant an alternative preparation was sought.

For terminal alkynes, the Corey-Fuchs procedure is a cheap, catalyst-free alternative to the Sonogashira reaction. 5-bromo-1-methyindole was converted to the aldehyde by a microwave assisted Grignard reaction, in near quntitative yield, by modification of the route described by [Mutule 05]. This was then converted, under a modified Corey-Fuchs procedure to the alkyne in good yield (57 %), with the product isolatable as a yellow oil after column chromatography [Matsumoto 80]. This was then reacted to form the desired dithiol-2-one, as outlined in scheme 5.4. Column chromatography could be avoided in this instance, and pure **4** was isolated in good yield (68 %) by triturating the crude product in warm MeOH. This route holds many advantages over the [Hénon 06] route as it can utilise the cheaper 5-bromoindole as the indolyl feedstock, expensive palladium catalysts can be avoided, it has fewer synthetic steps, and only reqires one purification by column chromatography - an important consideration if a route is to be useful on scale.

By this method, a cheap, quick and relatively simple procedure has been developed toward a novel dithiolene ligand precursor. From this point, complex synthesis was investigated for both nickel (**6**) and copper (**7**).

The nickel TBA salt could be synthesised by the route described by [Anjos 08]. However, unlike for their study on [Ni(b-3ted)][TBA] ([**10**][TBA]) (see chapter 7), [**6**][TBA] did not oxidise to the neutral species in air, and so oxidation was effected using elemental iodine in MeCN in moderate overall yield (32 %). Improvements in yield were obtained by forming the TMA salt by reaction of **4**, in tetrahydrofuran (THF), with a

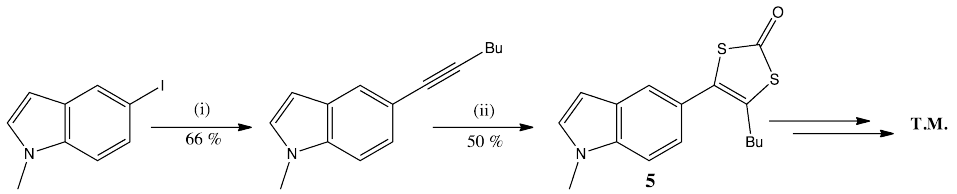

Scheme 5.5: Synthetic route towards **5**: (i) $Pd(PPh_3)_2Cl_2$, CuI, NEt_3, 1-hexyne, DMF; (ii) diisopropylxanthogen disulfide, AIBN, benzene, Δ.

methanolic solution of [TMA][OH], and subsequent addition of $NiCl_2{\cdot}6H_2O$ in MeOH. As before, neutral **6** could be isolated by oxidation with elemental iodine in MeCN, giving an overall yield of (63 %).

In order to prepare the copper analogue, a reaction with NaOMe/MeOH, and subsequent addition of $CuCl_2{\cdot}2H_2O$, was attempted. On addition of $CuCl_2{\cdot}2H_2O$, precipitation occurred immediately. The precipitate was suggested to be neutral **7** by elemental analysis, however, the complex was shown to be unstable in the few solvents in which it was soluble (DMF and DMSO), and thus a rigorous molecular characterisation was prohibited. It seemed therefore that the insolubility of **7** appeared to drive the reaction away from the formation of a monoanionic complex, as was observed for a structurally analogous system, $[Cu(4\text{-pedt})_2][PPh_4]$ (4-pedt = 1-(pyridin-4-yl)-ethylene-1,2-dithiolate), as studied by [Rabaça 09]. For mi-5edt, only the neutral copper *bis*-dithiolene **7** could be isolated, as a brown precipitate. Formation of the stable monoanionic salt could be achieved, however, using [TMA][OH] as a base in THF, followed by addition of $CuCl_2{\cdot}2H_2O$, and leaving the flask open to atmospheric oxidation, with pure [**7**][TMA] precipitating slowly from solution, and isolated by filtration as a dark brown precipitate.

Towards M(mi-5hdt)$_2$ (where M = Ni = 8, where M = Cu = 9)

For the formation of the dithiol-2-one protected mi-5hdt (**5**), the formation of a non-terminal alkyne was required as a precursor to **5**, by the [Gareau 98] route. A Corey-Fuchs procedure is not suitable for forming non-terminal alkynes, and thus a Sonogashira route was investigated. Using 5-iodo-1-methylindole as a feedstock [Winn 01], the alkyne could be isolated in good yield (66 %), after cross coupling, by column chromatography. Sonogashira reactions are not especially sensitive to the presence of water, so the solvents could be used as purchased, however, the yields were shown to be highly sensitive to oxygen [Chen 09], and therefore great care was taken to degas the solution before the catalyst was added. Yields were shown to be sensitive to the history of the indole feedstock - it seemed that older samples of 5-iodo-1-

methylindole gave poorer yields, and in some cases failed completely. This was thought due to the gradual oxidation of indole in air upon storage, seen by a pinking of the crystalline material over time. This effect could be limited by using freshly prepared 5-iodo-1-methylindole, or by performing a recrystallisation from hexane shortly before use.

The alkyne could then be converted to the dithiol-2-one **5** as before [Gareau 98]. Unlike for **4**, column chromatography could not be avoided in the purification of **5**. This purification was further complicated by the co-elution of the target material with 2-cyanopropan-2-yl isopropyl carbondithioate, a known by-product of the reaction, under a range of solvent system investigated (varying mixtures of ethyl acetate (EtOAc) and hexane, mixtures of DCM and hexane, mixtures of EtOAc and petroleum ether and mixtures of DCM and petroleum ether). However, pure product could be obtained, after column chromatography, by Kugelrohr distillation of the by-product, leaving behind pure **5** in reasonable yields as a straw-coloured oil.

The [TBA] salt of Ni(mi-5hdt)$_2$ ([**8**][TBA]) could be synthesised by the route described by [Anjos 08]. Again, like [**6**][TBA], [**8**][TBA] did not oxidise in air, and so oxidation was effected using elemental iodine in MeCN in rather poor yield (22 %). An improved route to neutral **8** was achieved by reacting **5** with [TMA][OH] in THF, followed by the dropwise addition of $NiCl_2{\cdot}6H_2O$ in MeOH. Neutral **8** could be achieved from its TMA salt by passing a DCM solution of **8**[TMA] over a silica plug. This softer oxidation method, compared to iodine oxidation, appeared to give far superior yields (78 % from **5**). Although the mechanism of this oxidation reaction is not fully understood, it is proposed that the high solubility of **8** in DCM pulls the anion away from its TMA counter-ion on the column, with oxidation of the isolated anion achieved on the silica surface. This mechanism is supported by the fact that improved yields were seen for wider surface area silica plugs, or when fresh silica was added to the top of the cake. This procedure does not work nearly as well for [**6**][TMA], presumably reflecting the reduced solubility of **6** in the mobile phase, yielding only (34 % from **4**).

In order to synthesise the copper complex, reaction of the ligand precursor with NaOMe in MeOH, followed by dropwise addition of $CuCl_2{\cdot}2H_2O$ did not lead to the immediate precipitation of the neutral dithiolene as for **7**, but instead, the complex remained in solution until it was added to a methanolic solution of PPh_4Br, whereupon the complex precipitated as the monoanionic tetraphenylphosphonium salt, [Cu(mi-5hdt)$_2$][PPh_4] ([**9**][[PPh_4]) in rather poor yield (15 %). It therefore appears that the decreased solubility of **7** in methanol drives the reaction towards the isolation of the

neutral complex, whereas the solubility of **9** aids the formation of the monoanionic salt. Improved yields of a monoanionic salt could be achieved using the [TMA][OH]/THF route, as for **7**, with pure [**9**][TMA] isolated by filtration as a bronze precipitate (46 %).

5.2.2 Structure

For systems where the ligands are substituted unsymmetrically, as in this study, there remains a question over their predominant conformation in solution. The majority of nickel dithiolenes with unsymmetrically substituted ligands have been shown to crystallise in the *trans* conformation, though some examples of the *cis* conformation, especially where the steric difference is small, have been reported [Belo 05, Belo 06]. This is most likely due to a more favorable packing of the centrosymmetric geometry in the crystal lattice. However, recent literature has suggested that this may not be the case in solution [Sugimori 96, Jeannin 05]. These studies investigated the solution conformation of unsymmetrically substituted nickel dithiolenes by variable temperature NMR. The studies showed a coalescence of signals at higher temperatures, separating into two distinct peaks at low temperature. This suggests that such complexes exist in two isomeric forms, *cis* and *trans*, and that they are rapidly interconverted at room temperature. [Jeannin 05] went on to estimate the free energy of activation for this process. From such a study it would be possible to assess the likelihood of different mechanisms of isomerisation. The barrier to inversion via a tetrahedral intermediate has been calculated to be more than twice that observed by NMR, and thus it is likely that the process goes by another route, possibly linked to the lability of the ligand observed for nickel dithiolenes [Bigoli 01]. [Sugimori 96] discounted a simple ligand exchange mechanism, however, due to the time scale observed for such a process, as shown by a ligand scrambling experiment, monitored by ^{1}H NMR.

Such an ambiguity over the solution conformation of unsymmetrically substituted dithiolenes may yield distinct differences in the properties of such complexes in solution, compared to the solid-state. For example, as polymerisation is (initially) a solution based process, the effects of such an isomerisation may be significant, as it could affect the way the molecules couple upon oxidation. However, as yet, this effect has not undergone a detailed study.

Like most reported examples of unsymmetrically substituted nickel dithiolenes (see *e.g.* [Mueller-Westerhoff 87]), **8** crystallised in the *trans* geometry (see Fig. 5.2(a)). Crystallisation failed under a myriad of growing conditions, favoring instead the formation of continuous films over the vessels (plastic, glass, and hexamethyldisilane

Bond	Bond Length / Å			
	Complex **8**		Complex **6**	Ligand **4**
	Observed	Calculated	Calculated	Observed
Ni(1)-S(2)	2.1260(8)	2.124090	2.126509	
Ni(1)-S(9)	2.1217(8)	2.123360	2.126562	
S(2)-C(3)	1.707(3)	1.718131	1.699005	1.737(5)
S(9)-C(8)	1.714(3)	1.725658	1.728363	1.746(5)
C(3)-C(8)	1.377(5)	1.391029	1.384233	1.336(7)
Angle	Angle Size / °			
	Observed	Calculated	Calculated	Observed
S(2)-C-C-S(9)	0.28	0.02	0.80	0.43
C-C-C-C	59.89	53.93	30.14	30.96

Table 5.1: (above) Selected bond lengths of **6** and **8**, showing a good general agreement of calculated bond lengths with those observed for single crystal XRD data of **8**, and a reduction in the C-S bond lengths and increase in the C=C bond lengths, compared to that of the single crystal XRD data of free ligand **4**, confirming the aromatic nature of the NiSCCS ring. (below) Selected torsion angles of **6** and **8** showing an overall square planar coordination geometry with the pendent indolyl groups twisted away from planarity.

(HMDS) treated glass). However, optimal growing conditions were found to be elevated temperatures (for Scotland) of 25°C in a wide-based conical flask from a EtOH/DCM mixture. This was attributed to the minimised exposure of fresh air/liquid/glass interface upon evaporation, thus favoring homogeneous crystallisation, rather than film deposition.

The packing structure of **8** showed the complex to crystallise in a columnar stacking arrangement, with an interplanar distance of 3.822 Å, approaching the van der Waals limit for efficient sulfur nickel overlap (see Fig. 5.2(b)). Close contact between the stacks was achieved through the indolyl pyrrole unit (C2) and the dithiolene S (see Fig. 5.2(a)). As observed for other pendent aromatic systems [Sugimori 96, Hill 95], the indolyl groups were twisted out of the molecular plane by some 60°, thus prohibiting a closer packing of the dithiolene cores. This was interesting as the incorporation of a flexible butyl group was included to allow the in-plane twist of the indolyl group, and thus suggested that the origin of this twist perhaps did not lie solely with sterics (see section 5.2.4). Compared to the crystal structure of the free ligand precursor (not shown), which showed classical dithiolate bond lengths for the C-S and C=C bonds (see Tab. 5.1), the complexed ligand showed a shortening of the C-S bonds, and a lengthening of the C=C bond, consistent with a more delocalised aromatic π system over the NiSCCS ring.

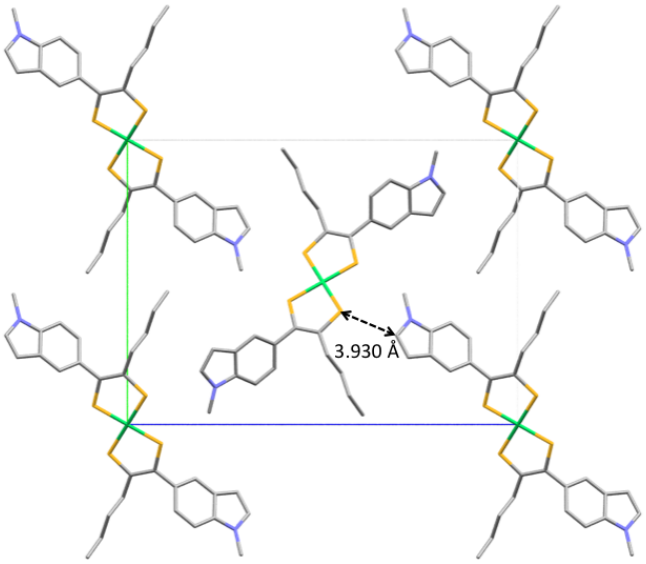

(a) **8**

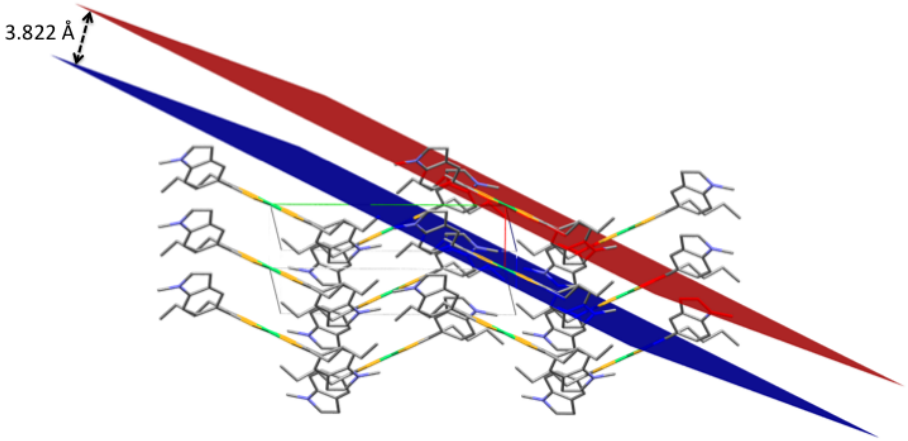

(b) **8**

Figure 5.2: Single crystal X-ray data for **8** showing (a) packing in a plan view of the unit cell with close contacts between the molecules through the indolyl pyrrole unit (C2) and the dithiolene S (3.930 Å; (b) stacking of the dithiolenes molecules down the a-axis with short interplanar distance of 3.822 Å.

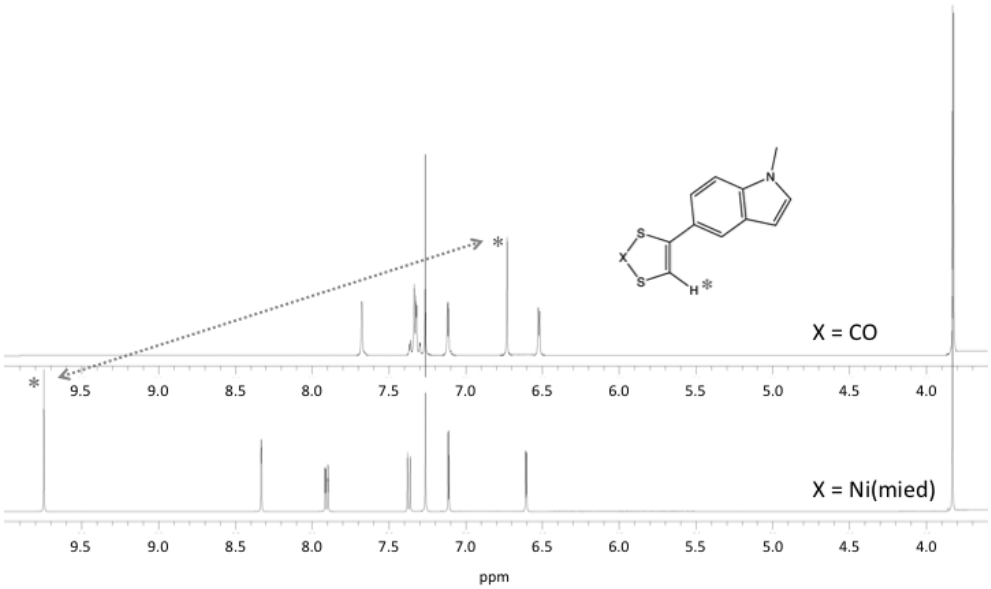

Figure 5.3: An expansion of the ^{1}H NMR spectra of **4** and **6**, showing the increased aromaticity of the dithiolene upon complexation by the large shift to higher frequency for the ethylene proton (∗).

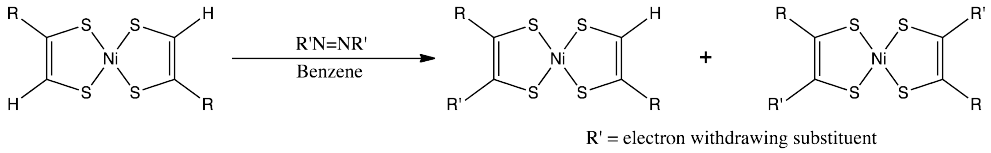

Figure 5.4: Future modification of **6**, inspired by the work of [Sugimori 96, Kajitani 96], to tune the physical and electronic properties in a top-down fashion.

No crystals suitable for XRD could be obtained for **6**, however, the aromatic nature of the dithiolene core could also be observed by ^{1}H NMR by the large shift to higher frequency for the SCCS ring -H upon complexation, from 6.73 ppm in the free ligand (**4**) to 9.74 ppm in the complex (**6**) (see Fig. 5.3). The increase in the aromaticity of this hydrogen has led some groups to investigate the reactivity of such dithiolene complexes [Sugimori 96, Kajitani 96], and could be a possible future step for simple tuning the physical or electronic properties of **6** without the need for a bottom-up synthetic approach (see Fig. 5.4).

For the copper dithiolene TMA salts, small single crystals of **9** were obtained by slow evaporation of an acetone/isopropyl alcohol (IPA) mixture, however, the crystals

diffracted poorly and, as such, no structural data could be obtained by single crystal XRD. For **7**, the complex seemed to decompose in solution upon standing for periods of time necessary for single crystal growth, and thus no data could be obtained for either copper dithiolene system.

5.2.3 Spectroscopic studies

Electronic absorption spectroscopy was performed on the neutral nickel complexes **6** and **8**, and the monoanionic copper complexes [**7**][TMA] and [**7**][TMA] to characterise the nature of the electronic transitions within the complexes.

UV/Vis/NIR spectroscopy of **6** and **8** in DCM showed an intense peak in the UV region and a single peak in the NIR region [910 nm (10,989 cm^{-1}, ϵ = 25,576) and 840 nm (11,905 cm^{-1}, ϵ = 23,546) for **6** and **8**, respectively] (see Figs. 5.5(a) and 5.5(b)). This intense absorption in both nickel complexes was calculated to be due to a mixed HOMO and HOMO-2 to LUMO transition, confirming the contribution of the pendent indolyl group to the frontier orbitals (see section 5.2.4). For **6**, this absorption occurred at 1,006 cm^{-1} lower energy than for **8**.[1] For nickel ditholenes, electron donating groups raise the energy of the HOMO more than that of the LUMO, resulting in a smaller HOMO/LUMO gap, and thus a lower energy absorption in the NIR. Since -Bu is weakly donating, through induction, compared to -H, this suggests that the dominant effect of the -Bu group in **8** is to sterically disfavour a more planar geometry, and thus reduce the extent of donation through resonance from the indole group, compared to **6**.

As already mentioned, neutral **7**, isolated by the NaOMe/MeOH route, was shown to be unstable in solution, with decomposition occurring immediately upon dissolution (see section 5.2.3). This instability of the neutral copper dithiolene contrasted with the study of [Ueda 98] on neutral copper dithiolenes (see Fig. 5.6). However, since [Ueda 98] represents the only isolated neutral copper dithiolenes reported, it is likely that the TTF-functionalised ligands used for the studied complexes act to better stabilise the formed radical. As discussed in section 2.5.1, TTF possesses its own rich redox behaviour, with oxidation processes occurring at low potentials (E), thus is is conceivable that stability of the neutral radical is achieved through delocalisation into the large aromatic TTF ligand system, and thus it is more likely an oxidation of the TTF, than of the dithiolene core, that was achieved upon oxidation of the monoanion. Such stabilisation is clearly not possible from the indolyl group in **7** and **9**, and the

[1] The relative change in the energies of the transitions are quoted in wavenumbers ($\overline{\nu}$) as it is a linear scale with respect to energy (E).

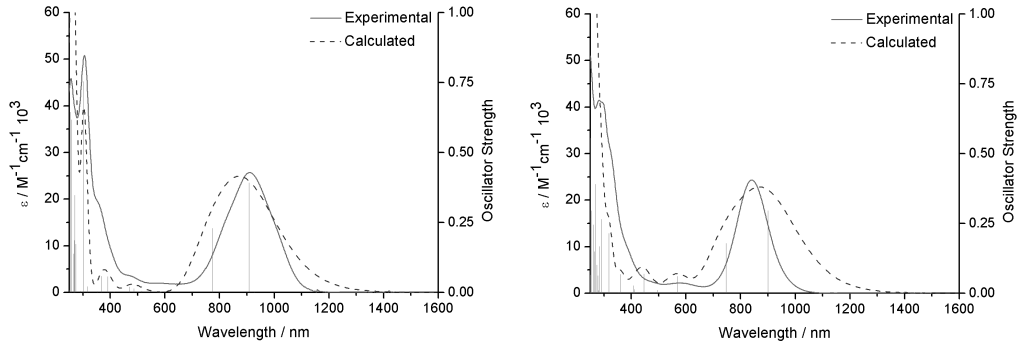

(a) **6** (b) **8**

Figure 5.5: Experimental and calculated UV/Vis/NIR absorbance spectra, where the absorption intensity is given as the molar extinction coefficient (ϵ): (a) **6** in DCM showing excellent approximation of all the transitions; (b) **8** in DCM showing good approximation of all the transitions and showing the NIR absorption at higher energy than for **6**.

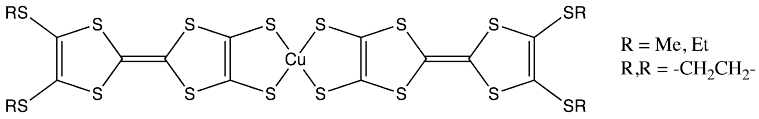

Figure 5.6: Molecular structure of stable neutral copper dithiolenes synthesised by [Ueda 98], containing TTF-functionalised ligands.

complexes were shown to decompose perhaps by the the loss of at least one dithiolene ligand, as suggested by mass spectrometry.

The TMA salts of **7** and **9**, however, showed greater solution stability and, unlike for the nickel dithiolenes, showed only very weak absorption in the NIR region at 1557 nm (6423 cm^{-1}, $\epsilon = 550$) and 1486 nm (6729 cm^{-1}, $\epsilon = 523$) for [**7**][TMA] and [**9**][TMA], respectively. By comparison with the redox series of the nickel dithiolenes, the monoanionic copper dithiolenes are isoelectronic with the dianionic nickel dithilolenes. The comparative weakness of the NIR absorptions, compared to **6** and **8**, can therefore be understood by the orbital, corresponding to the LUMO in **6** and **8**, being full, thus prohibiting an analogous $\pi \rightarrow \pi^*$ transition. The weak absorption observed in [**7**][TMA] and [**9**][TMA], is therefore due to d→d transitions on the copper centre. Such an electronic description is supported by the spectroscopic data by both the weak absorption in the NIR region, and the low sensitivity to ligand structure, when compared to their nickel analogues.

Both complexes showed one strong absorption in the UV/Vis region of the electromagnetic spectrum [418 nm (23,923 cm^{-1}, $\epsilon = 11{,}220$) for [**7**][TMA] and 393 (25,445 cm^{-1},

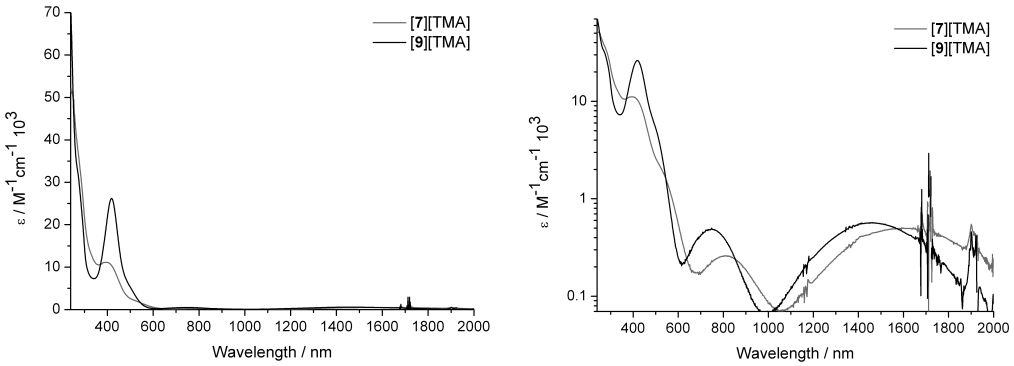

(a) **7** and **9** (b) **7** and **9**

Figure 5.7: Experimental UV/Vis/NIR absorbance spectra, where the absorption intensity is given as the molar extinction coefficient (ϵ): (a) [**7**][TMA] and [**9**][TMA] in MeCN showing weak absorptions in the Vis/NIR region, and a strong absorption in the UV/Vis region; (b) a logarithmic plot of [**7**][TMA] and [**9**][TMA] in MeCN, to visualise the weak Vis/NIR absorptions.

ϵ = 26,181)] for [**9**][TMA], and a second absorption outside the solvent window for spectroscopic investigation. The intensity and energy of the UV/Vis transition suggests it to be a ligand centred transition. Over several days, the spectra of [**7**][TMA] changed, losing the peak at 418 nm, with the resulting spectrum reminiscent of that of chemically synthesised **7** after decomposition in DMF. This suggests that the complex was slowly oxidised in solution, whereupon it underwent the same fate as was observed for **7** in solution. This might explain the difficulties encountered on single crystal growth. Such a process is not observed for [**9**][TMA], suggesting that is more resistant to oxidation, possibly due to the more out-of-plane indolyl group, not raising the HOMO level as much as for [**7**][TMA].

5.2.4 Computational modelling

Single molecule calculations for nickel dithiolenes

Computational modeling was performed, as in section 4.2.4, to support the experimental data of the molecular properties, namely the geometry and electronic absorption behaviour, as it is a useful tool for the visualisation of the electronic origins of these properties (see section 3.4).

Ab initio single molecule calculations were carried out on **8** from the single crystal geometry of **8**, and on **6** by modifying the structure of **8**, as measured by XRD, using the program ArgusLab4.0. The calculations were run using the same basis sets and level of theory as detailed in section 3.4. Geometry optimisation of both complexes

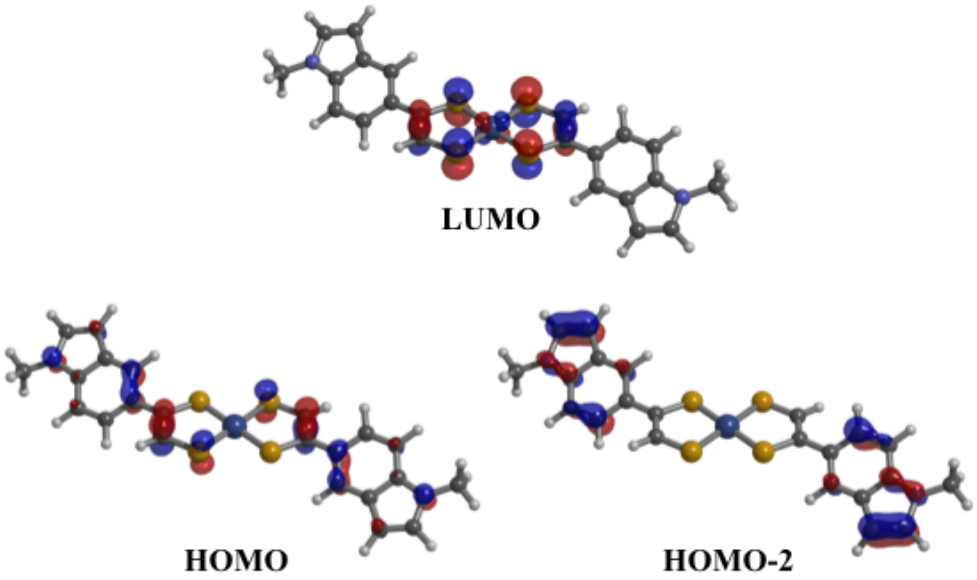

(a) **6**

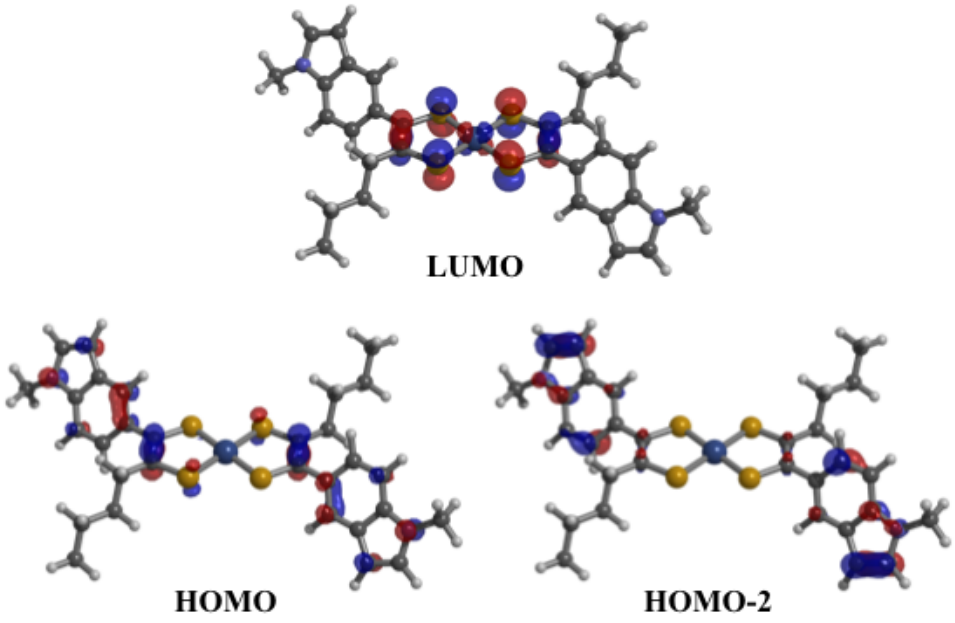

(b) **8**

Figure 5.8: Frontier molecular orbitals of **6** (a) and **8** (b) that contribute to the low energy absorption in the NIR region, calculated from the geometry optimised structures, with starting geometry based on single crystal X-ray data obtained for **8**.

Complex	Wavelength (nm)	Osc. Strength	Major contributions
6	921.1	0.3164	HOMO→LUMO (57 %)
			H-2→LUMO (22 %)
	786.5	0.2828	H-2→LUMO (73 %)
			HOMO→LUMO (10 %)
8	899.7	0.2955	HOMO→LUMO (70 %)
			H-2→LUMO (14 %)
	747.0	0.1789	H-2→LUMO (78 %)
			HOMO→LUMO (4 %)

Complex	Orbital	Orbital location %	
		Ni	ligand (SCCS)
6	LUMO	17.13	82.87 (72.71)
	HOMO	1.44	98.56 (50.17)
	HOMO-2	0.48	99.52 (9.75)
8	LUMO	17.83	82.17 (72.53)
	HOMO	1.69	98.31 (46.22)
	HOMO-2	0.69	99.31 (19.75)

Table 5.2: TD-DFT data: (above) calculated energies and intensities of the transition observed in **6** and **8** (see Fig. 5.5); (below) calculated contributions to the frontier molecular orbitals contributing to the NIR absorption of **6** and **8**. The data confirm the low energy absorption to be due to transitions between orbitals delocalised over the dithiolene core, with substantial contribution from the indolyl groups. The large oscillator strength is consistent with the high degree of spatial overlap of the frontier orbitals.

showed excellent agreement of the bond lengths with the observed X-ray data for **8**, and showed the HOMO and LUMO orbitals distributed over the whole dithiolene unit, with symmetries in keeping with previous calculations (see Tab. 5.2 (below)) [Curreli 04]. The HOMO orbital in both complexes had a more substantial contribution from the pendent aromatic, compared to previous examples (see section 4.2.4) (see Fig. 5.8, and Fig. 4.4 in chapter 4).

Following optimisation, information regarding the nature of the electronic transitions for **6** and **8** was sought using time-dependent density functional theory (TD-DFT). This was done to model the electronic absorption spectra, as measured in section 5.2.3, and probe the origins of the individual absorptions. The calculations were carried out using a polarisable continuum model of MeCN ($\epsilon = 35.688$) (see section 3.4). TD-DFT calculations showed excellent agreement with the experimentally determined absorption spectra, and showed the low energy NIR absorption [910 nm (10,989 cm^{-1}) and 840 nm (11,905 cm^{-1}) for **6** and **8**, respectively] to be due to a mixed HOMO and HOMO-2 to LUMO transition. Since the HOMO-2 orbital was predominantly ligand based (see Figs.

5.8(a) and 5.8(b) and Tab. 5.2 (below)), this suggests extensive indole contribution to the electronic properties of the complex (see Fig. 5.5; see Tab. 5.2 (above)). The lower energy NIR transition for **6** is suggested to be due to a more extensive contribution from the HOMO-2 orbital, reflecting its increased contribution to the frontier molecular orbitals, due to its more in-plane conformation.

Rotational studies of nickel dithiolenes with pendent aromatic groups

For systems where both ligand R groups are heterocyclic, such as in **3a** and **3b**, studied in chapter 4, there exists a large steric constraint on the ligand. This is shown in the single crystal XRD structures by the out-of-plane twist of the pendent groups [Anjos 08, Sartain 66]. This twist imparts a large effect on the redox properties of the complex, and may help to explain the observed reversibility of the oxidation of the dithiolene core to the monocationic species for **3a** and **3b** (see section 4.2.5). For systems where this steric constraint is reduced (as in *e.g.* **8**), or removed altogether (as in *e.g.* **6**), better electronic communication between the dithiolene core and the polymerisable ligands may be achieved by the free rotation of the ligand, and the reversibility of the dithiolene oxidation is reduced [Kean 01], or removed entirely as the radical cation can be easily delocalised to the periphery. Accordingly, for polymerisable systems, this oxidation can then result in polymerisation of the peripheral heterocycles.

Interestingly, even in systems where such steric constraints are removed altogether, such as for $Ni(ped)_2$ (ped = 1-phenyl-ethylene-1,2-dithiolate), where the ligand consists of a single phenyl group attached to the SCCS core, the complexes are shown to crystallise with the aromatic group twisted out of the molecular plane by a minimum of $\sim 25^\circ$. [Hill 95, Sugimori 96]. This has previously been attributed to lattice constraints, or ignored altogether. However, the geometry optimised structures of a single molecule of **6** and **8** in the gas phase also show such a twist. To investigate this effect further, computational studies, modeling the rotation of the pendent aromatic, were carried out using the same level of theory as outlined in section 3.4.

The designed experiment calculated the change in energy of the molecule in response to the change in torsion angle between the pendent aromatic and the dithiolene core (shown as C_1-C_2-C_3-C_4 in Fig. 5.9(a)). The modeled complexes were **8** and $Ni(ped)_2$, in their neutral state, with the starting geometry modeled from single crystal XRD data [Sugimori 96]. The torsion angle of one ligand was fixed at different angles at 10° intervals for a 360° rotation. By fixing this torsion angle, the structure is prevented from finding a true energy minimum, and thus the energies calculated are not those of

observable structures, but serve as a gauge for how far from ideality the forced structure is.

The calculations suggested that, on twisting about the C_2-C_3 bond (see Fig. 5.9(a)), the energy of both **8** and Ni(ped)$_2$ increases towards a forced planar conformation, but also towards a forced perpendicular conformation, with low energy structures at conformations intermediate to these structures (see Fig. 5.9(c)). Though the energy barriers were calculated to be greater for the more sterically crowded **8** model, a similar shape of energy surface was observed for of Ni(ped)$_2$. The barrier to rotation is calculated to be relatively small for both complexes at ∼5-15 KJ mol^{-1} (similar to that of butane rotation), however, it seems to be sufficient to affect the packing structure of the pendent aromatic groups in the crystal lattice [Sugimori 96]. Whilst planarity might be disfavoured on steric grounds, the energy barrier to a perpendicular arrangement cannot be explained by this arguement. One possible reason for the low energy twisted conformation, observed in the crystal structure of **8** might be due to electronic interactions between the two aromatic systems (that of the pendent aromatic, and the dithiolene core). By expanding the isosurface plot of the HOMO of **8**, it can be seen that a node exists in the HOMO orbital between the dithiolene core and the pendent indolyl group on the linking C_2-C_3 bond (see Fig. 5.9(d)). Planarity of the structure may, therefore, be disfavoured by a repulsive electronic interaction between the out-of-phase π systems, in a similar manner to the case observed in biphenyl systems [Richardson 01, Richardson 09]. If this were the case, it might be thought that a perpendicular arrangement would be the most energetically favourable. Fig. 5.9(b) shows a representation of the phase of the HOMO orbital on the two ring systems to help understand the origin of the low energy twisted conformation. When the rings are perpendicular, there is an equal and opposite interaction between the rings. However, in the twisted conformation, the favourable interaction is maximised due to a secondary conjugative interaction between the rings (see Fig. 5.9(b)) [Minkin 04].

In summary, single molecule calculations were performed to model some of the observed properties of the nickel dithiolenes synthesised in this study (**6** and **8**). The level of theory used showed good agreement between the observed geometry of the molecules, as well as good agreement with their electronic absorption properties. Using the same level of theory, it was possible to investigate aspects of the observed molecular structure, in terms of the origins of the twisted aromatic groups, seen in all know examples of dithiolenes with pendent aromatics. This twist may have an effect on the resultant film morphology of both molecular and polymeric films by prohibiting the close packing of the dithiolene cores or, for polymerisable systems, by promoting cross-linking of the

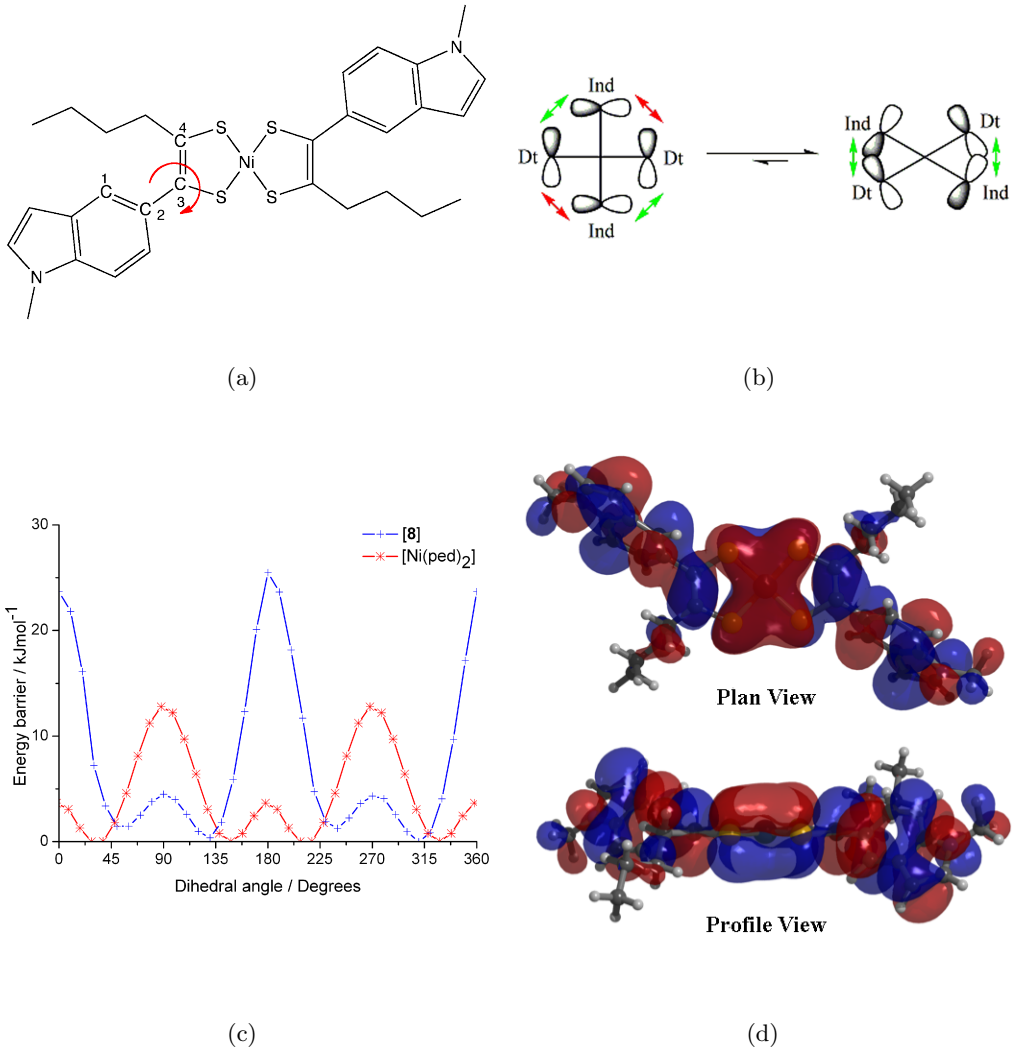

(a) (b)

(c) (d)

Figure 5.9: Modelling the rotation of the pendent aromatic in **8** as a function of the $C_1C_2C_3C_4$ torsion angle: (a) pictorial representation of the investigated ligand rotation of **8**; (b) pictorial representation of the HOMO density on the adjoining dithiolene (Dt) and indole (Ind) rings, showing favourable and unfavourable interactions in a perpendicular and twisted conformation; (c) DFT calculated torsional potential surfaces for $Ni(ped)_2$ and **8** in their neutral state; (d) plan and profile view of the HOMO of **8** (isosurface value is 0.01 e / $Å^3$).

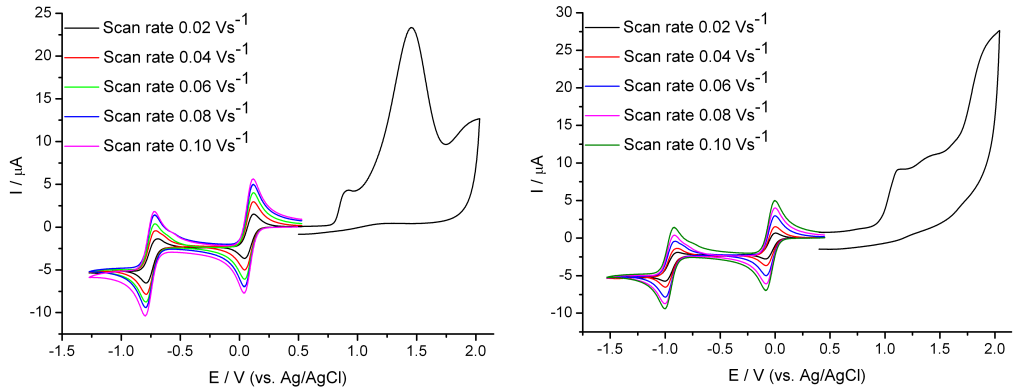

(a) **6** (b) **8**

Figure 5.10: Cyclic voltammetry, measuring current (I), in response to an applied potential (E), in 0.3 M $TBABF_4$/DCM: (a) **6** shows two reversible redox processes, assigned to sequential reduction of the dithiolene, and two irreversible oxidation processes, suggesting the formed radical is not stabilised; (b) **8** shows two reversible redox processes, assigned to sequential reduction of the dithiolene, and two irreversible oxidation processes, suggesting the formed radical is not stabilised on the dithiolene core. Both reduction processes occur at more negative potentials than for **6**.

polymer chains for systems with more than one polymerisation terminal per ligand, such as the systems studied in chapter 4 and by [Anjos 08].

5.2.5 Electrochemistry

The electrochemistry of both the nickel dithiolenes (**6** and **8**), as well as both the stable copper dithiolene salts ([**7**][TMA] and [**9**][TMA]), formed in section 5.2.1, was investigated to probe the energy of the frontier orbitals, as well as their distribution over the molecule. The electrochemistry of each complex was also investigated at higher monomer concentrations in the electrolyte, in an effort to induce polymerisation through oxidative coupling of the pendent indolyl groups.

Electrochemical studies of nickel dithiolenes at low monomer concentrations

Cyclic voltammetry of **6** and **8** in DCM showed two reversible one-electron processes (at ${E^1}_{1/2}$ = -0.76 V and -0.90 V, and ${E^2}_{1/2}$ = +0.07 V and -0.03 V, for **6** and **8**, respectively), as well as two irreversible oxidation processes above +1 V (see Fig. 5.10; see Tab. 5.3). The first two processes correspond to sequential reduction of the neutral complex to a mono (${E^2}_{1/2}$) and a dianion (${E^1}_{1/2}$), similar to previously reported neutral metal *bis*-dithiolene complexes [Mueller-Westerhoff 87].

The reduction processes of **6** occured at more positive potentials (E) than for **8**. This

Complex	$E^1_{1/2}$ / V	$E^2_{1/2}$ / V	E^3_{ox} / V	E^4_{ox} / V
6	-0.76	0.07	0.92*	1.46*
8	-0.90	-0.03	1.12*	1.46*

Table 5.3: Redox potentials of **6** and **8** (vs. Ag/AgCl) in 0.3 M $TBABF_4$/DCM solution. All processes are reversible, unless otherwise stated; *irreversible.

suggests that the LUMO orbital, into which the electrons are added, is lower in energy for **6** than **8**. This is in agreement with the UV/Vis/NIR studies, which showed a NIR absorption at lower energies for **6** than **8**, consistent with a smaller HOMO/LUMO separation. Additionally, the decreased separation of the redox processes for **6** than **8** ($\Delta E_{1/2}$ = +0.83 V and +0.87 V, between the two reduction processes of **6** and **8**, respectively) suggest that **6** is better able to stabilise two negative charges developed on the complex, possibly due to increased delocalisation onto the indolyl groups. Such a processes would be supported by a more in-plane conformation of the indolyl groups, as suggested by single molecule calculations (see section 5.2.4).

Electrochemical studies of nickel dithiolenes at high monomer concentrations

The irreversible nature of the oxidation processes, as observed at low monomer concentration, suggested that the radical formed upon oxidation of the complex to not be stabilised by the dithiolene core. One reason for this was thought to be due to the better electronic communication between the dithiolene core, and the pendent aromatic groups, compared to **3a** and **3b** (see section 5.2.4, compared to section 4.2.4). If the radical can be delocalised to the aromatic groups, this might result in oxidative coupling of the indolyl groups, and hence the loss of reversibility for the oxidation process(es).

In order to assess the potential for polymerisation of **6** and **8**, electrochemical studies were performed at higher monomer concentrations (∼10 mmol). This was done to facilitate efficient coupling at the working electrode by reducing the time between radical formation, and subsequent coupling.

For more concentrated solutions of **6** in DCM, cycling the potential (E) into the third (irreversible) process (between -0.3 and +1.0 V) resulted in the deposition of a conducting film on the electrode (see Fig. 5.11(a)). This was shown by the increase in peak current ($|I_p|$) on sequential scans - as current can only be passed at the working electrode if the surface remains conducting, the increase in peak current ($|I_p|$) indicates

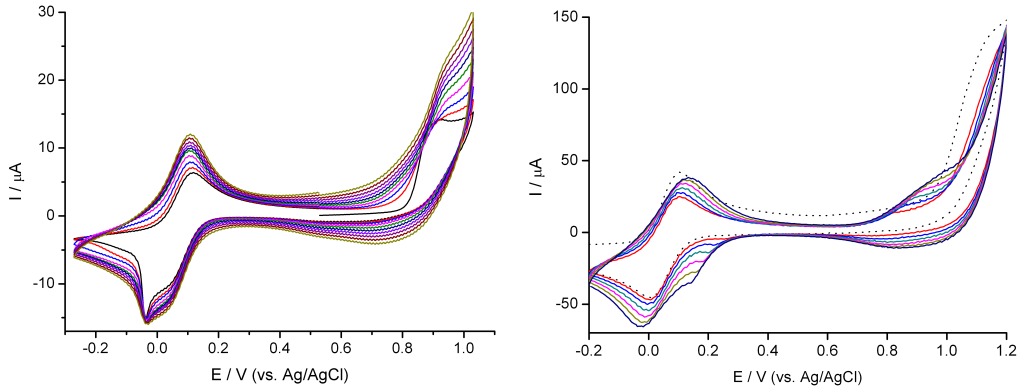

(a) **6** (b) **8**

Figure 5.11: Potential cycling into the first irreversible oxidation process to facilitate polymerisation (1000 mVs^{-1}), measuring the current (I) response to a cycling potential (E): (a) a concentrated solution of **6** in 0.3 M $TBABF_4$/DCM, between -0.2 V and +1.1 V and (b) a concentrated solution of **8** in 0.1 M $TBABF_4$/MeCN, between -0.3 V and +1.2 V. Peak currents ($|I_p|$) increase with potential cycling, indicating the deposition of a conducting film.

the increasing quantities of redox active material deposited on the electrode. The insolubility of the film in DCM, compared to the monomer, suggested the film to be polymeric in nature. Therefore, it seemed that the radical, formed on the dithiolene upon oxidation, resided, as least partially, on the indolyl group, and its formation resulted in the oxidative coupling of the indolyl groups.

For **8**, film growth was adversely affected by the solubility of the nascent film in DCM, however, polymerisation could be achieved by cycling the potential (E) into the third (irreversible) process (between -0.2 and +1.2 V) for a concentrated solution of **8** in MeCN. As for **6**, polymerisation was observed by the increase in peak current ($|I_p|$) on sequential scans.

In order to investigate the redox properties of the generated polymer films, and to compare them to the monomer, the working electrode, with the grown film, was transfered to a monomer-free electrolyte solution. Cycling of poly-**6** and poly-**8** in monomer-free electrolyte solution (of the same electrolyte and solvent, as for their formation) showed two chemically reversible processes, corresponding to the sequential reduction of the polymer films (see Figs. 5.12(a) and 5.12(b)), as well as an irreversible oxidation process at a similar potential to the monomers (not shown). For both **6** and **8**, films formed at faster scan rates (v) (up to 1.0 Vs^{-1}) appeared to show improved film redox behaviour. This was attributed to a shorter residence time at strongly oxidising

potentials.

For poly-**6**, both reduction processes were shown to be chemically reversible (see Fig. 5.12(a)), however, the second process diminished at faster scan rates ($v > 0.5$ Vs^{-1}). Additionally, the peak currents ($|I_p|$) of the two reduction processes were rather unbalanced, with the reduction to the monoanion producing a larger current response than the reduction to the dianion. Both these observations were consistent with the theory that a large steric barrier exists for the incorporation of two molar equivalents of $[TBA]^+$ into the film. A more dense (or thick) film would be harder to penetrate for bulky counter ions, and thus complete reduction of the film to the dianionic state may be prevented by the inability of the TBA^+ to penetrate the film. However, both reduction processes could clearly be observed, with the redox processes for poly-**6** at very similar potentials to **6** in solution, suggesting that, contrary to previous results from thienyl containing systems (see section 4.2.5) [Kean 01, Pozo-Gonzalo 02], the dithiolene redox processes were largely unaffected by incorporation into a polymer film.

For poly-**8**, the redox processes also appeared largely unchanged upon incorporation into a polymer film. However, the current response (I_p) of the two reduction processes appeared to be more balanced, suggesting improved ion transfer through the film, compared to poly-**6** (although the reason for the split oxidation process of $E^2_{1/2}$ in **8** is not completely understood) (see Fig. 5.12(b)). The more balanced reduction processes in poly-**8** may be due to the formation of a less dense polymer network, facilitating improved ion transport through the film. This is possibly caused by the steric bulk of the -Bu group on the dithiolene ring, disfavouring close packing of the polymer chains. This is supported by the smaller peak currents ($|I_p|$) for poly-**8**, than for poly-**6**, as seen in Figs. 5.12(a) and 5.12(b), as well as a visibly more coloured film for poly-**6**, suggesting a smaller dithiolene content in the film of poly-**8**.

As mentioned above, the minimal change in redox levels upon polymerisation of **6** and **8** is in contrast to all previous studies for dithiolene polymers [Kean 01, Pozo-Gonzalo 02]. In order to determine the reason for this difference, it is necessary to consider the differences between the molecules investigated.

For complexes **6** and **8**, polymerisation occurs through the indolyl group. Previous studies on 5-substituted indoles has previously shown the monomers to couple at the 3 position under electrooxidative conditions and, with the 4 and 5 positions blocked by the fused benzene ring, further coupling is limited to the 2 position, which generally leads to discrete cyclic trimers [Waltman 84b, Mount 98, Jennings 97]. Therefore, for

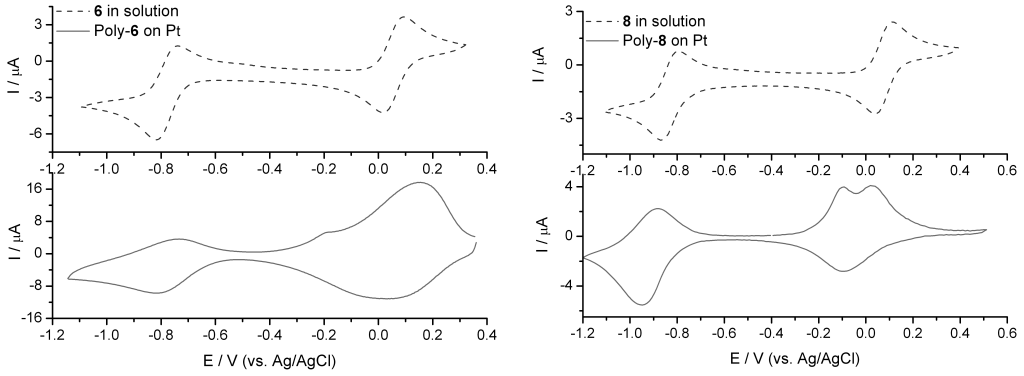

(a) **6** (b) **8**

Figure 5.12: Cyclic voltammetry of a polymer coated platinum electrode in monomer free electrolyte solution (bottom), compared to the redox behaviour of the monomer (top), measuring the current (I) response to a cycled potential (E): (a) poly-**6** coated platinum electrode; (b) a poly-**8** coated platinum electrode. Both polymers show clean redox behaviour, and minimal change in $E_{1/2}$ of both reduction processes, compared to their respective monomers, upon incorporation into a polymer film.

6 and **8**, extensive conjugation through the ligand is restricted by the structure of the indolyl group.

For thienyl substituted systems, [Kean 01] has previously shown poly-[Ni(b-2ted)$_2$], a tetra-2-thienyl substituted dithiolene, to preserve cleanly the redox processes of the monomer upon polymerisation, but with the reduction processes shifted to more positive potentials (E) by ∼0.1 and +0.15 V for the first and second reduction processes, respectively. Whilst it could be argued that this change in the redox levels was due to a change in junction potential[2] on moving to a monomer-free solution of a different electrolyte (see *e.g.* [Barrière 06]), it could also reflect the possibility of increased conjugation length, compared to poly-**6** or poly-**8**. The group also looked at a similar system, where one of the ligand thienyl groups was replaced with a phenyl group [Ni(p-2ted)$_2$ (p-2ted = 1-phenyl-(2-thienyl)-ethylene-1,2-dithiolate)]. In this case, the change in redox levels was not nearly so marked as for poly-[Ni(b-2ted)$_2$], despite making the same electrolyte switch.

It therefore seems that, for systems where the ligand polymer chain length is restricted to dimers (or trimers), as in **6**, **8** and Ni(p-2ted)$_2$, the metal centre does not propagate conjugation, and the redox processes of the monomer are preserved at the same energy levels in the polymer (see Fig. 5.13(a)). However, where greater conjugation

[2] A different potential difference (E) at the electrode interface between dissimilar solutions, which arises from differences in diffusion constants between different ions.

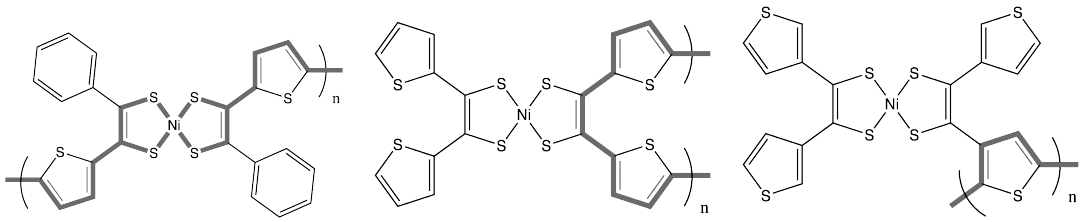

Figure 5.13: Possible conjugation modes for polymeric nickel dithiolenes: (a) conjugation through the metal centre; (b) conjugation through the ethylene backbone; (c) conjugation through the ligand.

is facilitated along the ligand ethylene backbone, the monomer redox processes are preserved, but with energies shifted to less negative potentials, consistent with a lowering of the LUMO orbital upon polymerisation (see Fig. 5.13(b)).

A third conjugation mode could perhaps be envisioned, whereby conjugation goes neither via the nickel centre, nor the ligand ethylene backbone, but instead via the pendent groups, such that the dithiolenes themselves become pendent to a polymer chain (see Fig. 5.13(c)). However, since the only example of such a conjugation mode in the literature was for a tetra-3-thienyl substituted nickel dithiolene [Ni(b-3ted)$_2$ [**10**], which showed rather poor redox actvity for the polymer film, thought to be due to poor counter-ion transport through highly cross-linked polymer chains [Anjos 08], it is not possible to assess the effect of such a conjugation mode on the redox processes. The only other example of such a conjugation mode is for heteroleptic dithiolenes (see section 4.2.5), however, the unsymmetrical contribution of the ligands to the frontier orbitals make these systems not directly comparable, as the electronic distribution is fundamentally different.

Therefore, it can be seen that, for dithiolenes with pendent polymerisable indolyl groups, the effect of the indole group is to restrict the chain length of the coupled ligands, and thus preserve the redox properties of the monomer units in a polymer film.

In order to further characterise the nature of the formed polymers, films were grown on a fluorine-doped tin oxide (FTO) coated glass electrodes and were investigated by UV/Vis/NIR spectroscopy (see Figs. 5.14(a) and 5.14(b)). For poly-**6**, the absorption spectrum of the formed film showed a broadening of the UV absorption. This is consistent with the linking of the indolyl groups upon polymerisation, as an increase in conjugation would push the indole based transitions to lower energy (see section

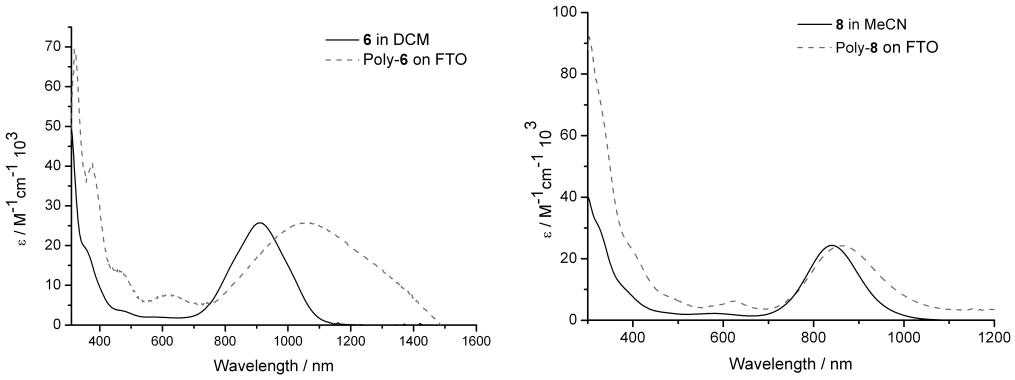

(a) **6** (b) **8**

Figure 5.14: UV/Vis/NIR spectra of polymer films grown by potential cycling on an FTO coated glass electrodes, where the absorption intensity is given as the molar extinction coefficient (ϵ), and the polymer absorptions are normalised relative to the NIR absorption of the monomer: (a) a poly-**6** coated electrode, compared to the solution spectra of **6** in DCM; (b) a poly-**8** coated electrode, compared to the solution spectra of **8** in MeCN.

3.3) (see Fig. 5.14(a)). The absorption spectrum also showed the NIR absorption to be shifted to to lower energies [1055 nm (red-shifted by 1,522 cm^{-1})]. This shift for poly-**6** might be due to a number of factors: longer conjugated chain length in the ligand might increase the delocalisation in the polymer backbone, thus reducing the HOMO/LUMO separation; increased planarity upon polymerisation might also raise the HOMO level, resulting in a reduced HOMO/LUMO gap. Although a broad chain length distribution might account for the broadening of the redox processes in poly-**6** (see Fig. 5.12(a), both these processes might perhaps be expected to change the the position of at least the first reduction process. A third possibility might be that, due to the increased film density (or thickness d), some dithiolene species might remain as the monoanion in the film, resulting in an absorption being observed for both neutral and monoanionic poly-**6**.

For poly-**8**, the absorption spectrum of the formed film, again, confirmed indole linkage by a broadening of the UV absorption, however, in comparison to poly-**6**, a negligible shift of the NIR absorption was observed. This was in keeping with the electrochemical results of poly-**8**, which showed negligible change in the redox processes upon polymerisation, and suggested only limited delocalisation of the dithiolene core into the polymer network.

In both cases, the shift in the NIR absorption was less than that observed by [Kean 01]

for the absorption spectra of poly-Ni(b-2ted)$_2$, which showed the NIR absorption to shift by 1896 cm^{-1} further into the NIR upon polymerisation. It also contrasts with the electropolymerised dithiolenes based on a fused thiophene backbone [Ni(b-2tted)$_2$, as studied by [Pozo-Gonzalo 02], who observed broad redox processes and a broad absorption across the whole Vis/NIR range, arising from the extensive poly-terthiophene component which, in some cases, masked the dithiolene characteristics altogether. Therefore, it seems that, by restricting the degree of polymerisation in the ligands for **6** and **8**, such that chain growth is necessarily through the metal centre, the redox behaviour, as well as the optical properties remain very similar to those of the monomer.

Electrochemical studies of copper dithiolenes

The electrochemistry of the stable copper dithiolene salts [**7**][TMA] and [**9**][TMA] was investigated in order to characterise their redox properties, and to compare them to the redox properties of the nickel dithiolenes **6** and **8** (*vide supra*).

The electrochemistry of both [**7**][TMA] and [**9**][TMA] was investigated in a 0.1 M $TBABF_4$ electrolyte solution of MeCN. Both complexes showed one electrochemically reversible redox process at $E^2{}_{1/2}$ = -0.59 V and -0.80 V for [**7**][TMA] and [**9**][TMA], respectively. This was assigned to the $[ML_2]^{2-/1-}$ redox couple, as zero current (I) was observed on scanning the potential from $E = 0$ towards this redox couple. This redox process was observed to be highly sensitive to the ligand environment, with the reduction to the dianion occurring at less negative potentials (E) for [**7**][TMA] than for [**9**][TMA]. By a similar arguement to the nickel dithiolenes (**6** and **8**), this is likely due to the more in-plane twist of the indolyl group in [**7**][TMA] being better able to stabilise the development of a second negative charge, through greater delocalisation, than for [**9**][TMA].

For [**7**][TMA], a second reduction process was observed ($E^1{}_{1/2}$ = -1.62), that was shown to be chemically reversible, though not electrochemically reversible, as the associated oxidation current (I_p^{ox}) was reduced at faster scan rates (v). This presumably corresponds to a $Cu^{2+/1+}$ transition, since the ligand environment is already fully reduced. This process is usually associated with a geometry change from (*pseudo*) square-planar to tetrahedral, and thus is not expected to be electrochemically reversible [Razuvaev 78]. The fact that an associated oxidation process is observed, at low over-potential, might suggest that the observed geometry change is slight, and that the solution geometry may not be rigorously square planar [Mahadevan 86]. On cooling

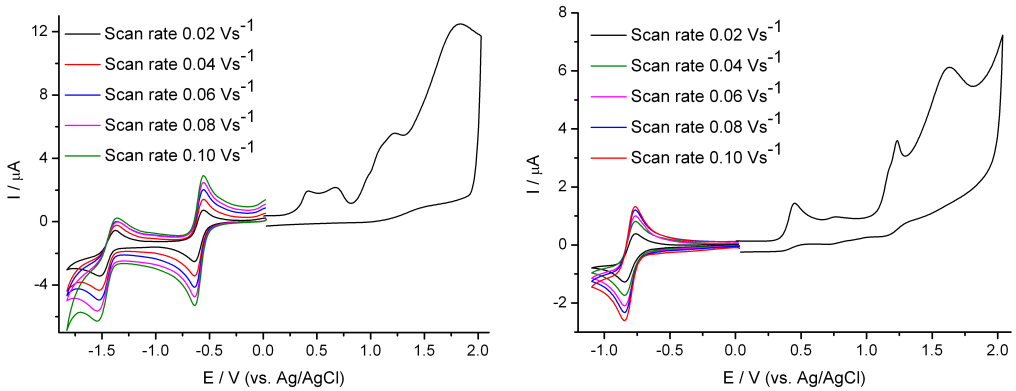

(a) **7** (b) **9**

Figure 5.15: Cyclic voltammetry in 0.1 M $TBABF_4$/MeCN, measuring the current (I) response to a cycled potential (E): (a) [**7**][TMA] shows two reduction processes, with the process at $E^1_{1/2}$ = -1.45 V shown to be irreversible, and the process $E^2_{1/2}$ = -0.59 V shown to be reversible. The complex also undergoes several irreversible oxidation processes at positive potentials (E); (b) [**9**][TMA] shows one reversible reduction process at $E^2_{1/2}$ = -0.8 V, as well as several irreversible oxidation processes at positive potentials.

Name	$E^1_{1/2}$ / V	$E^2_{1/2}$ / V	E^3_{ox} / V
[**7**][TMA]	-1.45[§]	-0.59	0.42*
[**9**][TMA]		-0.80	0.45*

Table 5.4: Redox potentials of [**7**][TMA] and [**9**][TMA] in 0.1 M $TBABF_4$/MeCN. All processes are reversible, unless otherwise stated; *irreversible, [§]quasi reversible.

the electrochemical cell to -40°C, the reduction process shifted outside the solvent range for electrochemical analysis (electrochemical window) and, as such, no associated oxidation process was observed, consistent with a slower geometry change at reduced temperatures.

On scanning to positive potentials, an irreversible process was observed at $E^3{}_{ox}$ = 0.42 V and 0.45 V for [**7**][TMA] and [**9**][TMA], respectively[3], corresponding to a $[ML_2]^{1-/0}$ transition, followed by several other irreversible oxidation processes. In MeCN, this first oxidation process led to the deposition of a film on the electrode surface for both [**7**][TMA] and [**9**][TMA]. For both complexes, by scanning the coated electrode back to negative potentials, past E^2, a greater reduction current (I_p^{red}) was observed, at the same potential for $E^2_{1/2}$, compared to an identical scan cycle for a clean electrode (see Figs. 5.16(a) and 5.16(b)). On scanning back to positive potentials, past E^2, no increase in the oxidation current (I_p^{ox}) was observed, compared to the clean electrode.

[3]Peak position is characterised by E_{ox}, and not by $E_{1/2}$ as it is an irreversible process.

This suggested that the deposited films were molecular in nature, due to their identical redox behaviour to the monomer in solution, and that the formed films were of neutral **7** and **9**. The formed neutral films could then be quantitatively reduced, and thus redissolved, by scanning past E^2.

In order to characterise the electrogenerated films of **7** and **9** further, films were grown on FTO coated glass electrodes, so that the electronic absorption properties could be investigated. Continuous films of **7** and **9** were grown under potentiostatic control by maintaining a potential E, and recording the charge (Q) passed with time ($E = 0.5$ V and 0.6 V for the electrodeposition of **7** and **9**, respectively) (see Fig. 5.16(c)). The deposited film of **7** was shown to be more conducting than **9** due to the passing of a greater current at the working electrode (since $Q = I \cdot t$), however both **7** and **9** showed extensive growth on the working electrode, resulting in the formation of continuous films that were gold in colour, for both complexes. The UV/Vis/NIR absorption spectra of both complexes showed pronounced differences to their respective monoanions, investigated in solution (see section 5.2.3 and Fig. 5.16(d)). Both complexes showed an intense absorption in the NIR range [$\sim$1270 nm (7,849 cm^{-1} for both **7** and **9**)], as well as several across the visible region of the spectra. This suggested that the formed films were indeed neutral molecular copper *bis*-dithiolenes, with the oxidation processes corresponding to the loss of an electron form the dithiolene ligand, facilitating an intense $\pi \rightarrow \pi^*$ transition, as observed for isoelectronic monoanionic nickel dithiolenes.

The films of neutral **7** and **9**, deposited from MeCN, were completely soluble in DMF, and thus their absorption properties could be investigated in solution. However, the UV/Vis spectra of the dissolved films were shown to be very different from those in the solid-state, losing all the absorption processes in the Vis and NIR regions of the spectra (see Fig. 5.16(d)). The observed spectra for the dissolved films were similar to that of **7** formed by chemical synthesis (see section 5.2.1), which was shown to decompose upon dissolution (see section 5.2.3). It therefore seemed that electrodeposition provided a route to thin films of neutral **7** and **9**, that were otherwise unobtainable by solution methods. However, due to the instability of both complexes in solution, and the films being of insufficient thickness to perform elemental analysis, a thorough molecular characterisation could not be performed.

In an effort to stabilise the neutral copper dithiolene complexes, in order to exploit their redox activity, solid-state polymerisation was attempted from the electrodeposited neutral films. This was performed by transferring freshly grown films (washed with MeCN) to a monomer free electrolyte solution, wherein they were subjected to

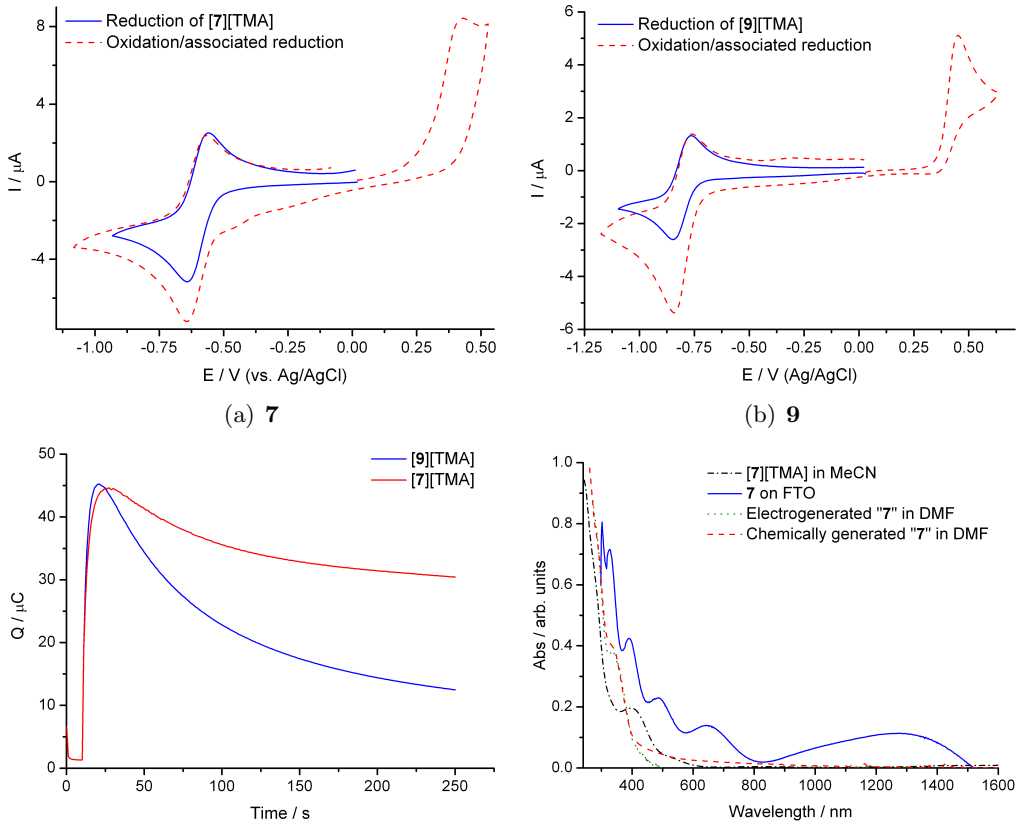

(a) **7** (b) **9**

(c) **7** and **9** (d) **7**

Figure 5.16: Studies on deposited films **7** and **9**: (a) associated reduction of the first oxidation process of [**7**][TMA]; (b) associated reduction of the first oxidation process of [**9**][TMA]. Both plots show that the films deposited (at $E = 0.5$ V and 0.6 V, for **7** and **9**, respectively) could be quantitatively reduced at the same potential as for their TMA salts, indicating that intact neutral **7** and **9** had been deposited on the electrodes. Scales depict current (I) in response to an applied voltage (E). (c) potentiostatic growth of neutral films of **7** and **9** on a platinum electrode, suggesting the deposition of a conducting film upon oxidation. Scale depicts charge (Q) passed at the working electrode with time; (d) UV/Vis/NIR spectroscopy of a electrodeposited film of neutral **7** on FTO, compared to the stable monoanionic complex [**7**][TMA] in MeCN, and showing the decomposition of neutral **7** upon dissolution. Quotation marks "x" denote that the species is no longer its identity upon dissolution, due to an unknown decomposition process.

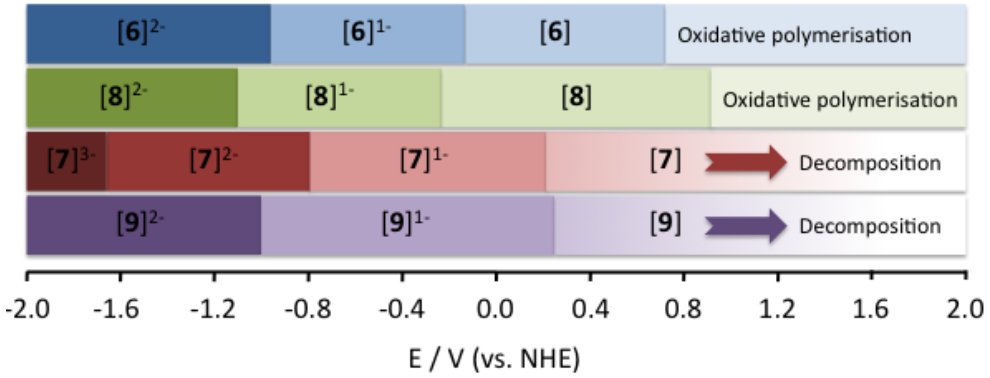

Figure 5.17: Pictorial representation of the redox behaviour of the studied metal *bis*-dithiolenes, standardised against a Normal Hydrogen Electrode (NHE) reference, showing differing behaviour of nickel and copper analogues upon reduction and oxidation.

increasingly positive potentials (E) to try to invoke polymerisation. No clear oxidation processes could be observed for the neutral films, and instead, a steady increase in the current (I) was recorded as the potential (E) was scanned. This did not correspond to polymerisation of the film, as the films were observed to decompose upon scanning, by their total disappearance from the electrode on applying a voltage (E) greater than E^3_{ox} for each film. This suggested that further oxidation of the neutral films resulted in the decomposition of the monomers, rather than indole linkage.

In summary, studying the electrochemical behaviour of both the nickel (**6** and **8**) and copper ([**7**][TMA] and [**9**][TMA]) dithiolenes showed them both to have rich redox behaviour. The redox processes are outlined in Fig. 5.17, and show multiple redox processes for both the nickel and copper dithiolenes. For the nickel systems, polymerisation could be achieved by oxidation of the neutral dithiolenes, which facilitated oxidative coupling of the pendent indolyl groups, resulting in the deposition of redox active polymer films. For the copper systems, oxidation of the stable [TMA] monoanionic salts in MeCN resulted in the deposition of neutral molecular films, that are otherwise unobtainable by conventional solution methods.

5.3 Conclusion

In conclusion, two new dithiolene ligand systems have been synthesised, and their incorporation into complexes of nickel and copper has been demonstrated. The ligands impose distinct characteristics upon the complexes, both in terms of their physical properties, but also their electronic properties. The reduced steric bulk of a hydrogen

atom, compared to a butyl group on the dithiolene ring allows a more in-plane twist of the pendent aromatic. This, in turn, raises the energy of the dithiolene ligand bonding orbital, allowing for more facile reduction.

The choice of metal centre also has a large effect on the resulting complex. Whilst nickel dithiolenes could be isolated in both the monoreduced and neutral form as air stable materials, the copper complexes could only be isolated, by chemical means in their monoreduced state. This affects the functionality of the complexes formed, as both nickel complexes can be incorporatied into polymeric films, with redox and optical properties similar to that of the monomer. Polymerisation of the copper complexes could not be achieved, however, oxidation of their anionic salts was shown to lead to the deposition of neutral copper *bis*-dithiolenes, stablised in the solid-state.

For the nickel systems, their behaviour is in keeping with other polymerisable dithiolenes, however the extent of conjugation is restricted in these complexes by the nature of the ligand. Such systems would be useful in the construction of polychromatic NIR laser switching dyes, as the resultant film might be reversibly switched between three absorption states, within the NIR region, by sequential filling of the LUMO orbital. For the copper systems, this behaviour represents the first reported stable thin-films of neutral copper *bis*-dithiolenes, and might be interest for magnetoshielding or magnetoinductive application.

Future work might look at radical substitution of unfunctionalised terminal on the dithiolene ring in **6**. By adjusting the electronic contribution of the free R group substituent, it would be possible to tune the electronic properties of the complex, such as the NIR absorption, whilst adjusting the steric contribution of the alkyl substituent could tune the physical properties of the complex, such as its packing structure or crystallinity.

5.4 Experimental

1-Methylindole-5-carboxaldehyde To an oven dried microwave vial (25 ml), equipped with a Teflon-coated stirrer bar, was added freshly recrystallised 5-bromo-1-methylindole (3.15 g, 15.0 mmol) and Mg turnings (401 mg, 16.5 mmol) and the flask flushed with nitrogen before being sealed using an aluminium open-top seal with a polytetrafluoroethylene (PTFE) faced septum. Dry THF (15 ml) was charged via syringe and the reaction mixture microwave-irradiated for 30 mins at 120°C, whereupon the flask was cooled to 0°C, and dry DMF (1.16 ml, 15.0 mmol) was added via syringe.

The reaction mixture was stirred for 30 mins at 0°C before being warmed to room temperature. The reaction mixture was poured into a saturated solution of NH_4Cl (50 ml), and extracted with Et_2O (4 x 20 ml). The organics were combined and dried over $MgSO_4$ and solvent removed under reduced pressure. The product was purified by recrystallisation from hexane. (2.32 g, 97 %). δ_H (250 MHz; $CDCl_3$) 3.84 (s, 3H, -NMe), 6.65 (dd, 1H, J = 3.1, 0.8 Hz, H_b), 7.15 (d, 1H, J = 3.1 Hz, H_a), 7.40 (d, 1H, J = 8.5 Hz, H_e) 7.80 (dd, 1H, J = 8.5, 1.5 Hz, H_d), 8.15 (dd, 1H, J = 1.5, 0.8 Hz, H_c), 10.03 (s, 1H, C(O)H).

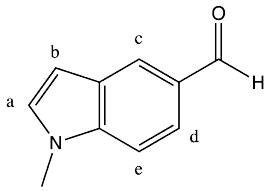

5-Ethyny-1-methylindole To a stirred suspension of bromomethyltriphenylphosphonium bromide (6.07 g, 13.9 mmol) in dry THF (40 ml) at -78°C was added portionwise potassium tert-butoxide (3.12 g, 27.8 mmol). The reaction mixture was stirred at -78°C for 30 mins, during which time the yellow ylid formed. A solution of 1-methylindole-5-carboxldehyde (2.21g, 13.9 mmol) was added in THF (10 ml), and the reaction was stirred for a further 30 mins at -78°C before being warmed to room temperature overnight. After 12 hours, the reaction was shown to be complete by the complete consumption of the aldehyde, observed by thin layer chromatography (TLC) and the reaction quenched by addition of NH_4Cl solution (100 ml). The product was extracted with EtOAc (4 x 100 ml) and the organics washed with brine and dried over $MgSO_4$. The crude product was purified by flash chromatography (Hex:EtOAc, 6:1), yielding the target material as a pale yellow oil (1.22 g, 57 %). δ_H (250 MHz; $CDCl_3$) 3.00 (s, 1H, CCH), 3.76 (s, 3H, -NMe), 6.47 (dd, 1H, J = 3.1, 0.8 Hz, H_b), 7.06 (d, 1H, J = 3.1 Hz, H_a), 7.24 (d, 1H, J = 8.5 Hz, H_e) 7.35 (dd, 1H, J = 8.5, 1.5 Hz, H_d), 7.81 (dd, 1H, J = 1.5, 0.8 Hz, H_c).

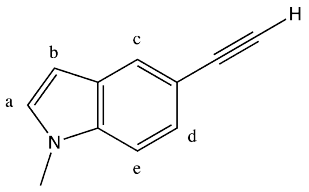

4-(1-methyl-5-indol-5-yl)-[1,3]dithiol-2-one (4) To a stirred solution of 5-ethynyl-1-methylindole (1.16 g, 7.47 mmol) in benzene (75 ml) was added AIBN (551 mg,

3.36 mmol) and diisopropylxanthogen disulfide (2.22 g, 8.22 mmol), and the reaction mixture stirred at reflux under a flow of nitrogen for 24 hours. The solvent was removed under reduced pressure and the crude product purified by trituration in warm methanol (6 hours), yielding pure product after filtration (1.26 g, 68 %). δ_H (360 MHz; $CDCl_3$) 3.82 (s, 3H, -NMe), 6.52 (d, 1H, J = 3.1 Hz, H_b), 6.73 (s, 1H, C(S)H), 7.11 (d, 1H, J = 3.1 Hz, H_a), 7.30 (dd, 1H, J = 8.5, 1.5 Hz, H_d) 7.34 (d, 1H, J = 8.5 Hz, H_e), 7.67 (bd, 1H, H_c).

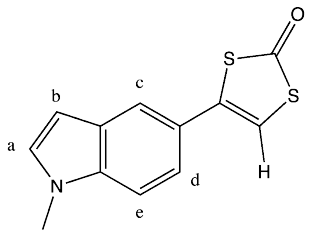

[Ni(mi-5edt)$_2$][TBA] ([6][TBA]) To a stirred solution of freshly cut sodium (117 mg, 5.10 mmol) in dry degassed MeOH (35 ml) under nitrogen was added **4** (600 mg, 2.43 mmol), and the solution stirred with gentle warming for 1 hour until complete dissolution. [TBA]Br was added and allowed to dissolve, whereafter a solution of $NiCl_2{\cdot}6H_2O$ (289 mg, 1.22 mmol) in MeOH (25 ml) was added dropwise over 45 mins. The flask was opened to air and stirring was continued for one hour before cooling in the freezer for one hour. The crude product was filtered, and washed with cold MeOH and purified by recrystallisation from DCM/EtOH, affording the title compound as a brown precipitate (480 mg, 53 %). Anal calcd for $C_{38}H_{54}N_3S_4Ni$: C, 61.69; H, 7.36; N, 5.68; S, 17.34; found C, 61.73; H, 7.43; N, 5.57; S, 17.45.

[Ni(mi-5edt)$_2$] (6)

Route 1 Complex [**6**][TBA] (300 mg, 0.405 mmol) was dissolved in MeCN (20 ml) and I_2 (206 mg, 0.810 mmol) was added in MeCN (10 ml). A green precipitate formed immediately, and was filtered and washed with EtOH. The crude product was recrystallised from DCM/EtOH to yield **6** as a dark green precipitate (121 mg, 60 %). δ_H (500 MHz; $CDCl_3$) 3.83 (s, 6H, -NMe), 6.60 (d, 2H, J = 3.1 Hz, H_b), 7.11 (d, 2H, J = 3.1 Hz, H_a), 7.37 (d, 2H, J = 8.7 Hz, H_e) 7.90 (d, 2H, J = 8.7, 1.7 Hz, H_d), 8.33 (d, 2H, J = 1.7 Hz, H_c), 9.75 (s, 2H, C(S)H).

Route 2 To a stirred solution of **4** (594 mg, 2.40 mmol) in THF (24 ml) was added [TMA][OH]$\cdot 5H_2O$ (958 mg, 5.29 mmol) in MeOH (2 ml). After 5 mins, $NiCl_2{\cdot}6H_2O$

(286 mg, 0.515 mmol) in MeOH (2 ml) was added and the reaction mixture stirred at room temperature overnight. [**6**][TMA] was filtered off as a brown precipitate. [**6**][TMA] was dissolved in MeCN (40 ml), and I_2 (974 mg, 3.84 mmol) was added in MeCN (20 ml). A green precipitate formed immediately, and was filtered and washed with EtOH. Recrystallisation in DCM/Et_2O yielded pure **8** as a dark green precipitate (736 mg, 63 %). δ_H (500 MHz; $CDCl_3$) 3.83 (s, 6H, -NMe), 6.60 (d, 2H, J = 3.1 Hz, H_b), 7.11 (d, 2H, J = 3.1 Hz, H_a), 7.37 (d, 2H, J = 8.7 Hz, H_e) 7.90 (d, 2H, J = 8.7, 1.7 Hz, H_d), 8.33 (d, 2H, J = 1.7 Hz, H_c), 9.75 (s, 2H, C(S)H). Anal calcd for $C_{22}H_{18}N_2S_4Ni$: C, 53.13; H, 3.65; N, 5.63; found C, 53.06; H, 3.53; N, 5.56, λ_{max} = 418 nm ($\epsilon = 25.6\times10^3$ $M^{-1}cm^{-1}$).

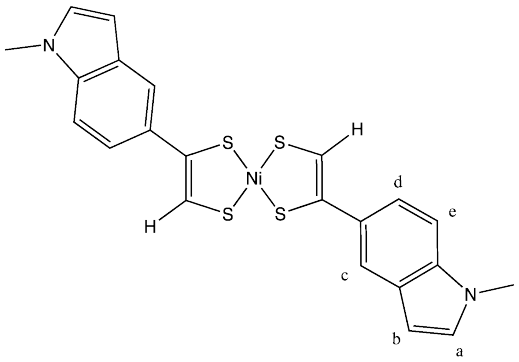

[Cu(mi-5edt)$_2$][TMA] ([7][TMA]) To a stirred solution of **4** (297 mg, 1.20 mmol) in THF (10 ml) was added [TMA][OH]·$5H_2O$ (478 mg, 2.64 mmol) in MeOH (2 ml). After 5 mins, $CuCl_2$·$2H_2O$ (102 mg, 60 mmol) in MeOH (2 ml) was added and the reaction mixture stirred at room temperature overnight. Pure [**7**][TMA] was filtered off as a dark brown precipitate, and washed with EtOH (292 mg, 42 %). δ_H (500 MHz; DMSO) 3.08 (s, 12H, TMA), 3.77 (s, 6H, -NMe), 6.33 (s, 2H, C(S)H), 6.39 (dd, 2H, J = 3.0, 0.5 Hz, H_b), 7.27 (d, 2H, J = 3.0 Hz, H_a), 7.31 (d, 2H, J = 8.7 Hz, H_e) 7.44 (dd, 2H, J = 8.7, 1.8 Hz, H_d), 7.70 (dd, 2H, J = 1.8, 0.5 Hz, H_e); anal calcd for $C_{26}H_{30}N_3S_4Cu$: C, 54.18; H, 5.25; N, 7.29; found C, 54.32; H, 5.37; N, 7.15; λ_{max} = 393 nm ($\epsilon = 11.2\times10^3$ $M^{-1}cm^{-1}$).

[Cu(mi-5edt)$_2$] (7) To a stirred solution of freshly cut sodium (95 mg, 4.12 mmol) in dry degassed MeOH (50 ml) under nitrogen was added **4** (509 mg, 2.06 mmol), and the solution stirred with gentle warming for 1 hour until complete dissolution. A solution of $CuCl_2$·$2H_2O$ (175 mg, 1.03 mmol) in MeOH (25 ml) was added dropwise over 10 mins. A pale brown precipitate formed immediately and was stirred further for 1 hour in air, whereupon pure **7** could be isolated by filtration and washing with

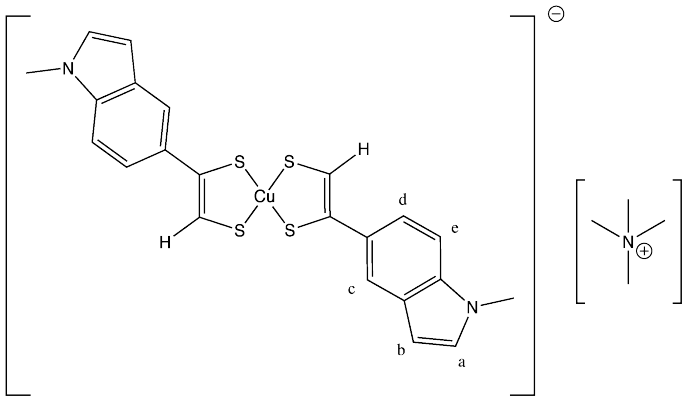

MeOH, affording the title compond as a pale brown precipitate (145 mg, 28 %). Anal calcd for $C_{22}H_{18}N_2S_4Cu$: C, 52.62; H, 3.61; N, 5.58; S, 25.54; found C, 52.69; H, 3.67; N, 5.63; S, 25.47.

5-Hex-1-yny-1-methylindole To a stirred, degassed solution of *N*-methyl-5-iodo-indole (3.30 g, 13.6 mmol) in dry DMF (13 ml) and freshly distilled NEt_3 (8.25 ml) under a nitrogen atmosphere was added CuI (64.6 mg, 0.340 mmol) and $Pd(PPh_3)_2Cl_2$ (477 mg, 0.679 mmol). Stirring was continued for 5 mins and 1-hexyne (1.87 ml, 16.3 mmol) was added and the reaction mixture was stirred under a nitrogen atmosphere at room temperature for 30 hours. The reaction mixture was diluted with EtOAc (200 ml), filtered through celite and the organics washed with brine (2 x 200 ml), deionised H_2O (2 x 200 ml) and brine (200 ml). The organics were dried over $MgSO_4$ and the crude product purified by flash chromatography (DCM:hexane, 1:1) yielding the title compound as a yellow oil (1.78 g, 66 %). δ_H (250 MHz; $CDCl_3$) 0.98 (t, 3H, J = 7.0 Hz, -CH_3) 1.44-1.70 (m, 4H, -CH_2CH_2-), 2.45 (t, 2H, J = 6.7 Hz, -$CCCH_2$-), 3.77 (s, 3H, -NMe), 6.45 (dd, 1H, J = 3.1, 0.8 Hz, H_b), 7.04 (d, 1H, J = 3.1 Hz, H_a), 7.22 (d, 1H, J = 8.5 Hz, H_d) 7.28 (dd, 1H, J = 8.5, 1.4 Hz, H_e), 7.72 (dd, 1H, J = 1.4, 0.8 Hz, H_c).

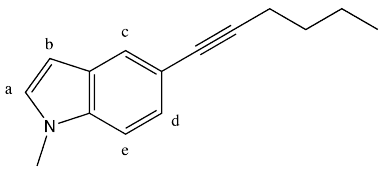

4-Butyl-5-(1-methyl-5-indol-5-yl)-[1,3]dithiol-2-one (5) To a stirred solution of 5-Hex-1-yny-1-methylindole (1.78 g, 9.03 mmol) in benzene (85 ml) was added AIBN (635 mg, 4.06 mmol) and diisopropylxanthogen disulfide (2.51 g, 9.23 mmol) and the reaction mixture stirred at reflux under a flow of nitrogen for 50 hours.

The solvent was removed under reduced pressure and the crude product purified by flash chromatography (hexane:toluene, 1:1) followed by Kugelrohr distillation (64°C at 2.0×10^{-2} bar) yielding the title compound as a thick yellow oil (1.37g, 50 %). δ_H (250 MHz; $CDCl_3$) 0.85 (t, 3H, J = 7.3 Hz, -CH_3) 1.30 (m, 2H, -CH_2CH_3), 1.54 (m, 2H, -$CH_2CH_2CH_3$) 2.61 (t, 2H, J = 7.5 Hz, $CSCH_2$-), 3.83 (s, 3H, -NMe), 6.52 (dd, 1H, J = 3.1, 0.7 Hz, H_b), 7.13 (d, 1H, J = 3.1 Hz, H_a), 7.19 (dd, 1H, J = 8.5, 1.7 Hz, H_d) 7.35 (d, 1H, J = 8.5 Hz, H_e), 7.60 (dd, 1H, J = 1.7, 0.7 Hz, H_c); HRMS (ESI) (m/z) calcd for $C_{16}H_{17}NOS_2$ + H^+: 304.0830; found 304.08353.

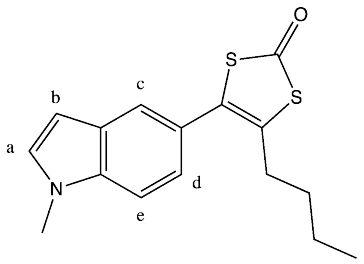

[Ni(mi-5hdt)$_2$][TBA] ([8][TBA]) A solution of freshly cut sodium (68.5 mg, 2.98 mmol) in dry degassed MeOH (20 ml) was added under nitrogen to **5** (430 mg, 1.42 mmol), and the solution stirred for 1 hour until homogeneous. [TBA]Br (914 mg, 2.84 mmol) was added and allowed to dissolve, whereafter a solution of $NiCl_2{\cdot}6H_2O$ (168 mg, 0.709 mmol) in MeOH (10 ml) was added dropwise over 45 mins. The flask was opened to air and stirring was continued for one hour before cooling in the freezer for one hour. The crude product was filtered and washed with cold MeOH, and purified by recrystallisation from DCM/EtOH, affording the title compond as a brown precipitate (297 mg, 49 %). Anal calcd for $C_{46}H_{70}N_3S_4Ni$: C, 64.84; H, 8.28; N, 4.93; found C, 64.96; H, 8.15; N, 4.84.

[Ni(mi-5hdt)$_2$] (8) To a stirred solution of **5** (300 mg, 0.990 mmol) in THF (10 ml) was added [TMA][OH]$\cdot5H_2O$ (394 mg, 2.18 mmol) in MeOH (1 ml). After 5 mins, $NiCl_2{\cdot}6H_2O$ (122 mg, 0.515 mmol) in MeOH (1 ml) was added and the reaction mixture stirred at room temperature overnight. [**1**][TMA] was filtered off as a bronze precipitate. [**8**][TMA] was dissolved in DCM and passed through a silica plug, whereupon the solution turned green. Recrystallisation in DCM/Et_2O yielded pure **8** as a dark green precipitate (235 mg, 78%). δ_H (250 MHz; $CDCl_3$) 0.84 (t, 6H, J = 7.2 Hz, -CH_3) 1.22-1.38 (m, 4H, -CH_2CH_3), 1.76-1.90 (m, 4H, -$CH_2CH_2CH_3$) 2.93 (t, 4H, J = 7.7 Hz, $CSCH_2$), 3.85 (s, 6H, -NMe), 6.57 (d, 2H, J = 3.2 Hz, H_b), 7.14 (d, 2H, J = 3.2 Hz, H_a), 7.35 (dd, 2H, J = 8.5, 1.5 Hz, H_d) 7.39 (d, 2H, J = 8.5 Hz, H_e), 7.77 (d, 2H, J =

1.5 Hz, H_c); anal calcd for $C_{30}H_{34}N_2S_4Ni$: C, 59.11; H, 5.62; N, 4.60; S, 21.04; found C, 59.62; H, 5.15; N, 4.54; S, 20.98; λ_{max} = 841 nm ($\epsilon = 23.5\times10^3$ $M^{-1}cm^{-1}$).

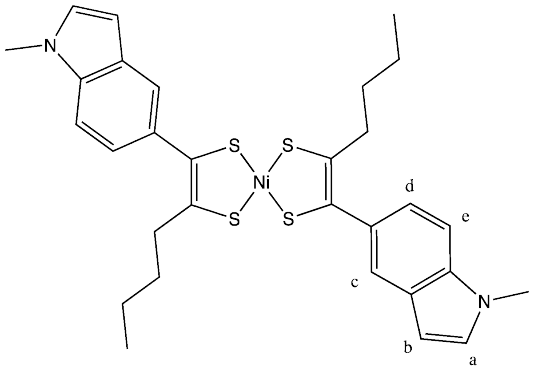

[Cu(mi-5hdt)$_2$][TMA] ([9][TMA]) To a stirred solution of **5** (247 mg, 0.815 mmol) in THF (9 ml) was added [TMA][OH]·$5H_2O$ (324 mg, 1.79 mmol) in MeOH (1 ml). After 5 mins, $CuCl_2$·$2H_2O$ (72 mg, 0.407 mmol) in MeOH (1 ml) was added and the reaction mixture stirred at room temperature overnight. Pure [**7**][TMA] was filtered off as a bronze precipitate and washed with EtOH (292 mg, 46 %). δ_H (500 MHz; DMSO) 0.76 (t, 6H, J = 7.4 Hz, -CH_3) 1.18 (m, 4H, -CH_2CH_3), 1.48 (m, 4H, -$CH_2CH_2CH_3$) 2.25 (t, 4H, J = 7.6 Hz, $CSCH_2$), 3.09 (s, 12H, TMA), 3.77 (s, 6H, -NMe), 6.40 (d, 2H, J = 3.0 Hz, H_b), 7.09 (dd, 2H, J = 8.4, 1.1 Hz, H_d), 7.29 (d, 2H, J = 3.0 Hz, H_a) 7.33 (d, 2H, J = 8.4 Hz, H_e), 7.44 (d, 2H, J = 1.1 Hz, H_c); anal calcd for $C_{34}H_{46}N_3S_4Cu$: C, 59.31; H, 6.73; N, 6.10; found C, 59.22; H, 6.63; N, 5.98; λ_{max} = 418 nm ($\epsilon = 26.2\times10^3$ $M^{-1}cm^{-1}$).

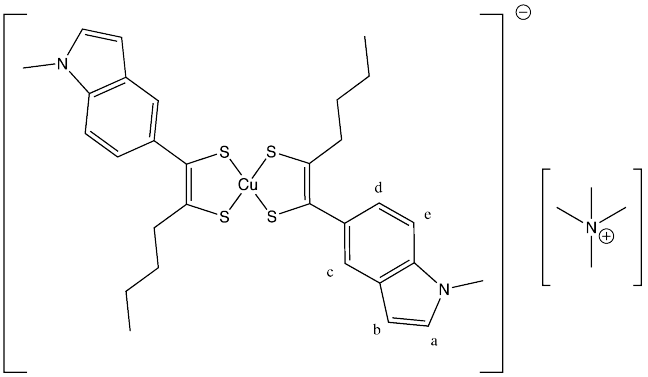

5.4.1 X-ray crystallography

4-(1-methyl-5-indol-5yl)-[1,3]dithiol-2-one (4) Colourless shard (dimensions 0.17 × 0.14 × 0.06 mm^3) $C_{12}H_9NOS_2$, T = 100 K, space group $P2_1/c$, M_r = 247.32,

monoclinic, a = 6.6997(3) Å, b = 7.3685(4) Å, c = 22.4087(12) Å, β = 93.852(5)°, V = 1103.74(10) Å^3, D_c = 1.488 Mg m^{-3}, μ = 4.168 mm^{-1}, no. of reflections for cell = 1937, Θ_{max} = 72.6537°, Z = 4, 3096 reflections collected, unique [R_{int}] = 2124 [0.0350], T_{min}/T_{max} = 0.3299/0.7900, parameters 146, R_1 [$F > 4\sigma(F)$] = 0.0674, wR = 0.1751.

[Ni(mi-5hdt)$_2$] (8) Dark green plate (dimensions 0.25 × 0.19 × 0.06 mm^3) $C_{30}H_{34}N_2Ni_1S_4$, T = 100 K, space group P2$_1$/c, M$_r$ = 609.59, monoclinic, a = 4.31010(13) Å, b = 15.6910(4) Å, c = 21.4795(7) Å, β = 91.526(3)°, V = 1452.14(8) Å^3, D_c = 1.394 Mg m^{-3}, μ = 0.978 mm^{-1}, no. of reflections for cell = 5598, Θ_{max} = 28.478°, Z = 2, 8971 reflections collected, unique [R_{int}] = 3166 [0.046], T_{min}/T_{max} = 0.62/0.94, parameters 169, R_1 [$F > 4\sigma(F)$] = 0.0458, wR = 0.1299, $\Delta\rho_{max}/e$ Å^{-3} = 0.67, $\Delta\rho_{min}/e$ Å^{-3} = -1.01.

Chapter 6

Devices from Ni(mi-5hdt)$_2$

6.1 Introduction

Two novel dithiolene ligand systems, with pendent indolyl groups, were synthesised in the previous chapter, and shown to form complexes of copper and nickel (see section 5.2.1). Metal dithiolenes, especially those of copper and nickel, have been the subject of intense interest and investigation within the field of materials chemistry. For the nickel dithiolenes, far the most advanced application is related to their optical properties - an intense absorption in the near IR region coupled with high thermal and photochemical stability. This has led to their investigation and commercialisation as passive Q-switch dyes for NIR lasers [such as Nd:YAG (YAG = yttrium aluminum garnet) which emits at 1064 nm] [Mueller-Westerhoff 91]. However, more recently, their conductive properties have made such advances as to warrant a sustained and systematic investigation into the potential of these materials as highly tuneable electronic systems. Whilst several instances of superconductivity have been reported [Cassoux 99], the critical temperature for such behaviour is so low as to be prohibitive to any widespread practical application, although they remain important systems for the understanding of charge transport in organic superconductors. Clear evidence of metallic behaviour has seen dithiolenes being applied as electrodes in the fabrication of all-organic flexible transistor arrays [Nunes 07], whilst recent reports of n-type and ambipolar semiconductive behaviour, with mobilities (μ) of the order 10^{-3} cm^{2}V^{-1}s^{-1}, have already prompted some groups to systematicaly test the effect of electron density and sterics on the conducting properties of the nickel dithiolenes [Cho 07, Wada 07].

In this chapter, several devices are investigated, incorporating one of the nickel dithiolenes synthesised in chapter 5, namely Ni(mi-5hdt)$_2$ (**8**). The devices investigated were electrochromic devices (ECDs), based on poly-**8** (see section 6.2), chosen for study due to the clean redox and optical properties of the polymer, as observed in section 5.2.5; field-effect transistors (FETs) based on **8** (see section 6.3), prompted by the high solubility of the complex, as well as a close interplanar distance in the solid-state

(see section 5.2.2); bulk-heterojunction photovoltaic (PV) devices, based on **8** (see section 6.4), due to its low lying LUMO orbital favoring efficient electron transport, and complementary absorption to conventional photovoltaic hole transport materials (see section 5.2.3).

6.2 Electrochromic Devices (ECDs)

In essence, electrochromism is the ability of a material to change colour under an applied potential (E) sufficient to invoke a change in redox state. For their incorporation into functional devices, some fundamental requirements need to be met. The devices must have good long-term stability (both under switching, and at rest), they must display fast redox switching, with a large change in optical transmittance, and have high colouration efficiency [Yen 09]. Historically, optical changes in the visible region of the electromagnetic spectra (400-800 nm) were targeted for the development of tunable windows and electrochromic displays. However, recently the attention has shifted, or at least broadened to investigate systems active in the NIR region (800-2000 nm) for application in environmental control (*e.g.* heat loss from buildings) and optical signal transmission. The NIR region is of particular significance to silica fibre-optic communication networks as silica is most transparent in this region - the 'telecommunications window' - with signals routinely being transmitted in the 1300-1550 nm region [Ward 05]. A device that could reliably control the optical signal strength of such transmissions would act as a variable optical attenuator (VOA), and is an integral component to such technologies to compensate for signal fluctuation caused by other components in the circuitry.

A typical device design comprises an electrochromic layer deposited on a transparent electrode, an electrolyte, and a transparent counter electrode. However, more commonly, two active layers are deposited on opposing electrodes with complementary absorptions (anodic and cathodic colouring) to enhance the optical response of the device. The electrolyte performs two functions in the device: it is an ionic conductor, but also a source or sink for ions to permeate the film during electron transfer [Zheng 09]. Advances have been made in an effort to replace the conventional liquid electrolyte with less volatile systems, such as ionic liquids, and solid-state systems [Mizumo 04,Ohno 01]. Such advances are key to extending device lifetime, by negating solvent loss through evaporation, and limiting the effect of solvent-assisted degradation of the devices. The electrochromic layer has been the subject of sustained interest over many years [Beaujuge 10], with the majority of studies looking at polymeric systems, due to the enhanced stability of polymers to dissolution upon redox cycling. These polymers can

either be chemically synthesised, with thin films formed by spin coating [Zheng 09], or electrochemically grown directly onto the electrode [Gunbas 08].

The availability of *n*-type organic semiconductors for cathodic coloring, especially those displaying a pronounced NIR optical response, is limited, in part, due to the reduced stability of their charged states [Wang 05]. Therefore, there is a great deal of interest for novel, cathodically NIR-colouring, stable organic polymers, either for single component ECDs, or as a complementary colourant to existing *p*-type electrochromic materials.

Polymerisable nickel dithiolenes may be of interest as the electrochromic layer in *n*-type ECDs. Nickel dithiolenes have been shown to display several reversible redox processes, corresponding to the sequential filling of a low lying LUMO orbital, and an intense absorption in the NIR region corresponding to a HOMO→LUMO transition, the nature of which is changed upon reduction [Mueller-Westerhoff 91]. These properties can be maintained upon polymerisation (see section 5.2.5) [Kean 01], thus forming an electrochromic polymer, optically active in the NIR range, with *n*-type behaviour. For such a system to be useful, fast switching and good stability are prerequisites [Wu 07], and therefore an experimental setup was designed to test, not only the optical response to various applied potentials (E), but also the speed and stability of the optical response to these potentials (E).

6.2.1 Results and discussion

In the first instance, a simple three electrode electrochemical setup was designed, with the electrochemical cell comprising a quartz cuvette, with a poly-**8** coated FTO coated glass working electrode, a platinum wire counter electrode, and a Ag/AgCl reference electrode, in an acetonitrite solution of $TBABF_4$ as electrolyte. The solvent was dried and the electrolyte solution was degassed before use, though no attempt was made to exclude oxygen during the experiment. The electrochemical cell was placed in the cavity of a UV/Vis/NIR spectrometer to enable the measurement of the absorption spectra of poly-**8**, under applied potentials (E).

The absorption spectrum was recorded at potentials (E) sufficient to induce changes in the redox state, as measured in section 5.2.5, and showed that the NIR absorption profile could be modified under different applied potentials (E) (see Fig. 6.1). At an applied potential (E) of -0.4 V, the polymer was reduced, resulting in a decrease in the intensity, and a red-shift (1,139 cm^{-1}), of the NIR absorption. At an applied potential (E) of -1.0 V, the absorption in the whole NIR range was switched off

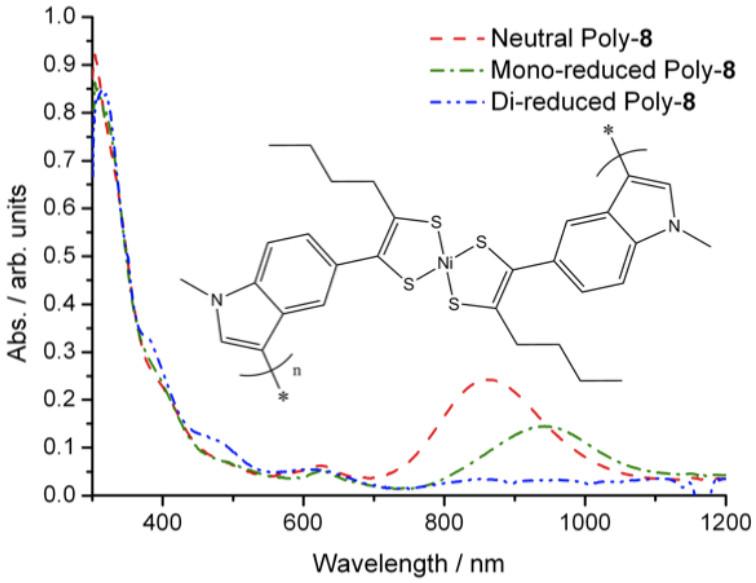

Figure 6.1: UV/Vis/NIR spectra of poly-**8** in the neutral, mono- and di-reduced state, under applied potentials (E) of +0.3 V, -0.4 V and -1.0 V, respectively.

completely. As discussed above, the NIR absorption corresponds to a HOMO→LUMO transition based on the dithiolene ligands, and sequential reduction of the dithiolene corresponds to the sequential filling of the LUMO orbital, thus affecting the NIR transition. Addition of one electron to the LUMO orbital perturbs the transitions across a reduced HOMO/LUMO gap (as observed by a shift to lower energies for the NIR transition), whilst a complete filling of the LUMO orbital prohibits such a transition altogether. As can be seen in Fig. 6.1, at a wavelength (λ) of $\sim$ 810 nm, the absorption could be switched off by an applied potential ($|E|$) of greater than -0.4 V, whilst at $\lambda \approx$ 890 nm, the absorption could be effectively halved at an applied potential of E = -0.4 V, or switched off at E = -1.0 V. As such, a three way optical switch, effective in the NIR region, has been developed.

The clean, reversible nature of the redox processes of poly-**8**, as shown in Fig. 6.2, suggested that these absorption states might be reversibly switched under various applied potentials. Dynamic optical attenuation was tested by a square wave potential step experiment, by switching the potential between 0.3 V and -0.4 V. The electrochemical measurements were coupled with UV/Vis/NIR spectroscopy, measuring the change in absorbance at 860 nm in response to applied potential (E) (see Fig. 6.3 (above)). This wavelength (λ) was chosen to allow a three state switch to be subsequently investigated. For the first reduction process, the absorption intensity was modulated, corresponding to a switch between the neutral and mono-reduced state.

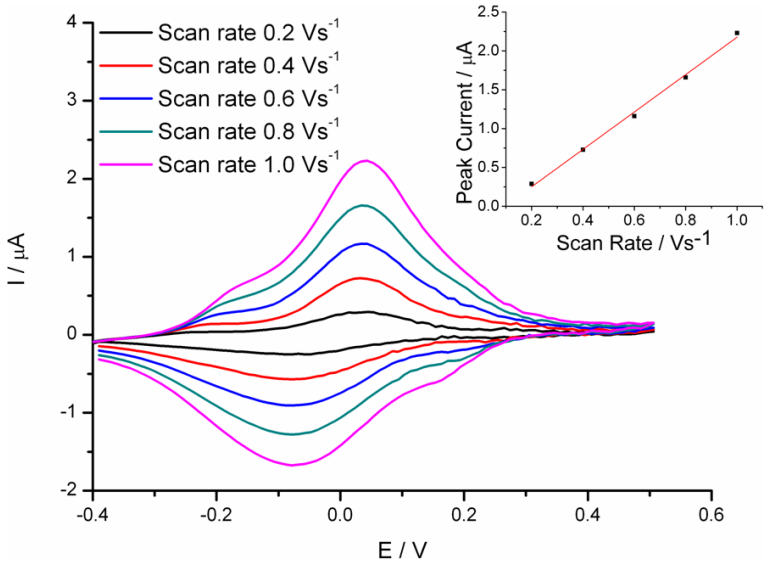

Figure 6.2: Cyclic voltammetry of a poly-**8** coated platinum electrode in monomer free electrolyte solution, measuring the current (I) in response to applied potential (E), and showing reversibility of the first reduction process, confirmed by a plot of peak current (I_p) vs. scan rate (v) (inset).

The switching of the absorption intensity showed relatively minor degradation over 100 cycles [$\sim$ 20 %, as measured by the difference in peak current (I_p) upon switching, see Fig. 6.3 (below)], and with no lengthening in switching speed on cycling. Switching was achieved in under 1 second for all switching transitions. On switching between the mono- and dianionic state (-0.4 V and -1.0 V), the absorption intensity changed more slowly, corresponding to a slower switching speed, and the reversibility of the process diminished after only a few cycles (not shown). This was consistent with the redox behaviour of poly-**8** observed in section 5.2.5, which showed electrochemical reversibility for the first reduction process, but a loss of reversibility for the second process at faster scan rates (v). This was attributed to the steric difficulty of incorporating two bulky TBA^+ counterion into the film.

In an effort to improve the reversibility of the second process, and to improve the device lifetime, a closed system was designed, using an electrolyte with a smaller cation ($TEAPF_6$), to facilitate ion transfer through the film, required for charge balancing of the reduction processes. The device was designed as described in Fig. 6.4, and comprised of a FTO glass cathode with two holes drilled in opposite corners, to allow electrolyte addition to the cell (*vide infra*) [see Fig. 6.4, step (i)]. This was fixed opposed to a poly-**8** coated FTO glass anode [step (ii)], by thermally sealing a Surlyn spacer [step (iii)] (sealed at 100°C for 10 seconds). An electrolyte solution of $TEAPF_6$ in MeCN

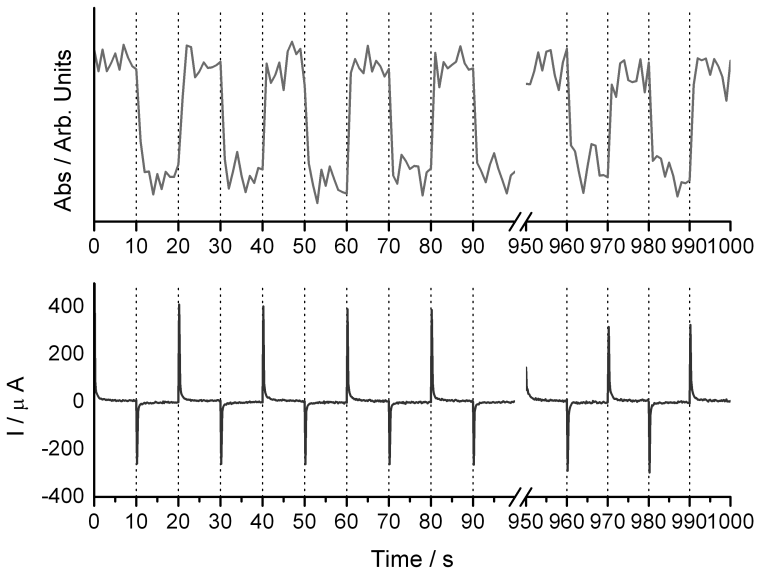

Figure 6.3: Switching of the absorption intensity (above) of poly-**8** at 860 nm, under an oscillating potential (E) of 0.3 V and -0.4 V for holding time intervals of 10 seconds; (below) the current (I) passed at the working electrode, oscillating potential (E) of 0.3 V and -0.4 V for holding time intervals of 10 seconds. Film shows fast switching (switching complete within 1 second) and good stability over 100 cycles (∼20 % loss, as measured by the change in peak current (I_p) over 100 cycles.

was injected through holes made in the anode in step (i) [step (iv)]. The electrolyte was rigorously dried to ensure that trace water did not affect the reversibility of the redox processes. The cell was then sealed with chemically resistant Capton tape to minimise the detrimental effect of oxygen on the second reduction process [step (v)]. The cell was then transfered to the cavity of the UV/Vis/NIR spectrometer, and connected in a two electrode arrangement (with the reference electrode connected to the cathode, providing a *pseudo* reference for the electrochemical processes).

Unlike for the open system, the sealed device showed none of the redox processes of poly-**8**, either for the reduction or oxidation processes. The absorption spectra of the devices showed a characteristic dithiolene NIR absorption, though this was reduced in intensity, compared to the spectrum of the film recorded before manufacture. Therefore, some aspect of the manufacturing processes had resulted in some level of film decomposition, causing it to becoming insulating, as well as reducing the intensity of the NIR transition. By comparing the electrochemistry of a freshly prepared polymer film to that of the film after thermal treatment (100°C for 10 seconds), the treated film was shown to become insulating by cyclic voltammetric analysis, losing both the reduction processes of the dithiolene, and the oxidation processes of the indole. Therefore, for such a device to

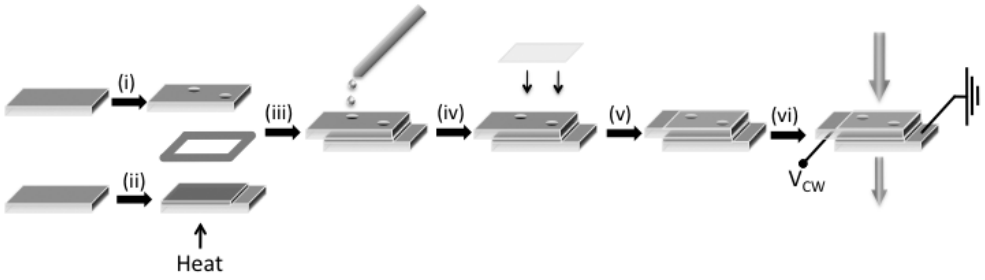

Figure 6.4: Manufacturing process of a basic electrochromic device (ECD). (i) holes drilled in FTO counterelectrode for electrolyte filling; (ii) electropolymerisation of polymer film onto FTO working electrode; (iii) cell assembled with Surylin spacer; (iv) cavity filled with electrolyte; (v) cell sealed with transparent cover slip; (vi) absorption response to an applied potential (V_{CW}) measured.

be operational, the manufacture process should not include a thermal treatment step, if the redox properties of the dithiolene are to be maintained.

6.2.2 Summary and outlook

This study showed that it is possible to tune the absorption properties of polymer films of nickel dithiolenes in the NIR region over three distinct absorbing states. Such a switchable system might find application as a variable optical attenuator (VOA), effective in the NIR region. Devices with these properties might find use in the telecommunications field as silica fibre-optics are most transparent in the NIR region of the electromagnetic spectra.

Whilst the switching was demonstrated for crude devices, open to atmospheric degradation, a closed system could not be developed, due to the thermal sensitivity of the polymer films. Future work might look at alternative device designs that utilise softer fabrication conditions to create closed-system devices with an inherently longer lifetime. In the first instance, a mechanical seal could be envisioned, where the cell is sealed by pressure, rather than heat, such as by miniaturised clamps.

In the longer term, it would also be desireable to tune the dithiolene moiety in such a way as to raise the HOMO level sufficiently to reduce the energy of the NIR transition into the most transparent silica fibre-optic window of λ = 1300-1550 nm. Switching in this region of the electromagnetic spectra may also be possible for the molecular films of the neutral copper dithiolenes formed in section 5.2.5, as they were shown to absorb in the range 1200-1400 nm.

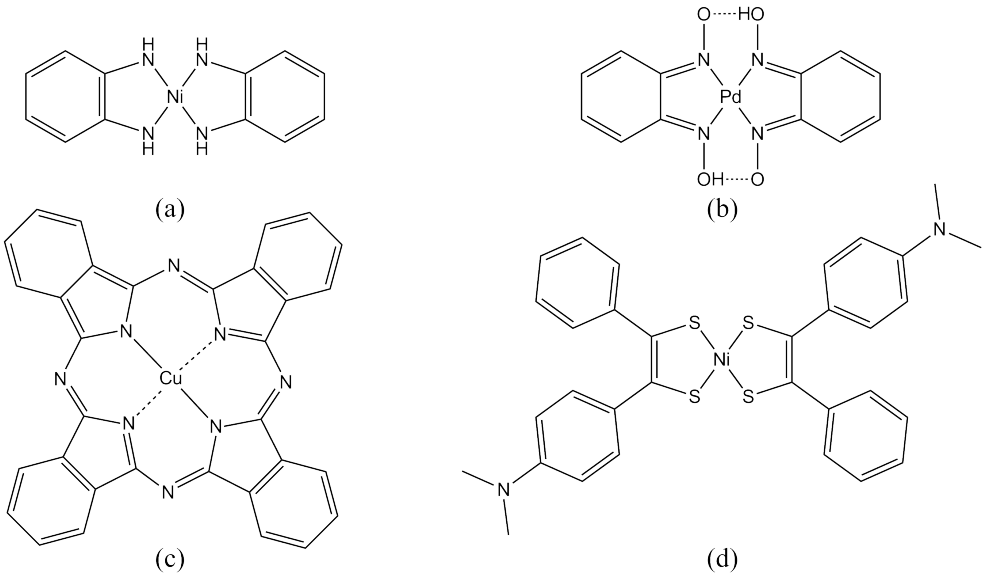

Figure 6.5: Examples of late transition metal complexes that have been studied for FET application: (a) *bis*-(*o*-diiminodenzosemiquinolate)nickel [Noro 05]; (b) *bis*-(benzoquinonedioximato)platinum [Sakai 06]; (c) copper pthalocyanin [Bao 96]; (d) *bis*-(4-dimethylaminodithiobenzyl)nickel [Anthopoulos 06].

6.3 Field-effect transistors (FETs)

The study of **8** in chapter 5 showed the complex to be highly soluble in a range of organic solvents, preferentially forming films, rather than crystallising, on coming out of solution (see section 5.2.2). Such behaviour is desirable for the formation of organic electronic devices, such as FETs, as it allows the formation of thin films by solution methods, rather than energy intensive vapour methods (see section 2.7).

Organic field-effect transistors are on the verge of reaching maturity, with confirmed reports of mobilities (μ) comparable to those of amorphous silicon [Dimitrakopoulos 02]. Whilst their switching speeds are unlikely to ever be sufficient to suit the inorganic dominated high end electronic applications, such as for computer circuitry, organic semiconductors are a serious rival for low end devices, where fast switching is not required, and device improvements are sought, rather in terms of reduced manufacturing costs [Allard 08]. Added to this, their improved solubility, and ease of functionalisation, has led to devices that benefit, or in some cases, rely on their secondary functionality - their flexibility.

Whilst the initial research into organic semiconductors focussed on purely organic systems (see section 2.5), in recent years, focus has broadened to look at transition

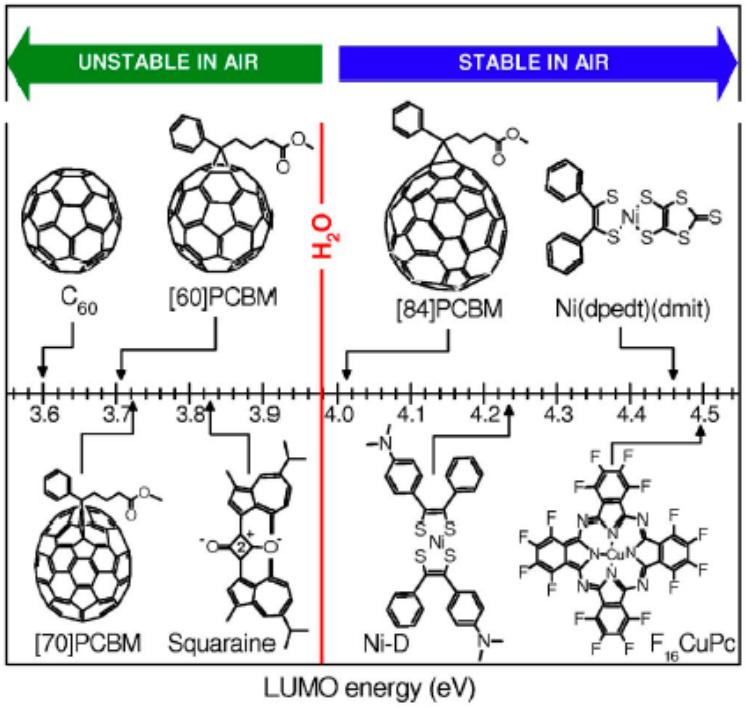

Figure 6.6: LUMO levels of commonly studied organic semiconductors, on a scale of potential (V in units of eV). The red line at an energy of 3.98 eV indicates the redox potential for water reduction (at pH = 7). The green arrow indicates the LUMO energy range for unstable n-channel molecules towards ambient conditions. The blue arrow indicates the LUMO energy range for air-stable n-channel molecules. Figure reproduced from [Anthopoulos 07].

metal complexes [Wada 07, Anthopoulos 06, Anthopoulos 07]. Incorporating a transition metal into the structure allows for the precise tuning of the physical and electronic properties by variation of the metal centre, and the nature of the ligand. Transition metal complexes often display multiple stable redox states, corresponding to electron transfer processes based on the metal (*innocent* complexes) or spread over the ligand (*non-innocent* complexes), and the frontier orbitals are often relatively non-bonding in nature, leading to low reorganisation energies upon electron transfer and, as such, are attractive targets for stable charge transport in organic devices [Cho 07].

Whilst hole accumulation (p-type behaviour) has been readily observed in many organic semiconductors, electron accumulation (n-type) has been observed only rarely [Chua 05]. One reason for this is the poorer environmental stability of the reduced species upon n-doping, leading to rapid carrier loss at the air/semiconductor, or substrate/semiconductor interface [Dodabalapur 05]. Organic transition metal complexes, based on late transition metals (such as those depicted in Fig. 6.5), have

shown promise as air stable ambipolar semiconductors. What seems to be common to all these complexes is the similarity in energy levels between the ligand moieties and the metal centre, giving rise to some degree of 'non-innocent' behaviour. In addition, with the frontier orbitals spread, at least partially over the ligand, extensive interaction of the frontier orbitals in the solid-state is favoured [Cho 07]. All the complexes shown in Fig. 6.5 display a high electron affinity (due to a low lying LUMO orbital), and therefore can be readily reduced. [de Leeuw 97], and later [Anthopoulos 07] and [Wada 07], suggested that the limit for ambient stability of n-type semiconductors was dictated by the oxidation processes with atmospheric water, taking place at E = -0.658 V [relative to a saturated calomel electrode (SCE)]. Therefore, semiconductors with a reduction process to the monoanionic form greater than about -0.66 V ($\sim$ 4 eV) are predicted to show air stable n-channel operation. (see Fig. 6.6).

Nickel dithiolenes often show non-innocent character, with the multiple redox processes occurring at low potentials ($|E|$) due to a low lying LUMO orbital, and efficient delocalisation of the electron density over the ligand [Mueller-Westerhoff 91]. This has prompted several groups to look at their incorporation in field-effect transistors, and complementary-like circuits. [Anthopoulos 06] showed *bis*(4-dimethylaminodithiobenzyl)-nickel to show ambipolar behaviour with typical hole and electron mobilities (μ) of $\sim 10^{-4}$ for both channels. [Wada 07] and [Anthopoulos 07] have since investigated other nickel dithiolenes, varying the nature of the ligand moiety of homoleptic dithiolenes, and looking at heteroleptic dithiolenes, however the improvements in device performance were slight.

The ability of **8** to form continuous films from a range of solvents, combined with its facile reduction (suggesting high electron affinity), as observed by cyclic voltammetry (see section 5.2.5), warrented investigation, in collaboration with the group of Dr. Anthopoulos at Imperial College, to look at the FET performance of this novel nickel dithiolene.

6.3.1 Results and discussion

Cyclic voltammetry measurements (see section 5.2.5) in acetonitrile show a narrow separation (1.4 V) between the oxidation and reduction processes, with the HOMO and LUMO energy levels estimated to be at 5.4 and 3.9 eV, respectively (using the method of [D'Andrade 05], as described in section 3.2.1.1, Eq. 3.2). These values were in good agreement with the optical band gap observed for the NIR (HOMO$\rightarrow$LUMO) transition in MeCN, which showed a maximum absorption (λ_{max}) at 841 nm (1.47 eV),

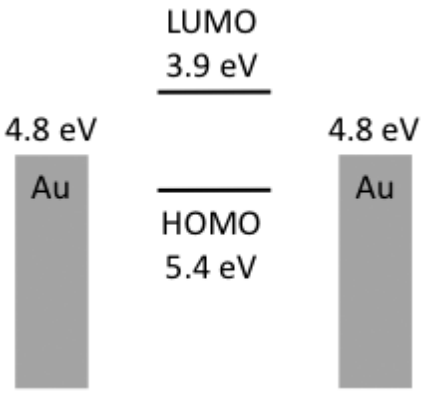

Figure 6.7: Pictorial representation of the energy levels of **8**, calculated by the method of [D'Andrade 05], compared to the experimentally determined work function of the gold source and drain electrodes [de Boer 05].

with onset of absorption at $\lambda \approx$1050 nm (1.18 eV). To investigate the effect of deposition on the energy levels of **8**, a thin film was deposited on a glass substrate by spin coating. In the solid-state, the NIR absorption was shifted to lower energy, giving a maximum absorption at 915 nm (1.36 eV), with onset of absorption ∼1323 nm (0.94 eV). The shift in the NIR absorption suggested at least some degree of interaction in the solid-state (as discussed in section 2.3).

Field-effect transistors are routinely fabricated using inert metals, such as gold or platinum, as the source and drain electrodes, as they are easy to deposit, and the devices can generally be stored for long periods without appreciable degradation. The Fermi level of gold is approximately 4.8 eV [de Boer 05], and lies between the estimated energy levels of the frontier orbitals of **8**, giving a barrier to injection of less than 1eV for both charge carriers (see Fig. 6.7). Such electrodes are therefore suitable for investigating ambipolar charge transport behaviour in **8**.

In an effort to assess the performance of **8** as the active layer for FET devices, a bottom contact, bottom gate substrate design was used (see section 2.6.1, Fig. 2.8). Such a device design is commonly employed when using inert metal source and drain electrodes, as the substrates can be prepared *en masse*, with device fabrication achieved by deposition of the semiconductor directly onto the electrodes, rather than the thermal deposition of electrodes onto the semiconductor.

The FET substrates were constructed from a heavily doped *p*-type Si wafer gate electrode, with a 200 nm thermally oxidised SiO_2 dielectric layer (with a capacitance

(C_i) of 17 nFcm^{-2}). The source and drain electrodes were photolithographically deposited gold of channel dimensions (L = 2μm, W = 10 mm). A 10 nm layer of titanium was used as an adhesion layer, to improve the mechanical contact of the gold on the SiO_2 surface. Prior to semiconductor deposition, the substrates were cleaned in a sonic bath (5 mins acetone, 5 mins IPA), and treated with hexamethyldisilane (HMDS) to passivate the SiO_2 layer.

The deposition of the semiconductor is preferentially achieved by spin coating, as it generally yields more uniform films, due to the even spreading out of the film under centrifugal force (see section 2.7). Initially, film deposition from chlorobenzene was investigated, as chlorobenzene has a high boiling point, favouring the formation of extensive crystalline regions, by slow evaporation. However, spin coating of **8** from chlorobenzene (10 mg/ml) was shown to yield an array of non-continuous droplets over the substrates at spin speeds of ω = 500 or 1000 rpm. Such films are unsuitable for FET devices as the inter-electrode region is poorly covered, resulting in poor performance.

To fabricate continuous films from chlorobenzene, a drop casting method was employed, whilst heating the substrate at 50°C, to aid evaporation of the solvent. The devices formed from chlorobenzene showed negligible gate voltage (V_{GS}) dependence to the drain current (I_{DS}), in either hole or electron accumulation mode, as shown by the transfer characteristics in Figs. 6.8(a) and 6.8(b), respectively. Measurement of the transfer characteristics of an FET device shows how I_{DS} responds to a V_{GS} when a potential difference (V_{DS}) is applied between the source and drain electrodes. No modulation of I_{DS} could be observe for applied potentials ($|V_{GS}|$) of 20, or 50 V. By measuring I_{DS} as a function of V_{DS} at different applied gate voltages (V_{GS}), the devices showed slightly improved gate dependence for the electron channel than for the hole channel, though for both channels, the extent of gate modulation was very poor (see Figs. 6.8(d) and 6.8(c), respectively). Though the exact reason for the poor performance of the films formed by drop casting from chlorobenzene is not completely understood, the poor gate dependence (and thus poor ON/OFF ratio) could be due to the thick nature of the films following drop coating, giving rise to bulk conduction. This would make the devices hard to turn OFF.

In an effort to improve device performance through improved film morphology, film deposition from chloroform was investigated. Chloroform has a lower boiling point than chlorobenzene, thus film formation from solution is more rapid, and thus reduces the extent of droplet as precipitation occurs before droplet aggregation.

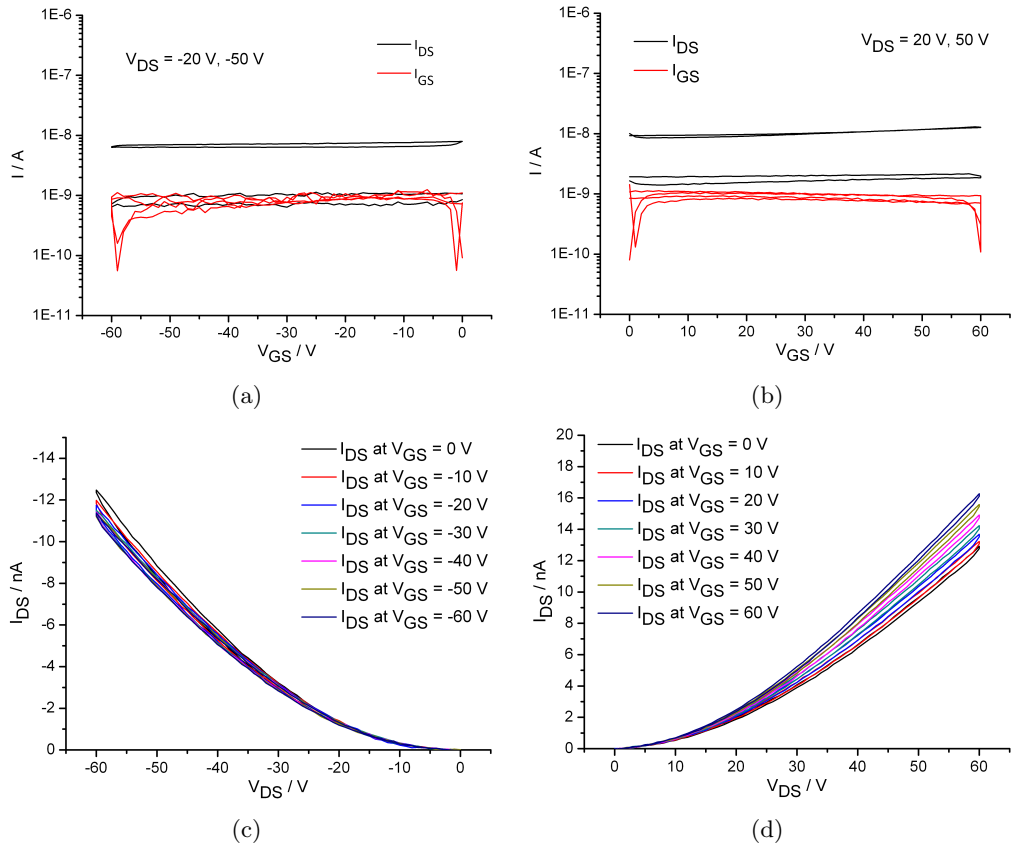

Figure 6.8: Performance of FETs using **8** as the active layer, drop cast from a chlorobenzene solution, and annealed at 50°C. (a) Transfer characteristics in hole accumulation mode, and (b) transfer characteristics in electron accumulation mode. Measurements taken recorded the drain current (I_{DS}) as a function of gate voltage (V_{GS}) when a potential difference (V_{DS}) was applied between the source and drain electrodes. The small gate leakage current (I_{GS}), compared to I_{DS} confirmed the devices were working correctly; (c) gate dependence of holes to an applied potential; (d) gate dependence of holes to an applied potential. Measurements recorded the drain current (I_{DS}) as a function of drain potential difference (V_{DS}) at different gate voltages (V_{GS}). The data shows predominant *n*-type behaviour, however negligible gate modulation of the drain current (I_{DS}) was observed.

Continuous films of **8** could be formed by spin coating at ω = 500, or 1000 rpm. The devices formed from chloroform showed improved gate dependence, compared to those from chlorobenzene (see Figs. 6.9(a) and 6.9(b)), shown by the increased current response (I_{DS}) as a function of gate voltage (V_{GS}), when a potential difference was applied between the source and drain (V_{DS}). By measuring I_{DS} as a function of V_{DS}, at different applied gate voltages (V_{GS}), the devices displayed clear ambipolar behaviour, however the channels were rather unbalanced (see Figs. 6.9(c) and 6.9(d)). The mobility, as calculated from the linear regime (see section 2.6.1, Eq. 2.4), showed the electron (n) channel to have a mobility (μ) of about an order of magnitude higher than the hole channel. This cannot be explained by a simple energy level argument, as it is the HOMO orbital, rather than the LUMO orbital, that is better aligned with the Fermi level of the gold electrodes (see Fig. 6.7). One reason for the improved electron transport in the devices might be due to the presence of impurity traps in the material which are better aligned with the HOMO than the LUMO, hence hampering hole transport more than electron transport. The mobility of neither carrier was particularly high, with the peak electron mobility of the order 10^{-4} cm^{2}V^{-1}s^{-1}, about an order of magnitude lower than the best reported for other nickel dithiolenes [Wada 07]. This low value may, at least in part, be due to the use of chloroform as the solvent. Since chloroform has a low-boiling point, it evaporates relatively quickly, resulting in smaller crystal grains than for higher boiling solvents.

Annealing of the devices, after deposition, can yield improved device performance due to the reorganisation of the molecules at higher temperatures into more continuous crystalline domains that better support charge transport. The effect of annealing was investigated for the devices formed by spin coating from chloroform. However, after annealing at 50°C for 30 minutes, the devices showed an unchanged mobility, suggesting that no reorganisation had occurred. After annealing at 100°C, the devices became insulating, which suggested that a detrimental phase change had occurred somewhere between 50°C and 100°C.

6.3.2 Summary and outlook

In a study carried out by the Anthopoulos group at Imperial College (UK), the group showed that field-effect transistors could be fabricated using **8** as the active layer. The best performing devices showed ambipolar behaviour, with maximum charge carrier mobility (μ) of $\sim 10^{-4}$ cm^{2}V^{-1}s^{-1} for electrons, and $\sim 10^{-5}$ cm^{2}V^{-1}s^{-1} for holes. Deposition conditions were shown to have a large effect on the device properties, illustrating the need for a thorough screening of the deposition conditions, when

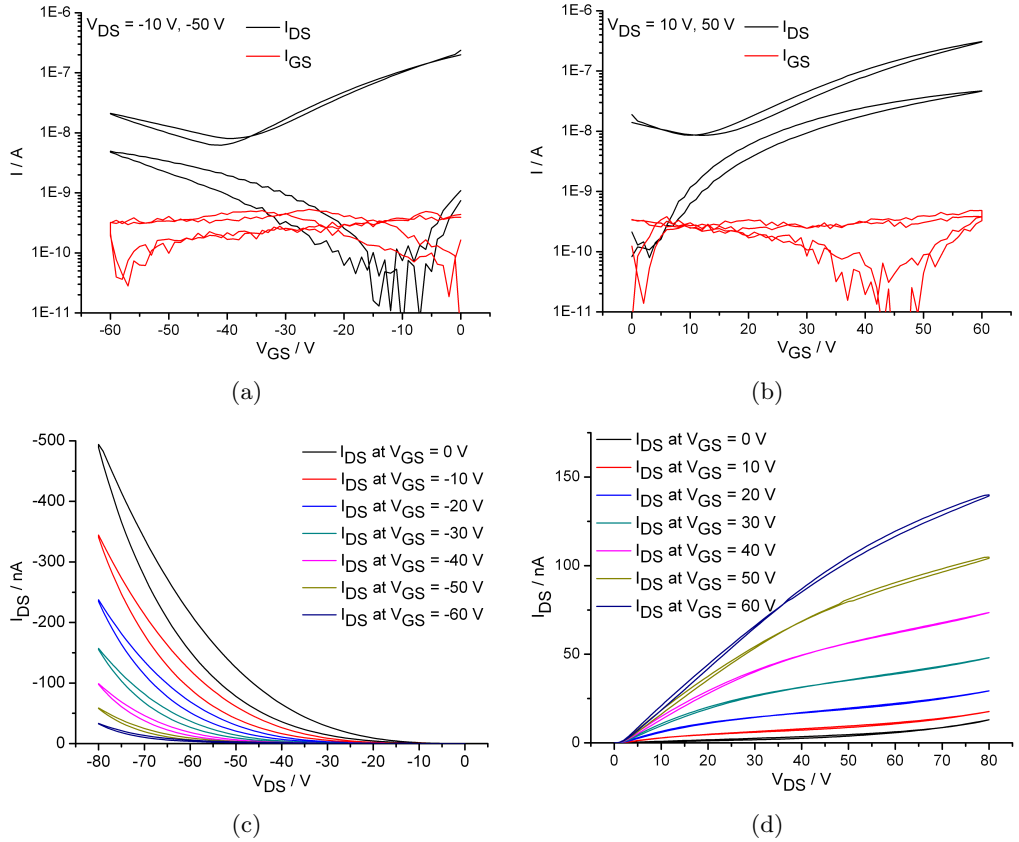

Figure 6.9: Performance of FETs using **8** as the active layer, spin cast from a chloroform solution. (a) Transfer characteristics in hole accumulation mode, and (b) transfer characteristics in electron accumulation mode. Measurements taken recorded the drain current (I_{DS}) as a function of gate voltage (V_{GS}) when a potential difference (V_{DS}) was applied between the source and drain electrodes. The small gate leakage current (I_{GS}), compared to I_{DS} confirmed the devices were working correctly; (c) gate dependence of holes to an applied potential; (d) gate dependence of holes to an applied potential. Measurements recorded the drain current (I_{DS}) as a function of drain potential difference (V_{DS}) at different gate voltages (V_{GS}). The data shows clear ambipolar behaviour for the formed devices, but with unbalanced channels, favouring *n*-type behaviour. Improved gate modulation of the drain current (I_{DS}) was observed, compared to devices from chlorobenzene.

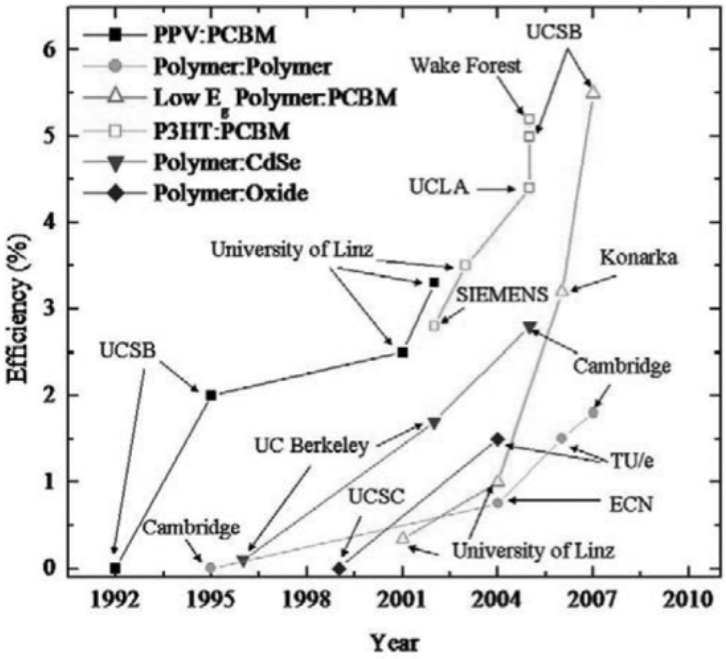

Figure 6.10: Reported efficiencies of bulk heterojunction (BHJ)-PVs with time. The abbreviations are: University of California, Santa Barbra (UCSB); University of California, Santa Cruz (UCSC); University of California, Berkeley (UC Berkeley); University of California, Loa Angeles (UCLA); Technische Universiteit Eindhoven (TU/e). The observed improvements, in terms of device efficiencies, are linked by their structure; PPV = poly(2-methoxy-5-(3',7'-dimethyloctyloxy)-1,4-phenylene-vynylene), PCBM = (6,6)-phenyl-C_{61}-butyric acid methyl ester, P-3HT = regioregular poly-3-hexylthiophene. Figure reproduced from [Mayer 07].

assessing the performance of a novel semiconductor.

Future work might look at alternative surface treatments of the dielectric layer to improve the film continuities from higher boiling solvents, in an effort to increase the size of the crystalline domains, and hence the charge carrier mobilities (μ).

6.4 Bulk-heterojunction photovoltaic (BHJ-PV)

Form the previous study into FET devices of **8** (see section 6.3), it was shown that the complex displayed predominant electron transport, with a charge carrier mobility (μ) $\sim 10^{-4}$ cm^{2}V^{-1}s^{-1} for electrons. **8** also showed strong absorption in the NIR region of the electromagnetic spectra (see section 5.2.3), a region that is poorly covered by other organic semiconductors. Within the field of organic photovoltaic devices, extending the absorption further into the NIR region is an active area of interest that would allow for a greater region of the solar spectrum to be harvested for light-to-energy conversion.

Both the electron transport properties, and the absorption properties of **8** are ideally suited for incorporation into such devices.

Organic photovoltaic (PV) devices (see section 2.6.2) have been the subject of sustained interest for nearly twenty years [Mayer 07], with improvements in power conversion efficiencies being steadily reported, as each of the many steps involved in their light-to-energy conversion are understood, and then tuned (see Fig. 6.10). Although in its essence, the device structure is similar to the long studied, commercially available inorganic equivalent - a *p*-*n* junction, based on amorphous silicon (see section 2.6.2) - the mechanism of operation is very different, and this is reflected in the subtle changes in design that have seen organic PV efficiencies increases from being purely of academic interest, to devices with efficiencies greater than 5 %, and suitable for incorporation into applications that rely on their secondary functionality - their flexibility. The inherent solubility of the organic moieties used for organic PVs means they can be processed at low temperatures by solution methods onto plastic substrates, thus forming truly flexible devices.

The majority of BHJ-PVs are fabricated from a light-harvesting *p*-type conducting polymer, blended with an *n*-type semiconductor. The polymer component of the device architecture generally serves two functions within the device: exciton generation, and hole transport. The low band gap of polymers used, such as regioregular poly-3-hexylthiophene (P-3HT) or poly(2-methoxy-5-(3',7'-dimethyloctyloxy)-1,4-phenylene-vynylene (MDMO-PPV, herein referred to as PPV) (see Fig. 6.11(a)), means that excitation of an electron, from the HOMO to the LUMO orbital, can occur by interaction of a photon with an energy that lies in the visible region of the spectrum. The promoted electron relaxes to form an exciton, with a binding energy of the order 0.1-1.4 eV [Mayer 07]. This binding energy is far greater than for inorganic materials (generally of the order of 1-2 meV) due to a more localised wavefunction for organic materials, and thus a larger Coulombic attraction between charge carriers. This exciton must then migrate (under diffusion control as the exciton has no net charge) to an interface with a sufficient chemical potential to facilitate charge separation. Once at the interface, the charges may still remain associated, over the interface, as a geminate pair [Peumans 04], but must be dissociated by the internal field of the cell to become truly mobile. Having separated, the charges may then drift under the built in voltage of the cell through the polymer to the anode (for electrons) or through the electron transport layer to the cathode (for holes). The bulk of the research into organic PVs has used fullerene derivatives, such as PCBM, to effect electron transport, due to its superior electron transport properties, and appreciable solubility in organic solvents,

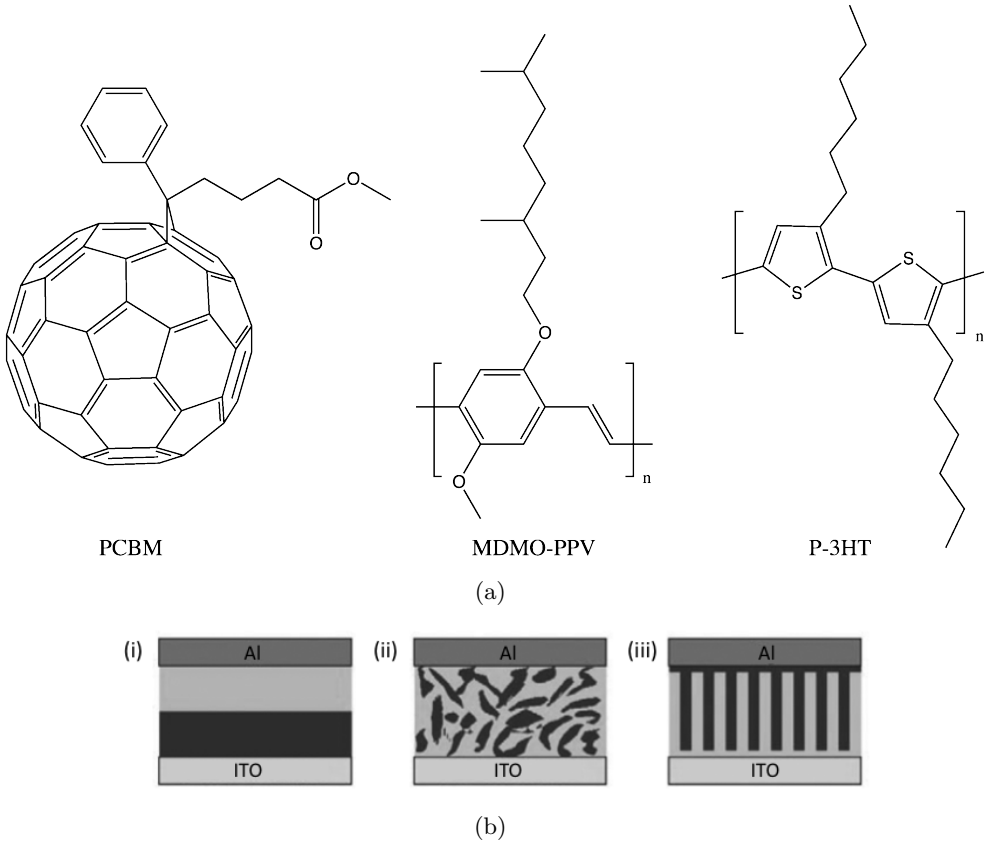

Figure 6.11: Aspects of organic PV design: (a) components routinely used for the construction of organic PV devices. From left to right, PCBM: (6,6)-phenyl-C_{61}-butyric acid methyl ester; MDMO-PPV: poly(2-methoxy-5-(3',7'-dimethyloctyloxy)-1,4-phenylene-vinylene; P-3HT: regioregular poly-3-hexylthiophene; (b) different polymer solar cell heterojunction designs. (i) an illustration of a bilayer design; (ii) an illustration of a bulk heterojunction (BHJ) design; (iii) an illustration of an ordered heterojunction design. Figure modified from [Mayer 07].

and optimisation has focussed on solvent conditions and PCBM loading to improve device performance [Shaheen 01a, Baek 10].

Previous studies have shown that the diffusion distance of excitons, before recombination, is relatively short (3-10 nm), in comparison to the layer thickness in simple bi-layer devices [Mayer 07]. So, with this mechanism of charge separation understood, device design moved from a simple bilayer system, where one layer could be deposited on top of another [see Fig. 6.11(b) (i)], to a bulk-heterojunction design, where the *p*-type and *n*-type semiconductor were mixed before deposition, and applied as a two-component mixture [see Fig. 6.11(b) (ii)]. This meant that a greater proportion of the excitons generated by photoexcitation could be harvested at a larger interface. Cell

design has since moved on to look at more ordered systems [Peiró 06], replacing the n-type semiconductor with a mesostructured inorganic semiconductor (such as ZnO or TiO_2) [see Fig. 6.11(b) (iii)]. However, the inherent complexity of a nano-structured architecture means that such systems are, as yet, a long way from maturity, and thus the bulk heterojunction (BHJ) design remains the most successful architecture, due to its simplicity, and highly folded design, resulting in a large interface between the p-type and the n-type semiconductor.

In order to achieve high photocurrents, light absorption over a large part of the solar spectrum is required. Some groups have addressed this challenge by functionalising the polymer to reduce the band-gap, and hence catch more of the solar spectrum that reaches earth [Shaheen 01b]. An alternative approach is to optimise the electron transport component to capture light, with a complementary absorption to the polymer component, and extend the absorption into the NIR range. This has been achieved for binary systems by replacing PCBM with $PC_{71}BM$, which has an optical density twice that of PCBM, or by developing ternary systems with a sensitiser molecule incorporated to effect light capure at longer wavelengths [J.Peet 08, Johansson 09, Koppe 10, Ismail 09]. Such a ternary design has succeeded in extending the absorption of the blend to longer wavelengths, however, the increased complexity of the electron transfer processes, between multiple species, means that increases in the efficiencies of the devices are yet to be realised from these ternary systems. Any improvements in device efficiency are likely to come from careful tuning of the component ratios, to optimise the electron transfer processes, as well as to tune the resultant film morphologies.

Nickel dithiolenes, such as **8**, characteristically show very intense absorption in the NIR region ($\epsilon > 10^4$ $M^{-1}cm^{-1}$) (see section 5.2.3), as well as n-type semiconductivity ($\mu \approx 10^{-4}$ $cm^2V^{-1}s^{-1}$), with high ambient stability (see section 6.3). These desirable properties, combined with the possibility of forming continuous films of **8** from a range of solvents, prompted the investigation of **8** for incorporation into BHJ-PV devices, in collaboration with the group of Prof. Greenham at Cambridge University (UK).

6.4.1 Results and Discussion

The decided structure for the device was a binary bulk heterojunction (BHJ) architecture, with **8** as the electron transport material, and either P-3HT or PPV, used as the hole transport material, since the photophysics of both these polymer systems is well documented [Greenham 95].

6.4.1.1 Optical properties

In the first instance the optical properties of the blended films were investigated to ensure both components had been incorporated into the film. Films were spin coated at a range of speeds (ω) onto quartz substrates, and the UV/Vis spectra measured. For P-3HT, a 1:1 weight ratio of dithiolene to polymer was dissolved in chlorobenzene (at 70°C), giving a total dissolved content of 40 mg/ml. This blend was spin coated at ω = 2000, 2500, 3000 and 3500 rpm. For PPV, due to its reduced solubility in chlorobenzene, compared to P-3HT, a 1:1 weight ratio of dithiolene to polymer, with a total dissolved content of 10 mg/ml, was used. The blend was spun at ω = 1500, 2000, 2500 and 3000 rpm.

The UV/Vis absorption for both P-3HT and PPV showed incorporation of both species into the film, with the dithiolene component enhancing the absorption in the UV, and extending the absorption properties of the film to lower energies by a discreet absorption in the NIR (see Fig. 6.12(a) and 6.12(b), for the P-3HT and PPV blend, respectively). It seemed that, upon blending, the extent of red-shifting of the dithiolene NIR absorption (as observed in solution) was reduced for both P3HT and PPV blends, when compared to spin coated films of pure **8** (a red-shift of 113 and 278 cm^{-1} for blends of P-3HT and PPV, respectively, compared to a red-shift of 990 cm^{-1} for pure **8**). This suggested less ordering in the dithiolene phase, due to the intermolecular interactions of the dithiolene being broken up by the polymer component.

The thicknesses (d) of these films were analysed using a Dektak surface profiler, showing film thicknesses (d) of between 60-130 nm, with thicker films formed at slower spin speeds (ω). Devices with an active layer $d \approx 100$ nm are routinely constructed as they provide a balance between efficient light harvest and efficient charge collection, and therefore, such film dimensions were targeted to provide a comparison with the state-of-the-art. As devices formed from P-3HT have been shown to benefit from an annealing step [Huang 09], due to the reorganisation of the polymer to form more crystalline domains, the effect of annealing on the UV/Vis absorption was also investigated. The UV/Vis spectra of the annealed films showed negligible change in the intensity or wavelength of maximum absorption (λ_{max}) for the polymer, and no change in the dithiolene absorption (not shown). A slight reduction in film thickness ($d \approx 5$ %), was observed on annealing, which was consistent with only a minimal reorganisation process taking place.

One of the fundamental properties of a photovoltaic is its ability to separate

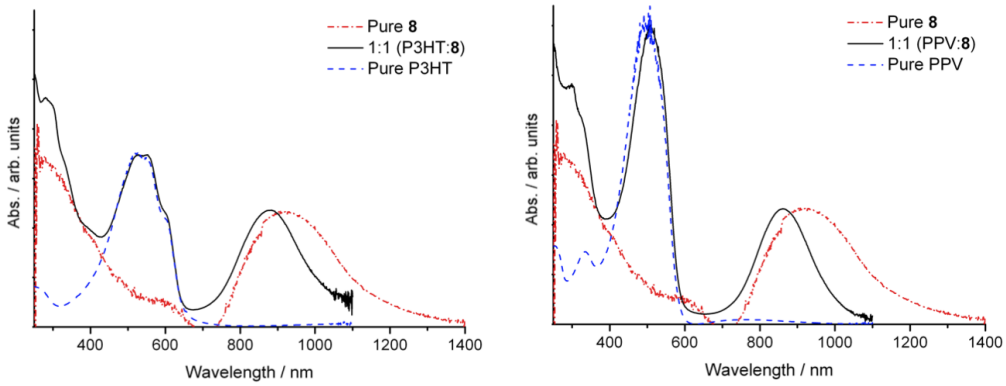

(a) (b)

Figure 6.12: UV/Vis absorbance spectra of spin coated films of, with the spectra of the pure films normalised with respect to the absorptions of the blend; (a) 1:1 P-3HT:**8** blend, compared to pure P-3HT and pure **8**; (b) 1:1 PPV:**8** blend, compared to pure PPV and pure **8**.

charge. In order to assess whether charge separation might occur in such devices, photoluminescence (PL) measurements were performed on the deposited films (see section 3.3). By exciting the polymer component with light of wavelength $\lambda = 500$ nm, an excited state is formed, corresponding to a $\pi \rightarrow \pi^*$ electronic transition. For both P-3HT and PPV, the excited state decays radiatively, emitting light of lower energy than the excitation wavelength (λ) (in these cases). For a two component system, the emitted radiation, from the polymer, may be quenched by the second component if charge transfer occurs between the excited polymer and the second component, as the excited electron cannot return to its ground state by a polymer based radiative decay. Measuring the PL spectra of a polymer blend, in comparison to the spectra of the pure polymer can, therefore, probe whether charge separation occurs in a BHJ-PV device, on a faster timescale than the rate of radiative decay.

As mentioned above, excitation of each of the polymers was achieved with light of wavelength $\lambda = 500$ nm, and the effect on the intensity of the emitted radiation, on increasing dithiolene loading in the films, could be observed. The emission spectra were recorded, perpendicular to excitation beam, to avoid saturation of the photodetector by the excitation beam. Similarly, the spectra were recorded for wavelengths (λ) between 550 and 950 nm, again, to avoid saturation of the photodetector by reflectance of the excitation beam, or of overtone bands.

For P-3HT, the incorporation of dithiolene (at a ratio of 5:1 of P-3HT:**8**) resulted in a reduction of the intensity of the emission by $\sim$95 % (at $\lambda_{max} = 718$ nm), with

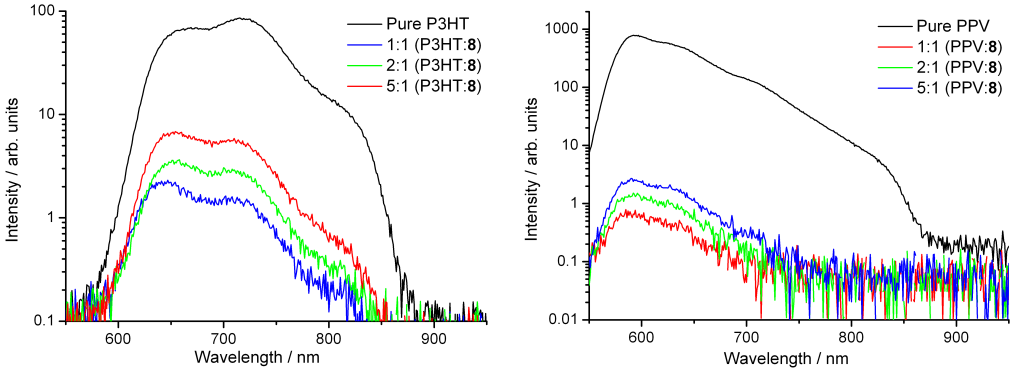

(a) (b)

Figure 6.13: Photoluminescence spectra of spin coated films of: (a) pure P-3HT, compared to P-3HT:**8** blends of weight ratios 1:1, 2:1 and 5:1; (b) pure PPV, compared to PPV:**8** blends of weight ratios 1:1, 2:1 and 5:1.

greater quenching at longer wavelengths, possibly due to reabsorption by the dithiolene moiety (see Fig. 6.13(a)). Whilst reabsorption of the emitted radiation cannot be ruled out as a cause for the reduction in emission intensity, the limited overlap of the emission band of the polymer and the absorption band of the dithiolene suggests the the extent of reabsorption to be minimal. Therefore, the high degree of quenching observed, even at low dithiolene concentration, suggest that efficient charge transfer had occured. Further increases in dithiolene concentration (for a 2:1 and 1:1 P-3HT:**8**) resulted in less marked reductions in the emission intensity, suggesting that, at a 5:1 (P-3HT:dithiolene) ratio, the majority of excitons had been separated, with only slight emission due exciton formation in regions of high polymer denisty, unable to diffuse to a suitable interface. The small subsequent reductions in emission, for higher dithiolene loadings, may possibly reflect the reduced polymer content in the film at higher dithiolene concentrations.

For PPV, quenching of the emission at a 5:1 (PPV:**8**) ratio was far greater, with quenching of over 99 % (at $\lambda_{max} = 591$ nm), again, with little increase in the quenching at higher dithiolene loadings (see Fig. 6.13(a)). It therefore seems that even at low dithiolene loadings, efficient quenching of the polymer excited state of both P-3HT and MDMO-PPV takes place, consistent with efficient energy transfer between the polymer and the dithiolene.

From the initial studies on the polymer/dithiolene blends, it seemed that continuous amorphous films of reproducable thickness, could be produced for both P-3HT and PPV, with various loadings of dithiolene. These blended films showed extensive

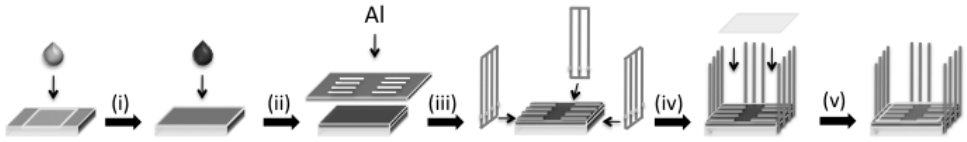

Figure 6.14: Manufacturing steps for a BHJ-PV: (i) spin coat PDOT:PSS as a hole blocking layer onto ITO substrate (anneal); (ii) spin coat donor-acceptor blend onto device substrate (anneal where necessary); (iii) sputter deposit aluminium cathodes through a shadow mask; (iv) attach electrode legs to anode and cathode (iv) seal cells with a glass cover slip by an epoxy resin.

coverage of the UV/Vis/NIR region of the electromagnetic spectra, as observed by electronic absorption spectroscopy, with the dithiolene component extending the absorption into the NIR region. PL measurements suggested that charge separation was achieved in the blends, shown by the near total quenching of the polymer emission processes, even at low dithiolene loadings in the film.

6.4.1.2 Device construction

Photovoltaic devices were constructed by a standard procedure (see Fig. 6.14), using the same 1:1 weight ratios of polymer:dithiolene, in chlorobenzene solution, as for the optical measurements. The substrates used were indium tin oxide (ITO) coated glass, and were cleaned in an ultrasonic bath (10 mins IPA, 10 mins acetone) before use. An anodic buffer layer of poly(3,4-ethylene-dioxythiophene):poly(styrene sulfonate) (PDOT:PSS) was first spin coated (ω = 6000 rpm, 60 seconds), and annealed (250°C, 10 mins) [Fig. 6.14 step (i)]. Inclusion of this buffer layer aids device performance as it serves to smooth the surface of the ITO anode, whilst enhancing the adhesion of the organic layer to the substrate. It also decreases the hole injection barrier due to its relatively higher work function (5.1 $\pm$ 0.1 eV) [Zhou 06]. Under air free conditions, the active layers were then spin coated at ω = 2000 rpm for 60 s for both polymers, affording films of thickness $\sim$100 nm [step (ii)]. In order to assess whether an annealing step resulted in better performance for the P-3HT devices, half of the P-3HT substrates were annealed at 70°C for 10 mins (not shown in Fig. 6.14). Aluminium cathodes were thermally evaporated through a shadow mask defining 8 pixels per device of area 0.1 cm^2 [step (iii)]. The electrodes were attached, and devices were sealed with a glass cover slip by an epoxy resin [step (iv) and (v), respectively]. The devices manufactured were 1:1 P-3HT:**8**, 1:1 P-3HT:**8** with an annealing step, and 1:1PPV:**8**. All devices were made in duplicate, yielding 16 testable units for each device architecture.

6.4.1.3 Device measurements

The results of the PL measurements suggested that energy transfer could be achieved between the polymer and the dithiolene. However, to assess the performance of the dithiolene as an electron transport material, the current response (I) under device illumination was measured, to gauge the light harvesting ability of **8**, in conjunction with the polymer component. Under no illumination, all devices showed diode-like behaviour (not shown), as current (I) only passed through the device under a positive bias (V). This suggested that the devices were all operating correctly (see section 2.6.2).

In the first instance, the external quantum efficiency (EQE) of each device was measured by recording the current response (I) to applied light of different wavelengths (λ), in order to determine which absorption processes in the device contribute to the photocurrent (I). This measurement was performed under low light intensities, to avoid saturation of the device, so that the proportion of incident photons, converted to electrons, at different wavelengths (λ), could be established (see Eq. 6.1).

$$EQE = \frac{\text{output}}{\text{input}} = \frac{\text{current/(charge of one electron)}}{\text{(total power of photons)/(energy of one photon)}} \tag{6.1}$$

Form the EQE data (see Fig. 6.15(a)), it was clear that, for the P-3HT devices, the dithiolene contributed to the overall efficiency of the cell, due to a photocurrent generated from an absorption centred around 860 nm. It seemed that the annealing step for the P-3HT devices increased the efficiency of the P-3HT devices for both the dithiolene and polymer contributions. For the PPV devices, however, negligible photocurrent (I) was generated by the dithiolene, and the efficiency for the PPV component was also far lower than for P-3HT. The EQE was low for all regions of the spectra, for all the devices tested (compared with ∼20 % for P-3HT:PCBM), with maximum external quantum efficiencies for the best performing device of 0.15 % and 0.95 % for the dithiolene and polymer absorptions, respectively. Whilst these values were very small, the concept of using a dithiolene moiety as a NIR absorbing species for simultaneous light harvesting and electron transport, was shown to work. The exact reason for the low EQE values was not known, however, one reason for these low values may be due to poor electron transport in the dithiolene, prohibiting higher currents being passed through the device, due to the build up of charge (Q) in the active layer.

Under higher light intensities, the IV characteristics of the devices were tested. By observing the current (I) response as a function of the applied electric filed (V), the open circuit voltage (V_{OC}) and the short circuit current (I_{SC}) could be determined

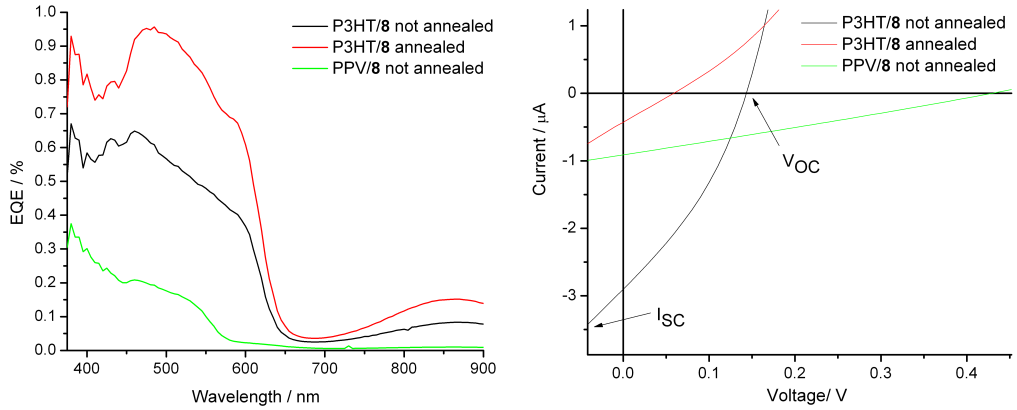

(a) (b)

Figure 6.15: Device performance for a 1:1 P-3HT:**8** blend (annealed and unannealed), as well as a 1:1 PPV:**8** blend (unannealed); (a) external quantum efficiency (EQE) measurements, performed at low light intensities, recording the wavelengh (λ) dependence of photocurrent (I) for the devices. The measurements showed superior efficiencies across the whole spectrum for P-3HT blends, compared to PPV, with improvements in performance observed for annealed films; (b) current (I) vs. voltage (V) plots, under high light intensities of a modeled solar spectrum, showing a reduction in both open circuit voltage (V_{OC}) and short circuit current (I_{SC}), and hence, the overall cell efficiency, upon annealing for P-3HT, but low overall efficiencies for all devices tested.

(see section 2.6.2). From these values, it was possible to calculate the overall device efficiency as the ratio of the power generated by the device (P_{out}) to the (solar) power applied to the device (P_{in}) (see Eq. 2.6, section 2.6.2).

In contrast to the EQE experiments, it seemed that the annealed films performed considerably worse than the non-annealed films of P-3HT/**8**. It is not clear why under low light intensity, annealing leads to improved efficiency, whereas under high light intensity, the efficiency is reduced. One possible reason for this may be that the efficiency of electron transport in the dithiolene may be rather poor, therefore, at higher light intensities, the build up of charge in the device leads to space-charge effects, which effectively block the flow of charge in the device. The devices yielded poor cell efficiencies, with the efficiency of the best performing device (unannealed P-3HT:**8**) at < 0.1 % [as calculated by the method described in section 2.6.2 (see Eq. 2.6)].

It is clear from the PL and EQE data that the principle works: the incorporation of a NIR absorbing electron transport material leads to increased spectral coverage for the devices, however, this did not result in an improved device efficiency.

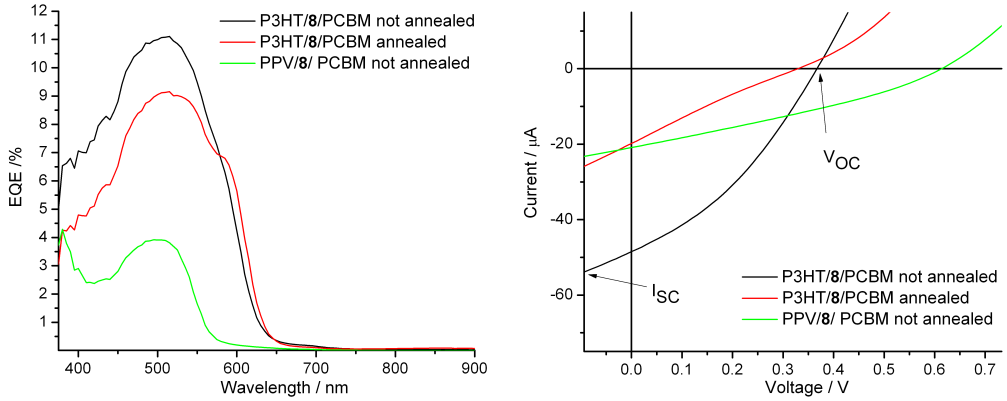

(a) (b)

Figure 6.16: Device performance for a 1:1:2 P-3HT:**8**:PCBM blend (annealed and unannealed), as well as a 1:1:2 PPV:**8**:PCBM blend (unannealed); (a) external quantum efficiency (EQE) measurements, performed at low light intensities, recording the wavelengh (λ) dependence of photocurrent (I) for the devices. The measurements showed negligible contribution to the photocurrent (I) from the dithiolene component (in the NIR region) for both the P-3HT and PPV ternary blends; (b) current (I) vs. voltage (V) plots, under high light intensities of a modeled solar spectrum, showing an larger open circuit voltage (V_{OC}) and short circuit current (I_{SC}) for annealed P-3HT device, but low overall efficiencies for all devices tested.

In an effort to improve the device efficiency by improving electron transport in the blend, a ternary system was investigated for both P-3HT and PPV, using PCBM as the electron transport layer, and **8** as a NIR sensitiser species within the blend. The devices were fabricated as for the binary systems, incorporating two weight equivalents of PCBM into the blend (giving a weight ratio of 1:1:2 for polymer:**8**:PCBM). The efficiencies of the devices showed significant improvements in EQE, over the binary systems, with maximum EQE of 11 % for the polymer component of the best performing device (unannealed P-3HT:**8**:PCBM) (see Fig. 6.16(a)). However, negligible contribution from the dithiolene was observed, and, in comparison to binary systems of P-3HT:PCBM (with EQE $\approx$ 20 %), this represented a reduction in device performance upon incorporation of dithiolene. The device performance under high light intensities, again showed the best performing device to be unannealed P-3HT:**8**:PCBM, however the overall efficiency of this device was still below 0.1 % [as calculated by the method described in section 2.6.2 (see Eq. 2.6)] (see Fig. 6.16).

6.4.2 Summary and outlook

In collaboration with the Greenham group at Cambridge University (UK), BHJ-PV devices were fabricated using a nickel dithiolene as both an electron transport material,

and a NIR sensitiser. For binary systems with P-3HT, the dithiolene moiety was shown to contribute to the efficiency of the cell, though the recorded cell efficiencies were poor. For binary systems of PPV, the dithiolene contribution to the efficiency was negligible, and the overall cell efficiencies were reduced, compared to the P-3HT system. From the photoluminescence data, it seemed that charge transfer from the polymer to the dithiolene was achieved in the blends, however, the low efficiencies are likely due to poor charge transport within the blend, following charge seperation. Therefore, future work should focus on improving the charge transport by tuning the blend composition.

Several different variations in the design could be envisioned to improve device performance. Since both light harvesting and charge transfer had been demonstrated, it seemed that the devices failed for charge collection. One possible solution to this would be to use higher dithiolene loadings. The extended chain structure of organic polymers leads to a high volume fraction in the blend. This may result in localised pockets of nickel dithiolene that are poorly connected in the solid-state. This is supported by the reduced red-shift in the dithiolene NIR absorption upon blending, which suggests that extensive dithiolene interaction is prohibited in the polymer blend. In this instance, charge transport in the dithiolene would be reduced, causing the build up of charge in the device.

Alternatively, different device architectures could be investigated, such as spin coating the dithiolene onto a nanostructured inorganic *p*-type semiconductor, such as nickel oxide [Sasi 07]. Nickel oxide has been used effectively for the construction of dye-sensitised solar cells, and shows good charge transport properties. In such a design, the dithiolene would be the sole absorbing species, and thus such a study would yield valuable information on the light harvesting ability of the dithiolene, as well as the lifetime of the dithiolene excited state.

6.5 Conclusions

This chapter looked at the possibility of incorporation of a novel nickel dithiolene, which was synthesised in chapter 5, into a number of devices, namely electrochromic devices (ECDs), field-effect transistors (FETs), and bulk-heterojunction photovoltaics (BHJ-PVs).

For the ECDs, a poly-**8** film, grown by electrodeposition onto a transparent electrode, and fabricated as a crude ECD, was shown to switch the absorption profile within the NIR region between three absorbing states, upon different applied voltages. The

switching corresponded to sequential reduction of of the dithiolene moiety in the film. Whilst good stability and reversible switching could be demonstrated for the first reduction process, the second reduction was shown to swiftly degrade upon repeated switching. Future work should focus on improving the reversibility of the second reduction process by tuning the electrolyte for better charge balancing of the film, as well as extending the device lifetime by forming a closed device system.

Incorporation of **8** as the active layer for FETs showed the formed devices to display clear ambipolar behaviour, with charge carrier mobilities (μ) of $\sim 10^{-4}$ $cm^2V^{-1}s^{-1}$ for electrons, and $\sim 10^{-5}$ $cm^2V^{-1}s^{-1}$ for holes. The morphology, and performance, of the devices was heavily dependent on the solvent used for deposition, with the best performing devices formed by spin coating from chloroform. Whilst the low boiling point of chloroform favoured the formation of continuous films, the fast rate of evaporation, and thus of film deposition, meant that extensive polycrystalline domains were limited, due to a short reorganisation time between deposition and evaporation.

The favourable electron transport properties of **8**, as observed from the FET studies, as well its strong NIR absorption, prompted the investigation of its incorporation into BHJ-PV devices. By using **8** as an electron transport layer, the absorption profile of the P-3HT and PPV blended binary films was extended into the NIR region. The dithiolene based absorption was shown to contribute to the overall photocurrent (I) of the device, however the measured efficiencies were low (< 0.1 %) for all the devices tested. Investigations are ongoing in an effort to improve device performance by improving the electron transport in the films by increasing the dithiolene content of the films.

Chapter 7

Electrodeposition as a novel route to thin films

7.1 Introduction

In the previous chapter, the incorporation of a novel nickel dithiolene, synthesised in chapter 5, into field-effect transistor (FET) and bulk-heterojunction photovoltaic (BHJ-PV) devices, was investigated. These devices represent, perhaps, the most active areas of interest for organic electronics. For efficient operation of these devices, and many others, the formation of high quality films is essential, as the film dimensions and morphology have been shown to greatly affect device performance (see sections 6.3 and 6.4) [Mas-Torrent 06].

Film formation by solution methods, such as drop and spin coating [Kagan 99, Isotalo 95, Takahashi 01], have been used very successfully to develop high quality films. However, the suitability of such techniques is reliant on the solubility of the material in question (see section 2.7). One major obstacle to the development of molecular electronics is often the poor solubility of the materials. Whilst it is a goal for synthetic chemists to develop materials with a large degree of molecular interaction, such as π-stacking, this inevitably leads to their reduced solubility. As a result, assessing the performance of such materials in a practical device, such as an FET, becomes difficult. For particularly insoluble systems, vapour techniques, such as physical vapour deposition (PVD) and chemical vapour deposition (CVD), can form high quality films [Mas-Torrent 06, Noda 05]. However, such techniques are performed under high vacuum conditions and, as such, are unsuitable for large scale devices, due to the huge costs of evacuating large volumes.

Square planar metal *bis*-dithiolenes are attractive materials for electronic application (see chapter 6), due to their multiple stable redox states, and their highly planar molecular geometry, allowing for extensive intermolecular interaction [Kato 04].

However they present an interesting problem for device incorporation: their boiling point is often too high, or thermal stability too low for sublimation [Mas-Torrent 06] and, without deliberate structural modification, their solubility is often too low for effective solution processing [Marshall 06]. As a result, other alternative methods for processing neutral metal dithiolene films, in a cheap and reproducible manner, are of great interest in materials chemistry.

Electrodeposition is a technique whereby a material can be deposited on a conducting electrode from solution by the change of its redox state, and may be a potential solution to this problem [Buschmann 98]. In the case of dithiolenes, their multiple stable redox states mean that salts, often with greatly improved solubility, can be isolated easily. Under electro-oxidative conditions, these salts may be oxidised to the less soluble neutral species, and thus deposit on a conducting electrode. This technique is not limited to dithiolenes. Salts of many common semiconductors can be formed by reduction or oxidation. Once in their reduced state (oxidised state), they may be transferred to an electrochemical cell for deposition on a conducting electrode, by applying a potential sufficient to re-oxidise (re-reduce) the salt species. One particularly relevant example, for non-dithiolene systems, would be pentacene. Pentacene has shown some of the highest reported mobilities ($\mu > 5$ cm^{2}V^{-1}s^{-1}) as thin films [Kelley 04], however, it is particularly difficult to process, due to its insolubility in all common organic solvents, and thus devices must be fabricated by more expensive vapour methods, that are unsuitable for large-scale fabrication. Pentacene has been shown to reduce to the monoanion with Na in THF, whereupon it readily dissolves [Buschow 65], and therefore may be suitable for electrodeposition. This techniques has an additional advantage insofar as, for film growth to propagate, the film itself must be conductive thus, for systems with more than one crystalline phase, it is conceivable that the more conducting phase may be deposited by such a process.

Electrodeposition of dithiolenes has previously been investigated by some groups as a route to thin films [de Caro 05, Cui 04, Bates 96]. However, in all reported examples of dithiolene electrodeposition, at least some level of residual ionic species was observed in the film following electrodeposition. Indeed, it was this residual ion doping that in some cases led to their investigation as gas sensors. [Bates 96] showed that residual doping, in the formed dithiolene film, resulted in a high conductivity (σ) due to the presence of mixed valence species within the film. In the presence of gaseous SO_2, the partially oxidised film was rereduced, and the conductivity (σ), accordingly, was reduced.

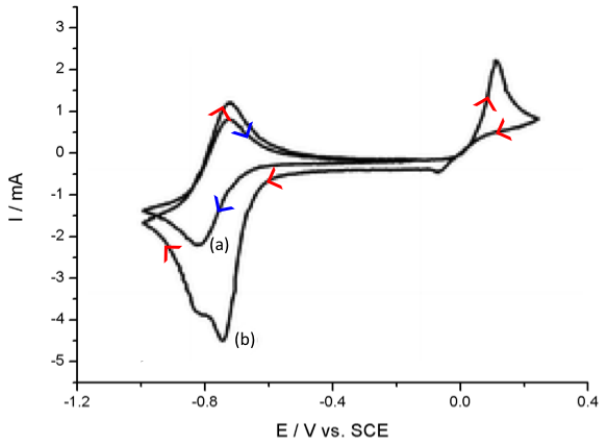

Figure 7.1: Cyclic voltammogram of [**10**][TBA] in CH_3CN/0.1 M [TBA][PF_6] at 50 mVs^{-1}, where the current (I) was measured as function of applied voltage (E), relative to a Saturated Calomel reference Electrode (SCE); (a) (blue) a potential (E) cycle between -0.11 and -1.01 V, showing a reversible redox process, corresponding to the $[\mathbf{10}]^{1-/2-}$ redox couple; (b) (red) a potential cycle (E) between -0.11 V to +0.29 V, then -1.01 V and back to -0.11 V. The potential (E) is cycled to +0.29 V to induce deposition of **10**, which is shown to (di)reduced to $[\mathbf{10}]^{2-}$ at the same potential as the solution based species in (a). Figure reproduced from [Anjos 08].

During the course of an investigation into the electropolymerisation of [Ni(b-3ted)$_2$] (**10**) (b-3ted = *bis*(3-thienyl)-1,2-ethylenedithiolene), [Anjos 08] attempted to increase the concentration of monomer feedstock in the electrolyte by using the monoanionic salt ([**10**][TBA]). This was done, in an effort to improve the coupling efficiency at the working electrode, as polymerisation of the neutral **10** had been shown to couple poorly at achievable concentrations. On cycling [**10**][TBA] to oxidising potentials, a film did form on the working electrode. The formed film, which was dark green in colour, was though to be molecular, due to its complete solubility in DCM, and identical UV/Vis/NIR absorption spectra in solution, compared to **10**. It seemed that the insolubility of **10** in MeCN, compared to the monoanion, resulted in it being deposited on the working electrode before polymerisation could occur. [Anjos 08] showed that, by cycling to a potential sufficient to oxidise [**10**][TBA] to **10** (to +0.29 V), an identical film was formed on the working electrode (see Fig. 7.1). On reversal of the potential cycle (to -1.01 V), no associated reduction for the $[\mathbf{10}]^{0/-1}$ redox couple was observed. However, a steady bleed of current (I) was recorded, preceding a reduction processes at the same potential (E), as for the solution based $[\mathbf{10}]^{1-/2-}$ redox couple, though with a larger peak current (I_p^{red}) (see Fig. 7.1 (a) and (b)). On reversal of the scan direction (back to -0.11 V), an oxidation process was observed, at the same potential (E) as for the solution based $[\mathbf{10}]^{2-/1-}$ redox couple, this time with a similar peak current (I_p^{ox}) to the solution based $[\mathbf{10}]^{2-/1-}$ redox couple. The study concluded that,

upon electrochemical oxidation of [**10**][TBA], a molecular film of **10** could be deposited on the working electrode. This film could be rereduced, but only upon cycling to the potential (E) of the $[\mathbf{10}]^{1-/2-}$ redox couple, whereupon the film could be rapidly rereduced to the dianion, and as a result, redissolved. This behavour was suggested to be due to the slow ingress of sterically hindered TBA, required for charge balancing of the reduction process. The film appeared to be reasonably conductive, due to its continued growth upon cycling. This observed conductivity contrasted with the poor conductivity ($\sigma \approx 1.5$ x 10^{-6} Scm^{-2}) reported in the study for a pressed pellet sample of chemically synthesised **10**, and therefore warranted further investigation.

In this study the physical and electronic properties of films of **10**, formed by electrodeposition, were compared to those formed by a more conventional drop casting method. The study was performed in collaboration with the group of Prof. Awaga at Nagoya University (Japan).

7.2 Results and discussion

7.2.1 Film preparation and morphology

As discussed above, electrodeposition may be a potential alternative for the formation of thin films, especially where the material in question is difficult to process by other means. However, to gauge the potential of this technique, films by conventional methods needed to be formed for comparison with the electrodeposited films.

Films by solution deposition

In the first instance, film formation by spin coating was investigated. **10** was shown to be poorly soluble in all common organic solvents, with a maximum dissolved content observed for DCM of ~3 mg/ml. This solution was spin coated onto indium tin oxide (ITO) coated glass substrates at spin speeds (ω) of 500, 1000 and 2000 rpm. The deposited samples appeared visibly discontinuous, with small, discreet crystallites over the substrate surface. For faster spin speeds (ω), the density of crystallites was severely reduced, with very few crystallites remaining on the substrate surface. Under Scanning Electron Microscopy (SEM), the samples were shown to consist of discreet, well formed, bar-shaped crystals (length of longest axis $l \approx 1\mu$m), that were not supported in a film, but rather scattered over the substrate surface (see Fig. 7.2(a)). Such samples were unsuitable for direct comparison of the physical or electronic properties with the electrodeposited films of **8** (*vide infra*), as the sample density was too low.

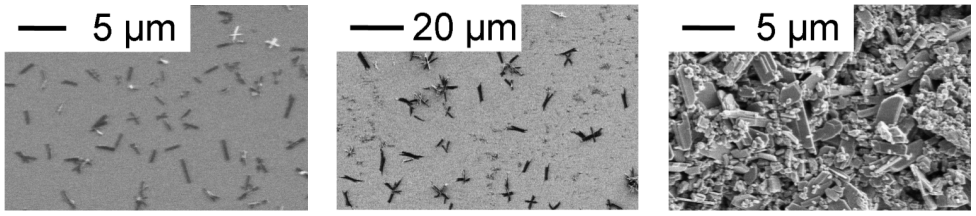

(a) (b) (c)

Figure 7.2: Scanning Electron Microscopy (SEM) images of solution deposited films of **10**, formed by; (a) spin coating, and (b) drop coating; (c) *pseudo* drop coating.

In an effort to increase the sample density of the films, the same solution was drop coated onto ITO coated glass substrates. Under SEM, the drop cast samples also appeared as discreet crystallites, though the crystallites were generally larger than for the spin coated samples (length of longest axis $l \approx 5\mu$m) (see Fig. 7.2(b)). The film density was similarly low for the drop cast films, and thus could not be used for comparison. Continuous films of **10** could be formed by dropping a partially dissolved suspension in DCM onto the substrate, and allowing the suspending solvent to evaporate. This *pseudo* drop casting technique is commonly used as way around such a solubility problem [Matsushita 05]. SEM showed the film to be continuous over the substrate surface, consisting of crystallites with a wide range of sizes (see Fig. 7.2(c)). This was likely due to the dissolved content of **10** crystallising as small crystallites over the larger, suspended crystallites.

Films by electrodeposition

In order to investigate the films grown by electrooxidation of [**10**][TBA], a three electrode electrochemical cell was set up using an indium tin oxide (ITO) coated glass electrode as a working electrode. Films were initially grown from a 5 mM [**10**][TBA] solution in dry MeCN using 0.3 M $TBABF_4$ as supporting electrolyte. The films could be deposited on the ITO electrode by maintaining a potential (E) sufficient to oxidise the monoanionic TBA salt (0.5 V). Electrodeposition was performed potentiostatically to ensure the complete oxidation to the neutral species upon deposition, but also to ensure that the potential did not become sufficient to effect polymerisation of the pendent thienyl groups in the solid-state during film growth [Anjos 08].

Films were grown by maintaining a potential $E = +0.5$ V for 5 minutes, before switching the cell off. On applying a potential, an initial drop in current (I) was observed, due to the local depletion of the dithiolene salt in the area close to the electrode surface, after which, a stable current (I) was maintained throughout film growth. Current (I) was

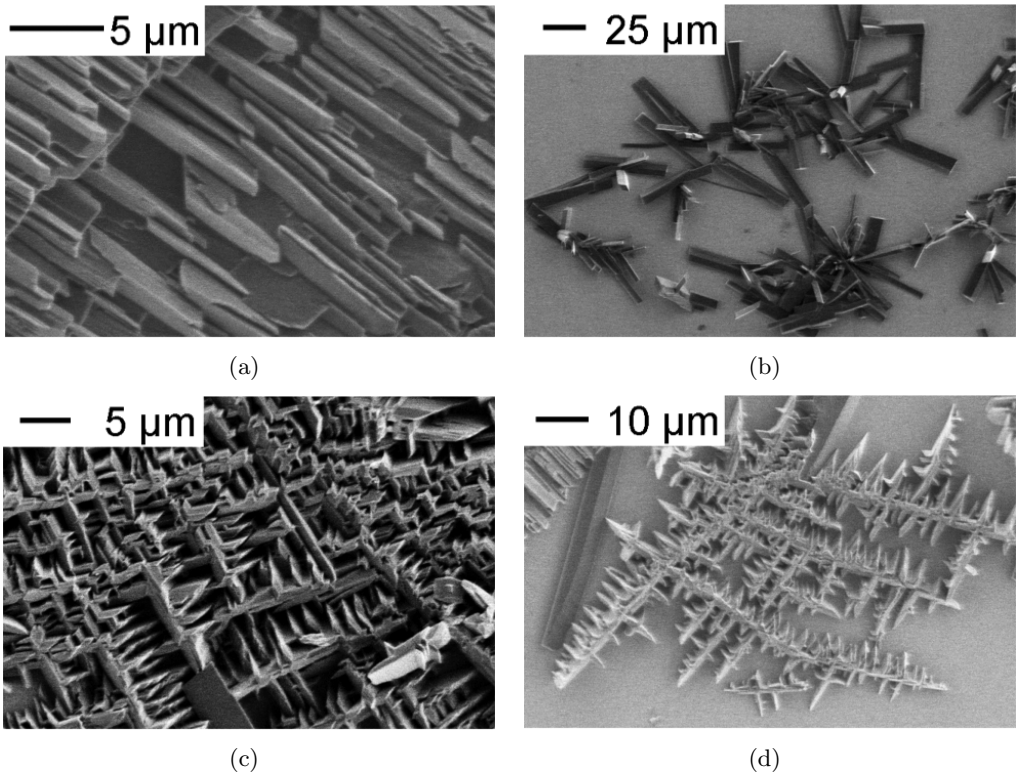

Figure 7.3: Scanning electron microscopy (SEM) images of electrodeposited films of **10** on ITO: (a) resultant film morphology for films formed in dilute (5 mmol dm^{-3}) monomer solution without stirring; (b) initial crystallite formation in dilute (5 mmol dm^{-3}) monomer solution without stirring; (c) resultant film morphology for films formed in concentrated (10 mmol dm^{-3}) monomer solution under the effect of stirring; (d) initial crystallite formation in concentrated (10 mmol dm^{-3}) monomer solution under the effect of stirring.

passed, even beyond total electrode coverage, suggesting the deposition of a conducting film on the working electrode (an example of how the current (I) changed with time (t), under an applied voltage (E), can be seen in Fig. 7.4). The grown films were then washed to remove surface bound ionic species, by immersion in a fresh acetonitrile solution for one minute, and were then dried in a vacuum desiccator overnight. Analysis of the films by SEM showed them to be highly crystalline in nature, with good connectivity of the crystallites achieved through a layered crystalline arrangement (see Fig. 7.3(a)). Shorter growth times (< 1 minute) resulted in incomplete coverage of the electrode surface, as seen by SEM (see Fig. 7.3(b)). The crystallites seemed to have grow from certain points over the ITO surface. These crystallites had branched and, upon collision, continued to grow in new directions, suggesting good electronic contact between the crystallites by their continued growth.

Element	Theoretical	Synthesised (**10**)	Electrodeposited (**10**)
C	42.33	42.41	42.31
H	2.13	2.18	2.85
N	0	0	0

Table 7.1: Elemental analysis of electrodeposited **10**, compared to synthesised **10**.

The film morphology was shown to be highly dependent on the conditions used for electrodeposition. By stirring the solution during film growth, and therefore removing the diffusion control of the growth rate, the morphology of the films could be modified. The formed films showed an increase in the branching of the crystallites, forming a criss-crossed network over the electrode surfaces, as observed by SEM (see Fig. 7.3(c)). For shorter growth times ($<$ 1 minute), branching of the nascent crystallites could also be observed, suggesting that this structure was developed at an early stage of film growth, and was not formed only after total electrode coverage (see Fig. 7.3(d)).

For more concentrated solutions of [**10**][TBA] ($\sim$10 mM), without the aid of stirring, but under otherwise identical growth conditions, the film morphology was shown to be similar to the stirred (low concentration) samples, forming a similar criss-crossed network of crystallites. This suggested that the more branched crystallite structure was rather an effect of a faster growth rate, than of physical agitation of the electrolyte solution.

In order to assess whether the films grown under different conditions were the same material, and were indeed **10**, the UV/Vis/NIR absorption spectra was recorded for dissolved portions of each film in DCM, and compared to chemically synthesised **10**. The spectra showed no change in the wavelengths (λ), or relative intensisies of the NIR or UV absorption processes, suggesting that the formed films were indeed **10**, and that any partially oxidised species, which have a distinct absorption profile to neutral **10** (see section 3.3.3), were present at levels below detection by absorption spectroscopy.

In an effort to better assess the extent of residual doping in the films, elemental analysis was performed on films scraped from the ITO electrode after deposition. To provide sufficient samples for elemental analysis, thick films of electrodeposited **10** were required. Elemental analysis could not be performed on the films formed from low monomer concentrations, as film growth ceased (as the current (I) dropped to zero) before sufficient material could be obtained. However, for more concentrated solutions, with stirring, thicker films could be obtained, and elemental analysis could be performed. The percentage composition of electrodeposited film of **10** was consistent

with the theoretical values expected, and were similar to that of chemically synthesised **10** (see Tab. 7.1). However, the hydrogen content of the film was rather high. Whilst this could be attributed to impurities present in the film, the excellent agreement of the C and N values with the theoretical levels, suggest that it is rather a result of the small quantity of material provided for analysis, than the presence of residual organic doping.

In summary, from the morphology studies, as performed by SEM, it seemed that electrodeposition could yield structurally continuous films, with improved connectivity between the crystallites, as compared to films formed by solution methods. The films were shown to be pure **10** in composition, by comparison of their absorption spectra and elemental analysis, compared to chemically synthesised **10**.

As mentioned above, the ability of a conductive material to form continuous thin films dictates, to a large extent, its potential for incorporation into electronic devices, such as those described in chapter 6. These films should be reproducible in terms of their physical and electronic properties, so that the formed devices operate in their intended manner. Previous studies of electrodeposited dithiolenes showed residual doping in the formed films due to incomplete oxidation of the dithiolene salt upon deposition [Bates 96]. The presence of even small amounts of dopant would affect the electronic properties of a material, either by reducing the conductivity, by trapping charge carriers, or, as observed by [Bates 96], increasing the conductivity, due to the formation of mixed valence species. Such doping would lead to large variations, and thus poor reproducibility, of the formed devices. It is therefore essential to assess the level of residual doping in the electrodeposited films by techniques more sensitive than elemental analysis, to assess the suitability of this technique for forming films for electronic application.

An experiment was therefore designed to accurately gauge the extent of residual doping in the electrodeposited films of **8**. The conductivity (σ) of a material is not only sensitive to the level of doping, but also to the nature of the dopant species. This is due, not only to the size of the dopant ion, which would affect σ by variable disruption of the packing structure, but also to the distinct energy levels of the mixed valence species formed, producing traps of different depths in the material. Therefore, the sensitivity of (σ) of the films to the electrolyte medium (the source of ionic dopant), and the growth conditions (outlined in section 7.2.1) was investigated.

7.2.2 Electrolyte doping studies

As discussed above, since the conductivity of the electrodeposited films is dependent on the level and nature of the ionic impurities, electrodeposition was performed from several background electrolyte solutions ($TBABF_4$, $TEABF_4$ and $TEAPF_6$), and at various concentrations of dithiolene. Such a test is a very sensitive measure of the extent of residual ion doping in the grown films, and would detect trace ion dopants at a level well below the detection limits of elemental analysis. The films were grown from the different electrolyte solutions (of the same concentration) by an identical method to that described in section 7.2.1, with initial [**10**][TBA] concentrations of 5 and 10 mM. In order for the conductivity (σ) of the films to be measured, the films were grown on a working electrode consisting of an interdigitated array of platinum electrodes (electrode gap $L = 2$ μm). The extent of film growth was controlled by fixing the total charge passed (5 mC) for each sample, and thus effectively standardising the film dimensions by fixing the number of dithiolene anions oxidised at the electrode surface. Standardising the film dimensions was done to allow the conductivities of the deposited films to be directly compared, and to discount differing film thicknesses (d) as a reason for differing σ values.

The conductivities of the grown films were compared by measuring the resistance (R) across the interdigitated region at room temperature. This was done by connecting the electrodes to a voltage (V) source, and measuring the current (I) in response to an applied potential. From Ohm's Law, we see that the resistance (R) is proportional to the current (I) at a given potential (V):

$$R = V/I \tag{7.1}$$

This can be related to σ by the equation:

$$\sigma = 1/\rho \tag{7.2}$$

where ρ is the resistivity, and is related to the resistance by the equation:

$$\rho = R \cdot A/L, \tag{7.3}$$

where L is the channel length (here, an electrode gap $L = 2$ μm), and A is the cross-sectional area of the material (here, assumed to be standardised for all films, by controlling the charge (Q) passed upon deposition). The conductivity of the material is therefore inversely proportional to the recorded resistance of the samples, and thus

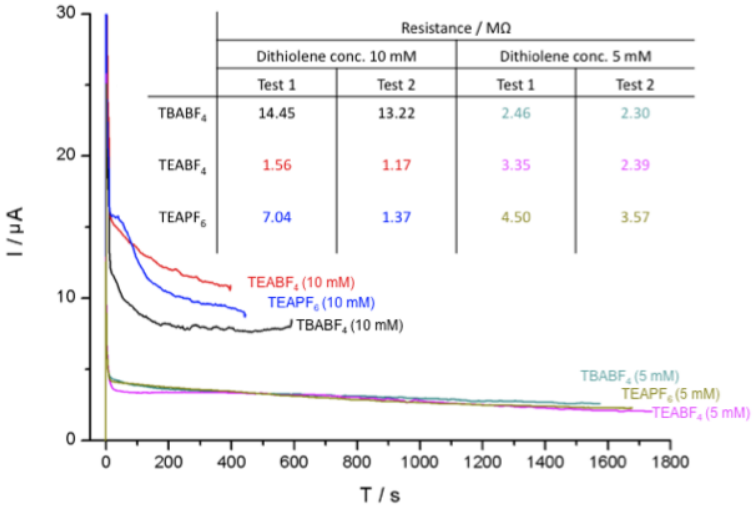

Figure 7.4: (left) Potentiostatic growth of thin film of **10** on interdigitated platinum electrode arrays (of channel length $L = 2$ μm), grown from different background electrolytes. The plot shows the passing of current (I) at the working electrode as a potential $E = +0.5$ V is applied for time (t); (right) the measured resistance (R) of devices formed from different background electrolyte solutions at different concentrations. The results suggest that at lower concentrations of dithiolene, the choice of electrolyte has less of an effect on the resistance (R) of the formed films. The associated errors of the resistance measurements are given in appendix A.2

with the standardised cross-sectional area (A) of the films not known, the materials are compared in terms of their resistance (R).

The films grown from higher dithiolene concentrations (10 mM) grew faster than the films at lower concentrations (5 mM), due to the presence of more dithiolene species in the vicinity of the working electrode (see Fig. 7.4 (left)). All conditions were run in duplicate (Test 1 and Test 2) to assess the reproducibility of the deposition process. The resistances (R) of the films from each electrolyte, and at each dithiolene concentration, were broadly similar, varying by just one order of magnitude, suggesting minimal residual doping in the films. However, the resistances of the samples grown at higher dithiolene concentrations (10 mM) showed slightly greater variation between the films formed from different electrolytes, than at lower concentrations (5 mM) (see Fig. 7.4 (right)), suggesting that the slower growth rate of the dilute solutions resulted in films of higher purity.

Conductivity values display one of the largest ranges of any experimental observable (from $\sim 10^{-14}$ Sm^{-1} for air, to $\sim 10^{7}$ Sm^{-1}for the best electrical conductor, silver), and thus the variations observed in the resistance (R) for the measured devices formed

at low concentration suggest their formation by electrodeposition to be reasonably reproducible, with very little residual doping in the films.

From the low conductivity values (σ = 1.5 x 10^{-5} Scm^{-1}) for a pressed pellet of **10**, reported by [Anjos 08], it seemed, perhaps, surprising that film deposition proceeded past total electrode coverage, as the conductivity of the nascent film might not be sufficient to support continued film growth. It therefore seemed that some aspect of the electrodeposition process improved the conductivity (σ) of the nascent film (compared to the chemically generated material), which facilitated continued, and extensive, film deposition. In order to assess this observed improvement in the conductivity upon electrodeposition, compared to chemically synthesised **10**, conductivity (σ) measurements from comparable films of electrogenerated **10**, and chemically synthesised **10**, were required.

7.2.3 Conductivity measurements

In order to compare the conductivities (σ) of the electrodeposited sample and the chemically generated sample, films of the same dimensions were required to discount differing film thicknesses (d) as a reason for differing σ values.

By using a *pseudo* drop coating method, a film of chemically synthesised **10** could be deposited over the whole interdigitated region (see Fig. 7.5(a)), with a thickness $d \approx 20$ μm (as measured by profile imaging by SEM[1] of a snapped substrate). By measuring the resistance, as described in section 7.2.2, the conductivity (σ) could be calculated by Eq. 7.2, having determined the film dimensions. The conductivity (σ) of the solution deposited film (σ = 5 x 10^{-11} Scm^{-1}) was shown to be far lower than the pressed pellet sample measured by [Anjos 08] (σ = 1.5 x 10^{-5} Scm^{-1}). In order to confirm the measurements reported by [Anjos 08], pressed pellet measurements were performed on the same batch of **10** as used for *pseudo* drop casting. This was done by a four electrode method, where four gold electrodes were attached to the pressed pellet, in parallel, using a conducting graphite paste[2] to fix the electrodes to the sample. The current (I) was measured between the two inner electrodes, with a potential (V) applied between the two outer electrodes. The conductivity (σ) of this pressed pellet was very similar to that reported by [Anjos 08] (1.2 x 10^{-5} Scm^{-1}), and well within the errors of the experimental design.

[1] The thickness was determined after conductivity measurements were performed, as the measurement required the destruction of the device.

[2] A graphite paste was used, rather than a conventional gold paste, to avoid any surface reaction between the dithiolene and the gold particles.

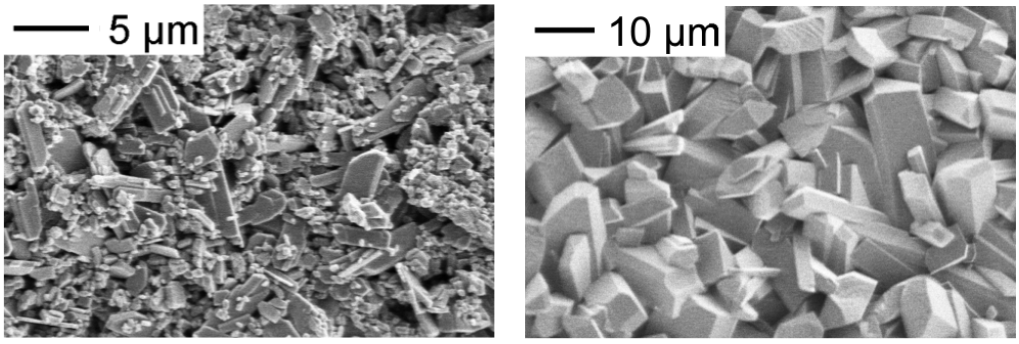

(a) (b)

Figure 7.5: Scanning electron microscopy (SEM) images of **10** on interdigitated electrode array substrates: (a) a *pseudo* drop cast film of **10**, showing film to cover total interdigitated region with crystallites of a wide size distribution; (b) an electrodeposited film of **10**, showing film to cover total interdigitated region, with a continuous array of large crystallites with a small size distribution.

Films of the same thickness (d) as the *pseudo* drop cast sample, could be formed by electrodeposition by a trial and error method. SEM showed the films to have grown over the whole interdigitated electrode region (see Fig. 7.5(b)). The conductivity of the electrodeposited films could, therefore, be directly compared to the solution processed films, and was shown to be 2 x 10^{-9} Scm^{-1}, about 40 times greater than that of the *pseudo* drop cast film (5 x 10^{-11} Scm^{-1}). The conductivity (σ) values for both the deposited films were well below that of the pressed pellet measurement. This difference between the pressed pellet values and both the formed films could be due to many factors, such as poorer electrode contacts, or a lower sample density in the films. Additionally, the conductivity (σ) is based on the assumption that charge is passed through the thickness of the whole film, which is unlikely to be the case in reality, and thus highlights how poorly the optimised properties of a material are often reproduced in a device. The observed difference in σ between the two films may be explained by their different morphologies. The *pseudo* drop cast film deposited as a polycrystalline film with large range of crystallite sizes, due to the precipitation of dissolved **10** onto larger suspended crystallites (see Fig. 7.5(a)). This led to films of low density, and poor connectivity between crystallites. Under electrodeposition, however, **10** deposited as larger crystallites of a much narrower size distribution. These crystallites appeared to be closely packed, giving a high film density. This higher density, as well as the larger crystallites, would inevitably lead to improved electronic contact between the crystallites, and thus show improved conductivity (σ).

In order to assess the effect of larger crystallites in the film on its conductivity (σ), measurements were performed on a single crystal of **10**, formed by slow evaporation of DCM/MeCN. The conductivity was measured by a four probe technique, as for the pressed pellet, and showed σ = 2.5 x 10^{-5} Scm^{-1}. This small increase in σ, compared to the pressed pellet sample, suggested that larger crystallites in electrodeposited **10** were not the only reason for the improved σ, compared to the *pseudo* drop cast film. If the difference in σ was not due to the size of the crystallites in the film, then perhaps it was the nature of the crystallites, formed by electrodeposition, that improved σ.

Organic semiconductors have been shown to have very different electronic properties for the same material, depending on the way the molecules orient themselves upon crystallisation [Fraxedas 08, Cornil 01, Schiefer 07]. Materials that are shown to crystallise with different molecular packing arrangements are described as showing polymorphism, and the different packing arrangements are known as polymorphs. The difference in electronic properties between polymorphs reflects the different intermolecular interactions in the crystal lattice. It is conceivable that the process of electrodeposition may, in some instances, have an effect on the polymorph that forms on the electrode, since only conducting crystallites will continue to grow. This effect is commonly observed in conventional galvanostatic electrocrystallisation [Bryce 91]. To assess whether the packing structure of **10** in the electrodeposited film was different than that *pseudo* drop cast film, X-ray diffraction (XRD) was performed on the thin films.

7.2.4 Polymorph studies

Thin film XRD is a powerful tool for the resolution of molecular ordering in thin films. Similar to single crystal XRD, the technique allows the distances between repeating molecular units (d spacing) in the film structure to be resolved by recording the diffraction pattern of a beam of X-ray radiation, as a function of the incident and scattered angle of the radiation (for a more rigourous discussion of XRD, see [Ladd 03]). As such, information on the packing structure of the molecules can be determined. Whilst information on the unit cell dimensions can be gained from thin film XRD data by using structural modeling refinement techniques (*e.g.* Rietveld refinement), it is usually quicker and easier to compare the data to that obtained from single crystal XRD. From the single crystal data, a powder pattern can be generated directly from the raw data, using programs such as Mercury2.3 [Cambridge Crystallographic Data Centre (CCDC)], which can be compared to the obtained thin film XRD data, in terms of d spacing, and thus unit cell dimensions. The generated powder pattern can be

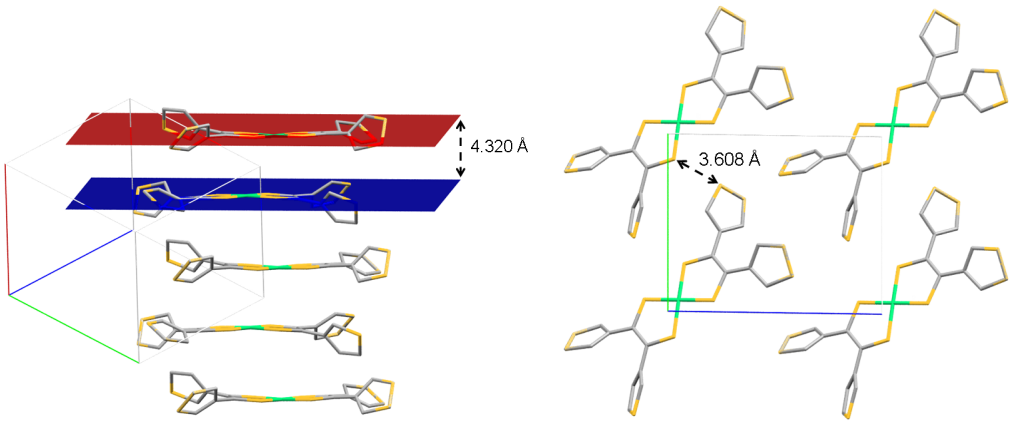

Figure 7.6: Packing structure of **10**, measured by single crystal XRD [Anjos 08], showing; (a) large interplanar distance (4.320 Å) between the dithiolene cores, prohibiting extensive intermolecular interaction in the solid-state; (b) the closest S-S closest contacts at 3.608 Å, between the electronically disconnected thienyl groups.

compared to the thin film data, however caution should be applied when making this comparison, as the constraints of the thin film are different from that of randomly oriented, free flowing powders, and thus differences in relative peak heights can be observed, corresponding to preferred orientation effects in the film.

To compare the packing structure of the molecules within the films, it was first necessary to consider the packing of the molecules within the singe crystals, as measured by single crystal XRD. The single crystal XRD structure, reported by [Anjos 08], showed the molecules to pack as slipped stacks in the unit cell (see Fig. 7.6(a)). The large interplanar distance of the dithiolene cores in the crystal lattice (4.320 Å) accounted for the poor conductivity of the material (as measured from the single crystal), as no significant intermolecular interaction could be developed. The shortest S-S contact was 3.608 Å, and was between the pendent thienyl groups, which had previously been shown to be electronically disconnected from the dithiolene core (Fig 7.6(b)) (see section 5.2.4).

A powder pattern was generated from the single crystal data using the program Mercury2.3 (CCDC), and compared to the thin film XRD spectra recorded for the *pseudo* drop cast, and electrodeposited films of **10** formed on ITO substrates (see Fig. 7.7). The films were investigated on ITO as the FET samples were too small to be analysed by this technique. The results showed that, although some preferred orientation existed in the electrodeposited film, shown by the difference in relative peak heights compared to the *pseudo* drop cast film, the repeating distance of molecular units

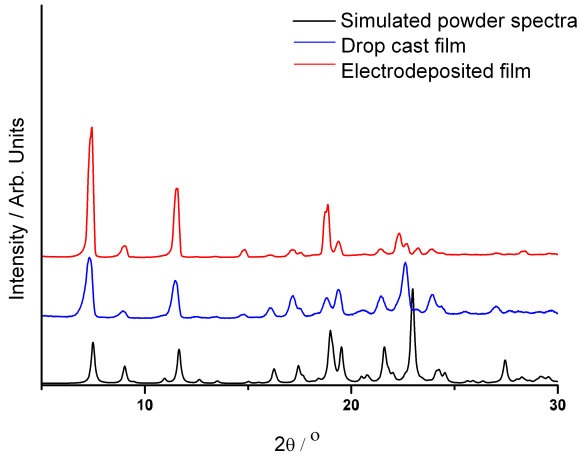

Figure 7.7: Thin film XRD data for electrodeposited and *pseudo* drop cast films of **10**, deposited on an ITO coated glass electrode, compared to a generated powder pattern from single crystal data of **10** using the CCDC Mercury powder XRD pattern software.

within the films, was essentially the same for both films. This could be seen by the good correlation of peaks, with respect to the angle of the applied radiation (2θ). By comparison with the calculated powder XRD spectrum, modeled from the single crystal data, it could be seen that the unit cell dimensions were the same for both films, with the 0,0,1 and 0,1,0 axes clearly observed at the same 2θ value for both films and the generated pattern.

From the thin film XRD data, it seemed that the crystal structure in the films was the same as that of the only polymorph observed by single crystal XRD (Fig 7.6). It should be noted that, although several distinct shapes of single crystal (needles and blocks) had been isolated by the slow evaporation of DCM/MeCN, for the single crystal σ measurements of **10**, the unit cell dimensions of all these crystals were the same as that observed by [Anjos 08].

Following this study, it seemed that it was not the way the molecules arranged in the crystallites that improved σ in the electrodeposited film, as the crystal structure was essentially the same for both films. From the residual electrolyte doping studies performed in section 7.2.2, it seemed that the levels of residual doping were very low in the films, and that any doping would rather decrease the conductivity (σ) of the film, rather than increase it. From the single crystal σ studies, it seemed that the larger crystallite size, as observed in the electrodeposited films, would result in a small

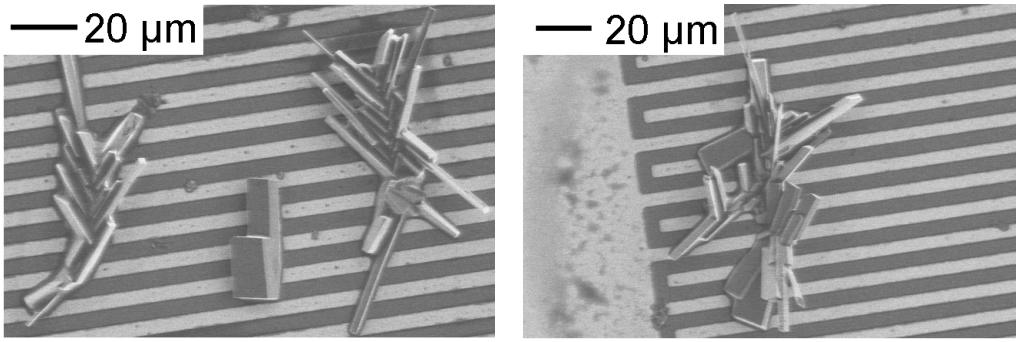

Figure 7.8: Scanning electron microscopy (SEM) images of the initial stages of growth (< 1 minute at a potential $E = +0.5$ V) for an electrodeposited film of **10** on an interdigitated platinum electrode array (electrode gap $L = 2$ μm).

increase in σ, as crystallites, commonly of widths > 10 μm, could easily bridge the 2 μm electrode gap, giving a conductivity measurement closer to the single crystal value. However, larger crystallites were perhaps not the complete answer, as is shown by the relatively small increase in conductivity of the single crystal over the pressed pellet (see section 7.2.3). What is more likely to result in an increase in the conductivity is the improved electronic contact of the crystallites with the electrode, and with each other (see Figs. 7.5(a) and 7.5(b)). Crystal growth will only propagate if a good electronic contact with the electrode is made, thus the film is dominated by crystallites that have a good electronic connection with the electrode (see Fig. 7.8), as those that do not will stop growing. This Darwinian model of film formation by electrodeposition of **10** contrasts with the random arrangement of crystallites deposited over the electrodes by *pseudo* drop casting of **10**. Additionally, for the electrodeposited film, the crystallites connect at branch points, or collisions sites, in both cases providing intimate contact between the crystallites, whereas for *pseudo* drop casting, inter-crystalline links are formed by the crystallisation of the small amount of **10** dissolved in the suspending solvent upon drop casting.

It therefore seemed that continuous polycrystalline molecular films of **10** could be obtained by a method of electrodeposition. Using this method, the films formed on interdigitated electrode arrays appeared to be more continuous, with better electronic communication between the crystallites, as well as better contact to the electrodes. It was these improvements that likely led to the improvements in σ observed in the films. As discussed in the introduction, the formation of high quality films of organic conductive materials is of great importance, if these materials are to be useful in device application. The suitability of this technique for the formation of devices was therefore investigated, not just to assess the potential of **10** as an electronic material, which was

likely to be poor due to the large interplanar distance, observed in the crystal structure, but to gauge the potential for electrodeposition as a technique for the direct formation of devices. Electrodeposition of **10** was therefore investigated for the formation of field-effect transistors (FETs), as the conductivity (σ) measurements of electrodeposited films of **10** had already shown them to deposit over interdigitated electrode arrays, similar to those commonly used as the source and drain electrodes for FETs (see section 2.6.1).

7.2.5 FET measurements

As continuous films of **10** could be formed by electrodeposition over an interdigitated electrode array, the field-effect characteristics of a bottom-contact FET device could be investigated (see section 2.6.1), by growing the film directly onto predefined source and drain electrodes.

The FET substrates used for this study comprised an n-doped silicon wafer and SiO_2 layer as the gate electrode and insulating layer, respectively. Platinum source and drain electrodes were deposited onto the insulating layer, with an electrode gap of 2 μm. The substrates were cleaned from dust with compressed nitrogen prior to use, however no surface treatment of the devices was performed. Onto these devices was electrodeposited **10** in an identical manner to that described in section 7.2.3, to a similar thickness (d) used for the conductivity measurements (20 μm).

By measuring current at the drain electrode (I_{DS}) as a function of the applied voltage (V_{DS}) between the source and drain electrode, at different applied gate voltages (V_{GS}), the FET performance of the device could be characterised (see Fig. 7.9). The measurements showed very poor mobilities (μ) for electron and the hole channel ($\mu \sim 1$ x 10^{-8} $cm^2V^{-1}S^{-1}$) [as calculated from the linear regime (see Eq. 2.4, section 2.6.1)], and showed only negligible V_{GS} dependence to I_{DS}, thus the ON/OFF ratio of the device was, accordingly, very poor.

The poor mobility of electrodeposited **10** was perhaps not surprising, given the poor intermolecular overlap, as observed in the single crystal, prohibiting efficient transfer of charge in the device. However, it seems that, even for a poor semiconductor, electrodeposition could yield films with a superior morphology for electronic applications, than by solution methods. This is especially apparent for **10**, as its solubility in common organic solvents is far too low for effective solution processing, thus in order to form films by solution methods, a *pseudo* drop casting method needed to be employed, which

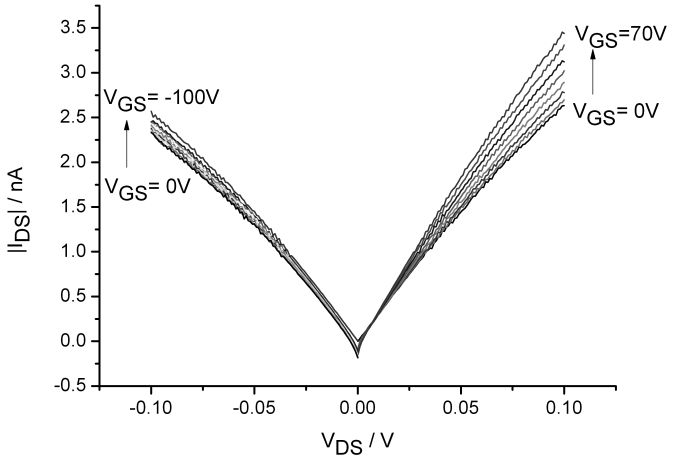

Figure 7.9: FET characteristics of a device, with the active layer formed by the electrodeposition of **10** onto a bottom contact FET substrate, with source-drain channel length 2 μm and a SiO_2 layer thickness of 300 nm. Figure depicts the change in drain current (I_{DS}) as a function of applied source-drain potential (V_{DS}) at various applied gate voltages (V_{GS}).

resulted in a wide range of crystallite sizes, with poor electronic contact with the electrodes, and with each other.

Electrodeposition is therefore seen to be a viable route to thin films of potential semiconductors. This technique can yield improvements in the conductivity (σ) of the films, as their nature of growth necessarily requires good electronic contact between the electrodes, and between the crystallites. It remains to be seen whether this technique would work, in practice, for semiconductors with better electronic properties than **10**.

7.3 Conclusions

Potentiostatic electrodeposition was shown as a novel technique for the formation of neutral films of [Ni(b-3ted)$_2$], by the electrooxidation of its TBA salt. This technique offers the possibility of forming high quality polycrystalline films of organic semiconductors that have distinct properties over other deposition methods. The nature of film growth is such that the crystallites form a good electrical contact with the electrode, and with other crystallites, resulting in films with particularly favorable electronic properties. This technique would be appropriate for existing organic semiconductors, that display much higher conductivities, currently deposited by solution or vapour methods. However, it is particularly suited to the systems that

are unprocessable by conventional techniques, due to their high boiling point, or poor solubility, and might lead to the formation of high quality films that would otherwise be unobtainable by conventional methods.

10 shows poor conductivity as a single crystal, due to the poor overlap of the molecules in the solid-state and, as such, is of little practical use for electronic application. However, it serves to demonstrate that, if film growth can propagate, even for a poor molecular conductor, and result in high quality polycrystalline films, then such a technique would be suitable for a large range of systems, with a large range of conductive properties. The technique was demonstrated for a nickel dithiolene, due to its multiple air stable oxidation states, allowing for a more simple experimental design. The technique could also be extended to other ditholenes, which have shown much better electronic properties, and shown strong gate dependence in FET devices [Anthopoulos 06, Smits 06, Anthopoulos 07, Wada 07, Cho 07]. This technique of electrodposition has also been demonstrated for copper dithiolenes in section 5.2.5. However, the scope of this technique is not limited to dithiolenes, and would be applicable to systems such as the highly studied polycyclic aromatics, such as pentacene [Bendikov 04]. These systems can form stable anionic salts [Buschow 65], with a solubility much greater than their neutral forms, and thus, electrodeposition may provide an alternative route to high quality polycrystalline films of these, and other systems. Future work should focus on expanding this technique to look at the deposition of other organic molecular conductors.

7.4 Experimental

Both **10** and [**10**][TBA] were prepared as previously described [Anjos 08]. Single crystals of **10** were grown by slow evaporation of DCM in the presence of 5 % MeCN. The solvents used for electrodeposition and solution deposition of **10** were purchased anhydrous from Wako pure chemicals, or Sigma-Aldrich, and used as received. All electrolytes for electrodeposotion were purchased as electrochemical grade from Wako pure chemicals or Sigma-Aldrich, and dried under vacuum at 60°C prior to use.

Electrodeposition was performed at room temperature on a ∼5 mM, or ∼10 mM [**10**][TBA] solution in dry MeCN, using 0.3 M $TBABF_4$, $TEABF_4$, or $TEAPF_6$, as supporting electrolyte in a three electrode cell. The working electrode was either an ITO coated glass electrode, or an FET substrate. The FET architecture comprised an *n*-doped silicon wafer as gate electrode, with a 300 nm thermally grown SiO_2 (with a capacitance (C_i) of 17 nFcm^{-2}) layer as dielectric. The platinum source

and drain electrodes were arranged as an interdigitated electrode array deposited by photolithography (for which the channel dimensions correspond to W = 100 cm width and L = 2 μm length). During the electrodeposition, the gate contact was masked with chemically resistant Capton tape. The reference electrode was Ag/AgCl (0.1 M KCl), calibrated against ferrocene/ferrocenium (+0.55 V), and the counter electrode was a Pt gauze.

Thin film X-ray diffraction was recorded on a Rigaku RINT2000 diffractometer (CuK_{α}, $\lambda = 0.15418$ nm). Spectra were recorded on a sample width 0.02 cm, with beam width 0.5 mm, between 2θ = 5-50°, at a scan rate of 1.0°/min.

Scanning electron microscopy was performed using a Hitachi S-4300 electron microscope at 3 kV, giving a resolution of 5.0 nm, or better. Samples were visualised at a working distance of 5.0 mm.

The resistance (R) of pressed pellet and single crystal samples were measured using a four probe technique, attaching gold wires (diameter 25 μm) with a graphite paste [Podzorov 03]. R was measured in the Ohmic region of the current (I) response to an applied potential (V). The resistance (R) of the films was measured by a two probe technique, connected directly to the interdigitated electrode arrays, and measuring the Ohmic region of the IV plot. FET measurements were recorded on an HP probe station, measuring the drain current (I_{DS}) as a function of applied source drain voltage (V_{DS}) at various applied gate voltages (V_{GS}).

Chapter 8

Conclusion

In this study, various aspects of dithiolene chemistry were investigated, in an effort to develop novel deposition techniques that would be suitable for the formation of electronic, and optoelectronic devices, based on metal dithiolenes.

The formation of extensive polymeric networks by electropolymerisation of a heteroleptic dithiolene, with pendent thienyl groups, was demonstrated in chapter 4. The formed films were shown to retain some of the redox functionality of the monomer, and showed the low energy electronic transitions of the dithiolene red-shifted to very low energy upon polymerisation. However, the usefulness of this polymeric material, for device application, was limited by its poor redox activity. This was attributed to poor ion transport through the film, required for charge balancing the redox processes. This was thought to be due to the formation of highly cross-linked polymer chains, facilitated by the multiple polymerisation sites on the dithiolene.

Chapter 5 sought to improve on the molecular design of the molecules studied in chapter 4 by developing novel ligand systems with a reduced number of polymerisation sites per ligand. This was done in an effort to reduce the extent of cross-linking in the polymer chain, and thereby improve the redox activity of the film by facilitating improved ion transport. Two novel ligand systems, incorporating pendent polymerisable indolyl groups, were formed, and complexed with nickel and copper. The complexes of nickel could be isolated in their neutral state and, upon electrooxidation, form high quality, redox active polymer films. In contrast, the complexes of copper could only be isolated, by chemical means, in their monoanionic state. For these complexes, their electroxidation led to the formation of stable neutral copper dithiolene films which were otherwise unobtainable by solution means.

Owing to its favourable physical and electronic properties, one of the nickel dithiolenes, studied in chapter 5 was investigated for the incorporation into devices. Electrochromic devices were formed using, as an active layer, polymer films of a nickel dithiolene,

bearing pendent polymerisable indole units. The devices were able to switch their optical absorption profile through three absorbing states by application of a suitable potential difference across the film. Field-effect transistors were fabricated using molecular films of this novel dithiolene as the active layer. The devices showed ambipolar charge transport properties, and reasonable mobilities, compared to previous dithiolene based devices. Photovoltaic devices were formed by blending the nickel dithiolene with *p*-type conducting polymers, conventionally used for such heterojunction photovoltaic devices. The nickel dithiolene was shown to contribute to the overall efficiency of the device, however the performance was poor, it was thought, due to inefficient charge transport by the dithiolene in the film.

Whilst the solubility of the nickel dithiolene, studied in chapter 6, aided the formation of structurally continuous thin films, other nickel dithiolenes often do no display such high solubility, and are, accordingly, harder to processes as high quality thin films. Chapter 7 showed that, for such an insoluble dithiolene, improvements in film quality, and thus also the electronic properties, could be obtained by a process of electrodeposition. This technique yielded dense, well connected crystalline films, that were, essentially, free from residual ion doping. Electrodeposition was shown to form continuous films over interdigitated electrode arrays, and thus, this technique could be used to fabricate field-effect transistors. Whilst the observed mobilities, of both charge carriers, were very low, the study clearly demonstrated that electrodeposition was a viable method for the fabrication of thin films for electronic device application.

Appendix

A.1 Band structure data

The Brillouin zone (sometimes called the first Brilloin zone) yields a complete description of the energy levels of a given system, and is a cell representation in reciprocal space. Symmetry significant points (k-points) on the surface of this cell can be identified. The band structure of a system is generated by sampling the energy levels along vectors between the center of this cell Γ and these points, and thus gives a pictorial representation of the degree to which the the orbitals interact in a given direction [Hoffmann 87].

k points	Position in Brillouin zone		
Z	0	0	0.5
Γ	0	0	0
Y	0	0.5	0
A	-0.5	0.5	0
B	-0.5	0	0
D	-0.5	0	0.5
E	-0.5	0.5	0.5
C	0	0.5	0.5

Table A.1: Location of symmetry significant (critical) k-points in the Brilloin zone. The band structure is derived by repeated sampling of the energy levels as a path is mapped between these critical points.

A.2 Error calculations

The values of Test 1 and Test 2 are calculated as the mean of two measurements taken for each sample, with errors indicating the scattering of the results. Apart from $TEABF_4$ (5 mM), the errors are all below 2 %, which indicates a high precision of measuring the conductivity in these samples. By calculating the weighted mean of the two separately prepared samples, one can see that the scattering of the values

Electrolyte (initial dithiolene conc.)	Resistance / MΩ		
	Test 1	Test 2	Mean (weighted)
$TBABF_4$ (10 mM)	14.45(0.05)	13.2(0.2)	14.4(0.3)
$TEABF_4$ (10 mM)	1.564(0.004)	1.169(0.002)	1.2(0.2)
$TEAPF_6$ (10 mM)	7.04(0.02)	1.365(0.005)	2(2)
$TBABF_4$ (5 mM)	2.460(0.002)	2.295(0.003)	2.41(0.08)
$TEABF_4$ (5 mM)	3.4(0.2)	2.4(0.6)	3.3(0.3)
$TEABF_6$ (5 mM)	4.50(0.08)	3.57(0.02)	3.6(0.3)

Table A.2: Resistance measurements of electrodeposited films of **10a** with errors given [Bevington 03].

is dominating the error. With the exception of experiments $TEABF_4$ (10 mM) and $TEAPF_6$ (10 mM), the errors are below 10 %, however the large errors especially in $TEAPF_6$ (10 mM) imply the need for further tests to be able to estimate the conductivity to an accuracy of more than the order of magnitude.

Bibliography

[Allard 08] S. Allard, M. Forster, B. Souharce, H. Thiem & U. Scherf. *Organic semiconductors for solution-processable field-effect transistors (OFETs).* Angew. Chem. Int. Ed., vol. 47, no. 22, pages 4070–4098, 2008.

[Anjos 08] T. Anjos, S.J. Roberts-Bleming, A. Charlton, N. Robertson, A.R. Mount, S.J. Coles, M.B. Hursthouse, M. Kalaji & P.J. Murphy. *Nickel dithiolenes containing pendant thiophene units: precursors to dithiolene-polythiophene hybrid materials.* J. Mater. Chem., vol. 18, pages 475–483, 2008.

[Anthopoulos 06] T.D. Anthopoulos, S. Setayesh, E. Smits, M. Cölle, E. Cantatore, B. de Boer, P.W.M. Blom & D.M. de Leeuw. *Air-stable complementary-like circuits based on organic ambipolar transistors.* Adv. Mater., vol. 18, pages 1900–1904, 2006.

[Anthopoulos 07] T.D. Anthopoulos, G.C. Anyfantis, G.C. Papavassiliou & D.M. de Leeuw. *Air-stable ambipolar organic transistors.* Appl. Phys. Lett., vol. 90, page 122105, 2007.

[Argazzi 04] R. Argazzi, N.Y.M. Iha, H. Zabri, F. Odobel & C.A. Bignozzi. *Design of molecular dyes for application in photoelectrochemical and electrochromic devices based on nanocrystalline metal oxide semiconductors.* Coord. Chem. Rev., vol. 248, pages 1299–1316, 2004.

[Arias 10] A.C. Arias, J.D. MacKenzie, I. McCulloch J. Rivnay & A. Salleo. *Materials and applications for large area electronics: solution-based approaches.* Chem. Rev., vol. 110, no. 1, pages 3–24, 2010.

[Armaroli 07] N. Armaroli & V. Balzani. *The future of energy supply: challenges and opportunities.* Angew. Chem. Int. Ed., vol. 46, pages 52–66, 2007.

[Ashcroft 76] N.W. Ashcroft & N.D. Mermin. Solid state physics. Holt, Rinehart and Winston, New York, 1976.

[Atkins 05] P. Atkins & R. Friedman. Molecular quantum mechanics. Oxford University Press, Oxford, 2005.

[Bachler 02] V. Bachler, G. Olbrich, F. Neese & K. Wieghardt. *Theoretical evidence for the singlet diradical character of square planar nickel complexes containing two o-semiquinonato type ligands.* Inorg. Chem., vol. 41, no. 16, pages 4179–4193, 2002.

[Baek 10] W.-H. Baek, T.-S. Yoon, H.H. Lee & Y.-S. Kim. *Composition dependent phase separation of P3HT:PCBM composites for high performance organic solar cells.* Org. Electron., vol. 11, pages 933–937, 2010.

[Bao 96] Z. Bao, A. Lovinger & A. Dodabalapur. *Organic field-effect transistors with high mobility based on copper pthalocyanine.* Appl. Phys. Lett., vol. 69, no. 20, pages 3066–3068, 1996.

[Barrière 02] F. Barrière, N. Camire, W.E. Geiger, U.T. Mueller-Westerhoff & R. Sanders. *Use of medium effects to tune the $\Delta E_{1/2}$ values of bimetallic and oligometallic compounds.* J. Am. Chem. Soc., vol. 124, no. 25, pages 7262–7263, 2002.

[Barrière 06] F. Barrière & W.E. Geiger. *Use of weakly coordinating anions to develop an integrated approach to the tuning of $\Delta E_{1/2}$ values by medium effects.* J. Am. Chem. Soc., vol. 128, no. 12, pages 3980–3989, 2006.

[Bartlett 92] P.N. Bartlett, D.H. Dawson & J. Farrington. *Electrochemically polymerised films of 5-carboxyindole: preparation and properties.* J. Chem. Soc., Faraday Trans., vol. 88, no. 18, pages 2685–2695, 1992.

[Batail 98] P. Batail, K. Boubekeur, M. Fourmigué & J.-C.P. Gabriel. *Electrocrystallization, an invaluable tool for the construction of ordered, electroactive molecular solids.* Chem. Mater., vol. 10, no. 10, pages 3005–3015, 1998.

[Bates 96] J.R. Bates, R.W. Miles & P. Kathirgamanathan. *The modification of the room-temperature conductivity of electrodeposited $Bu_4NNi(dmit)_2$ with ambient gases.* Synth. Met., vol. 76, no. 1-3, pages 313–315, 1996.

[Beaujuge 10] P.M. Beaujuge & J.R. Reynolds. *Colour control in π-conjugated organic polymers for use in electrochromic devices.* Chem. Rev., vol. 110, pages 268–320, 2010.

[Belo 05] D. Belo, M.J. Figueira, J. Mendonça, I.C. Santos, M. Almeida, R.T. Henriques, T. Duarte, C. Rovira & J. Veciana. *Copper, cobalt and platinum complexes with dithiothiophene-based ligands.* Eur. J. Inorg. Chem., no. 16, pages 3337–3345, 2005.

[Belo 06] D. Belo, M.J. Figueira, J.P.M. Nunes, I.C. Santos, L.C. Pereira, M. Almeida & C. Rovira. *Magnetic properties of RBzPy[Ni(α-tpdt)$_2$] (R = H, Br, F): effects of cis-trans disorder.* J. Mater. Chem., vol. 16, no. 26, pages 2746–2756, 2006.

[Bendikov 04] M. Bendikov, F. Wudl & D.F. Perepichka. *Tetrathiafulvalenes, oligoacenenes, and their Buckminsterfullerene derivatives: the brick and mortar of organic electronics.* Chem. Rev., vol. 104, no. 11, pages 4891–4945, 2004.

[Bevington 03] P.R. Bevington & D.K. Robinson. Data reduction and error analysis for the physical sciences. McGraw-Hill, New York, 2003.

[Bigoli 01] F. Bigoli, C.-T. Chen, W.-C. Wu, P. Deplano, M.L. Mercuri, M.A. Pellinghelli, L. Pilia, G. Pintus, A. Serpe & E.F. Trogu. *[Ni(R_2pipdt)$_2$](BF_4)$_2$ (R_2pipdt = 1,4-disubstituted-piperazine-3,2-dithione) as useful precursors of mixed-ligand dithiolenes of interest for non-linear optics.* Chem. Commun., pages 2246–2247, 2001.

[Bigoli 02] F. Bigoli, P. Deplano, M.L. Mercuri, M.A. Pellinghelli, L. Pilia, G. Pintus, A. Serpe & E.F. Trogu. *Ion pair charge-transfer complexes between anionic and cationic metal-dithiolenes [M(II) = Pd, Pt].* Inorg. Chem., vol. 41, no. 20, pages 5241–5248, 2002.

[Billaud 95] D. Billaud, E.B. Maarouf & E. Hannecart. *Chemical oxidation and polymerization of indole.* Synth. Met., vol. 69, pages 571–572, 1995.

[Bray 55] R. Bray. *Minority carrier extraction in germanium.* Phys. Rev., vol. 100, no. 4, pages 1047–1055, 1955.

[Brédas 02] J.L. Brédas, J.P Calbert, D.A. Da Silva Filho & J. Cornil. *Organic semiconductors: a theoretical characterization of the basic parameters governing charge transport.* Proc. Nat. Acad. Sci. U.S.A., vol. 99, no. 9, pages 5804–5809, 2002.

[Bryce 91] M.R. Bryce. *Recent progress on conducting organic charge-transfer salts.* Chem. Soc. Rev., vol. 20, pages 355–390, 1991.

[Buschmann 98] W.E. Buschmann, S.C. Paulson, C.M. Wynn, M.A. Girtu, A.J. Epstein, H.S. White & J.S. Miller. *Reversed (negative) magnetization for electrochemically deposited high-T_c thin films of chromium hexacyanide magnets.* Chem. Mater., vol. 10, no. 5, pages 1386–1395, 1998.

[Buschow 65] K.H.J. Buschow, J. Dieleman & G.J. Hoijtink. *Association of aromatic hydrocarbon negative ions with alkali ions. A spectroscopic investigation.* J. Chem. Phys., vol. 42, no. 6, pages 1993–1999, 1965.

[Cancès 97] M.T. Cancès, B. Mennucci & J. Tomasi. *A new integral equation formalism for the polarizable continuum model: theoretical background and applications to isotropic and anisotropic dielectrics.* J. Chem. Phys., vol. 107, no. 8, pages 3032–3041, 1997.

[Cassoux 99] P. Cassoux. *Molecular (super)conductors derived from bis-dithiolate metal complexes.* Coord. Chem. Rev., vol. 185-186, pages 213–232, 1999.

[Charlot 07] M.-F. Charlot & A. Aukauloo. *Highlighting the role of the medium in DFT analysis of the photophysical properties of ruthenium(II) polypyridine-type complexes.* J. Phys. Chem. A, vol. 111, pages 11661–11672, 2007.

[Charlton 97] A. Charlton, A.E. Underhill, G. Williams, M. Kalaji, P.J. Murphy, K.M.A. Malik & M.B. Hursthouse. *Thiophene-functionalized TTF π-electron donors as potential precursors to conducting polymers and organic metals: synthesis, properties, structure, and electropolymerization studies.* J. Org. Chem., vol. 62, pages 3098–3102, 1997.

[Charlton 98] A. Charlton, M. Kalaji, P.J. Murphy, S. Salmaso, A.E. Underhill, G. Williams, M.B. Hursthouse & K.M.A. Malik. *Synthesis, electrochemical properties and electropolymerization studies on 3-thienyl substituted tetrathiafulvalenes. Single-crystal X-ray structure of 4,4′,5,5′-tetrakis-(3-thienyl)-tetrathiafulvalene.* Synth. Met., vol. 95, pages 75–78, 1998.

[Chen 98] C.-T. Chen, S.-Y. Liao, K.-J. Lin & J.-J. Lai. *Syntheses, charge distribution, and molecular second-order nonlinear optical properties of push-pull bisdithiolene nickel complexes.* Adv. Mater., vol. 3, no. 4, pages 334–338, 1998.

[Chen 09] X.-Y. Chen, C. Barnes, J.R. Dias & T.C. Sandreczki. *Investigation of sp^2-sp coupling for electron-enriched aryl dihalides under oxygen-free Sonogashira coupling reaction conditions using a two-chamber reaction system.* Chem. Eur. J., vol. 15, pages 2041–2044, 2009.

[Cho 07] J.-Y. Cho, B. Domercq, S.C. Jones, J. Yu, X. Zhang, Z. An, M. Bishop, S. Barlow, S.R. Marder & B. Kippelen. *High electron mobility in nickel bis(dithiolene) complexes.* J. Mater. Chem., vol. 17, pages 2642–2647, 2007.

[Chua 05] L.-L. Chua, J. Zaumseil, J.-F. Chang, E.C.-W. Ou, P.K.-H. Ho, H. Sirringhaus & R.H. Friend. *General observation of n-type field-effect behaviour in organic semiconductors.* Nature, vol. 434, pages 194–199, 2005.

[Cornil 01] J. Cornil, J.P. Calbert & J.L Brédas. *Electronic structure of the pentacene single crystal: relation to transport properties.* J. Am. Chem. Soc., vol. 123, no. 6, pages 1250–1251, 2001.

[Coronado 04] E. Coronado & P. Day. *Magnetic molecular conductors.* Chem. Rev., vol. 104, no. 11, pages 5419–5448, 2004.

[Cossi 02] M. Cossi, G. Scalmani, N. Rega & V. Barone. *New developments in the polarizable continuum model for quantum mechanical and classical calculations on molecules in solution.* J. Chem. Phys., vol. 117, no. 1, pages 43–54, 2002.

[Crispin 04] X. Crispin, J. Cornil, R. Friedlein, K.K. Okudaira, V. Lemaur, A. Crispin, G. Kestemont, M. Lehmann, M. Fahlman, R. Lazzaroni, Y. Geerts, G. Wendin, N. Ueno, J.L. Bredas & W.R. Salaneck. *Electronic delocalization in discotic liquid crystals: a joint experimental and theoretical study.* J. Am. Chem. Soc., vol. 126, pages 11889–11899, 2004.

[Crystal 06] Crystal. *Online Manual*, 2006.

[Cui 04] G. Cui, W. Xu, C. Guo, X. Xiao, H. Xu, D. Zhang, L. Jiang & D. Zhu. *Conducting nanopearl chains based on the dmit salt.* J. Phys. Chem. B, vol. 108, pages 13638–13542, 2004.

[Curreli 04] S. Curreli, P. Deplano, C. Faulmann, A. Ienco, C. Mealli, M.L. Mercuri, L. Pilia, G. Pintus, A. Serpe & E.F. Trogu. *Electronic factors affecting second-order NLO properties: case study of four different push-pull bis-dithiolene nickel complexes.* Inorg. Chem., vol. 43, no. 16, pages 5069–5079, 2004.

[D'Andrade 05] B.W. D'Andrade, S. Datta, S.R. Forrest, P. Djurovich, E. Polikarpov & M.E. Thompson. *Relationship between the ionisation and oxidation potentials of molecular organic semiconductors.* Org. Electron., vol. 6, pages 11–20, 2005.

[de Boer 05] B. de Boer, A. Hadipour, M.M. Mandoc, T. van Woudenbergh & P.W.M. Blom. *Tuning the metal work functions with self-assembled monolayers.* Adv. Mater., vol. 17, no. 5, pages 621–625, 2005.

[de Caro 05] D. de Caro, M. Basso-Bert, H. Casellas, M. Elgaddari, J.-P. Savy, J.-F. Lamère, A. Bachelier, C. Faulmann, I. Malfant, M. Étienne & L. Valade. *Metal complexes-based molecular materials as thin films on silicon substrates.* C.R. Chimie, vol. 8, pages 1156–1173, 2005.

[de Leeuw 97] D.M. de Leeuw, M.M.J. Simenon, A.R. Brown & R.E.F. Einerhand. *Stability of n-doped conducting polymers and consequences for polymeric microelectronic devices.* Synth. Met., vol. 87, pages 53–59, 1997.

[Deplano 10] P. Deplano, L. Pilia, D. Espa, M.L. Mercuri & A. Serpe. *Square-planar d^8 metal mixed-ligand dithiolene complexes as second order nonlinear optical chromophores: structure/property relationship.* Coord. Chem. Rev., vol. 254, pages 1434–1447, 2010.

[Dimitrakopoulos 02] C.D. Dimitrakopoulos & P.R.L. Malenfant. *Organic thin film transistors for large area electronics.* Adv. Mater., vol. 14, no. 2, pages 99–117, 2002.

[Ditchfield 71] R. Ditchfield, W.J. Hehre & J.A. Pople. *Self-consistent molecular-orbital methods. IX. An extended gaussian-type basis for molecular-orbital studies of organic molecules.* J. Chem. Phys., vol. 54, no. 2, pages 724–728, 1971.

[Dodabalapur 05] A. Dodabalapur. *Semiconductor technology - negatively successful.* Nature, vol. 434, pages 151–152, 2005.

[Doltsini 06] N.L. Doltsini. Time-dependent density functional theory, volume 31 of *Computational nanoscience: do it yourself!* John von Neumann Institute for Computing, Jülich, 2006.

[Dovesi 06] R. Dovesi, V. R. Saunders, C. Roetti, R. Orlando, C.M. Zicovich-Wilson, F. Pascale, B. Civalleri, K. Doll, N.M. Harrison, I.J. Bush, P. D'Arco & M. Llunell. *CRYSTAL06, University of Torino, Torino*, 2006.

[Elandaloussi 96] E.H. Elandaloussi, P. Frère & J. Roncali. *Soluble thienylenevinylene oligomers end-capped with 1,3-dithiole-2-ylidene groups.* Tetrahedron Lett., vol. 37, pages 6121–6124, 1996.

[Fabian 92] J. Fabian, H. Nakazumi & M. Matsuoka. *Near-infrared absorbing dyes.* Chem. Rev., vol. 92, pages 1197–1226, 1992.

[Farchioni 01] R. Farchioni & G. Grosso. Organic electronic materials. Springer, Berlin, 2001.

[Faulmann 04] C. Faulmann & P. Cassoux. *Solid-state properties (electronic, magnetic, optical) of dithiolene complex-based compounds.* Prog. Inorg. Chem., vol. 52, pages 399–489, 2004.

[Ferraris 73] J. Ferraris, D.O. Cowan, V.V. Walatka Jr. & J.H. Perlstein. *Electron transfer in a new highly conducting donor-acceptor complex.* J. Am. Chem. Soc., vol. 95, no. 3, pages 948–949, 1973.

[Förster 04] H. Förster. *UV/Vis spectroscopy.* Mol. Sieves, vol. 4, pages 337–426, 2004.

[Francl 82] M.M. Francl, W.J. Pietro, W.J. Hehre, J.S. Binkley, M.S. Gordon, D.J. DeFrees & J.A. Pople. *Self-consistent molecular-orbital methods. XXIII. A polarization-type basis set for second-row elements.* J. Chem. Phys., vol. 77, no. 7, pages 3654–3665, 1982.

[Fraxedas 08] J. Fraxedas. *Thin films of molecular organic materials - Preface.* J. Phys. - Cond. Matt., vol. 20, no. 18, page 180301, 2008.

[Frisch 04] M.J. Frisch, G.W. Trucks, H.B. Schlegel, G.E. Scuseria, M.A. Robb, J.R. Cheeseman, J.A. Montgomery Jr., T. Vreven, K.N. Kudin, J.C. Burant, J.M. Millam, S.S. Iyengar, J. Tomasi, V. Barone, B. Mennucci, M. Cossi, G. Scalmani, N. Rega, G.A. Petersson, H. Nakatsuji, M. Hada, M. Ehara, K. Toyota, R. Fukuda, J. Hasegawa, M. Ishida, T. Nakajima, Y. Honda, O. Kitao, H. Nakai, M. Klene, X. Li, J.E. Knox, H.P. Hratchian, J.B. Cross, V. Bakken, C. Adamo, J. Jaramillo, R. Gomperts, R.E. Stratmann, O. Yazyev, A.J. Austin, R. Cammi, C. Pomelli, J.W. Ochterski, P.Y. Ayala, K. Morokuma, G.A. Voth, P. Salvador, J.J. Dannenberg, V.G. Zakrzewski, S. Dapprich, A.D. Daniels, M.C. Strain, O. Farkas, D.K. Malick, A.D. Rabuck, K. Raghavachari, J.B. Foresman, J.V. Ortiz, Q. Cui, A.G. Baboul, S. Clifford, J. Cioslowski, B.B. Stefanov, G. Liu, A. Liashenko, P. Piskorz, I. Komaromi, R.L. Martin, D.J. Fox, T. Keith, M.A. Al-Laham, C.Y. Peng, A. Nanayakkara, M. Challacombe, P.M.W. Gill, B. Johnson, W. Chen, M.W. Wong, C. Gonzalez & J.A. Pople. *GAUSSIAN 03 (Revision E.01), Gaussian, Inc., Wallingford CT.*, 2004.

[Gareau 98] Y. Gareau & A. Beauchemin. *Free radical reaction of diisopropyl xanthogen disulfide with unsaturated systems.* Heterocycles, vol. 48, no. 10, pages 2003–2017, 1998.

[Gaussian 03] Gaussian. *Online Manual*, 2003. `http://www.gaussian.com`.

[Geary 07] E.A.M. Geary, L.J. Yellowlees, S. Parsons, L. Pilia, A. Serpe, M.L. Mercuri, P. Deplano, S.J. Clark & N. Robertson. *Influence of the R-substituents on the properties of [Ni(R$_2$pipdt)(dmit)] complexes and crystal structure where R = CH$_2$C$_6$H$_5$.* J. Chem. Soc., Dalton Trans., pages 5453–5459, 2007.

[Gelinck 96] G.H. Gelinck & J.M. Warman. *Charge carrier dynamics in pulse-irradiated polyphenylenevinylenes: effects of broken conjugation, temperature, and accumulated dose.* J. Phys. Chem., vol. 100, no. 51, pages 20035–20042, 1996.

[Germer 38] L.H. Germer & K.H. Storks. *Arrangements of molecules in a single layer and in multiple layers.* J. Chem. Phys., vol. 6, no. 5, pages 280–293, 1938.

[Grätzel 01] M. Grätzel. *Photoelectrochemical cells.* Nature, vol. 414, no. 6861, pages 338–344, 2001.

[Greef 85] R. Greef, R. Peat, L.M. Peter, D. Pletcher & J. Robinson. Instrumental methods in electrochemistry. Ellis Horwood Ltd., Chichester, 1985.

[Greenham 95] N.C. Greenham, I.D.W. Samuel, G.R. Hayes, R.T. Philips, Y.A.R.R. Kessener, S.C. Moratti, A.B. Holmes & R.H. Freind. *Measurement of absolute photoluminescence quantum efficiencies in conjugated polymers.* Chem. Phys. Lett., vol. 241, pages 89–96, 1995.

[Gross 06] E.K.U. Gross & K. Burke. Time-dependent density functional theory, volume 706. Springer, Heidelberg, 2006.

[Grossmann 06] E. Grossmann. High tech trash. Island Books, New York, 2006.

[Gunbas 08] G.E. Gunbas, P. Camurlu, I.M. Akhmedov, C. Tanyeli, A.M. Önal & L. Toppare. *A fast switching, low band gap, p- and n-dopable, donor-acceptor type polymer.* J. Electroanal. Chem., vol. 615, pages 75–83, 2008.

[Gutmann 67] F. Gutmann & L.E. Lyons. Organic semiconductors. Wiley, New York, 1967.

[Halik 03] M. Halik, H. Klauk, U. Zschieschang, G. Schmid, W. Radlik, S. Ponomarenko, S. Kirchmeyer & W. Weber. *High-mobility organic thin-film transistors based on α,α'-didecyloligothiophenes.* J. Appl. Phys., vol. 93, no. 5, pages 2977–2981, 2003.

[Hariharan 73] P.C. Hariharan & J.A. Pople. *Influence of polarization functions on molecular-orbital hydrogenation energies.* Theor. Chim. Acta, vol. 28, no. 3, pages 213–222, 1973.

[Hénon 06] H. Hénon, F. Anizon, R.M. Golsteyn, S. Léonce, R. Hofmann, B. Pfeiffer & M. Prudhomme. *Synthesis and biological evaluation of new dipyrrolo[3,4-a:3,4-c]carbazole-1,3,4,6-tetraones, substituted with various saturated and unsaturated side chains via palladium catalyzed cross-coupling reactions.* Bioorg. Med. Chem., vol. 14, no. 11, pages 3825–3834, 2006.

[Hill 95] C.A.S. Hill, A. Charlton, A.E. Underhill, K.M.A. Malik, M.B. Hursthouse, A.I. Karaulov, S.N. Oliver & S.V. Kershaw. *Preparation, properties and crystal structures of new nickel(II) complexes of 1,2-asymmetrically substituted dithiolenes for third-order non-linear optical applications.* J. Chem. Soc., Dalton Trans., pages 587–594, 1995.

[Hoffmann 87] R. Hoffmann. *How chemistry and physics meet in the solid state.* Angew. Chem. Int. Ed. Engl., vol. 26, pages 846–878, 1987.

[Horowitz 98a] G. Horowitz. *Organic field-effect transistors.* Adv. Mater., vol. 10, no. 5, pages 365–377, 1998.

[Horowitz 98b] G. Horowitz, R. Hajlaoui, H. Bouchriha, R. Bourguiga & M. Hajlaoui. *The concept of "threshold voltage" in organic field-effect transistors.* Adv. Mater., vol. 10, no. 12, pages 923–927, 1998.

[Huang 09] Y.-C. Huang, Y.-C. Liao, S.-S. Li, M.-C. Wu, C.-W. Chen & W.-F. Su. *Study of the effect of annealing process on the performance of P3HT/PCBM photovoltaic devices using scanning-probe microscopy.* Sol. Energy Mater. Sol. Cells, vol. 93, pages 888–892, 2009.

[Hursthouse 03] M.B. Hursthouse, M.E. Light & P.J. Murphy. *Private Communication, RefCode: 216340 from the Cambridge Crystallographic Data Centre (CCDC)*, 2003.

[Isaksson 81] R. Isaksson, T. Liljefors & J. Sandstroem. *Synthesis of some 5,6-membered, and 7-membered cyclic oxamides and their mono-thio and di-thio analogs.* J. Chem. Res. (S), no. 2, page 43, 1981.

[Ismail 09] Y. Ismail, T. Soga & T. Jimbo. *Improvement in light harvesting and performance of P3HT:PCBM solar cell by using 9,10-diphenylanthracene.* Sol. Energy Mater. Sol. Cells, vol. 93, pages 1582–1586, 2009.

[Isotalo 95] H. Isotalo, J. Paloheimo, Y.F. Miura, R. Azumi, M. Matsumoto & T. Nakamura. *Conductivity of tridecylmethylammonium-Au(dmit)$_2$ Langmuir-Blodgett films under hydrostatic pressure.* Phys. Rev. B: Condens. Matter, vol. 51, no. 3, pages 1809–1816, 1995.

[Jeannin 05] O. Jeannin, J. Delaunay, F. Barrière & M. Formigué. *Between Ni(mnt)$_2$ and Ni(tfd)$_2$ dithiolene complexes: the unsymmetrical 2-(trifluoromethyl)acrylonitrile-1,2-dithiolate and its nickel complexes.* Inorg. Chem., vol. 44, no. 26, pages 9763–9770, 2005.

[Jennings 97] P. Jennings, A.C. Jones, A.R. Mount & A.D. Thomson. *Electrooxidation of 5-substituted indoles.* J. Chem. Soc., Faraday Trans., vol. 93, no. 21, pages 3791–3797, 1997.

[Johansson 09] E.M.J. Johansson, A. Yartsev, H. Rensmo & V. Sundström. *Photocurrent spectra and fast kinetic studies of P3HT/PCBM mixed with a dye for photoconversion in the near-IR region.* J. Phys. Chem. C, vol. 113, pages 3014–3020, 2009.

[Jones 04] B.A. Jones, M.J. Ahrens, M.H. Yoon, A. Facchetti, T.J. Marks & M.R. Wasielewski. *High-mobility air-stable n-type semiconductors with processing versatility: dicyanoperylene-3,4:9,10-bis(dicarboximides).* Angew. Chem. Int. Ed., vol. 43, pages 6363–6366, 2004.

[Jørgensen 66] C.K. Jørgensen. *Differences between the four halide ligands, and discussion remarks on trigonal-bipyramidal complexes, on oxidation states, and on diagonal elements of one-electron energy.* Coord. Chem. Rev., vol. 1, pages 164–178, 1966.

[J.Peet 08] J.Peet, A.B. Tamayo, X.-D. Dang, J.H. Seo & T.-Q. Nguyen. *Small molecule sensitizers for near-infrared absorption in polymer bulk heterojunction solar cells.* Appl. Phys. Lett., vol. 93, pages 163306–163308, 2008.

[Jurchescu 06a] O.D. Jurchescu, A. Meetsma & T.T.M. Palstra. *Low-temperature structure of rubrene single crystals grown by vapor transport.* Acta Crystallogr., Sect. B: Struct. Sci., vol. 62, pages 330–334, 2006.

[Jurchescu 06b] O.D. Jurchescu & T.T.M. Palstra. *Crossover from one- to two-dimensional space-charge-limited conduction in pentacene single crystals.* Appl. Phys. Lett., vol. 88, page 122101, 2006.

[Kagan 99] C.R. Kagan, D.B. Mitzi & C.D. Dimitrakopoulos. *Organic-inorganic hybrid materials as semiconduction channels in thin-film field-effect transistors.* Science, vol. 286, pages 945–947, 1999.

[Kajitani 96] M. Kajitani, G. Hagino, M. Tamada, T. Fujita, M. Sakurada, T. Akiyama & A. Sugimori. *Electrophilic and radical substitution of 1,2,5-cobaltadithiolenes.* J. Am. Chem. Soc., vol. 118, no. 2, pages 489–490, 1996.

[Kanis 94] D.R. Kanis, M.A. Ratner & T.J. Marks. *Design and construction of molecular assemblies with large second-order optical nonlinearities. Quantum chemical aspects.* Chem. Rev., vol. 94, pages 195–242, 1994.

[Karl 03] N. Karl. *Charge carrier transport in organic semiconductors.* Synth. Met., vol. 133-134, pages 649–657, 2003.

[Kato 97] R. Kato, Y. Kashimura, H. Sawa & Y. Okano. *Synthesis, structure, and electrochemical properties of new "unsymmetrical" metal dithiolate complexes.* Chem. Lett., vol. 26, pages 921–922, 1997.

[Kato 04] R. Kato. *Conducting metal dithiolene complexes: structural and electronic properties.* Chem. Rev., vol. 104, no. 11, pages 5319–5346, 2004.

[Kean 01] C.L. Kean & P.G. Pickup. *A low band gap conjugated metallopolymer with nickel bis(dithiolene) crosslinks.* Chem. Commun., pages 815–816, 2001.

[Kean 02] C.L. Kean, D.O. Miller & P.G. Pickup. *Thiophene-substituted nickel dithiolene complexes. Precursors for low band gap conjugated metallopolymers.* J. Mater. Chem., vol. 12, pages 2949–2959, 2002.

[Kelley 04] T.W. Kelley, P.F. Baude, C. Gerlach, D.E. Ender, D. Muyres, M.A. Haase, D.E. Vogel & S.D. Theiss. *Recent progress in organic electronics: materials, devices and processes.* Chem. Mater., vol. 16, no. 23, pages 4413–4422, 2004.

[Kepler 60] R.G. Kepler. *Charge carrier production and mobility in anthracene crystals.* Phys. Rev., vol. 119, no. 4, pages 1226–1229, 1960.

[Kobayashi 04] A. Kobayashi, E. Fujiwara & H. Kobayashi. *Single-component molecular metals with extended-TTF dithiolate ligands.* Chem. Rev., vol. 104, pages 5243–5264, 2004.

[Koppe 10] M. Koppe, H.-J. Egelhaaf, G. Dennler, M.C. Scharber, C.J. Brabec, P. Schilinsky & C.N. Hoth. *Near IR sensitization of organic bulk heterojunction solar cells: towards optimization of the spectral response of organic solar cells.* Adv. Funct. Mater., vol. 20, pages 338–346, 2010.

[Krishnan 80] R. Krishnan, J.S. Binkley, R. Seeger & J.A. Pople. *Self-consistent molecular orbital methods. XX. A basis set for correlated wave functions.* J. Phys. Chem., vol. 72, no. 1, pages 650–654, 1980.

[Kuebler 96] S.M. Kuebler & R.G. Denning. *Population gratings in degenerate four-wave mixing studies of a nickel dithiolene at 1064 nm.* Chem. Phys. Lett., vol. 250, pages 120–127, 1996.

[Ladd 03] M. Ladd & R. Palmer. Structure determination by x-ray crystallography. Springer, Berlin, 2003.

[Lee 88] C. Lee, W. Yang & R. Parr. *Development of the Colle-Salvetti correlation-energy formula into a functional of the electron-density.* Phys. Rev. B: Condens. Matter, vol. 37, no. 2, pages 785–789, 1988.

[Liang 70] W.Y. Liang. *Excitons.* Phys. Educ., vol. 5, no. 4, pages 226–228, 1970.

[Mackintosh 94a] J.G. Mackintosh & A.R. Mount. *Electropolymerisation of indole-5-carboxylic acid.* J. Chem. Soc., Faraday Trans., vol. 90, no. 8, pages 1121–1125, 1994.

[Mackintosh 94b] J.G. Mackintosh, A.R. Mount & D. Reed. *Characterization of the unsymmetrical trimer of indole-5-carboxylic acid by proton NMR spectroscopy.* Magn. Reson. Chem., vol. 32, no. 9, pages 559–561, 1994.

[Mahadevan 86] C. Mahadevan. *1,2-Dithiolene complexes of transition metals - structural systematics and physical properties.* J. Cryst. Spectrosc., vol. 16, no. 347-416, 1986.

[Markovitsi 01] D. Markovitsi, S. Marguet, J. Bondkowski & S. Kumar. *Triplet excitation transfer in triphenylene columnar phases.* J. Phys. Chem. B, vol. 105, no. 7, pages 1299–1306, 2001.

[Marques 04] M.A.L. Marques & E.K.U. Gross. *Time-dependent density functional theory.* Annu. Rev. Phys. Chem., vol. 55, pages 427–455, 2004.

[Marshall 06] K.L. Marshall, B. Schudel & I.A. Lippa. *Transition metal dithiolene near-IR dyes and their applications in liquid crystal devices.* LLE Review, vol. 106, pages 112–128, 2006.

[Martín 98] N. Martín, L. Sánchez, B. Illescas & I. Pèrez. *C_{60}-based electroactive organofullerenes.* Chem. Rev., vol. 98, no. 7, pages 2527–2547, 1998.

[Mas-Torrent 06] M. Mas-Torrent & C. Rovira. *Tetrathiafulvalene derivatives for organic field effect transistors.* J. Mater. Chem., vol. 16, pages 433–436, 2006.

[Matsumoto 80] M. Matsumoto & K. Kuroda. *A convenient synthesis of 1-bromoolefins and acetylenes by a chain extension of aldehydes.* Tetrahedron Lett., vol. 21, pages 4021–4024, 1980.

[Matsushita 05] M.M. Matsushita, H. Kawakami, E. Okabe, H. Kouka, Y. Kawada & T. Sugawara. *A field-effect transistor consists of spin-polarized TTF-based donor.* Polyhedron, vol. 24, pages 2870–2875, 2005.

[Mayer 07] A.C. Mayer, S.R. Scully, B.E. Hardin, M.W. Rowell & M.D. McGehee. *Polymer based solar cells.* Mater. Today, vol. 10, no. 11, pages 28–33, 2007.

[McCleverty 68] J.A. McCleverty. *Metal 1,2-dithiolene and related complexes.* Prog. Inorg. Chem., vol. 10, pages 49–221, 1968.

[McCoy 11] H.N. McCoy & W.C. Moore. *Organic amalgams: substances with metallic properties composed in part of non-metallic elements.* J. Am. Chem. Soc., vol. 33, pages 273–292, 1911.

[McCulloch 09] I. McCulloch, M. Heeney, M.L. Chabinyc, D. DeLongchamp, R.J. Kline, M. Cölle, W. Duffy, D. Fischer, D. Gundlach, B. Hamadani, R. Hamilton, L. Richter, A. Salleo, M. Shkunov, D. Sparrowe, S. Tierney & W. Zhang. *Semiconducting thienothiophene copolymers: design, synthesis, morphology, and performance in thin-film organic transistors.* Adv. Mater., vol. 21, pages 1091–1109, 2009.

[McCullough 98] R.D. McCullough. *The chemistry of conducting polythiophenes.* Adv. Mater., vol. 10, no. 2, pages 93–116, 1998.

[McDonagh 00] A.M. McDonagh, S.R. Bayly, D.J. Riley, M.D. Ward, J.A. McCleverty, M.A. Cowin, C.N. Morgan, R. Varrazza, R.V. Penty & I.H. White. *A variable optical attenuator operating in the near-infrared region based on an electrochromic molybdenum complex.* Chem. Mater., vol. 12, no. 9, pages 2523–2524, 2000.

[Minkin 04] V.I. Minkin & A.G. Starikov. *Spiroconjugation energy of spiroheterocyclic structure.* Dokl. Chem., vol. 396, no. 1, pages 99–102, 2004.

[Mizumo 04] T. Mizumo & H. Ohno. *Molten lithium sulfonimide salt having poly(propylene oxide) tail.* Polymer, vol. 45, pages 861–864, 2004.

[Monk 07] P.M.S. Monk, R.J. Mortimer & D.R. Rosseinsky. Electrochromism and electrochromic devices. Cambridge University Press, Cambridge, 2007.

[Monkhorst 76] H.J. Monkhorst & J.D. Pack. *Special points for Brillouin-zone integrations.* Phys. Rev. B: Condens. Matter, vol. 13, no. 12, pages 5188–5192, 1976.

[Morin 94] B.G. Morin, C. Hahm, J.S. Miller & A.J. Epstein. *Molecular magnets $V(tetracyanoethylene)_x \cdot y(solvent)$: applications to magnetic shielding.* J. Appl. Phys., vol. 75, no. 10, pages 5782–5784, 1994.

[Mort 82] J. Mort & G. Pfister. Electronic properties of polymers. Wiley, New York, 1982.

[Mount 98] A. Mount & A. Thomson. *Electrooxidation of N-methylindole.* J. Chem. Soc., Faraday Trans., vol. 94, no. 4, pages 553–558, 1998.

[Mount 99] A.R. Mount & M.T. Robertson. *The redox reaction and induced structural changes of 5-substituted indole films.* Phys. Chem. Chem. Phys., vol. 1, pages 5169–5177, 1999.

[Mueller-Westerhoff 87] U.T. Mueller-Westerhoff & B. Vance. *Dithiolenes and related species.* In G. Wilkinson, R. D. Gillard & J. A. McCleverty, editeurs, Compr. Coordin. Chem., volume 2, pages 595–631. Pergamon, Oxford, 1987.

[Mueller-Westerhoff 91] U.T. Mueller-Westerhoff, B. Vance & D.I. Yoon. *The synthesis of dithiolene dyes with strong near-IR absorption.* Tetrahedron, vol. 47, no. 6, pages 909–932, 1991.

[Muscat 01] J. Muscat, A. Wander & N.M. Harrison. *On the prediction of band gaps from hybrid functional theory.* Chem. Phys. Lett., vol. 342, pages 397–401, 2001.

[Mutule 05] I. Mutule & E. Suna. *Arylzinc species by microwave assisted Grignard formation - transmetallation sequence: application in the Negishi coupling.* Tetrahedron, vol. 61, pages 11168–11176, 2005.

[Noda 05] B. Noda, M. Katsuhara, I. Aoyagi, T. Mori, T. Taguchi, T. Kambayashi, K. Ishikawa & H. Takezoe. *Organic field-effect transistor based on biphenyl substituted TTF.* Chem. Lett., vol. 34, no. 3, pages 392–393, 2005.

[Noro 05] S. Noro, H.C. Chang, T. Takenobu, Y. Murayama, T. Kanbara, T. Aoyama, T. Sassa, T. Wada, D. Tanaka, S. Kitagawa, Y. Iwasa, T. Akutagawa & T. Nakamura. *Metal-organic thin-film transistor (MOTFT) based on bis(o-diiminobenzosemiquinonate) nickel(II) complex.* J. Am. Chem. Soc., vol. 127, pages 10012–10013, 2005.

[Nunes 07] J.P.M. Nunes, M.J. Figueira, D. Belo, I.C. Santos, B. Ribeiro, E.B. Lopes, R.T. Henriques, J. Vidal-Gancedo, J. Veciana, C. Rovira & M. Almeida. *Transition metal bisdithiolene complexes based on extended ligands with fused tetrathiafulvalene and thiophene moieties: new single-component molecular metals.* Chem. Eur. J., vol. 13, pages 9841–9849, 2007.

[Ohno 01] H. Ohno. *Molten salt type polymer electrolytes.* Electrochim. Acta, vol. 46, pages 1407–1411, 2001.

[O'Regan 91] B. O'Regan & M. Grätzel. *A low-cost, high-efficiency solar-cell based on dye-sensitized colloidal TiO_2 films.* Nature, vol. 353, no. 6346, pages 737–740, 1991.

[Paier 07] J. Paier, M. Marsman & G. Kresse. *Why does B3LYP hybrid functional fail for metals?* J. Chem. Phys., vol. 127, no. 2, pages 24103–24112, 2007.

[Pavlishchuk 00] V.V. Pavlishchuk & A.W. Addison. *Conversion constants for redox potentials measured versus different reference electrodes in acetonitrile solutions at 25°C.* Inorg. Chim. Acta, vol. 298, pages 97–102, 2000.

[Peiró 06] A.M. Peiró, P. Ravirajan, K. Govender, D.S. Boyle, P. O'Brien, D.D.C. Bradley, J. Nelson & J.R. Durrant. *Hybrid polymer/metal oxide solar cells based on ZnO columnar structures.* J. Mater. Chem., vol. 16, no. 21, pages 2088–2096, 2006.

[Perdew 92] J.P. Perdew, J.A. Chevary, S.H. Vosko, K.A. Jackson, M.R. Pederson, D.J. Singh & C. Fiolhais. *Atoms, molecules, solids, and surfaces - applications of the generalized gradient approximation for exchange and correlation.* Phys. Rev. B: Condens. Matter, vol. 46, no. 11, pages 6671–6687, 1992.

[Perdew 96] J.P. Perdew, K. Burke & Y. Wang. *Generalized gradient approximation for the exchange-correlation hole of a many-electron system.* Phys. Rev. B: Condens. Matter, vol. 54, no. 23, pages 16533–16539, 1996.

[Perger 03] W.F. Perger. *Calculation of band gaps in molecular crystals using hybrid functional theory.* Chem. Phys. Lett., vol. 368, pages 319–323, 2003.

[Peterson 84] I.R. Peterson & G.J. Russell. *An electron-diffraction study of ω-tricosenoid acid Langmuir-Blodgett films.* Philos. Mag. A, vol. 49, no. 3, pages 463–473, 1984.

[Peterson 90] I.R. Peterson. *Langmuir-Blodgett-films.* J. Phys. D: Appl. Phys., vol. 23, no. 4, pages 379–395, 1990.

[Peumans 04] P. Peumans & S.R. Forrest. *Separation of geminate charge-pairs at donor-acceptor interfaces in disordered solids.* Chem. Phys. Lett., vol. 398, pages 27–31, 2004.

[Pilia 09] L. Pilia, F. Artizzu, C. Faulmann, M.L. Mercuri, A. Serpe & P. Deplano. *Square-planar d^8 metal push-pull dithiolene complexes: synthesis and characterization of [Pd(Me_2pipdt)(dmit)].* Inorg. Chem. Commun., vol. 12, no. 6, pages 490–493, 2009.

[Podzorov 03] V. Podzorov, S.E. Sysoev, E. Loginova, V.M. Pudalov & M.E. Gershenson. *Single-crystal organic field effect transistors with the hole mobility $\sim$8 cm^2/V s.* Appl. Phys. Lett., vol. 83, no. 17, pages 3504–3506, 2003.

[Polo 04] A.S. Polo, M.K. Itokazu & N.Y.M. Iha. *Metal complex sensitizers in dye-sensitized solar cells.* Coord. Chem. Rev., vol. 248, no. 13-14, pages 1343–1361, 2004.

[Pope 99] M. Pope & C.E. Swenberg. Electronic processes in organic crystals and polymers. Oxford University Press, New York, 1999.

[Pozo-Gonzalo 02] C. Pozo-Gonzalo, R. Berridge, P.J. Skabara, E. Cerrada, M. Laguna, S.J. Coles & M.B. Hursthouse. *A new family of conjugated metallopolymers from electropolymerised bis[(terthiophene)dithiolene] complexes.* Chem. Commun., pages 2408–2409, 2002.

[Rabaça 09] S. Rabaça, A.C. Cerdeira, A.I.S. Neves, S.I.G. Dias, C. Mézière, I.C. Santos, L.C.J. Periera, M. Fournugué, R.T. Henriques & M. Almeida. *Complexes based on asymmetrically substituted pyridine-dithiolene ligands [M(4-pedt)$_2$] (M = Au, Cu, Ni; 4-pedt = 1-(pyridin-4-yl)-ethylene-1,2-dithiolate): synthesis, structure and physical properties.* Polyhedron, vol. 28, pages 1069–1078, 2009.

[Rassolov 98] V.A. Rassolov, J.A. Pople, M.A. Ratner & T.L. Windus. *6-31G* Basis set for atoms K through Zn.* J. Chem. Phys., vol. 109, no. 4, pages 1223–1229, 1998.

[Rassolov 01] V.A. Rassolov, M.A. Ratner, J.A. Pople, P.C. Redfern & L.A. Curtiss. *6-31G* Basis set for third-row atoms.* J. Comput. Chem., vol. 22, no. 9, pages 976–984, 2001.

[Razuvaev 78] G.A. Razuvaev, V.K. Cherkasov & G.A. Abakumov. *ESR investigation of copper(I) complexes with o-semiquinolate ligands.* J. Organomet. Chem., vol. 160, pages 361–371, 1978.

[Richardson 01] P.R. Richardson. *Spectroscopic and computational studies on a number of conformationally flexible molecules.* PhD thesis, University of Edinburgh, Department of Chemistry, 2001.

[Richardson 09] P.R. Richardson & A.C. Jones, 2009. (Submitted).

[Roberts-Bleming 03] S.J. Roberts-Bleming, G.L. Davies, M.J. Kalaji & P.J. Murphy. *Synthesis and photoreactivity of 4,5-dithienyl[1,3]dithiol-2-ones.* J. Org. Chem., vol. 68, pages 7115–7118, 2003.

[Robertson 00] N. Robertson, S. Parsons, E.J. Maclean, R.A. Coxall & A.R. Mount. *Preparation, X-ray structure and properties of a hexabrominated, symmetric indole trimer and its TCNQ adduct: a new route to functional molecular systems.* J. Mater. Chem., vol. 10, pages 2043–2047, 2000.

[Robertson 02] N. Robertson & L. Cronin. *Metal bis-1,2-dithiolene complexes in conducting or magnetic crystalline assemblies.* Coord. Chem. Rev., vol. 227, pages 93–127, 2002.

[Robertson 06] N. Robertson. *Optimizing dyes for dye-sensitized solar cells.* Angew. Chem. Int. Ed., vol. 45, pages 2338–2345, 2006.

[Roncali 92] J. Roncali. *Conjugated poly(thiophenes): synthesis, functionalization, and application.* Chem. Rev., vol. 92, no. 4, pages 711–738, 1992.

[Runge 84] E. Runge & E.K.U. Gross. *Density-functional theory for time-dependent systems.* Phys. Rev. Lett., vol. 52, no. 12, pages 997–1000, 1984.

[Sakai 06] K. Sakai, T. Hasegawa, M. Ichikawa & Y. Taniguchi. *Field-effect characteristics of a one dimensional platinum chain compound, bis(1,2-benzoquinonedioximato)platinum(II).* Chem. Lett., vol. 35, no. 3, pages 302–303, 2006.

[Sarangi 07] R. Sarangi, S.D. George, D.J. Rudd, R.K. Szilagyi, X. Ribas, C. Rovira, M. Almeida, K.O. Hodgson, B. Hedman & E.I. Solomon. *Sulfur K-edge X-ray absorption spectroscopy as a probe of ligand-metal bond covalency: metal vs ligand oxidation in copper and nickel dithiolenes.* J. Am. Chem. Soc., vol. 129, no. 8, pages 2316–2326, 2007.

[Sartain 66] D. Sartain & M.R. Truter. *The crystal structure of bis-(cis-1,2-diphenylethene-1,2-dithiolato)nickel.* Chem. Commun., vol. 12, page 382, 1966.

[Sasi 07] B. Sasi & K.G. Gopchandran. *Nanostructured mesoporous nickel oxide thin films.* Nanotechnology, vol. 18, pages 115613–115621, 2007.

[Schiefer 07] S. Schiefer, M. Huth, A. Dobrinevski & B. Nickel. *Determination of the crystal structure of substrate-induced pentacene polymorphs in fiber structured thin films.* J. Am. Chem. Soc., vol. 129, no. 34, pages 10316–10317, 2007.

[Schrauzer 62] G.N. Schrauzer & V. Mayweg. *Reaction of diphenylacetylene with nickel sulfides.* J. Am. Chem. Soc., vol. 84, page 3221, 1962.

[Schrauzer 65] G.N. Schrauzer & V.P. Mayweg. *Preparation, reactions, and structure of bisdithio-α-diketone complexes of nickel, palladium, and platinum.* J. Am. Chem. Soc., vol. 87, no. 7, pages 1483–1489, 1965.

[Sergeyev 07] S. Sergeyev, W. Pisula & Y.H. Geerts. *Discotic liquid crystals: a new generation of organic semiconductors.* Chem. Soc. Rev., vol. 36, pages 1902–1929, 2007.

[Servaas 89] P.C. Servaas, D.J. Stufkens, A. Oskam, P. Vernooijs, E.J. Baerends, D.J.A. Deridder & C.H. Stam. *Structural, spectroscopic, and theoretical studies of novel d^6 fac-$Re(CO)_3LBr$ (L = Dithiooxamide) complexes.* Inorg. Chem., vol. 28, no. 22, pages 4104–4113, 1989.

[Shaheen 01a] S.E. Shaheen, C.J. Brabec, S. Sariciftci, F. Padinger, T. Fromherz & J. Hummelen. *2.5% efficient organic plastic solar cells.* Appl. Phys. Lett., vol. 78, no. 6, pages 841–843, 2001.

[Shaheen 01b] S.E. Shaheen, D. Vangeneugden, R. Kiebooms, D. Vanderzande, T. Fromherz, F. Padinger, C.J. Brabec & N.S. Sariciftci. *Low band-gap polymeric photovoltaic devices.* Synthetic Metals, vol. 121, pages 1583–1584, 2001.

[Sirringhaus 99] H. Sirringhaus, P.J. Brown, R.H. Friend, M.N. Nielsen, K. Bechgaard, B.M.W. Langeveld-Voss, A.J.H. Spiering, R.A.J. Janssen, E.W. Meijer, P. Herwig & D.M. de Leeuw. *Two-dimensional charge transport in self-organized, high mobility conjugated polymers.* Nature, vol. 401, pages 685–688, 1999.

[Smits 06] E.C.P. Smits, T.D. Anthopoulos, S. Setayesh, E. van Veenendaal, R. Coehoorn, P.W.M. Blom, B. de Boer & D.M. de Leeuw. *Ambipolar charge transport in organic field-effect transistors.* Phys. Rev. B: Condens. Matter, vol. 73, page 205316, 2006.

[Sonogashira 02] K. Sonogashira. *Development of Pd-Cu catalyzed cross-coupling of terminal acetylenes with sp^2-carbon halides.* J. Organomet. Chem., vol. 653, pages 46–49, 2002.

[Spiccia 04] L. Spiccia, G.B. Deacon & C.M. Kepert. *Synthetic routes to homoleptic and heteroleptic ruthenium(II) complexes incorporating bidentate imine ligands.* Coord. Chem. Rev., vol. 248, pages 1329–1341, 2004.

[Stiefel 04] E.I. Stiefel. Dithiolene chemistry: synthesis, properties and applications, volume 52 of *Prog. Inorg. Chem.* John Wiley & Sons, New Jersey, 2004.

[Su 00] W. Su, M. Hong, J. Weng, R. Cao & S. Lu. *A semiconducting lamella polymer $[\{Ag(C_5H_4NS)\}_n]$ with a graphite-like array of silver(I) ions and its analogue with a layered structure.* Angew. Chem. Int. Ed., vol. 39, no. 16, pages 2911–2914, 2000.

[Sugimori 96] A. Sugimori, N. Tachiya, M. Kajitani & T. Akiyama. *Radical substitution in the nickeladithiolene ring in bis(1-phenyl-1,2-ethenedithiolato)nickel(0).* Organometallics, vol. 15, pages 5664–5668, 1996.

[Sundar 04] V.C. Sundar, J. Zaumseil, V. Podzorov, E. Menard, R.L. Willett, T. Someya, M.E. Gershenson & J.A. Rogers. *Elastomeric transistor stamps: reversible probing of charge transport in organic crystals.* Science, vol. 303, pages 1644–1646, 2004.

[Sung 02] K.-M. Sung & R.H. Holm. *Functional analogue reaction systems of the DMSO reductase isoenzyme family: probable mechanism of S-oxide reduction in oxo transfer reactions mediated by bis(dithiolene)-tungsten(IV,VI) complexes.* J. Am. Chem. Soc., vol. 124, no. 16, pages 4312–4320, 2002.

[Szilagyi 03] R.K. Szilagyi, B.S. Lim, T. Glaser, R.H. Holm, B. Hedman, K.O. Hodgson & E.I. Solomon. *Description of the ground state wave functions of Ni dithiolenes using sulfur K-edge X-ray absorption spectroscopy.* J. Am. Chem. Soc., vol. 125, no. 30, pages 9158–9169, 2003.

[Takahashi 01] T. Takahashi, K. i. Sakai, T. Yumoto, T. Akutagawa, T. Hasegawa & T. Nakamura. *Structure and electronic properties of bis[bis(methylthio)tetrathiafulvalenedithiolate]-gold(III) Langmuir-Blodgett films.* Thin Solid Films, vol. 393, pages 7–11, 2001.

[Tant 05] J. Tant, Y.H. Geerts, M. Lehmann, V. de Cupere, G. Zucchi, B.W. Laursen, T. Bjornholm, V. Lemaur, V. Marcq, A. Burquel, E. Hennebicq, F. Gardebein, P. Viville, D. Beljonne, R. Lazzaroni & J. Cornil. *Liquid crystalline metal-free phthalocyanines designed for charge and exciton transport.* J. Phys. Chem. B, vol. 109, no. 43, pages 20315–20323, 2005.

[Tomasi 05] J. Tomasi, B. Mennucci & R. Cammi. *Quantum mechanical continuum solvation models.* Chem. Rev., vol. 105, pages 2999–3093, 2005.

[Tsumura 86] A. Tsumura, H. Koezuka & T. Ando. *Macromoleclar electronic device: field-effect transistor with a polythiophene thin-film.* Appl. Phys. Lett., vol. 49, no. 18, pages 1210–1212, 1986.

[Ueda 98] K. Ueda, M. Goto, M. Iwamatsu, T. Sugimoto, S. Endo, N. Toyota, K. Yamamoto & H. Fujita. *Highly-conducting neutral copper complexes substituted with two tetrathiaflvalenyldithiolato groups.* J. Mater. Chem., vol. 8, no. 10, pages 2195–2198, 1998.

[Valade 05] L. Valade, D. de Caro, M. Basso-Bert, I. Malfant, C. Faulmann, C. de Bonneval & J.-P. Legros. *Thin films of transition metal-containing molecule-based materials: a highlight on electrochemically processed systems.* Coord. Chem. Rev., vol. 249, pages 1986–1996, 2005.

[Vickers 05] S.J. Vickers & M.D. Ward. *Facile preparation of a visible- and near-infrared-active electrochromic film by direct deposition of a ruthenium dioxolene complex on an ITO/glass surface.* Electrochem. Commun., vol. 7, no. 4, pages 389–393, 2005.

[Vlček Jr. 07] A. Vlček Jr. & S. Zális. *Modelling of charge-transfer transitions and excited states in d^6 transition metal complexes by DFT techniques.* Coord. Chem. Rev., vol. 251, no. 3-4, pages 258–287, 2007.

[Vogler 82] A. Vogler & J. Kisslinger. *Intervalence transfer between hexaaminecobalt(III) and hexacyanoruthenate(II).* Angew. Chem. Int. Ed., vol. 21, no. 1, pages 77–78, 1982.

[Vyas 10] R.N. Vyas & B. Wang. *Electrochemical analysis of conducting polymer thin films.* Int. J. Mol. Sci., vol. 11, pages 1956–1972, 2010.

[Wada 07] H. Wada, T. Taguchi, B. Noda, T. Kambayashi, T. Mori, K. Ishikawa & H. Takezoe. *Air stability of n-channel organic transistors based on nickel coordination compounds.* Org. Electron., vol. 8, pages 759–766, 2007.

[Waltman 84a] R.J. Waltman & J. Bargon. *Reactivity/structure correlations for the electropolymerization of pyrrole: an INDO/CNDO study of the reactive sites of oligomeric radical cations.* Tetrahedron, vol. 40, no. 20, pages 3963–3970, 1984.

[Waltman 84b] R.J. Waltman, A.F. Diaz & J. Bargon. *Substituent effects in the electropolymerization of aromatic heterocyclic compounds.* J. Phys. Chem., vol. 88, no. 19, pages 4343–4346, 1984.

[Waltman 86] R.J. Waltman & J. Bargon. *Electrically conducting polymers: a review of the electropolymerization reaction, of the effect of chemical structure on polymer film properties, and of applications towards technology.* Can. J. Chem., vol. 64, pages 76–95, 1986.

[Wang 01] K. Wang & E.I. Stiefel. *Toward separation and purification of olefins using dithiolene complexes: an electrochemical approach.* Science, vol. 291, pages 106–109, 2001.

[Wang 05] S. Wang, E.K. Todd, M. Birau, J. Zhang, X. Wan & Z.Y. Wang. *Near-infrared electrochromism in electroactive pentacenediquinone-containing poly(aryl ether)s.* Chem. Mater., vol. 17, pages 6388–6394, 2005.

[Ward 05] M.D. Ward. *Near-infrared electrochromic materials for optical attenuation based on transition-metal coordination complexes.* J. Solid State Electrochem, vol. 9, pages 778–787, 2005.

[Waters 64] J.H. Waters, R. Williams, H.B. Gray, G.N. Schrauzer & H.W. Finck. *Tris(cis-1,2-stilbenedithiolato)vanadium(VI) or tris(dithiobenzil)vanadium(O). A novel vanadium complex.* J. Am. Chem. Soc., vol. 86, pages 4198–4199, 1964.

[Waters 06] T. Waters, H.-K. Woo, X.-B. Wang & L.-S. Wang. *Probing the intrinsic electronic structure of the bis(dithiolene) anions $[M(mnt)_2]^{2-}$ and $[M(mnt)_2]^{1-}$ (M = Ni, Pd, Pt; mnt = 1,2-$S_2C_2(CN)_2$) in the gas phase by photoelectron spectroscopy.* J. Am. Chem. Soc., vol. 128, no. 13, pages 4282–4291, 2006.

[Winn 01] M. Winn, E.B. Reilly, G. Liu, J.R. Huth, H.-S. Jae, J. Freeman, Z. Pei, Z. Xin, J. Lynch, J. Kester, T.W. von Geldern, S. Leitza, P. DeVries, R. Dickinson, D. Mussatto & G.F. Okasinski. *Discovery of novel p-aryltohio cinnamides as antagonists of leukocyte function-associated antigen-1/intercellular adhesion molecule-1 interaction. 4. Structure-activity relationship of substituents on the benzene ring of the cinnamide.* J. Med. Chem., vol. 44, no. 25, pages 4393–4403, 2001.

[Wu 07] C.-G. Wu, M.-I. Lu, S.-J. Chang & C.-S. Wei. *A solution-processable high-coloration-efficiency low-switching-voltage electrochromic polymer based on polycyclopentadithiophene.* Adv. Funct. Mater., vol. 17, pages 1063–1070, 2007.

[Wudl 72] F. Wudl, D. Wobschall & E.J. Hufnagel. *Electrical conductivity by the bis-1,3-dithiole-bis-1,3-dithiolium system.* J. Am. Chem. Soc., vol. 94, no. 2, pages 670–672, 1972.

[Würthener 01] F. Würthener. *Plastic transistors reach maturity for mass applications in microelectronics.* Angew. Chem. Int. Ed., vol. 40, no. 6, pages 1037–1039, 2001.

[Yamada 04] J.-I. Yamada, H. Akutsu, H. Nishikawa & K. Kikuchi. *New trends in the synthesis of π-electron donors for molecular conductors and superconductors.* Chem. Rev., vol. 104, no. 11, pages 5057–5083, 2004.

[Yamashita 09] Y. Yamashita. *Organic semiconductors for organic field-efect transistors.* Sci. Technol. Adv. Mater., vol. 10, no. 2, pages 024313–024321, 2009.

[Yen 09] H.-J. Yen & G.-S. Liou. *Solution-processable novel near-infrared electrochromic aromatic polyamides based on electroactive tetraphenyl-p-phenylenediamine moieties.* Chem. Mater., vol. 21, pages 4062–4070, 2009.

[Zaumseil 07] J. Zaumseil & H. Sirringhaus. *Electron and ambipolar transport in organic field-effect transistors.* Chem. Rev., vol. 107, no. 4, pages 1296–1323, 2007.

[Zhao 01] Y. Zhao, M. Hong, Y. Liang, R. Cao, J. Weng, S. Lu & W. Li. *A paramagnetic lamellar polymer with a high semiconductivity.* Chem. Commun., pages 1020–1021, 2001.

[Zheng 09] Y. Zheng, J. Zheng, L. Dou, W. Qiao & X. Wan. *Synthesis and characterization of a novel kind of near-infrared electrochromic polymers containing an anthraquinone imide group and ionic moieties.* J. Mater. Chem., vol. 19, pages 8470–8477, 2009.

[Zhou 06] Y. Zhou, Y. Yuan, J. Lian, J. Zhang, H. Pang, L. Cao & X. Zhou. *Mild oxygen plasma treated PEDOT:PSS as anode buffer layer for vacuum deposited organic light-emitting diodes.* Chem. Phys. Lett., vol. 427, pages 394–398, 2006.

Publications

The work presented in this thesis has lead to the following publications:

- S. Dalgleish, C. Morrison, D. Middlemiss, A. Mount, A. Collins, L. Pilia, A. Serpe, M. Mercuri, S. Roberts-Bleming, A. Charlton, P. Deplano, P. J. Murphy, and N. Robertson. Synthesis, structure and spectroscopic properties of a new class of polymerisable nickel dithiolenes, *J. Mater. Chem.*, 2009 (19), pp. 6194-6200.
- S. Dalgleish and N. Robertson. A stable near IR switchable electrochromic polymer based on an indole-substituted nickel dithiolene, *Chem. Commun.*, 2009, pp. 5826-5828.
- S. Dalgleish and N. Robertson. Electropolymerisable dithiolene complexes, *Coord. Chem. Rev.*, 2010 (254), pp. 1549-1558.
- S. Dalgleish, H. Yoshikawa, M. M. Matsushita, K. Awaga, and N. Robertson. Electrodeposition as a superior route to a thin film molecular semiconductor, *Chem. Sci.*, (in press), 2010.